

**Study of Electromagnetic Interactions in the MicroBooNE Liquid Argon
Time Projection Chamber**

David Caratelli

Submitted in partial fulfillment of the
requirements for the degree of
Doctor of Philosophy
in the Graduate School of Arts and Sciences

COLUMBIA UNIVERSITY

2018

ABSTRACT

Study of Electromagnetic Interactions in the MicroBooNE Liquid Argon Time Projection Chamber

David Caratelli

This thesis presents results on the study of electromagnetic (EM) activity in the MicroBooNE Liquid Argon Time Projection Chamber (LArTPC) neutrino detector. The LArTPC detector technology provides bubble-chamber like information on neutrino interaction final states, necessary to perform precision measurements of neutrino oscillation parameters. Accelerator-based oscillation experiments heavily rely on the appearance channel $\nu_\mu \rightarrow \nu_e$ to make such measurements. Identifying and reconstructing the energy of the outgoing electrons from such interactions is therefore crucial for their success. This work focuses on two sources of EM activity: Michel electrons in the 10-50 MeV energy range, and photons from π^0 decay in the ~ 30 -300 MeV range. Studies of biases in the energy reconstruction measurement, and energy resolution are performed. The impact of shower topology at different energies is discussed, and the importance of thresholding and other reconstruction effects on producing an asymmetric and biased energy measurement are highlighted. This work further presents a study of the calorimetric separation of electrons and photons with a focus on the shower energy dependence of the separation power.

Contents

List of Figures	v
List of Tables	xi
Acknowledgements	xiv
1 Introduction	1
2 Neutrino Physics and Oscillations	5
2.1 Neutrinos in the Standard Model	5
2.2 Neutrino Oscillation Physics	7
2.3 Counting Neutrinos	14
2.4 The MicroBooNE Experiment: Motivation	21
2.5 Upcoming Accelerator-Based Oscillation Physics Program	22
3 Astrophysical Neutrinos from Supernovae Bursts	24
3.1 Supernova Burst Dynamics	24
3.2 Supernova Neutrino Detection	26
3.3 Prospects for Supernova Neutrino Detection with large-scale LArTPC Detectors . .	28
4 The MicroBooNE Detector	33
4.1 Energy Loss in Liquid Argon	34
4.2 The MicroBooNE Time Projection Chamber	35
4.3 Light Collection System	39
4.4 Readout Electronics	40

4.5	Beam Timing	46
4.6	Detector Operations	46
5	The Booster Neutrino Beamline	48
5.1	The 8 GeV Booster Proton Beam	49
5.2	Beam Target and Focusing Horn	51
5.3	Beam Composition	53
6	Energy Loss of Electrons and Photons in Liquid Argon	55
6.1	Charged Particle Energy Loss in Liquid Argon	55
6.2	Electron Energy Loss	56
6.3	Photon Energy Loss	59
6.4	Summary and Implications for EM Reconstruction in LAr	61
7	Measurement of Electromagnetic Backgrounds in a Surface LArTPC	63
7.1	Methodology	64
7.2	Cosmogenic Background Rate Measurement	66
7.3	Cosmic-Ray Backgrounds to Supernova Neutrinos Burst	68
7.4	Conclusions	70
8	Study of EM Activity in the 10-50 MeV range with Michel Electrons	72
8.1	Electron and Photon Energy Loss at 0-50 MeV	73
8.2	Michel Electron Reconstruction	75
8.3	Energy Reconstruction	84
8.4	Effect of Radiative Photons on Energy Reconstruction: Monte Carlo Study	86
8.5	Reconstructed Michel-Electron Energy Spectrum from Data	89
8.6	Conclusions	92
9	Selection and Reconstruction of π^0 Events from Charged Current ν_μ Interactions	95
9.1	Importance of π^0 Channels in ν Interactions.	96
9.2	π^0 Production In Neutrino Interactions	97
9.3	ν_μ Charge Current π^0 Interaction Selection and Reconstruction	100

10 Studies of EM Shower Energy Reconstruction with π^0 induced Photons	116
10.1 Study of Energy Reconstruction Biases in EM Shower Reconstruction	117
10.2 Hand Clustering	122
10.3 Conclusions	130
11 Calorimetric Separation of Electrons and Photons	133
11.1 Limitations to Calorimetric e/γ Separation	135
11.2 Truth Studies of Photon dE/dx	136
11.3 Measurement of dE/dx in data	139
11.4 Conclusions	140
12 Conclusions	142
Bibliography	145
Appendix A Beam Trigger	153
Appendix B TPC Signal Reconstruction	157
B.1 TPC Signal Processing	157
B.2 Hit Finding	159
Appendix C Detector Energy Calibration	161
C.1 Ionization Energy Loss and Signal Formation	161
C.2 Absolute Energy Calibration With Stopping Cosmic-Ray Muons	165
C.3 Calibration of Non-Uniformities in Detector Response	177
C.4 Energy Calibration for EM Showers	179
Appendix D Michel Electron Reconstruction: Supplemental Material	185
Appendix E Track-Shower Separation	190
E.1 Cosmic Removal	190
Appendix F $\pi^0 \rightarrow \gamma\gamma$ Shower Reconstruction: Supplemental Material	198
F.1 Challenges of Reconstructing $\mathcal{O}(100\text{ MeV})$ Photons in a Surface LArTPC	199

F.2	Track-Shower Separation	201
F.3	Two-Dimensional Clustering and 3D Shower Reconstruction	203
F.4	Two Dimensional Clustering	203
F.5	Cluster Matching	205
F.6	Photon Re-Clustering	207
F.7	Shower Reconstruction	208
F.8	Shower Quality Filters	211
Appendix G Modeling Energy Loss Impact on EM Shower Energy Resolution		217

List of Figures

2.1	Accelerator oscillation experiment setup.	10
2.2	Uncertainties on mixing errors and mass splittings.	13
2.3	LSND Results.	19
2.4	MiniBooNE ν_e and $\bar{\nu}_e$ Results.	21
2.5	SBN experimental Setup.	22
2.6	DUNE experimental setup.	23
3.1	Kamiokande neutrino events from supernova 1987a.	27
3.2	SN1987a neutrino candidates from IMB	28
3.3	Neutrino-argon cross-sections at supernova energies.	30
3.4	Neutrino energy spectrum expectation for SNB neutrinos.	30
4.1	MicroBooNE TPC schematic drawing.	35
4.2	MicroBooNE TPC and wire-planes.	36
4.3	Signal formation cartoon	38
4.4	Neutrino interaction event display.	38
4.5	Photos of MicroBooNE's photomultiplier system.	39
4.6	Noise levels versus argon temperature.	41
4.7	PMT splitter circuit diagram.	42
4.8	Examples of PMT waveforms.	43
4.9	MicroBooNE readout format.	45
4.10	Beam and cosmic-discriminated PMT waveforms.	45
4.11	BNB neutrino beam timing.	47

4.12	Collected protons on target.	47
5.1	Fermilab accelerator complex and Booster target hall.	49
5.2	Beam injection to Booster.	51
5.3	Beam bunch timing.	51
5.4	Booster horn.	52
5.5	Neutrino flux prediction at MicroBooNE	54
6.1	Charged particle energy loss in LAr.	56
6.2	Electron energy loss in LAr.	57
6.3	Kinematic variables of bremsstrahlung interaction.	58
6.4	Cross-section for photons in argon.	59
6.5	Energy asymmetry for photon pair-production.	61
6.6	Photon absorption length in argon.	62
7.1	EM Background analysis method cartoon.	65
7.2	Impact Parameter distribution in TPC.	66
7.3	Fractional TPC coverage vs. Impact Parameter.	66
7.4	Rate vs. Impact Parameter for different energy thresholds.	67
7.5	Background rate in function of weighted distance to cosmic-ray muons.	68
7.6	Measured EM background radial decay constants.	68
7.7	Rate of uniformly distributed backgrounds vs. energy threshold.	69
7.8	Integrated event rate for an example of a simulated SNB burst.	70
7.9	Neutronization and steady SNB ν_e rate vs. uniform EM background rate.	71
8.1	Ionization vs. total energy loss for Michel electrons.	74
8.2	Energy spectrum and radial distrib. of Michel bremsstrahlung photons.	75
8.3	Michel energy spectrum for free and bound decays.	76
8.4	Michel electron energy spectrum with and without radiative photons.	77
8.5	Event display of candidate Michel electron from data.	78
8.6	Event display of reconstructed candidate Michel electron.	79
8.7	Bragg peak Michel electron algorithmic identification.	80

8.8	Event display of Michel electron candidate with tagged radiative photons.	82
8.9	Sample purity and vertex resolution for Michel electrons from simulation.	83
8.10	Michel electron reconstruction efficiency.	85
8.11	Ionization energy resolution for Michel electrons from simulation.	88
8.12	Michel electron energy resolution without photon tagging for simulation.	89
8.13	Michel electron energy resolution including photon tagging from simulation.	90
8.14	Fractional energy resolution vs. Michel electron energy with and without photon tagging.	91
8.15	Reconstructed Michel electron energy spectrum in data.	92
8.16	Reconstructed radiative photon energy spectrum from data.	93
9.1	Final state and secondary interactions in neutrino interactions.	98
9.2	Energy distribution of photons from BNB π^0 s.	99
9.3	Event display of EM showers from a 2 π^0 CC ν_μ event	103
9.4	Event display of Reconstructed EM showers.	105
9.5	EM shower reconstruction efficiency.	106
9.6	Reconstructed vs. true photon energy.	107
9.7	π^0 energy resolution.	110
9.8	Example of backgrounds from selection on data.	112
9.9	Reconstructed π^0 mass on data and simulation.	113
9.10	Reconstructed conversion distance for photons.	113
9.11	Data-MC comparison of reconstructed kinematic variables for π^0 s.	114
10.1	Energy spectrum of one-hit photon clusters in reconstructed EM showers.	118
10.2	Impact of hit-thresholding on EM shower energy reconstruction.	119
10.3	Impact of clustering on EM shower energy reconstruction.	119
10.4	Reconstructed π^0 mass from simulated BNB events with cosmics.	120
10.5	Data and simulation reconstructed π^0 mass.	121
10.6	Reconstructed mass with human-clustered charge.	123
10.7	Reconstructed mass with human-clustering, zoomed in.	124
10.8	Conversion distance for reconstructed γ showers.	124
10.9	Fractional containment of EM shower energy vs. radial integration.	126

10.10	Fractional containment of shower energy vs. charge integration radius from vertex. . .	127
10.11	π^0 mass bias and resolution vs. radial charge integration distance.	128
10.12	Individual photons in EM gamma shower.	128
10.13	Energy spectrum of individual photons in reconstructed EM showers.	129
10.14	Fitted energy spectrum of individual photons from EM showers.	130
10.15	γ fractional energy collected vs. photon threshold.	130
10.16	Bias and resolution on reconstructed mass vs. photon threshold.	131
11.1	Event displays of ν_e and π^0 candidate events from data.	134
11.2	Example of asymmetric $\gamma \rightarrow e^+ + e^-$ decay from data.	135
11.3	Energy asymmetry ($ E_{e^+} - E_{e^-} / E_{e^+} + E_{e^-} $) and opening angle of outgoing pair- production e^+/e^-	136
11.4	Measured dE/dx from simulation on γ photons.	137
11.5	Measured dE/dx vs. lower energy electron energy and e^+/e^- opening angle.	138
11.6	Measured dE/dx vs. photon shower energy.	138
11.7	dE/dx on pair-production photons for different radial integration distance values. . . .	139
11.8	Measured dE/dx for data photon showers.	140
11.9	Photon mis-identification rate as a function of photon energy.	141
A.1	Example PMT waveform with overlaid PHMAX determination algorithm output. . .	154
A.2	PHMAX sum from all 32 PMTs.	155
A.3	Software Trigger firing rate vs. PE threshold.	156
B.1	TPC signals before and after noise-removal.	158
B.2	TPC signals before and after deconvolution.	159
B.3	Signal processing and hit reconstruction examples.	160
C.1	Ion recombination vs. dE/dx.	163
C.2	Energy loss for muons in argon.	165
C.3	Angular dependence of dE/dx most probable value.	166
C.4	Truncated mean muon charge profile.	167
C.5	Truncated mean stopping muon profile example.	169

C.6	Distribution of Bragg peak selection metrics for all and stopping muon samples.	170
C.7	Time and position distributions for all and stopping muon samples.	171
C.8	Reconstructed muon end point resolution and sample purity after cuts.	172
C.9	Muon energy loss vs. residual range profile.	173
C.10	χ^2 minimization for gain extraction.	174
C.11	Examples of fits to dE/dx straddling distributions.	175
C.12	Measured dE/dx MPV vs. theory.	175
C.13	Calorimetry vs. range based energy measurement.	176
C.14	Angular dependence of dE/dx MPV.	177
C.15	Angular variation of detector response.	179
C.16	YZ variation of detector response.	179
C.17	Energy loss and recombination for electrons in LAr.	181
C.18	Recombination simulation compared to theory.	183
C.19	Recombination impact on EM showers.	184
D.1	Ionization only fractional energy resolution vs. true Michel electron energy.	186
D.2	Michel electron energy resolution vs. true energy excluding radiative photons in re-constructed energy.	187
D.3	Michel electron energy resolution vs. true energy including radiative photons.. . . .	188
D.4	χ^2 showing level of data-simulation Michel energy spectrum agreement.	189
E.1	Example event before and after cosmic track removal.	191
E.2	Impact parameter cut for cosmic track removal.	192
E.3	Vertex opening angle cut for cosmic track removal.	192
E.4	Example event before and after δ -ray removal.	193
E.5	Truncated Local Linearity and Summed Square Variance metrics for linearity mea- surement.	195
E.6	Impact of vertex-proximity and TLL cuts on neutrino track removal.	195
E.7	TLL vs. cluster hits and slope for π^0 s and tracks.	196
E.8	Impact of vertex and SSV cuts on neutrino track removal.	197

F.1	Candidate π^0 event displays.	200
F.2	Candidate π^0 event display.	201
F.3	Example event displays of EM activity at different energies.	201
F.4	Impact of track-shower separation on different samples.	203
F.5	Photon cluster tagging algorithm.	204
F.6	Clustered π^0 event display.	206
F.7	Plane-matching algorithm.	207
F.8	Charge re-clustering algorithm.	209
F.9	Shower containment energy correction.	211
F.10	Reconstructed 3D showers from π^0 event.	212
F.11	EM shower reconstruction efficiency.	213
F.12	Angular resolution of reconstructed showers.	214
F.13	Reconstructed vs. true photon energy.	214
F.14	Fractional energy resolution distributions at different true photon energies.	215
F.15	Fractional energy resolution vs. true photon energy.	216
G.1	Gaussian plus one-tail exponential function for different input parameters.	218
G.2	Fraction of distribution modeled by exponential vs. exponential constant.	219

List of Tables

2.1	Neutrino oscillation mixing angles and mass splittings.	12
9.1	π^0 selection cuts.	108
9.2	Breakdown of selected π^0 events.	108
C.1	Efficiency and purity for cuts in stopping muon selection.	172
F.1	Evaluation of track-shower hit-removal performance.	203

List of Abbreviations

ADC	Analog Digital Conversion
ASIC	Application-Specific Integrated Circuit
BNB	Booster Neutrino Beamline
CC	Charged Current
CE ν NS	Coherent Electron Neutrino Nucleus Scattering
CKM	Cabibbo-Kobayashi-Maskawa Matrix
CP	Charge-Parity
DC	Direct Current
DIS	Deep Inelastic Scattering
DUNE	Deep Underground Neutrino Experiment
EM	Electromagnetic
FEM	Front-End Module
FPGA	Field-Programmable Gate Array
FSI	Final State Interactions
HG / LG	High Gain / Low Gain
HV	High Voltage
IBD	Inverse Beta Decay
LAr	Liquid Argon
LArTPC	Liquid Argon Time Projection Chamber
LEE	Low Energy Excess
LINAC	Linear Accelerator
LSND	Liquid Scintillator Neutrino Detector
MIP	Minimally Ionizing Particle
NC	Neutral Current
PMT	PhotoMultiplier Tubes
PE	Photoelectron
PMNS	Pontecorvo-Maki-Nakagawa-Sakata Matrix
POT	Protons on Target
QE	Quasi-Elastic
QED	Quantum Electrodynamics
RES	Resonant Interaction

RFQ	Radio Frequency Quadrupole
RMS	Root Mean Square
RWM	Resistive Wall Monitor
SBN	Short Baseline Neutrino program
SM	Standard Model
SNB	Supernova Burst
SSV	Summed Square Variance
TDC	Time Digital Conversion
TDR	Technical Design Report
TLL	Truncated Local Linearity
TPB	Tetraphenyl Butadiene
TPC	Time Projection Chamber
VEV	Vacuum Expectation Value
VUV	Vacuum Ultra-Violet

Acknowledgements

I would like to thank my Ph.D. advisor, Mike Shaevitz, for his constant support. You have been a wonderful mentor from whom I have learned so much. Thank you in particular for your warmth and kindness, which made these years fun as well as fruitful.

I am honored to have been affiliated with Columbia Universities' Nevis Laboratories, working with so many talented people in a truly beautiful place. I would like to thank the staff, fellow students, and other researchers I have shared my time at the lab with, and in particular the members of the Neutrino group for the many discussions, lessons, and conversations which have helped form me as a scientist. From my time as a graduate student, I will especially cherish my experiences at Nevis.

I have been fortunate to work in an environment as diverse and stimulating as Fermilab. I could not think of a better way to form myself as an experimental particle physicist than by working on the MicroBooNE experiment at this world-class facility. To the countless people who have taken some of their time to train me or teach me something new, thank you.

Finally, thank you to my family for their encouragement and for giving me the opportunity to explore my interests. I am very fortunate.

Chapter 1

Introduction

The field of neutrino physics has rapidly evolved over the past two decades thanks to many successful experiments which have established that neutrinos have mass and oscillate between different flavors. More recently, many of the neutrino mixing parameters which govern oscillations have been precisely measured. If two decades ago the fundamental question being asked were whether neutrinos oscillate, today research efforts focus on exploring the implication of neutrino mass for Beyond the Standard Model (BSM) physics:

- Is the three-flavor neutrino picture complete? Are there additional, “sterile” neutrino states?
- How do neutrinos acquire their mass? Are neutrinos Dirac or Majorana particles?
- Do neutrinos and anti-neutrinos oscillate differently, implying a violation of the fundamental charge \times parity (CP) symmetry which could help explain the dominance of matter over anti-matter in the early universe?

All three questions lead to different, more technical ones, related to how to build and instrument detectors capable of reaching these physics goals. The first and last question can be addressed by precision measurements of neutrino oscillations. Neutrino oscillations manifest themselves experimentally as a change in the flavor content of a neutrino beam which depends on the neutrino energy and its propagation time. Measuring neutrino oscillation parameters thus requires the ability to identify neutrinos of different flavors and record their energy. Fermilab’s short- and long-baseline neutrino programs aim to perform measurements of neutrino oscillations which hope to conclusively address these two questions. To do so, Liquid Argon Time Projection Chamber (LArTPC)

detectors have been chosen for their fine-grained spatial and calorimetric resolution which can be used to accurately identify particles produced in neutrino interactions with low detection thresholds. Key to performing these measurements is the detection and reconstruction of ν_e events which comprise the oscillation appearance signal in a mostly ν_μ beam. Doing this requires being able to reconstruct the electromagnetic (EM) activity produced by the electron created in the neutrino interaction, and the ability to isolate backgrounds to this channel produced by other sources of EM activity. This thesis presents a study of EM interactions in argon from the MicroBooNE detector, with a focus on understanding the impact of different effects on their energy reconstruction. This is achieved by studying two sources of EM activity: Michel electrons produced by the decay-at-rest of cosmic-ray muons entering the detector, and photons from the decay of neutral pions produced in neutrino interactions.

Michel electrons have an energy which spans from 0 to ~ 60 MeV. At these energies electrons transition from depositing most of their energy via ionization to being dominated by radiative losses, making them particularly interesting to study. Additionally, this is an important energy range for signatures of electron neutrinos produced by supernovae bursts. The work presented here quantifies the impact of radiative photons on the energy measurement of such electrons. This is the first time that radiative photons are studied in a LArTPC for electrons at these energies. The results of this analysis shows how a better energy determination can be performed by including radiative energy losses in the electron energy definition, while at the same time pointing out the challenges of identifying such radiative photons. This work can help guide detector design and analysis strategies, and provide valuable input to the realistic study of the impact of detector and reconstruction effects on supernova neutrino and other low energy physics with LArTPC detectors.

The study of photons from π^0 decay allows to expand the energy range explored up to several hundred MeV. Relying on the invariant π^0 mass which can be reconstructed from the γ kinematics the biases and energy smearing associated with the photon energy reconstruction can be assessed in data and compared to simulation. The work included in this thesis presents the reconstruction employed to identify charged current ν_μ events with one π^0 in the final state, followed by detailed studies of EM energy reconstruction performed using photons from this sample. We present and discuss the two main contributions to energy bias and energy resolution smearing which impact EM energy reconstruction in a LArTPC: loss of charge caused by small energy depositions which are

below threshold and a deficit in the reconstructed charge attributable to the inefficiency in tagging all energy deposited by the EM shower. This second contribution is impacted by the significant spatial extent over which EM showers propagate, as well as the difficulty in distinguishing energy deposition from EM activity vs. ionizing tracks at low energies. The challenge of recovering the full EM shower energy is particularly difficult for LArTPC detectors located on the surface, which are impacted by significant cosmogenic backgrounds. We are able to account for the impact of these effects on the biased energy measurement, and show a level of agreement between data and simulation of order $\sim 5\%$.

In addition to the low detection threshold, LArTPCs are often associated with the ability to perform particle identification relying on calorimetric information. Distinguishing the final-state particles produced in neutrino interactions is necessary to recover the neutrino's flavor. Photons from neutral current interactions have in the past been the major background to ν_e appearance measurements. Topological and calorimetric information from a LArTPC detector can be used to separate electrons from photons, thus reducing the photon background. A study of the initial energy loss of photons from π^0 decay is presented, focusing on the characterization of potential backgrounds from photons to an electron selection. We find an energy dependence in the contamination of photons mis-identified as electrons, and associate this background to photons which undergo asymmetric pair-production. This energy-dependent background may, depending on the analysis, play a more significant role than Compton-scattering events to the total rate of backgrounds to a ν_e selection.

The work included in this thesis is presented as follows. Chapter 2 contains an overview of neutrino interactions and oscillations, describing the current state of the field and open questions to be addressed by upcoming experiments. Chapter 3 outlines the role neutrinos play in supernovae bursts and how these can be experimentally detected in LArTPC detectors. Much of the work described in this thesis at lower energies has implications for the detection and reconstruction of neutrinos from supernovae bursts. Chapters 4 and 5 describe the MicroBooNE detector and Booster Neutrino Beamline respectively. In chapter 6 an overview of the well-known theory of electron and photon energy loss in matter, and how this manifests itself in liquid argon is presented. Chapter 7 provides a measurement of background rates for EM interactions in a LArTPC on the surface. Chapter 8 presents results from the measurement of Michel electrons and studies of their energy reconstruction, and is followed by chapters 9 and 10 which present respectively the selection and

reconstruction employed to reconstruct γ photons from π^0 decay, and studies on EM energy resolution and bias obtained from this sample. A final study on the energy-dependence of the ability to calorimetrically separate electrons and photons in liquid argon is presented in chapter 11. Finally, results from this thesis are summarized in a concluding chapter (12).

Chapter 2

Neutrino Physics and Oscillations

This chapter reviews the current status of neutrino physics and the role these particles play in our understanding of the Standard Model (SM) and the physics which lies beyond it. A theoretical overview of neutrinos and their role in the standard model is presented in section 2.1, with a more detailed discussion of neutrino oscillations following in section 2.2. A discussion on the number of neutrino flavors, with experimental constraints and hints for additional neutrino states is presented in section 2.3.

2.1 Neutrinos in the Standard Model

The neutrino's role in the standard model is governed by the Electroweak (EW) theory, which originates from the $SU(2) \times U(1)$ gauge groups and dictates interactions amongst fermions. The fermion fields ψ_i represent particles under this theory. The index i stands for each of the three known generations of fermions. This field is composed of a left-handed and right-handed component, which transform as doublets and singlets respectively under $SU(2)$. The left-handed doublet fields are represented as

$$\Psi_i = \begin{pmatrix} \nu_i \\ l_i^- \end{pmatrix}, \quad \begin{pmatrix} u_i \\ d'_i \end{pmatrix} \quad (2.1)$$

with $d'_i = \sum_j V_{ij} d_j$ and V the CKM mixing matrix. The first term in equation 2.1 denotes the neutrino (ν_i) and charged lepton l_i^- , with the second term representing the quarks. EW symmetry

is broken by the addition of a scalar Higgs doublet $\phi = (\phi^+, \phi^0)$ with a potential

$$V(\phi) = \mu^2 \phi^\dagger \phi + \frac{\lambda^2}{2} (\phi^\dagger \phi)^2. \quad (2.2)$$

The Higgs field develops a vacuum expectation value (VUV) of $v/\sqrt{2}$ with $v \sim 246$ GeV. After symmetry breaking the Lagrangian for the fermion field becomes

$$\mathcal{L} = \sum_i \bar{\psi}_i \left(i \not{\partial} - m_i - \frac{m_i H}{v} \right) \psi_i \quad (2.3)$$

$$= -\frac{g}{2\sqrt{2}} \sum_i \bar{\Psi}_i \gamma^\mu (1 - \gamma^5) (T^+ W_\mu^+ + T^- W_\mu^-) \Psi_i \quad (2.4)$$

$$= -e \sum_i Q_i \bar{\psi}_i \gamma^\mu \psi_i A_\mu \quad (2.5)$$

$$= \frac{g}{2 \cos \theta_W} \sum_i \bar{\psi}_i \gamma^\mu (g_V^i - g_A^i \gamma^5) \psi_i Z_\mu. \quad (2.6)$$

With θ_W the Weinberg mixing angle, $\tan(\theta_W)$ equal to g'/g , g' and g the coupling constants to the gauge bosons in the theory, and e , the electric charge, equal to $g \sin \theta_W$. The first term of equation 2.3 includes a Yukawa coupling of the Higgs field to the fermion fields ($m_i H/v$) which leads to fermion masses proportional to the Higgs VUV, with the proportionality constant an experimental observable. The boson masses are given by $M_W = 1/2gv$, $M_Z = M_W/\cos \theta_W$, and $M_\gamma = 0$, leaving the photon as the only massless gauge boson in the theory after symmetry breaking. The third term gives rise to electromagnetic interactions (described by QED theory). The second and fourth terms describe charged (CC) and neutral current (NC) weak interactions respectively.

In the example of muon decay, following the notation of Halzen and Martin [1], the CC interaction term can be written as:

$$\left(\frac{g}{\sqrt{2}} \bar{u}_{\nu_\mu} \gamma^\sigma \frac{1}{2} (1 - \gamma^5) u_\mu \right) \frac{1}{M_W^2 - q^2} \left(\frac{g}{\sqrt{2}} \bar{u}_e \gamma_\sigma \frac{1}{2} (1 - \gamma^5) u_{\nu_e} \right) \quad (2.7)$$

The weak coupling g , in contrast to the QED coupling e has units of GeV^{-2} , and the interaction strength is modulated by the term $1/(M_W^2 - q^2)$. This formalism arises from the massive nature of

the W boson. At low momentum transfer q^2 the coupling can be expressed as

$$\frac{G}{\sqrt{2}} = \frac{g^2}{8M_W^2} \quad (2.8)$$

with G referred to as G -Fermi, or G_F . This low momentum approximation converges to Fermi's original treatment of weak interactions as point-like four particle interactions. From equation 2.8 we can also see how the term weak attributed to such interactions arises not from a difference in the magnitude of the couplings g and e , which differ by the sine of the Weinberg angle, but rather by the presence of the term $M_W \sim 80$ GeV in the denominator.

The first term in equation 2.3 contains a Dirac mass term. The absence of a right-handed neutrino in the SM EW theory causes neutrinos to be massless. Neutrinos (anti-neutrinos) are produced via weak interactions in a predominantly left-handed (right-handed) state. For non-zero neutrino masses, the neutrino field can be expressed as a linear superposition of a left-handed helicity $-1/2$ and right handed helicity $+1/2$ states, with the right-handed component heavily suppressed by a term proportional to m_ν/E . Right handed sterile neutrinos (which do not interact with the weak bosons W^\pm and Z^0) can be added as an extension to the SM. These new particle states can help address current questions related to the generation of extremely small neutrino masses and the observed matter-antimatter asymmetry of the universe.

2.2 Neutrino Oscillation Physics

Neutrino oscillations describe the phenomenon of neutrino flavor mixing which has now been observed by numerous experiments performing a variety of measurements. The first confirmation was obtained by the Super-K [2] and SNO [3, 4] collaborations. The mixing of neutrino flavors is fundamentally a quantum mechanical effect caused by the non-orthogonality of the neutrino flavor-eigenstate basis (through which neutrinos are observed as they interact via the weak force) and the mass-eigenstate basis which appears in the Hamiltonian and governs neutrino propagation.

2.2.1 Two-Flavor Mixing

The quantum mechanical formalism of neutrino oscillations is best explained under a simple, two-flavor hypothesis. The pedagogical derivation shown here is largely taken from reference [5].

We will derive the formalism associated to neutrino oscillations assuming the existence of two flavor states $|\nu_\alpha\rangle$ and $|\nu_\beta\rangle$ and two mass states $|\nu_1\rangle$ and $|\nu_2\rangle$. The relation between flavor and mass eigenstates is dictated by the unitarity matrix of Eq. 2.9:

$$\begin{pmatrix} |\nu_\alpha\rangle, & |\nu_\beta\rangle \end{pmatrix} = \begin{pmatrix} \cos \theta & \sin \theta \\ -\sin \theta & \cos \theta \end{pmatrix} \begin{pmatrix} |\nu_1\rangle \\ |\nu_2\rangle \end{pmatrix} \quad (2.9)$$

While neutrinos interact as well-defined flavor eigenstates, they propagate as eigenstates of the Hamiltonian. A neutrino which was originally produced in the flavor eigenstate $|\nu_\alpha\rangle$ will evolve as:

$$|\nu_\alpha(t, \vec{r})\rangle = \cos \theta e^{-ip_1 r} |\nu_1\rangle + \sin \theta e^{-ip_2 r} |\nu_2\rangle \quad (2.10)$$

Each mass eigenstate's momentum can be written (using natural units), assuming the neutrino is ultra-relativistic, as:

$$p = (E^2 - m_1^2)^{1/2} \approx E \left[1 - \frac{1}{2} \frac{m_1^2}{E^2} \right] \quad (2.11)$$

$$p_1 r = E \cdot t - \vec{p}_1 \vec{r} \approx (E - p_1) r = \frac{m_1^2}{2E} r \quad (2.12)$$

with r the distance traveled by the neutrino. Giving us:

$$|\nu_\alpha(r)\rangle = \cos \theta e^{-i \frac{m_1^2}{2E} r} |\nu_1\rangle + \sin \theta e^{-i \frac{m_2^2}{2E} r} |\nu_2\rangle \quad (2.13)$$

The probability of the neutrino being found in the flavor eigenstate $|\nu_\alpha\rangle$ will be given by the amplitude:

$$\begin{aligned}
P_{\alpha\alpha} &= |\langle \nu_\alpha | \nu_\alpha(r) \rangle|^2 \\
&= |(\langle \nu_1 | \cos \theta + \langle \nu_2 | \sin \theta) \left(\cos \theta e^{-i \frac{m_1^2}{2E} r} | \nu_1 \rangle + \sin \theta e^{-i \frac{m_2^2}{2E} r} | \nu_2 \rangle \right)|^2 \\
&= |e^{-i \frac{m_1^2}{2E} r} \cos^2 \theta + e^{-i \frac{m_2^2}{2E} r} \sin^2 \theta|^2 \\
&= \cos^4 \theta + \sin^4 \theta + \left(e^{-i \frac{(m_2^2 - m_1^2)}{2E} r} + e^{+i \frac{(m_2^2 - m_1^2)}{2E} r} \right) \cos^2 \theta \sin^2 \theta \\
&= \cos^4 \theta + \sin^4 \theta + 2 \cos^2 \theta \sin^2 \theta \cos \left((m_1^2 - m_2^2) \frac{L}{2E} \right)
\end{aligned} \tag{2.14}$$

Setting $(m_1^2 - m_2^2) = \Delta m_{12}^2$ and utilizing the identity:

$$(\cos^2 \theta + \sin^2 \theta)^2 = \cos^4 \theta + \sin^4 \theta + 2 \sin^2 \theta \cos^2 \theta = 1$$

We can write:

$$P_{\alpha\alpha} = 1 + 2 \sin^2 \theta \cos^2 \theta \left(\cos \left(\frac{\Delta m_{12}^2 L}{2E} \right) - 1 \right) \tag{2.15}$$

And using:

$$\sin^2 \theta = \frac{1 - \cos(2\theta)}{2}$$

$$\sin(2\theta) = 2 \sin \theta \cos \theta$$

We obtain:

$$\begin{aligned}
P_{\alpha\alpha} &= 1 - 4 \sin^2 \theta \cos^2 \theta \left(\frac{1 - \cos \left(\frac{\Delta m_{12}^2 L}{2E} \right)}{2} \right) \\
P_{\alpha\alpha} &= 1 - \sin^2(2\theta) \sin^2 \left(\frac{\Delta m_{12}^2 L}{4E} \right)
\end{aligned} \tag{2.16}$$

This two-flavor example allows us to study the way in which neutrino mixing manifests itself. The probability for a neutrino produced in a certain state to be detected in the same state (referred to as survival probability) depends on two fundamental quantities set by nature: the value of the

mixing angle θ , which dictates the oscillation amplitude, and the frequency term proportional to the square difference of the mass eigenstates Δm^2 . Two additional terms, the neutrino's propagation distance L and energy E contribute to determining the oscillation frequency.

2.2.2 Performing a Neutrino Oscillation Experiment

Measuring the mixing angles and mass-splittings of equation 2.16 requires mapping out the oscillation probability as a function of L and E . In order to do so one must be able to infer the neutrino energy, propagation distance, and neutrino flavor. Many different neutrino sources exist, spanning orders of magnitude in neutrino energy and baseline. Different sources have different advantages and disadvantages, such as technical challenge for detection, energy resolution, knowledge of baseline, and so forth. Accelerators are one such source. They have the advantage of a very well known baseline L , and their energy spectrum can somewhat be tuned. Furthermore, they provide a pulsed, intense source which helps with background rejection. The experimental setup for an accelerator-based oscillation experiment is shown in figure 2.1. If a second, “near” detector is placed close to the un-oscillated source, systematics associated to the neutrino flux can be significantly reduced by comparing rates at the two detectors. The “far” detector is to be placed at a baseline such that the oscillation feature being studied ($\Delta m^2 L/4E$) is enhanced. The detector's task is then to count neutrino interactions, tag their flavor, and measure the neutrino energy.

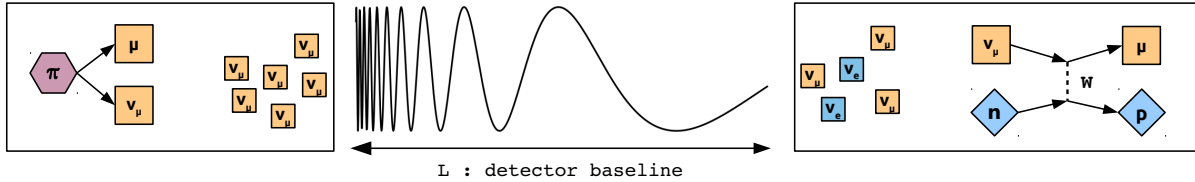


Figure 2.1: Setup for an accelerator-based neutrino oscillation experiment.

Oscillation experiments can be performed as either *appearance* or *disappearance* measurements. In the first case, one searches for the appearance of neutrinos of flavor β in a ν_α beam. For disappearance experiments the survival probability $P_{\alpha\alpha}$ of the state α is measured.

2.2.3 Three Flavor Neutrino Oscillations

The two-neutrino formalism of Sec. 2.2.1 can be expanded to include additional neutrino states. In the case of three neutrino flavors, the unitary matrix of EW. 2.9 is commonly expressed as:

$$\mathbf{U} = \begin{pmatrix} U_{e1} & U_{e2} & U_{e3} \\ U_{\mu 1} & U_{\mu 2} & U_{\mu 3} \\ U_{\tau 1} & U_{\tau 2} & U_{\tau 3} \end{pmatrix} \quad (2.17)$$

Which can be broken up into three terms, one for each mixing angle:

$$\mathbf{U} = \begin{pmatrix} 1 & 0 & 0 \\ 0 & \cos \theta_{23} & \sin \theta_{23} \\ 0 & -\sin \theta_{23} & \cos \theta_{23} \end{pmatrix} \times \begin{pmatrix} \cos \theta_{13} & 0 & \sin \theta_{13} e^{-i\delta} \\ 0 & 1 & 0 \\ -\sin \theta_{13} & 0 & \cos \theta_{13} \end{pmatrix} \times \begin{pmatrix} \cos \theta_{12} & \sin \theta_{12} & 0 \\ -\sin \theta_{12} & \cos \theta_{12} & 0 \\ 0 & 0 & 1 \end{pmatrix} \times \begin{pmatrix} e^{i\alpha_1/2} & 0 & 0 \\ 0 & e^{i\alpha_2/2} & 0 \\ 0 & 0 & 1 \end{pmatrix} \quad (2.18)$$

The full 3x3 matrix \mathbf{U} is called the *PMNS* matrix for Pontecorvo, Maki, Nakagawa, and Sakata. Oscillation probabilities can be derived as for the two-neutrino example, but now will exhibit contributions from three mixing angles and mass-splittings which interfere with each other. The mixing angles θ_{23} , θ_{13} , and θ_{12} of the *PMNS* matrix are now accompanied by three phases: δ_{CP} (δ in eq. 2.18) which measures the CP violating angle, and α_1 and α_2 which are the Majorana phases, important if neutrinos are Majorana particles. The Majorana phases, along the diagonal, cannot be measured with oscillation experiments. The generic oscillation probability in a three-flavor scenario is expressed in equation 2.19.

$$P_{\nu_\alpha \rightarrow \nu_\beta}(\bar{\nu}_\alpha \rightarrow \bar{\nu}_\beta) = \sum_i |U_{\beta i}|^2 |U_{\alpha i}|^2 + 2 \sum_{j>i} |U_{\beta j} U_{\alpha j}^* U_{\alpha i} U_{\beta i}^*| \cos \left(\frac{\Delta m_{ij}^2}{2E} L - (+)\phi_{\beta\alpha ji} \right). \quad (2.19)$$

With $\phi_{\beta\alpha ji}$ equal to $\arg(U_{\beta j} U_{\alpha j}^* U_{\alpha i} U_{\beta i}^*)$. The CP violating phase manifests itself only in a difference between neutrino and anti-neutrino oscillations, and can only be studied in appearance experiments.

2.2.4 Oscillation Parameter Measurements and Current State of the Field

Knowledge of neutrino mixing angles and mass splittings between the three states has grown significantly since the confirmation of neutrino oscillations two decades ago. Their values are reported in table 2.1

Table 2.1: Table containing current measured values of neutrino mixing angles and mass-splittings, from the 2017 edition of the PDG [6]. The table is split in best-fit values under the normal and inverted ordering scenarios. A “-” for inverted ordering denotes the same best fit as for the normal ordering.

	Normal Ordering	Inverted Ordering
$\sin^2(\theta_{12})$	0.307 ± 0.013	-
$\sin^2(\theta_{23})$	0.51 ± 0.04	0.50 ± 0.04
$\sin^2(\theta_{13})$	$(2.10 \pm 0.11) \times 10^{-2}$	-
Δm_{21}^2	$(7.53 \pm 0.18) \times 10^{-5} \text{eV}^2$	-
$ \Delta m_{32}^2 $	$(2.45 \pm 0.05) \times 10^{-3} \text{eV}^2$	$(2.52 \pm 0.05) \times 10^{-3} \text{eV}^2$

The mass splittings determine the L/E at which oscillation features are maximized for each mixing angle. Writing equation 2.16 with relevant units the mixing frequency term can be expressed as $\sim 1.27 \times (\Delta m^2/\text{eV}^2) \times (L/\text{km}) \times (\text{GeV}/E)$ which gives $\theta_{12} \rightarrow L/E \sim 10^4 \text{ km/GeV}$, θ_{23} and $\theta_{13} \rightarrow L/E \sim 10^2 \text{ km/GeV}$ or 10^2 m/MeV .

The mixing angles are often referred to as “solar” (θ_{12}), “atmospheric” (θ_{23}), and “reactor” (θ_{13}) mixing angles. The nomenclature arises from the neutrino source used in the experiments which first measured them.

Figure 2.2 shows the 1σ uncertainty on the mixing parameters as their measurement has improved over the past decade. Worthy of mention is the dramatic change in our knowledge of θ_{13} , which went from being constrained by an upper bound of ~ 12 degrees until 2011, to being the best-known mixing angle thanks to the measurements of the reactor neutrino experiments DayaBay [7], Double CHOOZ [8], and RENO [9]. It is the measurement of θ_{13} by these experiments, and specifically the finding that this mixing angle is non-zero and falls at the high-end of the previously constrained range (~ 8 degrees) which has opened up the possibility for meaningful precision measurements in neutrino oscillations. Had θ_{13} been close to zero it would have been impossible to address with oscillation experiments many of the open questions discussed below.

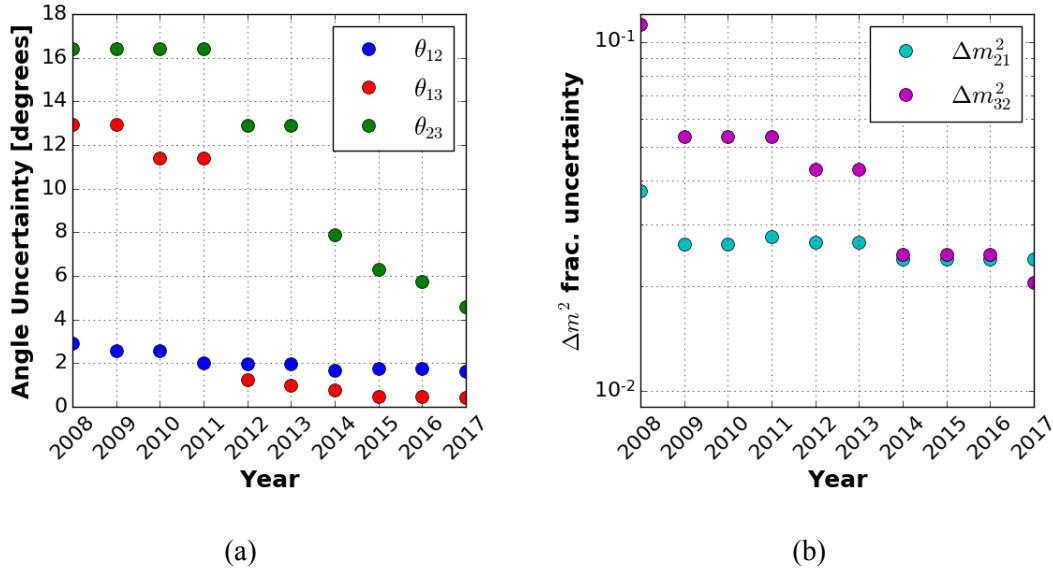


Figure 2.2: (a) Measured error on the mixing angles. (b) Measured fractional error on the mass splittings.

Open questions pertaining to neutrino oscillations concern several yet unknown quantities of the PMNS matrix which generally have significant implications for BSM physics. They are discussed here individually.

Mass Ordering The absolute sign of Δm_{32}^2 is unknown. This prevents us from knowing whether ν_1 or ν_3 is the lightest mass eigenstate. The reason this is not purely a matter of bookkeeping is due to the relation between charged leptons and their neutrino counterparts. The electron, the lightest charged lepton, is associated to the electron neutrino. In turn, ν_e is predominantly composed of the ν_1 mass eigenstate ($|U_{e1}|^2 \sim 2/3$). Therefore, the question can be rephrased as: “is ν_e , associated with the lightest charged lepton, primarily composed of the ν_1 mass eigenstate, associated with the lightest neutrino?” The symmetry between the ordering of the masses of charged leptons and neutrinos causes a specific nomenclature to be used: if ν_1 happens to be the lightest neutrino mass eigenstate, the ordering is referred to as *normal*. Otherwise, it is labeled *inverted*.

θ_{23} Octant The current value of θ_{23} is consistent with 45 degrees. If this were the case each neutrino flavor would have equal contents of ν_μ and ν_τ . Recently, results from the NOvA and T2K experiments seem to point in different directions, with NOvA data disfavoring $\theta_{23} = 45$ [10].

CP Mixing Angle The value of δ_{CP} is unknown. Hints of this quantity being non-zero (from T2K [11] and NOvA [12]) have recently surfaced. A non-zero value of δ_{CP} would imply violation of the CP symmetry, and have important consequences for leptogenesis, a model which helps address the question of why we live in a matter-dominated universe [13]. Sensitivity to this parameter shows up (only because θ_{13} is different from 0) as a difference in the oscillation probability for neutrinos and anti-neutrinos.

Unitarity In the quark sector, where mixing (to a smaller extent than for neutrinos) is also present, the unitarity of the CKM matrix (equivalent to the PMNS for neutrino oscillations) has been rigorously tested. The accuracy to which the mixing angles are known make conclusions on the unitarity of the PMNS matrix weak. A non-unitarity of this matrix could point to additional neutrino states not currently accounted for in the 3x3 formalism employed.

2.3 Counting Neutrinos

The picture of neutrinos and neutrino oscillations painted in sections 2.1 and 2.2 has evolved over time. The first half of neutrino physics' history was not centered on studying neutrino oscillations, but rather detecting the existence of this elusive particle which interacts only via the weak force. First postulated by Wolfgang Pauli in 1930 as a way to account for the missing energy in β decays not carried by the electron or nucleus, the elusive nature of such a neutral particle was immediately apparent. It was Fermi, in 1934, who formalized the role of the neutrino in weak interactions by postulating the four fermion interaction which governed the β -decay process $n \rightarrow p + e^- + \bar{\nu}_e$.

2.3.1 First one, then two, then three

Reines and Cowan are credited with the discovery in 1956 of the neutrino with the conclusive results of the Savannah River experiment [14] which detected neutrinos produced by inverse beta decay from fission fragments produced in the Savannah nuclear power plant. Their observation matched the theoretical expectation for the cross section of $\sim 10^{-44} \text{cm}^2$.

The discovery of the muon, a lepton identical to the electron except for its mass, opened up the possibility of additional flavors of neutrinos as well. Motivation from this arises from the fact that the process $\mu \rightarrow e + \gamma$ was never observed and rather, the decay occurs via $\mu^- \rightarrow e^- + \bar{\nu}_e + \nu_\mu$,

indicating a fundamental difference between electron and muon neutrinos. The observation of a second distinct neutrino flavor was reported in 1962 by Lederman and others who, by producing a beam of neutrinos obtained from the decay of pions into $\mu + \nu_\mu$, were able to observe the product of neutrino interactions on a target. The fact that the experiment observed only muons, and not electrons as a product of the interaction confirmed the different nature (lepton number) of the muon and electron neutrinos.

Finally, the discovery of the τ charged lepton naturally led to the hypothesis of a neutrino counterpart. The tau neutrino was not discovered until 2001, in the DONUT experiment which was set up similarly to the one which discovered the ν_μ . The main challenge faced in discovering the ν_τ was the need to produce neutrinos of high enough energy to produce a final state τ lepton.

As neutrinos of different flavors were being discovered and studied in reactor and accelerator experiments, a puzzle stemming from astrophysics was stimulating the interest of the neutrino physics community: the *solar neutrino problem*. If neutrinos produced in nuclear fusion reactions powering the sun, referred to as solar neutrinos, could be detected, a measurement of their flux would allow to experimentally validate solar models of nuclear fuel burning. The first detection of neutrinos from the sun was performed at the Homestake mine in South Dakota by Ray Davis and John Bahcall in 1962. The measurement consisted of counting ^{37}Ar produced by the reaction $\nu_e + ^{37}\text{Cl} \rightarrow ^{37}\text{Ar} + e^-$ which has a 0.814 MeV threshold. The amount of ^{37}Ar present was measured through its β -decay. This measurement, and others that followed, observed a deficit of ν_e : only one third of the expected flux was being measured. This deficit is what is referred to as the solar neutrino problem. Bruno Pontecorvo hypothesized in 1968 that neutrinos could oscillate between different flavors if they have mass. The deficit could then be explained as caused by the fact that a fraction of the neutrinos produced in the sun as ν_e had oscillated into different states, undetectable by the Homestake and other experiments.

A resolution to this problem came once the SNO detector was able to make a measurement of both the ν_e and total neutrino flux (contributed by all flavors) via neutral current interactions. The results showed that indeed the ν_e component of the solar flux was only a fraction of the total flux. The mechanism by which ν_e s produced in the sun's core oscillate is referred to as the MSW effect (Mikheyev, Smirnov, and Wolfenstein), which leaves them in a purely ν_2 eigenstate once they leave the sun.

2.3.2 Constraints from Collider Physics

In collider experiments neutrinos contribute to missing energy from recorded interaction as they escape the onion-layer trackers and calorimeters installed in a detector. While neutrinos cannot be observed directly, their presence can be studied by measuring decay rates and missing energy distributions. Neutrinos are one of the possible decay modes of neutral particles and therefore contribute to an overall suppression of the visible cross section of their decay. The number of neutrino flavors available for a particle to decay into will lead to different visible cross-sections. The most stringent limit on the number of active neutrinos comes from the measurement of the Z decay by the ALEPH, DELPHI, L3, and OPAL collaborations. The decay width of the Z particle is the sum of all possible decay modes:

$$\Gamma_Z = \Gamma_{ee} + \Gamma_{\mu\mu} + \Gamma_{\tau\tau} + \Gamma_{hadronic} + \Gamma_{invisible} \quad (2.20)$$

With the last term coming from decay to invisible neutrinos. Given the Standard Model prediction for Γ_Z and the measured visible contribution to the cross-section the invisible contribution from neutrinos can be inferred. Assuming lepton universality the invisible decay width can be related to the number of active neutrinos by:

$$\frac{\Gamma_{invisible}}{\Gamma_l} = N_\nu \left(\frac{\Gamma_{\nu\bar{\nu}}}{\Gamma_l} \right)_{SM} \quad (2.21)$$

By which the number of neutrino flavors is constrained to $N_\nu = 2.984 \pm 0.008$ [15, 16]. This measurement is sensitive to neutrino states which interact weakly (active neutrinos) which are kinematically allowed. Neutrinos with a mass smaller than $M_W/2$, if they exist, would have to not participate in the weak force and are thus referred to as *sterile*.

2.3.3 Constraints from Cosmology

Neutrinos are the second most abundant particle species in the universe and while their impact on cosmology is negligible today, they played an important role in the evolution of the early universe. As a consequence measurements of the properties of the primordial universe can teach us about the properties of neutrinos. Neutrinos of all flavors were abundantly produced via weak interactions in the early universe at high temperatures, and their momentum spectrum followed a Fermi-Dirac

distribution. Once the weak interaction rate falls below the universe's rate of expansion neutrinos decouple, effectively freezing their momentum distribution. This process happens at a temperature of 1 MeV, at which neutrinos are highly relativistic. This neutrino population has been propagating through the universe undisturbed ever since, and makes up the cosmic neutrino background ¹. Accounting for the universe's expansion to this day leaves the cosmic relic neutrino with an average energy of $\sim 1 \times 10^{-4} \text{ eV}$ and a density of $\sim 100 \nu/\text{cm}^3$. While directly detecting relic neutrinos is challenging due to their extremely low energies, measuring the impact they have played on observables of cosmological scale can help constrain both the total number of neutrinos as well as their total mass.

The total number of neutrinos (active and sterile) impacts, together with the photon density, the energy density of the universe at temperatures where this quantity is dominated by radiation. This in turn sets the universe's expansion rate. The value of the expansion rate at this time in the universe's evolution has an impact on Big Bang Nucleosynthesis, which governs the production of light elements such as helium and lithium. Measuring the relative abundance of these elements in the early universe can therefore provide a constraint on the total number of degrees of freedom contributed by neutrinos to the universe's energy density, and thus the total number of neutrino states.

Anisotropies in the Cosmic Microwave Background (CMB) are studied by measuring the point-to-point correlations in the CMB sky map. Neutrinos impact these anisotropies due to their different contribution to the matter density of the universe when they are relativistic $\rho \propto \alpha^{-4}$ vs. non-relativistic $\rho \propto \alpha^{-3}$. When this transition occurs, and thus at what correlation-scales it appears in the CMB, depends on the sum of the mass of all neutrino flavors. Current CMB measurements place this limit to be $\sum m_\nu < 0.16 \text{ eV}$.

2.3.4 Hints for Additional neutrino States

Hints for sterile neutrino states have emerged from several neutrino experiments performed with different sources and detectors. None of these measurements offer conclusive evidence for the existence of neutrino oscillations, and measurements which rule out the parameter space of interest to these positive results have also been conducted [17, 18, 19]. All potential signals, if interpreted

¹Neutrinos from the early universe are commonly referred to as relic neutrinos.

as due to oscillations, are compatible with a mass-splitting of order 1 eV^2 . We present a short overview of the three main hints for sterile neutrinos, discussing those obtained from accelerator-based measurements in more detail in the following section. A review of experimental results pertaining to sterile neutrino searches, and the analysis methods employed to search for sterile neutrinos is presented in reference [20].

Gallium Anomaly The neutrino detectors GALLEX and SAGE were designed to detect neutrinos from the sun of a few hundred keV of energy. These experiments performed calibrations with the neutrino sources ^{51}Cr and ^{37}Ar and measured a deficit of neutrinos from both of order $\sim 2\text{-}3\sigma$ [21]. The deficit of ν_e events for a low energy source ($\sim 400\text{-}700 \text{ keV}$) and $\sim 10 \text{ cm}$ scale of the detector had led to speculation that the cause for this deficit could be due to oscillation to eV^2 sterile neutrinos.

Reactor Anomaly In reactor neutrino experiments a widely observed deficit of a few percent of $\sim 1 - 10 \text{ MeV } \bar{\nu}_e$ events, uniform in energy, has been hypothesized to be caused by oscillations to a sterile neutrino. Much of the work in understanding the reactor neutrino anomaly involves studying the systematic errors associated to the prediction of the neutrino flux from reactors. The complex chain of fission fragments produced in nuclear reactors, and difficult modeling of atomic transitions makes this an arduous task. A recent measurement by the Daya Bay collaboration [22] seems to attribute, at least in part, the anomaly to the time-dependent composition of the nuclear fuel. A new generation of reactor-neutrino experiments designed to operate at test reactors, where they can be placed much closer to the source, are soon to come online. By taking advantage of the smaller fission core and shorter distance between the core and the detector in such reactor, experiments such as prospect [23] aim to observe the oscillatory L/E dependence of interactions due to a possible sterile neutrino.

Accelerator Anomalies The LSND and MiniBooNE experiments have observed an excess of ν_e events in a ν_μ beam. The initial observation by LSND, hypothesized to be caused by neutrino oscillations at the 1 eV^2 mass splitting, lead to the formation of the MicroBooNE collaboration aimed to investigate this anomaly. MicroBooNE's results also showed an excess of events, even though not fully compatible with LSND's (under the simplest sterile neutrino models). The experimental

setup and results of these two experiments are discussed in more detail in the remainder of this section. A thorough review of the LSND and MiniBooNE results can be found in reference [24].

2.3.5 The LSND Anomaly

The *Liquid Scintillator Neutrino Detector* (LSND) operated at Los Alamos recording neutrinos produced in the LANSCE neutrino beam. The beam was composed of electron and muon neutrinos from muon and pion decay at rest. The experiment was performed to study neutrino oscillations at the $\Delta m^2 \sim 1\text{eV}^2$ mass splitting at a time when there was great uncertainty on the frequencies at which to expect oscillations. It was, in other words, a neutrino oscillation experiment: no steriles invoked. The analysis consisted of a measurement of ν_e interactions from inverse β -decay (IBD) which could be efficiently tagged due to the delayed coincidence coming from neutron capture on a free proton, which produces a delayed ($\sim 200\ \mu\text{s}$) 2.2 MeV photon. The LSND results recorded an excess of ν_e interactions with respect to predictions for intrinsic events from the beam. The excess of events, in blue in figure 2.3a was fit to an oscillation appearance signal under a two-flavor hypothesis, leaving to the constrained parameter space shown in figure 2.3b.

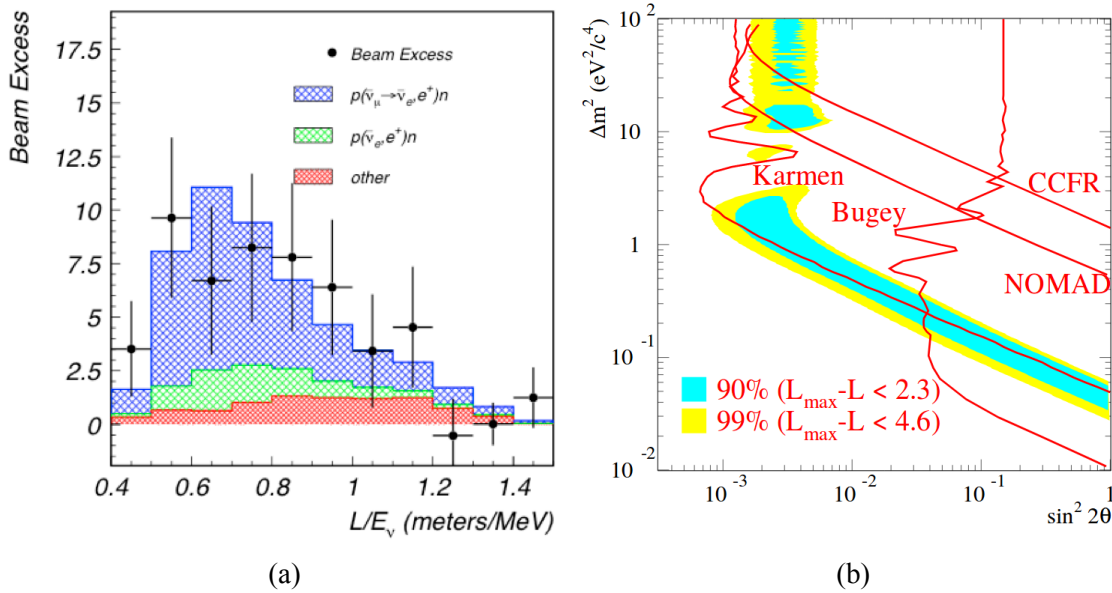


Figure 2.3: LSND results from reference [25]. (a) Distribution of measured ν_e events, with the best-fit excess modeled as oscillations in blue. (b) Constraints on parameter space under a two-flavor oscillation hypothesis.

The $\sim 1\text{ eV}^2$ mass splitting suggested by LSND's results' interpretation as neutrino oscillations is orders of magnitude larger than those associated with the standard 3-neutrino mixing of

section 2.2. While the result is considered by some controversial, and by all non-conclusive, it is the origin, for accelerator experiments, of the study of potential sterile neutrinos at the 1 eV^2 mass splitting. A detailed introduction to, and discussion of the LSND result can be found in *Celebrating the Neutrino – A Thousand Eyes* [26].

2.3.6 The MiniBooNE Low Energy Excess

The unresolved question of how to interpret the LSND results led to the proposal of an experiment which aimed to test the 1 eV^2 oscillation hypothesis: MiniBooNE. MiniBooNE's goal was to test oscillations at the same mass-splitting but with a different neutrino beam and detector in order to not be affected by the same systematics of LSND. The L and E for the oscillation signature were both increased by an order of magnitude, placing the detector ~ 400 meters from the $\sim 700 \text{ MeV}$ ν_μ Booster beam designed specifically for this experiment. The detector consists of an 800 ton circular tank filled with mineral oil surrounded by PMTs which observe Cherenkov light produced by leptons and other particles originating in neutrino interactions. The MiniBooNE experiment started operating in 2002, has taken data in neutrino and anti-neutrino mode, and continues to operate to this day. The experiment was setup as a ν_e appearance experiment in a largely ν_μ beam. The two topologies can be distinguished by the difference in the PMT signature of electrons and muons: the first produce a “fuzzy” Cherenkov ring caused by the broadening electromagnetic shower induced by electrons, while the second produces a sharp ring associated to the linear muon. The latest results of MiniBooNE's ν_e and $\bar{\nu}_e$ appearance searches in neutrino and anti-neutrino running mode are presented in reference [27] and reported below in figure 2.4.

The excess of events observed in both channels with respect to backgrounds falls below 475 MeV of reconstructed neutrino energy, below where an appearance signal consistent with that of LSND would have been expected. This excess (2.8σ for $\bar{\nu}$ and 3.4σ for ν) is referred to as the *Low Energy Excess* (LEE). Sterile neutrino states of $\Delta m^2 \sim 1 \text{ eV}^2$ have been invoked as an explanation of this excess as well, even though tensions between neutrino and anti-neutrino data have led to the introduction of more complex sterile neutrino models where two or three additional neutrino states, rather than a single one, contribute to this appearance signal.

While aiming to solve the LSND anomaly, MiniBooNE discovered one of its own. A clear picture for what is the nature of the MiniBooNE LEE is yet to be identified. The most significant

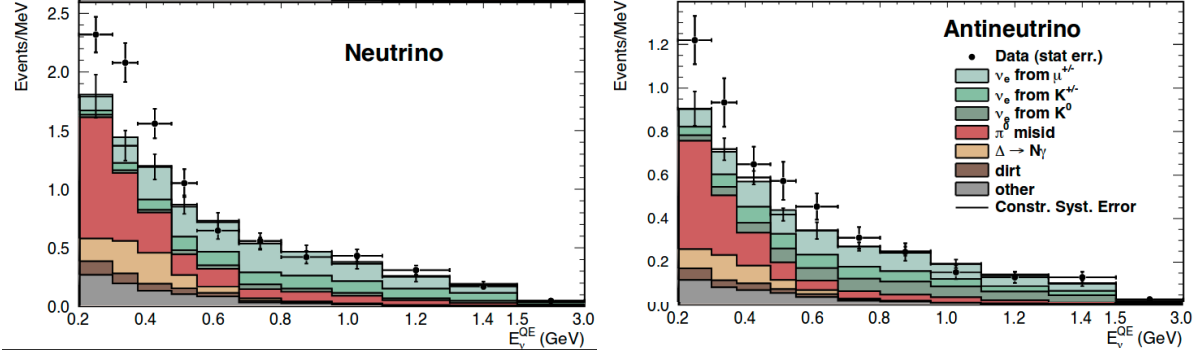


Figure 2.4: Neutrino mode (a) and anti-neutrino mode (b) results for a ν_e appearance search in the MiniBooNE detector. The excess of events at low energies (< 475 MeV) is referred to as the low energy excess (LEE). The same excess seen by LSND would show up in MiniBooNE at slightly higher energies. The dominant backgrounds to the selection are caused by single photon events from $\Delta \rightarrow N\gamma$ and neutral current π^0 production.

backgrounds to the MiniBooNE low-energy excess are of two types: intrinsic electron neutrinos in the muon neutrino beams, and interactions producing photons which are mis-identified as electrons. While the first background is irreducible, the second is present because MiniBooNE cannot distinguish between electrons and photons. Suppressing the significant photon-induced background in MiniBooNE is necessary to reach a definite answer on the nature of this excess.

2.4 The MicroBooNE Experiment: Motivation

The primary goal of the MicroBooNE experiment is to understand the nature of MiniBooNE's low energy excess. It aims to do so by employing the Liquid Argon Time Projection Chamber (LArTPC) detector technology in order to produce high-resolution images of neutrino interactions which will allow the separation of electrons and photons, thus suppressing MiniBooNE's largest background to ν_e appearance. At the same time, the MicroBooNE experiment aims to perform cross-section measurements which will help present a clearer picture of neutrino interactions on argon in the $\mathcal{O}(1 \text{ GeV})$ energy range. The complex nuclear structure of argon leads to a number of effects which complicate neutrino energy reconstruction and flavor tagging from knowledge of the interaction final state observables. Performing these measurements will help understand the impact of nuclear effects on neutrino-argon interactions, constraining the systematics of energy reconstruction.

2.5 Upcoming Accelerator-Based Oscillation Physics Program

Conclusively addressing the open questions in neutrino oscillation physics requires studying small features in the oscillation spectra which lead to subtle differences in the neutrino rates observed. Doing so requires performing experiments with intense neutrino sources and detectors capable of powerful background rejection. The LArTPC technology has been chosen for these detectors due to its ability to detect complete final state information from the interaction with low detection thresholds. By relying on calorimetric and topological information LArTPC detectors are also capable of performing particle identification, essential for background rejection. Different oscillation effects will lead to different signatures which manifest themselves at different values of L/E . Two separate research programs have been set up employing different beamlines at Fermilab in order to perform a *Short Baseline* experiment which aims to conclusively search for sterile neutrinos in the 1eV^2 region at $L/E \sim 1 \text{ Km/GeV}$, and a *Long Baseline* experiment hoping to measure the mass ordering and δ_{CP} violating phase.

The Fermilab Short Baseline Neutrino program [28] is a three-detector oscillation experiment sitting on the Booster Neutrino Beamline (see figure 2.5) at Fermilab which will rely on the SBND near-detector (112 tons at 110 meters) to measure and constrain the un-oscillated neutrino flux and on the MicroBooNE (87 tons at 470 meters) and ICARUS (476 tons at 600 meters) detectors to perform a ν_e appearance search.

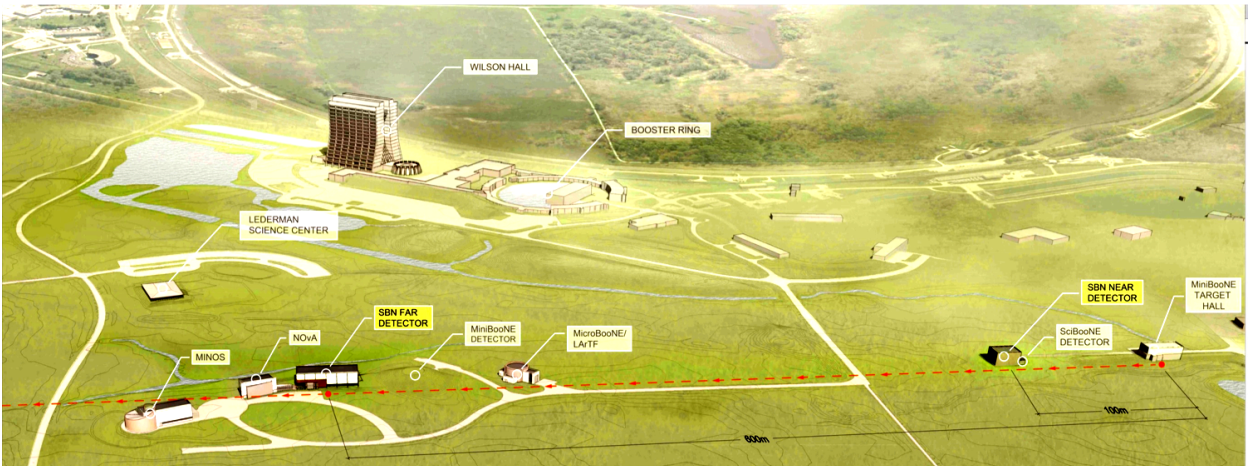


Figure 2.5: Layout of the SBN three-detector experiment on the Booster Neutrino Beamline at Fermilab.

Fermilab’s Long Baseline oscillation program will be carried out by a massive LArTPC detector, DUNE, comprised of four 10 kiloton modules placed underground in the Homestake mine in South Dakota at a distance of 1,300 km from the neutrino source. Positioning the detector underground substantially reduces the cosmic-ray flux which can pose a challenge to neutrino identification, especially in a slow readout detector. The long baseline is motivated by the fact that what makes the experiment sensitive to the impact of nonzero δ_{CP} on the oscillation pattern of neutrinos versus anti-neutrinos is the different impact that matter has on their oscillation probability. This effect is referred to as the *matter effect* and manifests itself as an additional term in the time-evolution of mass-eigenstates which only impacts the ν_e component of the PMNS matrix.

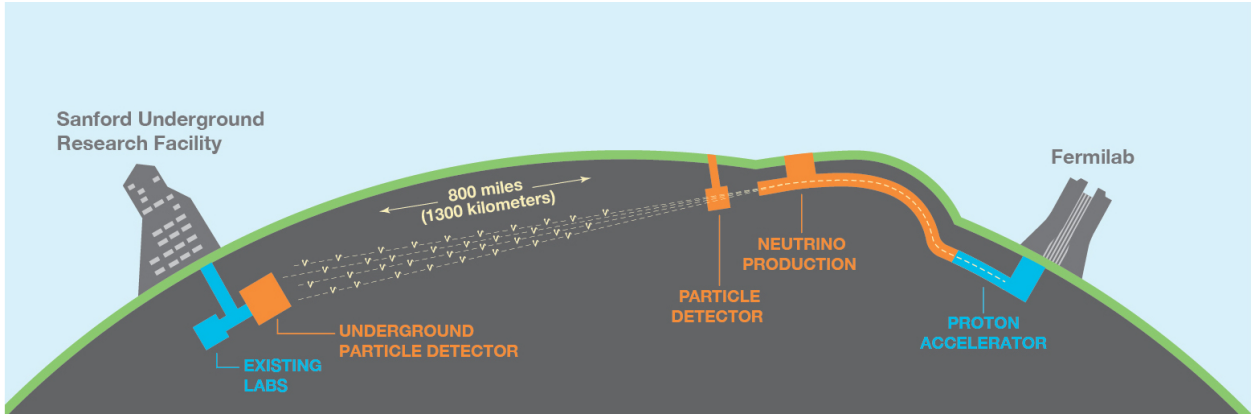


Figure 2.6: Cartoon of the DUNE experiment setup.

2.5.1 Role of Electron Identification and Energy Reconstruction in LArTPCs in Neutrino Oscillation Analyses

Much of the oscillation physics program outlined above depends on measuring $\nu_\mu \rightarrow \nu_e$ appearance and precisely measuring the ν_e energy in order to perform precision oscillation measurements. This requires being able to identify and reconstruct electromagnetic showers produced by the outgoing electron produced in ν_e charged current interactions. Detailed validations of energy reconstruction in EM interactions in LArTPC neutrino detectors are lacking. This work presents studies of EM activity reconstruction in the MicroBooNE detector over a wide range of energies of interest to ν_e oscillation experiments (tens to hundreds of MeV).

Chapter 3

Astrophysical Neutrinos from Supernovae Bursts

Supernovae bursts are violent astrophysical events undergone by certain categories of massive stars once they exhaust their nuclear fuel. Studying these events is of interest to many branches of physics and astrophysics. Certain categories of supernova burst events release almost the entirety of their gravitational binding energy in neutrinos, making them of interest to the neutrino physics community. This chapter provides an introduction to the complex dynamics of supernovae bursts, with a focus on the role played by neutrinos as catalysts to these events. A short review of the only measurement of neutrinos from a supernova burst to date is presented, along with a final section on the physics potential and detector requirements for detecting supernova neutrinos with large-scale LArTPC neutrino detectors.

3.1 Supernova Burst Dynamics

Stars maintain hydrostatic equilibrium by countering the force of gravity with the outward pressure provided by nuclear fusion reactions occurring in its core. For the majority of its life a star burns hydrogen producing helium nuclei. Once the hydrogen fuel in the core is exhausted, the star compresses, allowing the core to reach higher temperatures, which in turn allow heavier elements to be formed via thermonuclear fusion. As heavier elements are being produced, the amount of energy released per fusion becomes smaller. Fusion of iron into heavier elements costs energy,

rather than releasing it. This causes the mechanism by which a star maintains its equilibrium to come to a halt. Gravity, now alone dictating the dynamics of the star, causes the star's core to collapse. While the process which has lead to this point in the star's life may have lasted millions of years, the next phase of violent collapse will take place in less than one second.

As the core begins to collapse, photons produced in its center acquire enough energy to dissociate iron nuclei into free neutrons and alpha particles. At the same time the temperature and pressure within it begin to rise and electrons form a degenerate electron gas. Once their density becomes greater than approximately 10^{10} g/cm^3 and they acquire sufficient energy, electrons will begin to capture on protons via the process $p + e^- \rightarrow n + \nu_e$. The electron neutrinos produced in this process escape the core, further depleting it of its energy. As neutrinos escape further cooling the core, gravitational pressure compresses it faster and faster, accelerating the rate for electron capture and the rate of escaping neutrinos. During this process a flux of non-thermal electron neutrinos is produced, the first of many neutrino signatures of a core-collapse supernova.

Once densities in the core reach 10^{11} g/cm^3 neutrinos become trapped. This is caused by the large cross-section Coherent Electron Neutrino Nucleus Scattering ($\text{CE}\nu\text{NS}$) neutral current process [30] which causes neutrinos to scatter off regular matter rather than escape the stellar core. The trapped electron neutrinos continuously produced by electron capture maintain the lepton content of the star constant rather than depleting it.

The collapse comes to a halt once the core reaches nuclear densities and transitions to a uniform nuclear medium, becoming highly incompressible. Sound waves from this sudden halt (bounce) begin to travel outward. Electron capture continues to produce a large number of electron neutrinos. Once the shock wave has reached regions of the star with sufficiently low densities, the neutrinos are once again able to diffuse, and a large flux of ν_e is emitted in a *breakout burst*. This event takes place over tens of milliseconds. As the electron lepton number is depleted by the escaping electron neutrinos, an increasing concentration of positrons allows e^+e^- annihilation to create neutrinos of all flavors, and e^+ captures on neutrons begin to produce $\bar{\nu}_e$.

As the shock propagates to outer layers of the iron core it leads to the dissociation of atoms into free nuclei, which consumes energy. This, combined with the significant energy lost due to the burst of ν_e which manage to escape the star, causes the shock to stall. Behind the shock-wave, neutrinos are still in an opaque environment and continue to capture on free nucleons via the processes $\nu_e + n \rightarrow p + e^-$ and $\bar{\nu}_e + p \rightarrow n + e^+$. These processes provide pressure and energy to the shock, allowing it to rebound. The detailed mechanics of the *rebound* are still under debate and subject to significant variation depending on the specifics of the models used to simulate this phase of the burst. Recent studies indicate that the impact of spherically asymmetric effects in the convection of matter in the stellar core play an important role in allowing the burst to take place. Testing these models via numerical simulations is challenging due to the computing resources required.

Accretion of matter on the proto-neutron star continues as the shock propagates outward. Once the accretion process has ended, the proto-neutron star begins to cool by releasing additional gravitational energy in the form of escaping neutrinos of all flavors. Much like photons in the sun, neutrinos continuously scatter in the proto-neutron star due to the opaque environment caused by the high matter density, and are able to escape only once they reach a distance from the core where the opacity is sufficiently low. This artificial boundary is defined as the *neutrinosphere*, and is slightly different for neutrinos of different flavors and for neutrinos versus anti-neutrinos. Because neutrinos thermalize in order to reach the neutrinosphere, their energy spectra can be well modeled by a Fermi-Dirac distribution with the temperatures found at a radius of ~ 10 Km which are of order 10 MeV. Deviations are however present as neutrinos of different energies exhibit different interaction rates, causing the radius at which the opacity becomes low enough for neutrinos to escape to be somewhat energy dependent. This final phase of the supernova burst is referred to as neutrino cooling and lasts several seconds.

3.2 Supernova Neutrino Detection

A supernova burst occurring somewhere in the Milky way (~ 10 kpc from earth) with virtually all of its 10^{53} ergs of energy released in the form of 10 MeV neutrinos would produce on earth a flux of $10^{14} \nu/cm^2$. Even accounting for the very low neutrino cross-sections, this still leads to

significant event rates in reasonably sized neutrino detectors. The first experimental observation of neutrinos from a supernova burst occurred in 1987, with the detection of a handful of neutrino interactions in three neutrino detectors from a galactic supernova burst referred to as *SN 1987a*. This observation confirmed the important role neutrinos were thought to play in the dynamics of supernovae bursts.

Kamiokande II The Kamiokande II detector was a water Cherenkov detector filled with 2,140 tons of water which detects electron neutrinos via scattering ($\nu + e \rightarrow \nu + e$) and anti-electron neutrinos through IBD. The experiment detected twelve events in a \sim ten second time-span associated with the supernova burst [31]. Figure 3.1 shows the time distribution and signal amplitude for the events surrounding the burst, with the twelve candidate supernova neutrino events labeled in time-order.

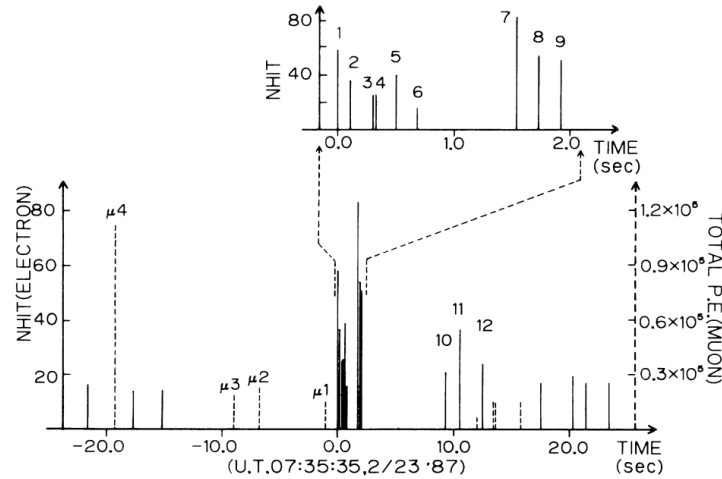


Figure 3.1: Kamiokande neutrino events from supernova 1987a.

IMB The Irvine-Michigan-Brookhaven (IMB) experiment, also a water-Cherenkov detector, recorded eight candidate burst events in a six second time-span associated with the supernova burst [32]. The table shown in figure 3.2 reports the time, energy, and direction of the eight candidate SNB events.

Baksan The Baksan detector, located underground with an 850 m.w.e. overburden, consists of segmented oil-based liquid scintillator detectors. This experiment reports observing six neutrino

TABLE III. Characteristics of the contained neutrino events recorded on 23 February.

Event No. ^a	Time (UT)	No. of PMT's	Energy ^b (MeV)	Angular distribution ^c (degrees)
33162	7:35:41.37	47	38	74
33164	7:35:41.79	61	37	52
33167	7:35:42.02	49	40	56
33168	7:35:42.52	60	35	63
33170	7:35:42.94	52	29	40
33173	7:35:44.06	61	37	52
33179	7:35:46.38	44	20	39
33184	7:35:46.96	45	24	102

^aThe event numbers are not sequential. Interspersed with the contained neutrino events are fifteen entering cosmic-ray muons.

^bError in energy determination is $\pm 25\%$ (systematic plus statistical).

^cIndividual track reconstruction uncertainty is 15° . Note that this angular distribution will be systematically biased toward the source because of the location of the inoperative PMT's.

Figure 3.2: SN1987a neutrino candidates from the IMB experiment.

interactions in a ten second time interval [33]. There is some discrepancy as to the time coincidence of the Baksan events with those reported by the IMB experiment.

The observation of SN1987a by multiple detectors allowed for the first time to test models of supernova burst evolution by studying their neutrino emission, including the measurement of the burst energy. Since this measurement has taken place the development of theoretical models for supernova bursts has flourished in part thanks to the powerful computational tools now available to simulate these events. It is up to current and future neutrino detectors to collect more detailed information from neutrinos produced in supernova bursts in order to provide additional much needed experimental constraints.

3.3 Prospects for Supernova Neutrino Detection with large-scale LArTPC Detectors

The goal for the next generation of neutrino detectors is to record hundreds to thousands of SNB neutrino interactions in order to test models related to the dynamics of core-collapse, and to study neutrino oscillations with such a unique source [34]. To achieve these goals it is important to study the time and energy distribution of interactions, as well as the neutrino flavor content of the burst activity. While water Cherenkov and scintillator detectors are well suited to detect $\bar{\nu}_e$ neutrinos, the large charged-current cross-section on argon makes this detector technology ideal to measure

ν_e interactions. The complementary nature of the observation on liquid argon can ensure a high-statistics measurement of the high flux of ν_e produced in the supernova shock breakout.

3.3.1 Interaction Channels in Liquid Argon

Neutrinos and antineutrinos of all flavors are produced during a supernova burst and the channel via which interactions will occur in a specific detector is highly dependent on the detector material and detection thresholds. Theoretical calculations for neutrino cross sections on argon in the relevant energy range for supernovae neutrinos are shown in figure 3.3, obtained from the Snowglobes [35] documentation. These values are obtained from calculations and have uncertainties of order 20%. The dominant interaction channel for liquid argon comes from inverse beta decay interactions of electron neutrinos with argon nuclei. This is complementary to the dominant $\bar{\nu}_e$ interaction channel for water Cherenkov detectors. Folding the time-integrated neutrino flux with the cross-section we obtain the expected energy spectra for various flavor neutrinos, shown in figure 3.4 for the two example flux models available in the SNOWGLOBES software package.

3.3.2 Signature of Supernova Neutrinos in a LArTPC

The dominant interaction channel for electrons in liquid argon is the charged current $\nu_e + {}^{39}\text{Ar} \rightarrow e^- + {}^{40}\text{K}^*$. This interaction produces a visible electron with an energy equal to the neutrino energy minus the 1.5 MeV ground-state energy difference of ${}^{39}\text{Ar}$ and ${}^{40}\text{K}$. In addition, because the transition to the ground state of potassium is third forbidden, a fraction of the neutrino energy will also go towards exciting the potassium atom. The excited potassium state will then decay towards the ground-state via a number of transitions producing a spectrum of de-excitation photons which varies event by event. The first calculation of de-excitation photon spectra of potassium from IBD interactions on argon was performed by R. S. Raghavan in 1986 [36], and additional references [37, 38] provide measurements for the de-excitation transitions performed using the isospin symmetric ${}^{40}\text{Ti} \rightarrow {}^{40}\text{Sc}$ transition.

Detecting tens of MeV electrons from neutrino interactions is required in order to study SNB physics. Challenges to this measurement come from the detection of low energy activity in large-scale detectors, and the impact of electron topology on the neutrino energy reconstruction. Currently, estimates of electron neutrino energy resolution used for LArTPC detectors (such as DUNE [39]) rely on measurements of electron energy reconstruction which do not take into consideration ra-

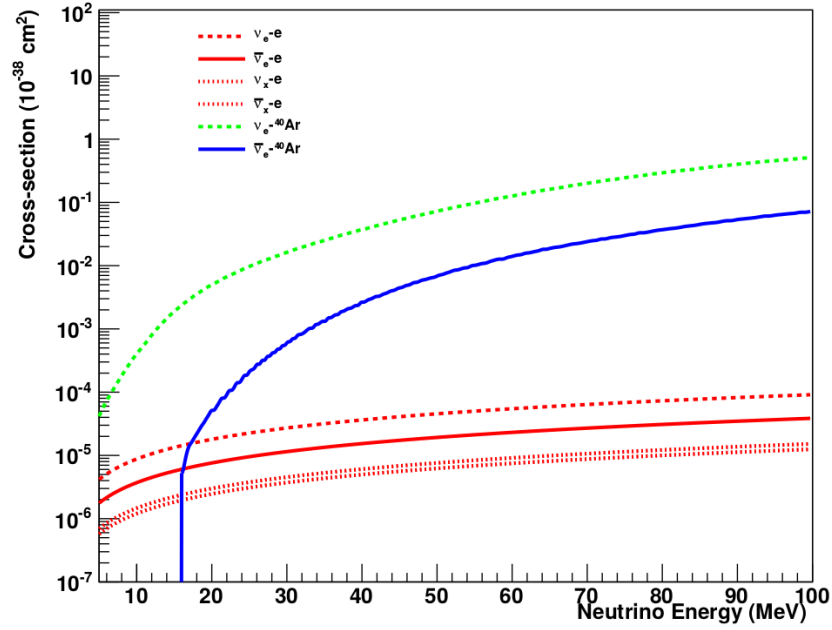


Figure 3.3: Calculated cross-sections for neutrinos and anti-neutrinos on argon below 100 MeV of energy. The electron neutrino cross section on argon dominates the others. In this figure the recently measured interaction channel of Coherent Elastic Neutrino Nucleus Scattering ($\text{CE}\nu\text{NS}$) is not shown. While larger still than the charged current interaction channel by about two orders of magnitude, this process is only detectable through the tens of keV recoil energy released by the interaction nucleus, a process not detectable with current LArTPC neutrino detectors.

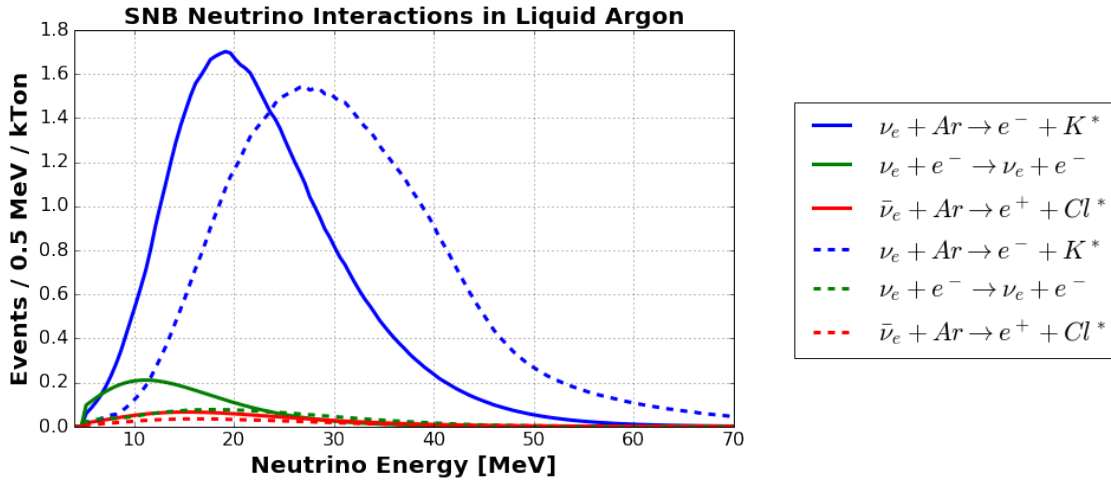


Figure 3.4: Energy spectra and event rate for the predicted supernova neutrino flux in a LArTPC detector. Solid and dashed lines represent the spectra for the same interaction channels obtained from two distinct flux predictions. The blue curves denote event rates for the $\nu_e + \text{Ar}$ charged-current channel, red shows the rates for anti-electron neutrino interactions on argon, and green those for electron neutrino - electron scattering.

diative energy losses [40]. The measurements presented in chapter 8 can provide useful input to studies of SNB detection in LArTPC detectors, addressing the impact of electron topology on the neutrino energy reconstruction, and the separation of de-excitation photons produced by the excited potassium atom from bremsstrahlung photons produced by the low-energy electron. Finally, the measurement of SNB events on the surface may be hampered by cosmogenic activity induced by a large cosmic-ray flux. Chapter 7 presents a first measurement of such backgrounds for LArTPC detectors, and show the impact these backgrounds have on SNB neutrino detection.

Readout and data-acquisition also play an important role in the ability to study SNB events with massive detectors. In order to be sensitive to a SNB event, a detector must have a 100% live-time. This is in sharp contrast to the data-taking required when studying neutrino interactions from a pulsed beam from an accelerator. The large data-volumes associated to a large-scale LArTPC make the transfer and preservation of large data-sets recorded continuously challenging. In order to overcome this a data decimation readout technique that preserves TPC signals from energy deposition while removing the large data-volume associated to quiet waveform regions is required. MicroBooNE has developed a data-suppression readout technique capable of reducing data-volumes to a rate which is sufficiently low to allow it to be transferred to DAQ machines, while preserving the data required to analyze neutrino interactions from SNB events. The continuous readout mode developed, referred to as *supernova stream*, performs channel-wise data-suppression through firmware algorithms loaded on the FPGA chips included in the warm readout electronics.

3.3.3 Relevance of EM interaction studies to SNB Physics

The work of Chapters 7 and 8 provide valuable measurements of the background rates and energy resolution of EM activity in the tens of MeV energy range which has a direct impact on the detection feasibility and energy resolution for supernova neutrinos in a LArTPC. Rates of EM backgrounds on the surface are found to be comparable to or below those of the expected SNB neutrino interaction rate, implying that the study of such events on the surface is feasible for large enough detectors. The study of energy resolution for electrons produced by muon decay-at-rest presented in Chapter 8 introduces and quantifies the significant impact radiative losses have at these energies. The measurement of the energy-dependent energy resolution of electrons in the 10-50 MeV range complements that performed by the ICARUS collaboration (presented in reference [40]) expand-

ing beyond the resolution of ionization-only energy deposition, thus providing a more complete assessment of the impact of electron reconstruction on the neutrino energy resolution attainable.

Chapter 4

The MicroBooNE Detector

This chapter presents an overview of the working principle of the Liquid Argon Time Projection Chamber (LArTPC) detector technology, with a focus on the design details of the MicroBooNE detector. The LArTPC detector technology, proposed by Willis and Radeka (1974) [41] and Rubbia (1977) [42], following the successful development of a TPC by David Nygren (1970), provides a fully active tracking detector which can measure charged particle interactions with accurate position and calorimetric resolution. In a LArTPC charged particles lose energy as they travel through the detector volume by exciting and ionizing the argon. Energy lost to ionization will manifest itself as a trail of electrons which faithfully maps the three-dimensional trajectory of a charged particle. Excited argon atoms can form excimers which then decay leading to the production of scintillation light. The energy lost by the traversing charged particle is split roughly equally between ionization charge and scintillation photons. Scintillation light will propagate isotropically through the detector volume and can be measured with photomultiplier tubes. Ionization charge, on the other hand, will remain stationary in the detector. In order to measure the ionization charge preserving the topological and calorimetric information it conveys an electric field is applied across the detector volume which drifts the ionization electrons towards a mesh or wires. Ionization electron clouds, by drifting past or being collected on the wires will induce a current which can be recorded. The pattern of charge deposited on the wires as a function of time can be used to produce an image of interactions in the detector of comparable quality to those produced by bubble-chamber detectors.

4.1 Energy Loss in Liquid Argon

4.1.1 Light Production

Scintillation light is produced when excited argon atoms form an excimer state by combining with an argon atom in the ground state and forming a Rydberg state in which an Ar_2^+ molecule shares a bound electron. The excimer then decays to two ground state argon atoms releasing a 128 nm photon. The time constant associated to this decay depends on the excited state of the Ar_2 molecule. Two excited states contribute to producing this scintillation light: an excited singlet state, with a 6 ns time constant, and a triplet state, with a much longer 1.5 μ s time constant. Argon has two attractive properties: it is transparent to its own scintillation light and the photon yield is quite high, at roughly 4×10^4 photons per MeV of deposited energy.

4.1.2 Ionization Signal

Approximately 4×10^4 free electrons are released for every MeV of energy deposited. The electric field applied in the TPC causes the electrons to continuously drift towards the readout wires preserving information on the position and energy released by the traversing charged particle. Two main effects can get in the way of the uninterrupted drift of electron clouds: ion recombination and ion absorption by impurities.

Ion recombination is the process by which free electrons recombine with neighboring Ar^+ ions producing a neutral argon atom. This effect occurs once the ionized electrons have thermalized and its magnitude is dependent on the local ion density. The ion density is, in turn, a function of the local electric field (which determines how much time oppositely charged ions spend close to each other before being drifted apart) and the original local energy deposition (measured by the observable dE/dx). In MicroBooNE, for minimally ionizing particles, the amount of ionized electrons which eventually recombine is close to 40%.

Being a noble gas, argon will not interact with the drifting electrons, allowing the signal to not be attenuated. Impurities such as water and oxygen can however quench the signal by absorbing electrons. The amount of signal attenuation caused by impurities is dependent on their concentration and electron affinity. This form of signal loss manifests itself as a drift-distance dependent attenuation: charge which drifts a longer distance will have been exposed to a larger amount of

quenching. It is important for large-scale detectors to obtain a low impurity concentration in order to obtain a relatively uniform position-dependent response in the detector, and allow for energy deposited close to the cathode-plane to still be visible.

4.2 The MicroBooNE Time Projection Chamber

MicroBooNE's TPC is a parallelepiped with dimensions of 10.36 m in the beam-direction, 2.32 m in the vertical direction, and 2.56 m in the horizontal drift direction with a coordinate system defined as shown in figure 4.1.

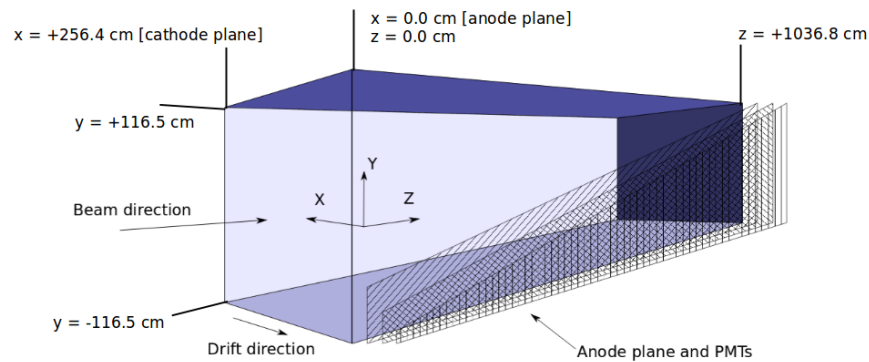


Figure 4.1: Cartoon drawing of MicroBooNE's TPC. The parallelepiped is placed with its longest side in the beam direction. The anode-plane on which wires where signals are formed is on the right-hand side, as seen from the beam. The cathode, where the drift HV is applied, is on the left.

The TPC has three main components: a cathode-plane, field cage, and anode plane. These are responsible for maintaining a uniform electric field in the detector volume allowing ionization electrons to drift towards the sense-wires. The cathode-plane consist of a sheet of stainless steel which is kept at an electric potential of -70 kV. The field cage is made up by 64 stainless steel tubes placed between the anode and cathode planes across which a resistor chain is installed in order to produce a uniform electric field. The field has a strength of 273 V/cm across the drift direction. The anode plane houses the sense-wires, arranged in three planes, separated by 3 millimeters and oriented at 60° with respect to each other. Wires on the three different planes are kept at a fixed electric potential in order to shape the electric field in a way that maximizes signal transparency.

Drifting electrons will pass by two wire-planes closest to the cathode, producing an induction signal, and will be collected on the last plane, denoted as the collection plane. By allowing the same electron cloud to leave a time-coincident signature on multiple planes with different orientations one is able to produce images which show different two-dimensional projections of the same three-dimensional energy deposition pattern. These multiple view points allow to triangulate the exact 3D location of energy deposited in the detector.

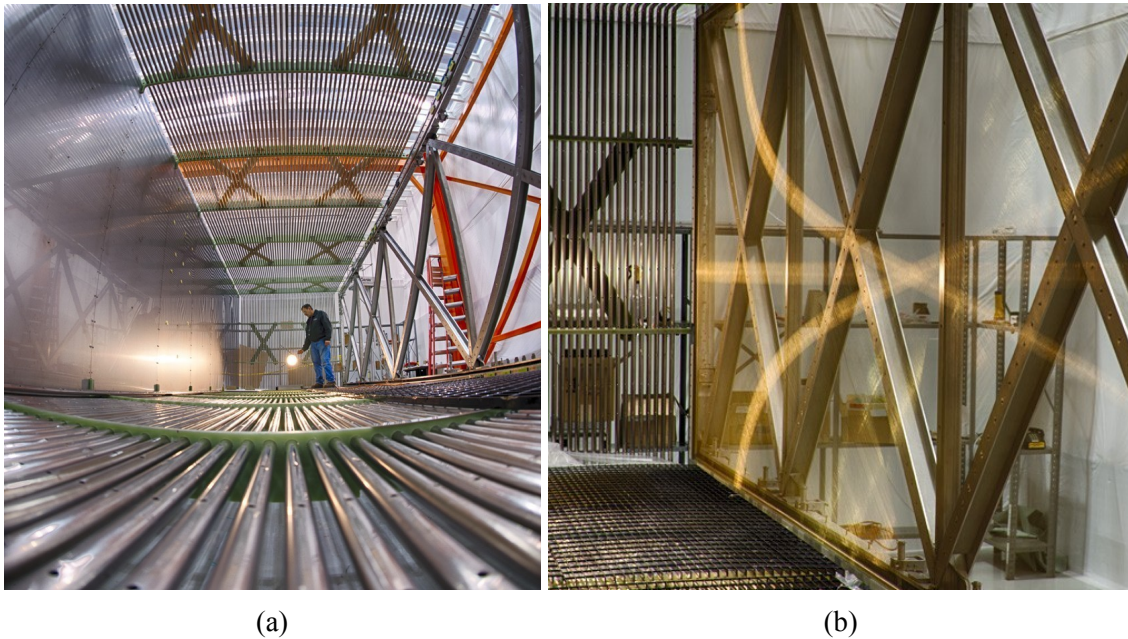


Figure 4.2: View of the TPC from the inside. (a) view along beam direction. (b) view of wire-plane mesh. Photo provided by Fermilab Visual Media Services.

4.2.1 The Challenge of Slow Ion Drift

Slow drifting signals require long readout windows for the full interaction to be recorded. In MicroBooNE, recording charge deposition which occurs during the $1.6\mu\text{s}$ beam-spill from the entire detector volume requires a 2.3 ms readout window. During this time roughly 20 cosmic-ray muons will enter the detector, superimposing their energy deposition on the readout signals produced by neutrino interactions. The slow readout makes it difficult to take full advantage of one of the strengths of an accelerator-based neutrino experiment: an intense pulsed beam useful to isolate interactions.

An additional, more practical challenge is associated with the data-volume output of a LArTPC detector. Reading out thousands of TPC channels with a fine sampling for milliseconds at a time

requires storing lots of data. This topic is discussed in more detail in section 4.4.5.

4.2.2 Signal Formation

Ionization electrons produced in the TPC are detected as induced currents caused by their passage through sense-wires placed on the anode-plane. The same ionization electrons will produce a signal on wires on all three planes. As they pass by the first two wire-planes electrons induce a bipolar signal. The signature on wires on the final plane, on which electrons are collected, is unipolar. Wires on different planes shield each other such that drifting electrons do not induce a current on a wire until the electrons have past by the preceding wire-plane. There is no shielding for the induction plane closest to the cathode, causing these wires to sense drifting charge over a larger distance and exhibit a stretched response. Figure 4.3 shows a schematic view of how drifting electrons induce signals on consecutive wire-planes. The image on the left shows a top-down view of the TPC. The negatively charged cathode is on the top of the image, with the anode-plane at the bottom. Blue, green, and red dots indicate the position of different wires. The time-profile of signals induced by the same drifting electrons on the three wire-planes is plotted next to the top-down view, aligned with their respective wire-planes. The right hand side of figure 4.3 shows for a small 6x6x6 cm cell in the detector signals induced on the three wire-planes by the same minimally ionizing cosmic-ray muon. The blue and green boxes show signals from the first and second induction-planes respectively, with collection-plane signals shown in red. Because of the different orientation of wires on the three planes, the wire-time profile of the muon appears rotated in the different views.

4.2.3 TPC Data: Overview

An example event display is shown in figure 4.4 to summarize the TPC data-format. This image represents a snippet of the full collection-plane data recorded during one event triggered by the BNB beam. It corresponds to a top-down view of the interaction occurring in the detector. Each TPC channel waveform is represented as a vertical line. The y-axis denotes the drift-time with successive channels ordered in the beam-direction displays on the x-axis. Color denotes the recorded ADC amplitude at each time-tick. The vast majority of the image is “empty”. In the center, an interaction vertex associated to a neutrino produces several outgoing tracks, in addition to EM activity. Overlayed on the image are several additional tracks, uncorrelated with the neutrino vertex,

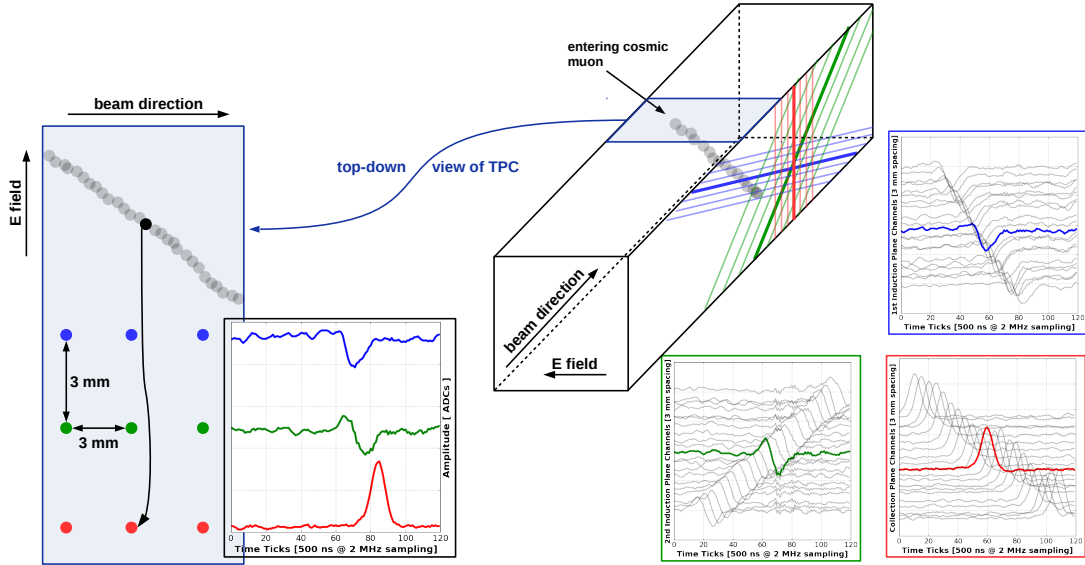


Figure 4.3: Signal formation cartoon.

induced by cosmic-ray muons which enter the TPC while the slow-moving ionization charge from the interaction is drifting.

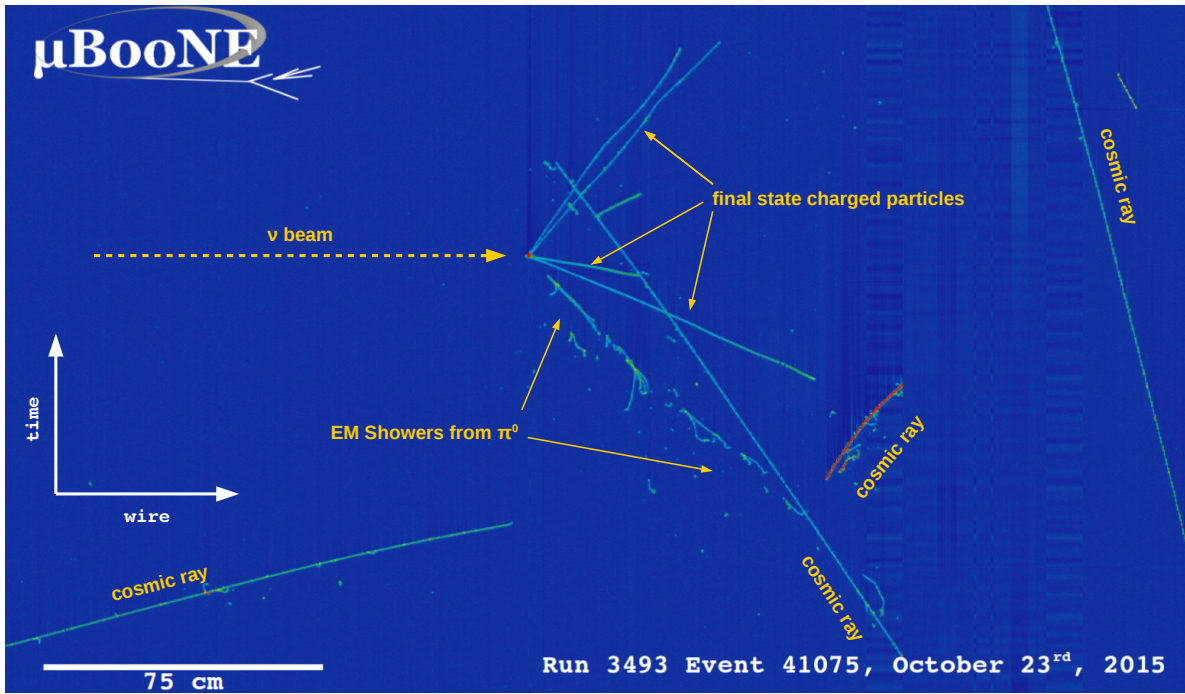


Figure 4.4: Example collection-plane image recorded with the MicroBooNE TPC.

4.3 Light Collection System

The MicroBooNE detector collects scintillation light produced in the detector with the primary purpose of recording the interaction time of energy deposited in the TPC. Light is collected by an array of 32 Hamamatsu photomultiplier tubes (PMTs) placed behind the anode wire-planes. The PMTs used are sensitive to optical light in the 4-500 nm wavelength. In order for the optical system to detect the 128 nm scintillation photons produced a wavelength-shifting plate is placed in front of each PMT. The wavelength-shifting material used is Tetraphenyl-butadiene (TPB), a molecule which absorbs vacuum-ultraviolet (VUV) photons and re-emits visible photons with a spectrum peaking at 425 nm. Photons emitted from the TPB are isotropically produced, which will lead to an inefficiency in collecting the scintillation light. A single PMT, with the plate on which the TPB coating is placed, is shown in figure 4.5a, with a view of the PMT array from inside the MicroBooNE cryostat shown in figure 4.5b.

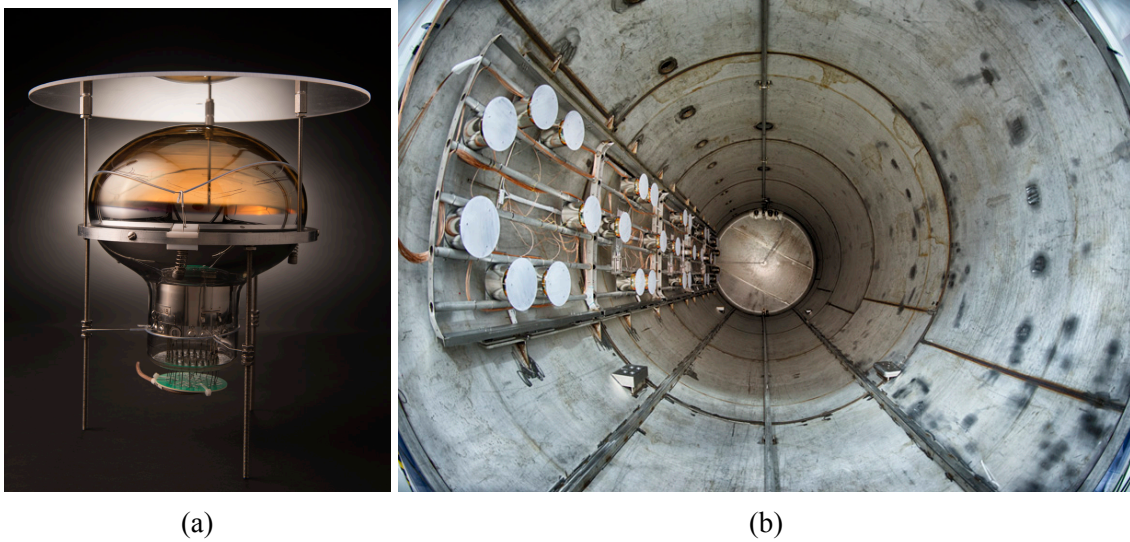


Figure 4.5: (a) View of a single 8-inch PMT. (b) PMTs mounted on frame in the MicroBooNE cryostat. Photo credit: Reidar Hahn, Fermilab Visual Media Services.

4.4 Readout Electronics

MicroBooNE’s readout electronics are responsible for forming, digitizing, and recording signals associated to the TPC and PMT systems. Data recorded from the TPC system needs to produce fine-grained millimeter-resolution images of interactions in the detector which can be used to perform tracking and particle identification. The PMT stream serves the purpose of providing timing information for neutrino interactions associated to the μs wide beam-spills, as well as other cosmic ray activity occurring throughout an event in the several milliseconds it takes for charge produced in the detector to fully drift to the anode-plane wires.

4.4.1 TPC Electronics

The MicroBooNE TPC electronics system is separated in “cold” electronics, submerged in liquid argon, and “warm” electronics located outside of the cryostat. The cold electronics are responsible for amplifying and shaping signals produced on the sense-wires. Performing these operations in the cold in close proximity to the wires allows MicroBooNE to obtain a high signal-to-noise ratio essential to perform accurate particle identification with low detection thresholds. The warm electronics are responsible for digitizing signals, compressing and formatting the data before it is sent to the data acquisition system.

The cold electronics are installed on motherboards which attach directly to the wire-carrier boards on the TPC anode-plane. The main electronics component on the motherboard is a front-end ASIC which uses the CMOS technology [43] to perform a pre-amplification and signal-shaping. The ASIC is configured to apply a gain of 14 mV/fC and shape the collected signal with a $2\mu\text{s}$ response.

A study of noise levels in the TPC as the detector was being cooled down to liquid argon temperatures was performed in the spring of 2015 [44]. Figure 4.6 shows the noise level in units of equivalent noise charge, measured as the pedestal RMS on collection-plane wires, as a function of the average temperature in the cryostat. The noise levels fall off rapidly before stabilizing below 150 K, with a total reduction of a factor of two.

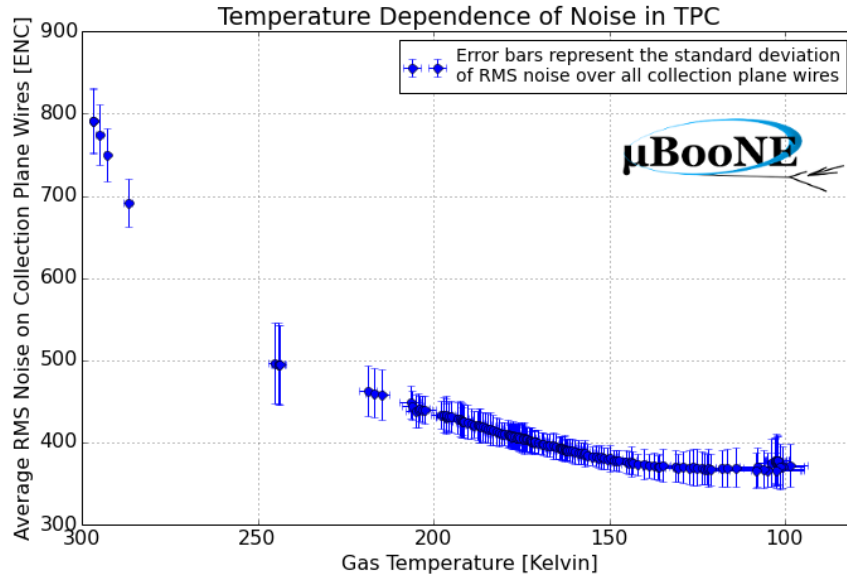


Figure 4.6: Noise on collection-plane wires vs. gaseous argon temperature inside the MicroBooNE cryostat. Noise measurements are shown in equivalent noise charge. Each data point shows the average RMS noise value on collection-plane wires for a given run. Error bars correspond to the spread in RMS noise values due to channel-to-channel variations.

Pre-amplified signals leave the cryostat on warm cables which carry signals from 32 channels each and connect in pairs to an ADC/FEM board housed in one of nine TPC readout crates. Signals are digitized by a 16 MHz clock in 16-bit words with a 4095 ADC dynamic range at 2 Volt / 4095 ADC. Digitized waveforms are processed by an FPGA chip in the FEM where they are down-sampled from 16 to 2 MHz (500 ns time-ticks). Each FPGA records waveforms from 64 channels, and produces as output time-ordered waveforms of three 1.6 ms (3,200 time-tick) frames with one preceding and two following the trigger time. In order to reduce data-rates, data from each frame is compressed by a lossless Huffman encoding scheme.

4.4.2 PMT Electronics

Signals from each PMT are carried out of the detector on the same cable which supplies HV to the PMT dynode chain. A splitter circuit, shown in figure 4.7, separates the readback signal from the constant supply HV, and splits the signal in a high-gain (HG) and low-gain (LG) channel which carry 18% and 1.8% of the total signal amplitude respectively.

Analog signals from the splitter circuit are split again leading to two identical copies of the

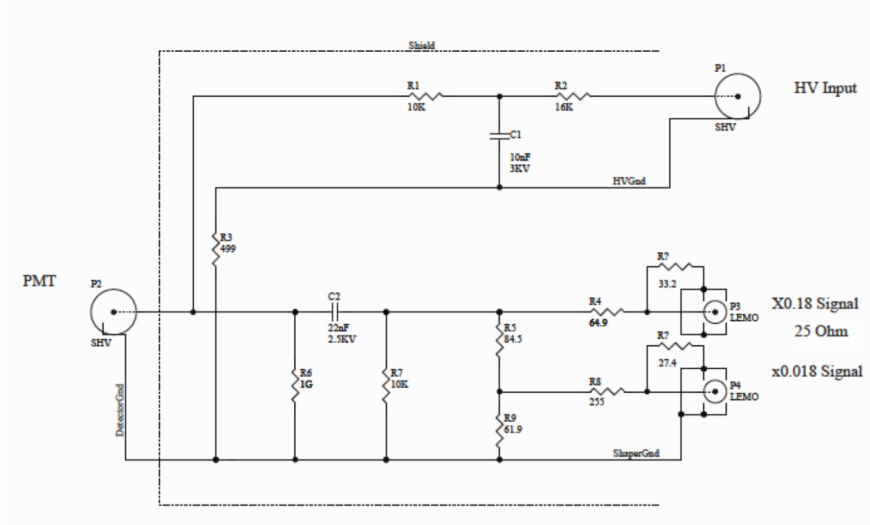


Figure 4.7: Drawing of the MicroBooNE splitter circuit. High voltage and readback signals travel on the same cable into the detector. Signals are separated from the DC HV via an AC-coupling capacitor (C2). Signals are then split into a high-gain and low-gain signal which carry 18% and 1.8% of the input signal respectively.

HG and LG signals. These signals are shaped with a unipolar response function with a 60 ns rise time. Finally, shaped pulses are digitized at 64 MHz (15.625 ns time-ticks) in 16-bit words. Figure 4.8 shows, with three different examples, the complementary role HG and LG channels play in increasing the PMT system’s dynamic range. The top image shows the case in which both the HG and LG channels are able to record the full characteristics of the pulse. The middle image shows single photo-electron pulses which are recorded with good signal to noise in the HG channel, but are out of the dynamic range of the LG channel due to waveform digitization. The bottom image shows a waveform which saturates the dynamic range of the HG channel but is fully characterized in the LG channel.

4.4.3 Accelerator Signals and Trigger Logic

One of the advantages of performing an accelerator-based neutrino experiment consist in the availability of a pulsed intense neutrino beam with a well defined time profile which can be used to trigger the detector readout. MicroBooNE relies on signals from the Fermilab accelerator complex to form triggers used to record activity in the detector. Additional “external” triggers used to collect data for background and calibration studies are also present.

MicroBooNE uses as its main neutrino trigger signals provided by the Fermilab accelerator

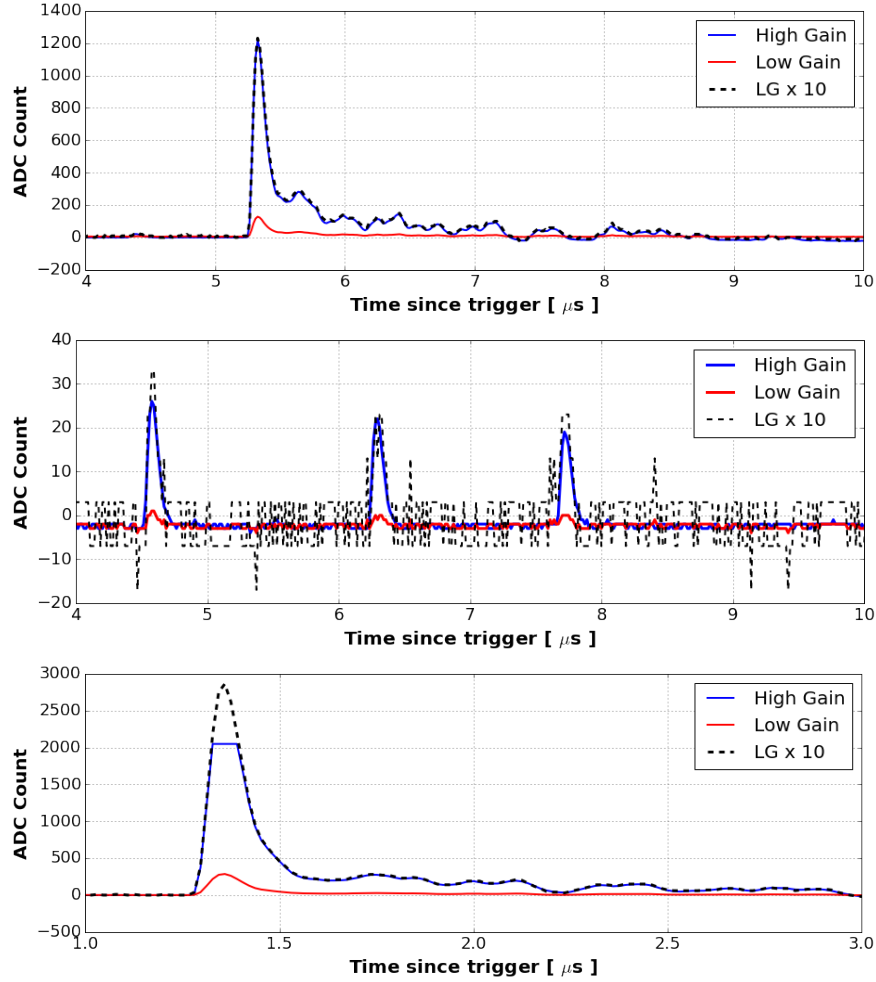


Figure 4.8: Three different examples of waveforms from the HG (blue) and LG (red) channels for a PMT. The black dashed line shows the LG waveform scaled by a factor of 10. All waveforms are shown after baseline subtraction.

division which indicate that the proton beam is about to be sent to the target. Two different signals exist for the BNB and NuMI beams. These signals, produced as protons are still circulating in either the Booster or Main Injector rings, arrive at the MicroBooNE detector hall before the neutrino spill reaches the detector.

4.4.4 Data Format

Data from the PMT and TPC system are recorded independently. While the TPC system is passive and is recorded with a fixed format once a trigger is received, the PMTs play an active role in both handling and issuing triggers. Two different data-formats are used to record light collected in-time with the beam and light associated with cosmic-rays produced elsewhere in the

event. Once a trigger is received, three 1.6 ms frames aligned with the trigger time are recorded from the TPC stream covering the time-interval $[-1.6, +3.2]$ ms with respect to the trigger time. The PMT system records data in two different formats: an unbiased readout meant to record activity in time-coincidence with the neutrino beam, and a threshold-based triggered readout, which records light from cosmic rays entering the detector throughout the event. The unbiased beam-gate readout consists of a 1,500 sample ($23.4 \mu\text{s}$) readout window surrounding the neutrino beam-spill. Outside of this window optical information is saved by each PMT independently in 40 sample ($0.6 \mu\text{s}$) triggered windows recorded when the PMT waveform passes a threshold condition referred to as the “cosmic discriminator”. The cosmic-discriminator readout, set with a threshold of 9.5 PE, allows the PMT system to record light activity produced by cosmic ray muons throughout the event. Unlike for the TPC, PMT frames are not aligned with the trigger. In order to make sure PMT data is recorded over the entire 4.8 ms event window cosmic-discriminated pulses which occur in the frame containing, the one preceding, and the two following the trigger are saved to the event. Figure 4.9 schematically shows the data format of the TPC and PMT streams for triggered events. Figure 4.10 shows for a data event in a $38 \mu\text{s}$ window surrounding the trigger where the 1,500 sample beam-gate unbiased readout as well as several $0.6 \mu\text{s}$ cosmic-discriminated waveforms are recorded.

4.4.5 Data Rates

An important consequence of the slow electron drift velocity in liquid argon is the long readout time required to fully record interactions in the TPC, and the high data-volume that this leads to. Recording a full event window (three frames) for all TPC channels requires

$$8,256 \text{ channels} \times 9,600 \text{ samples} \times 16 \text{ bits per word} = 150 \text{ MB/event} \quad (4.1)$$

Which scales down by a factor of roughly 5, to approximately 30 MB/event, after Huffman encoding is applied. If running at a 5 Hz beam trigger-rate this implies a data-volume of 13 TB/day. Because most spills from the neutrino beam lead to no interactions in the detector volume, a significant reduction in data-rates can be obtained if a decision can be made “on-the-fly” on whether to save data associated to any given trigger received from the accelerator. MicroBooNE employs a *software-trigger*, run within the DAQ, which relies on the PMT light timing to identify triggers

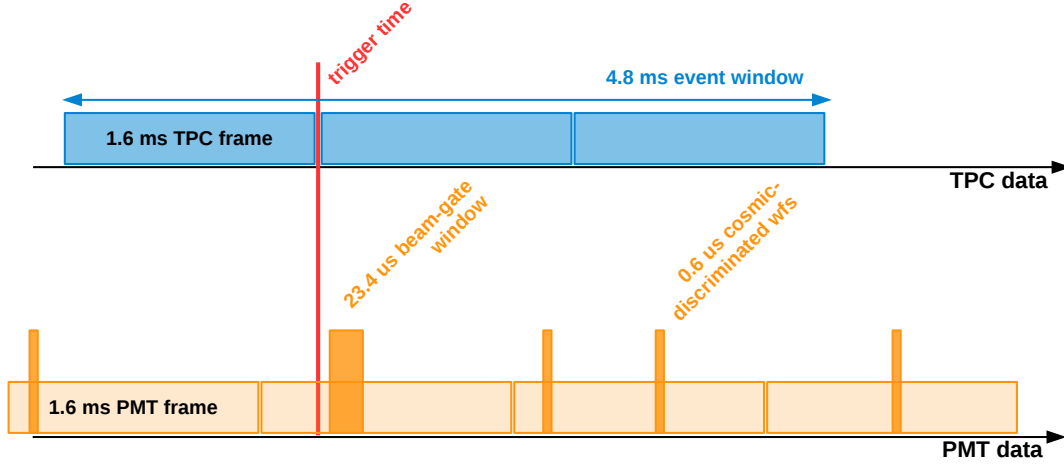


Figure 4.9: Diagram of how PMT and TPC data are recorded for triggered events. Three 1.6 ms TPC frames aligned with the trigger are recorded (one preceding and two following the trigger-time). A $23.4 \mu\text{s}$ unbiased beam gate window following the trigger is recorded for all PMT HG and LG channels. Cosmic-discriminated waveforms, recorded by each PMT channel independently, are saved if the pulse height passes a configurable threshold condition. These $0.6 \mu\text{s}$ waveforms are recorded in the four PMT frames which surround the trigger-time.

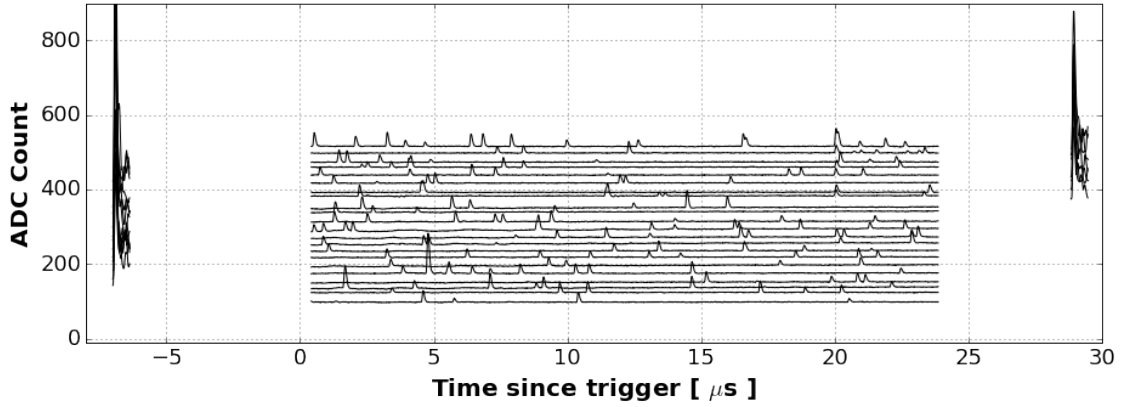


Figure 4.10: Subset of an event recorded by the PMT system in which both the $23.4 \mu\text{s}$ unbiased beamgate window and several $0.6 \mu\text{s}$ cosmic-discriminated waveforms are recorded. Waveforms from different PMTs are artificially offset. While waveforms from all PMTs are recorded during the beam-gate, regardless of the activity observed, cosmic-discriminated waveforms are saved only for PMTs which pass the cosmic discriminator threshold.

which contain activity in the detector in time-coincidence with the neutrino beam. Timing of the neutrino beam is described in section 4.5, and the description of the software trigger can be found in appendix A.

4.5 Beam Timing

Data recorded in the unbiased $23.4 \mu\text{s}$ beam-gate can be used to time-in the neutrino beams. This can be achieved by producing a time-distribution of recorded optical activity throughout the beam-gate window: cosmic rays will enter the detector and produce light randomly throughout this window, with light produced by neutrino interactions showing up as an excess of entries in coincidence with the beam-spill. Waveforms from the beam-spill are processed through the optical reconstruction which first identifies optical hits associated with pulses of light, and subsequently groups together time-coincident (within 100 ns) reconstructed hits in *flashes* which represent distinct bursts of light due to individual interactions occurring in the detector. Each reconstructed optical flash is characterized by a time with respect to the trigger and a total number of photoelectrons obtained by integrating the PEs associated to all optical hits in the flash. Figure 4.11 shows the time-distribution of optical flashes recorded from events triggered by the BNB beam in a subset of the beam-gate window. The width of the blue band centered at $y = 1$ represents the error on the measured cosmic rate. Red data-points indicate the measured flash time distribution for BNB triggered events, normalized to the cosmic rate. An excess of events indicates the location of the $1.6 \mu\text{s}$ BNB beam-spill window with respect to the trigger time. In order to enhance the neutrino contribution to the timing distribution only flashes with a reconstructed PE level greater than 50 PE and smaller than 1,500 PE were used to produce this plot.

4.6 Detector Operations

The MicroBooNE detector has been recording neutrino beam data since the fall of 2015. Figure 4.12 shows the amount of protons-on-target (POT) collected since the start of operations. The π^0 analysis presented in chapters 9 and 10 utilizes $5\text{E}19$ POT of data collected after the software trigger was implemented in the period February 23 to May 22, 2016.

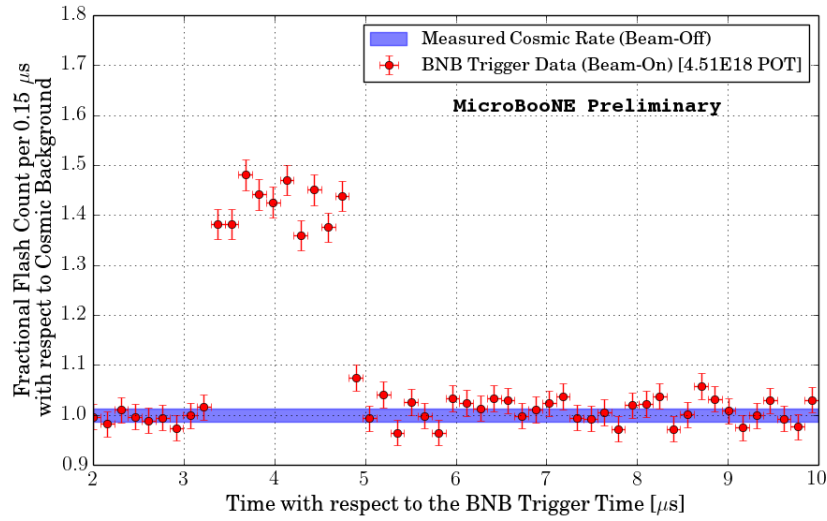


Figure 4.11: The measured distribution of flash times with respect to the trigger time for BNB triggered events, shown as a ratio to the expected cosmic rate from off-beam data. The blue band denoting the cosmic rate was centered at one, with a width corresponding to the measured uncertainty in the cosmic rate. A clear excess can be seen due to neutrinos between 3 and 5 μs after the trigger for BNB.

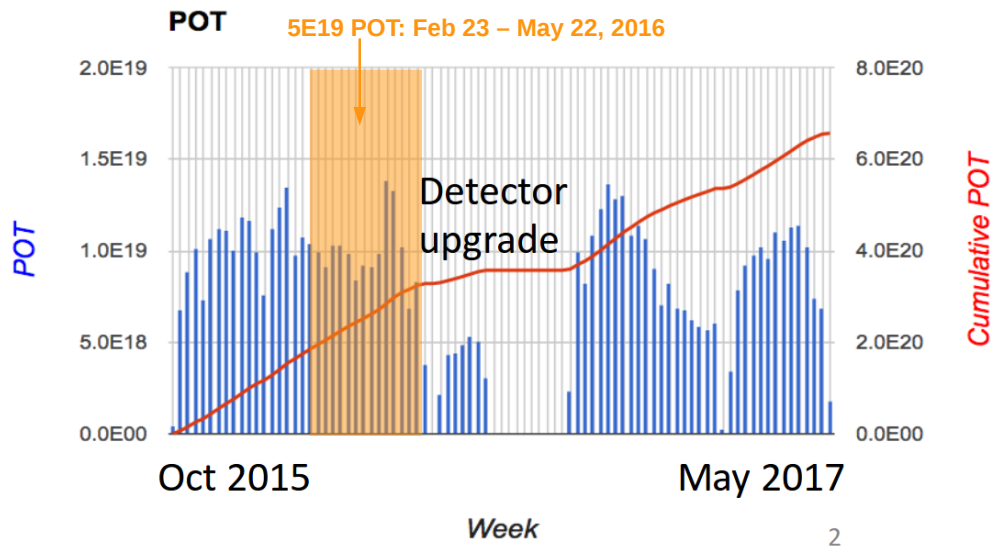


Figure 4.12: Protons on Target over MicroBooNE's two year data-taking period. Highlighted in orange is the period used for the pion analysis presented in this thesis.

Chapter 5

The Booster Neutrino Beamline

The Booster Neutrino Beam is the byproduct of the decay of short-lived pions and kaons which in turn are produced by the collision of the primary proton beam with a target. Knowledge of the neutrino beam flavor content and kinematics are essential in performing absolute cross-section measurements and studying neutrino oscillations. The BNB is predominantly a $\mathcal{O}(1)$ GeV ν_μ source. The beam starts as a hydrogen beam accelerated to 400 MeV in the LINAC. This beam is then sent to the Booster, which accelerates the protons to 8 GeV before sending them to the Booster target hall. Figure 5.1a shows an aerial overview of the various components of the BNB beamline, while figure 5.1b shows an edge-on view of the target hall where the secondary pion, and tertiary neutrino beams are produced.

This chapter describes in some detail the process by which neutrinos reaching the MicroBooNE detector are produced by the Booster Neutrino Beamline (BNB) and is subdivided in three sections describing the main stages involved: the production and extraction of an 8 GeV proton beam, in section 5.1; the beam target and focusing horn which lead to a secondary meson beam, in section 5.2; and the composition of the neutrino beam reaching the detector, in section 5.3. References for much of the content found in this section come from several detailed documents describing the Fermilab accelerator complex and BNB, such as the *Concepts Rookie Book* [45], *Linac Rookie Book: RIL chapter* [46], and *MiniBooNE Rookie Book* [47]. These references, written as documentation for beam operators and anyone interested in learning the technical details of the Booster beamline, were compiled by Dennis Barak, Beau Harrison, Adam Watts, and Michelle Gattuso. Additionally, content referring to the MiniBooNE target, horn, and neutrino flux is partially obtained from

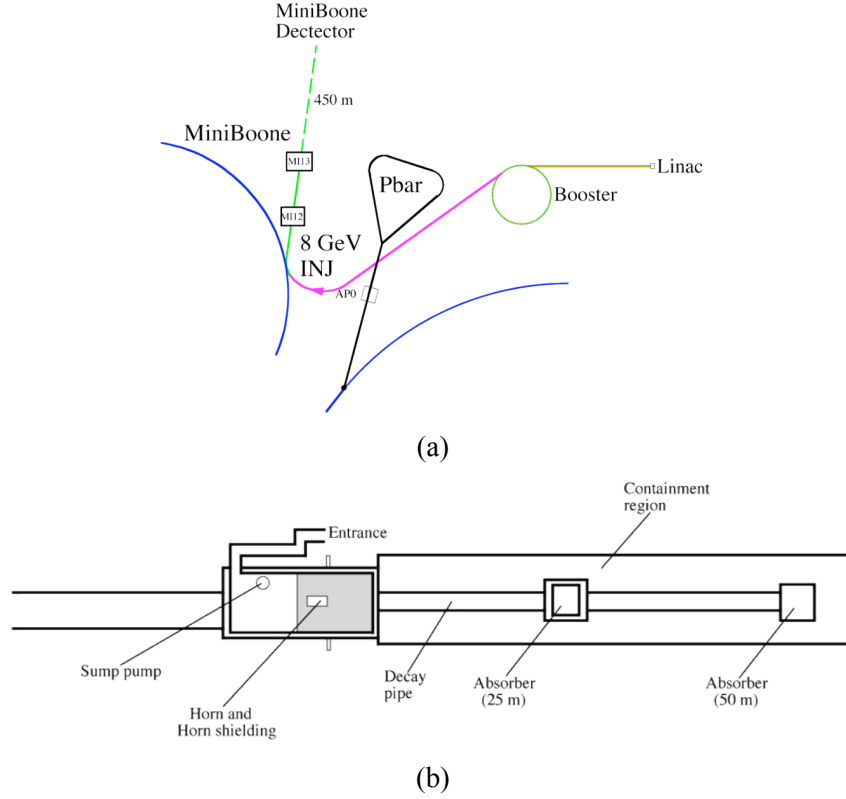


Figure 5.1: (a) Aerial view of the Fermilab accelerator complex. The BNB starts in Fermilab's LINAC (yellow), is then injected into the Booster (green) from which it is extracted and sent to the MiniBooNE target hall (pink) where the target and magnetic horn produce the focused neutrino beam (light green) which reaches MicroBooNE. (b) Lateral view of the target hall.

the MiniBooNE flux paper [48].

5.1 The 8 GeV Booster Proton Beam

The Booster proton beam starts as a beam of negatively charged hydrogen ions. hydrogen gas is allowed to fill a cavity in which a voltage is applied, causing an arc which ionizes the hydrogen and forming a plasma. A magnetic field sends H^+ towards the cathode. In flight some of the positive H^+ will capture two electrons from the plasma, producing H^- . Subsequently, the anode and cathode are pulsed with the same -35 kV voltage which causes H^- to move towards a grounded extractor cone, forming the primary H^- beam with an energy of 35 keV. The beam is then focused in order to match the phase-space requirements of the Radio Frequency Quadrupole (RFQ) which will perform the next stage of acceleration. Two solenoids are used to focus the beam, and

corrector magnets allow to further trim its horizontal and vertical dimensions. In order to counter the repulsive forces between H^- ions which would cause the beam to diffuse, positive H ions are injected at this stage. Finally, an Einzel lens is used to *chop* the beam: when grounded it allows the electron beam to continue, but when pulsed at a voltage higher than the kinetic energy of the ions in the beam, it is stopped. This operation is performed in order to transform a continuous stream of H^- into a pulsed structure which will match the requirements of the RFQ cavities. This first acceleration stage produces a $100\ \mu\text{s}$ wide beam, pulsed at 15 Hz. The RFQ provides an intermediate acceleration stage in which the beam is brought to an energy of 750 keV. This acceleration stage occurs before the beam is transported to the LINAC in order to minimize the space charge effect caused by the repulsive force of the H^- ions.

The LINAC accelerates H^- from 750 keV to 400 MeV via two series of RF cavities. The first operates at ~ 201 MHz and brings the beam up to 116.5 MeV, at which point the beam's longitudinal profile is modified to match the ~ 805 MHz frequency of the second series of RF cavities. The 400 MeV beam is then steered towards the Booster through a chopper, made up of two electrodes. A potential difference between the electrodes, placed on either side of the beam, allows it to be deflected. The time-interval during which this potential is applied is set to match the beam's travel time in the Booster, equal to $2.2\ \mu\text{s}$, referred to as a Booster *turn*. The total number of turns inserted depends on the desired intensity, and defines a *batch*. Once the beam has entered the Booster, the H^- ions are passed through a stripping foil, as shown in figure 5.2, producing a proton beam. The electron stripping happens after the H^- beam has been inserted into the Booster, in order to allow the same bending magnet to simultaneously bend injected H^- and circulating protons in the Booster's direction of curvature.

The Booster magnets cycle at 15 Hz, meaning that beam must be injected or extracted from the Booster at 15 Hz. The RF system captures the incoming DC beam into bunches which can then be accelerated. The resonant frequency of the RF cavities in the Booster sweeps from 37.8 MHz to 52.8 MHz as the beam is being accelerated from 400 MeV up to 8 GeV. This acceleration causes the revolution period to drop from $2.2\ \mu\text{s}$ to $1.6\ \mu\text{s}$ at extraction. Eighty-four bunches are extracted at once. A kicker magnet allows the circulating beam to be extracted. Because the magnet has a non-zero ramp-up time beam being extracted as the magnet is ramping would spray instead of

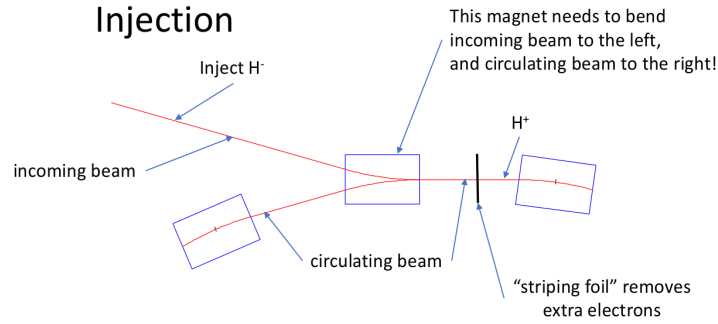


Figure 5.2: Image courtesy of Tom Kobilarcik. Beam injection into the Booster: The negatively charged H^- beam is bent into the Booster by the first magnet. A stripping foil then strips the electrons off the hydrogen ions, producing a proton beam, which continues to circulate.

remaining focused. To overcome this a *notch* in the beam (segment of the full circumference with no protons) is formed right after injection. The notch position is synchronized with the kicker magnet rise-time, allowing the extracted beam to remain focused as it leaves the Booster. The notch removes three of the 84 bunches. The extracted beam structure, composed of 81 bunches, each 2 ns wide, and spaced evenly in the $1.6 \mu\text{s}$ batch, is shown in figure 5.3.

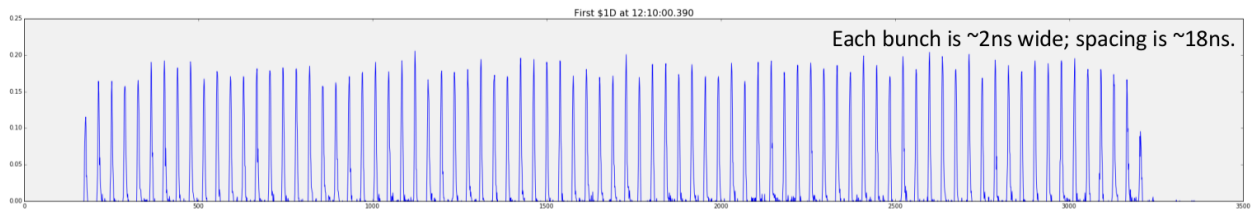


Figure 5.3: Image courtesy of Tom Kobilarcik. Beam bunches in the $1.6 \mu\text{s}$ Booster batch.

5.2 Beam Target and Focusing Horn

The target is used to produce a secondary beam of short-lived pions and kaons from the primary proton beam. It is made up of seven collinear cylindrical segments of beryllium, with a 0.51 cm radius and total length of 71.1 cm. These are contained within a *sleeve* (1.37 cm inner radius, 0.9 cm thickness) also made of beryllium, which is connected to each segment via three beryllium fins. Air is circulated between the sleeve and the target for cooling.

Charged pions produced by collisions of protons with beryllium leave the Target with a wide angular distribution which would lead to a diffuse neutrino beam. To produce a focused beam a magnetic horn is placed around the target. The horn, when pulsed, focuses charged pions and kaons in the beam-direction. The more focused the mesons are before the decay, the more focused will the neutrino beam be once it reaches the detector, enhancing the flux. The focusing horn is a toroidal magnet made of aluminum which is pulsed with a 174 kA current. A drawing of the horn structure is shown in figure 5.4. The horn is 185 cm long, and is composed of an inner and outer cylinder. A positive current travels down the inner conductor and arches back towards the front via the outer conductor, producing a magnetic field which points in the beam direction within its volume and falls off as $1/r$. The inner conductor is placed just outside the beryllium target. Right outside the inner conductor the strength of the magnetic field reaches 1.5 Tesla. The horn is cooled by water which is sprayed on the surface of the inner conductor.

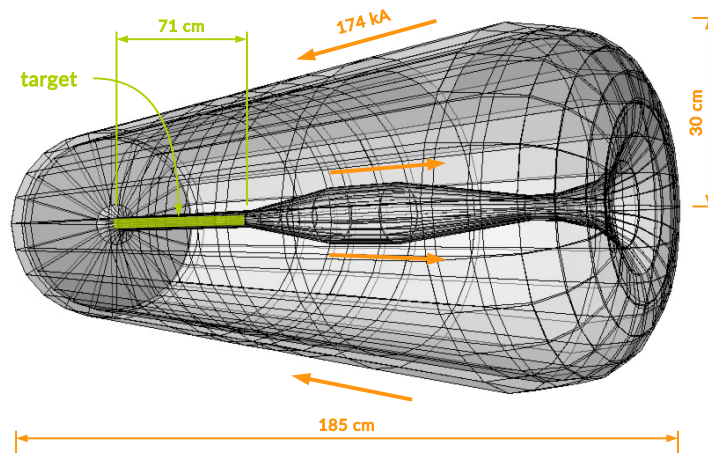


Figure 5.4: Drawing of MiniBooNE target and horn. In green is the beryllium target. Source: MiniBooNE Flux Prediction [48].

Focused charged pions and kaons next go through a collimator: a 2.14 meter thick block of concrete which absorbs particles which do not contribute to the neutrino flux, while at the same time reducing radiation levels elsewhere in the beamline. Next follows a 50 meter decay region: a cylindrical volume of air, 3 feet in diameter, in which pions and kaons decay, producing the tertiary neutrino beam which eventually reaches the detector. Remaining charged particles which have not yet decayed are blocked by beam stop. By this point the beam is composed almost entirely of

neutrinos which propagate through dirt before reaching the detector.

5.3 Beam Composition

The MicroBooNE neutrino beam is largely a ν_μ beam with small contaminations of $\nu_{\bar{\mu}}$ and ν_e . The beam composition is a product of the polarity at which the focusing horn is operated and the decay modes of charged pions which make up the majority of the secondary beam. Because the horn is pulsed with a positive current, positively charged mesons will be deflected towards the beam axis, while deflecting away negatively charged ones. Positively charged pions are in a spin-0 state, and decay via the weak force in a lepton plus neutrino. In the pion's rest frame, to conserve linear and angular momentum, they must propagate in opposite directions and exhibit opposite handedness. The low neutrino mass implies that the neutrino is always produced as left-handed. The lepton must as a consequence be right-handed but in a state of left helicity. The contribution to a left-helicity particle from its right-handed spin is proportional to m/E with m and E the mass and energy of the particle. This causes the decay to a muon to be much more likely than that to an electron, of significantly lower mass. The pion decay to $e^+ + \nu_e$ is suppressed with respect to the channel $\mu^+ + \nu_\mu$ by a factor of $\sim 10^{-4}$, leading to a largely muon neutrino beam. Contamination from other neutrino states in pion decay are caused by the following processes:

- $\bar{\nu}_\mu$: contamination in the beam from μ^- which are very forward going or very energetic and therefore are not deflected by the horn.
- ν_e : the decay of muons from pions in the secondary beam: $\mu^+ \rightarrow e^+ + \bar{\nu}_\mu + \nu_e$.

Neutrinos produced by the decay of kaons (K^\pm , K^0 , K_L^0) also contribute to the flux. Due to the smaller kaon production rate in the target this is a minor (but non-negligible) contribution to the total neutrino flux. For muon neutrinos, almost the entire flux below 2.5 GeV is contributed by events which originate from pion decay, while kaons contribute almost exclusively to those beyond this energy. Most importantly, because of the broader range of decay channels, kaons contribute significantly to the ν_e flux, even at lower energies. Table XI of reference [48] shows a complete list of the beam flux in neutrino mode from all four neutrino states as modeled by the MiniBooNE simulation, including the fractional composition subdivided in the different decay modes which

produced them. Figure 5.5 shows the neutrino flux split in the contributions from the four neutrino states as modeled by the MiniBooNE beam simulation and calculated at the MicroBooNE detector.

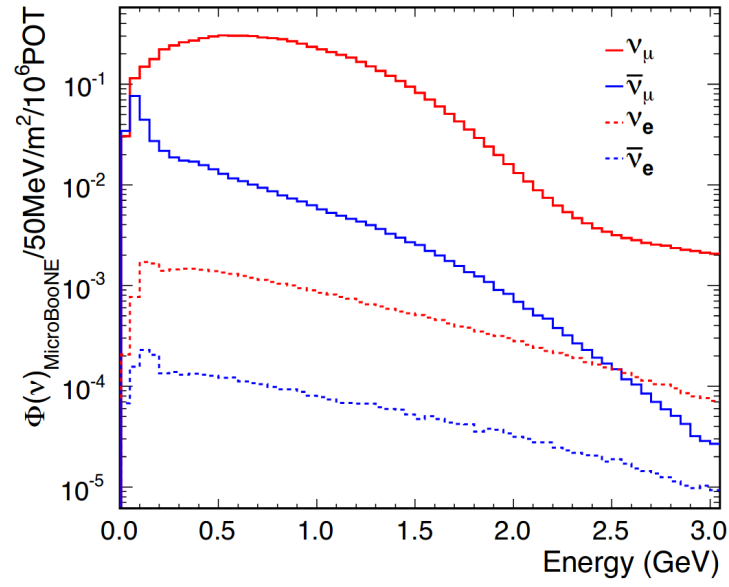


Figure 5.5: Neutrino flux prediction at MicroBooNE

Chapter 6

Energy Loss of Electrons and Photons in Liquid Argon

Particles traversing a medium lose energy via small, continuous collisions with nearby atoms, as well as by radiative processes which are discrete and stochastic in nature. While for most charged particles radiative losses become important only at energies beyond 100 GeV, these dominate the energy loss for electrons at $\mathcal{O}(100)\text{MeV}$, causing them to produce characteristic electromagnetic showers. The energy loss profile of electrons and photons in LAr impacts the techniques employed to identify EM activity and reconstruct the kinematic properties of these particles, which in turn impacts neutrino energy reconstruction and oscillation measurements. Section 6.2 covers the energy loss of electrons while section 6.3 describes photon interactions and cross-sections, with a discussion on the photon radiation length.

6.1 Charged Particle Energy Loss in Liquid Argon

The mean energy loss of charged particles traversing matter depends almost entirely on its velocity and is described by the Bethe equation [6],

$$-\left\langle \frac{dE}{dx} \right\rangle = K z^2 \frac{Z}{A} \frac{1}{\beta^2} \left[\frac{1}{2} \ln \frac{2m_e c^2 \beta^2 \gamma^2 T_{\max}}{I^2} - \beta^2 - \frac{\delta(\beta\gamma)}{2} \right]. \quad (6.1)$$

Where Z and A represent the atomic charge and mass of the detector medium, T_{\max} the maximum possible energy transfer in a single collision, I the mean excitation energy in eV , and $\delta(\beta\gamma)$ repre-

sents a density correction to the energy loss, important in the liquid phase. The value of constants and physics quantities in Eq. 6.1 can be found in Table 27.1 of reference [6]. Figure 6.1 shows the energy loss for charged particles in liquid argon as obtained from equation 6.1.

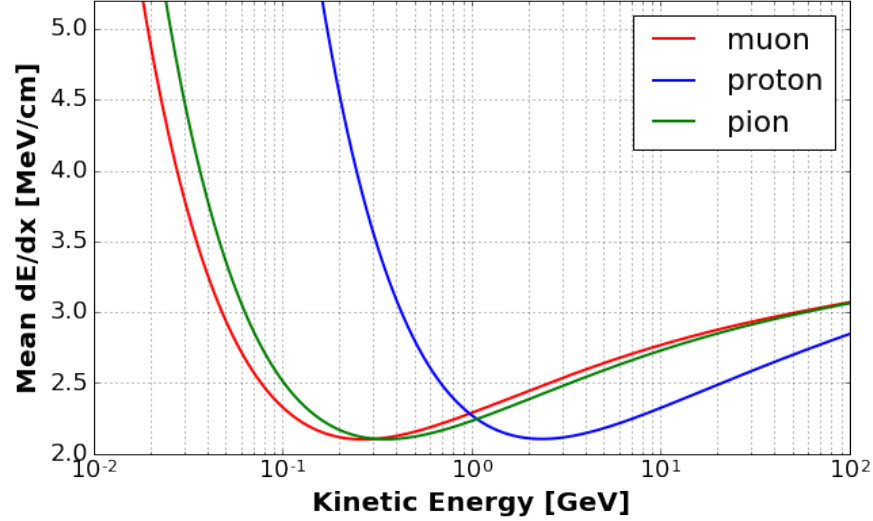


Figure 6.1: Mean collision energy loss (dE/dx) for muon, protons, and charged pions as a function of their kinetic energy in liquid argon.

6.2 Electron Energy Loss

Electron energy loss contributions from radiative photon production (largely in the form of bremsstrahlung photons) become significant at much lower energies than for heavier particles. Energy loss by ionization scales logarithmically with the electron's energy, while bremsstrahlung photon production scales linearly. In most materials bremsstrahlung photon production begins dominating the energy loss for electrons beyond a few tens of MeV. The value at which contribution to the total energy loss rate from these two processes is equal is referred to as the *critical energy* (E_c). Figure 6.2 shows the total energy loss as a function of electron kinetic energy, as well as the contributions from collision and radiative stopping power individually.

6.2.1 Collision Stopping Power

Collision stopping power for electrons differs from that of Bethe theory for heavier particles (Eq. 6.1). At high fractional energy transfer between incoming electrons and electrons orbiting nuclei of the target material energy loss is described by Moller (Bhabha) scattering for electrons

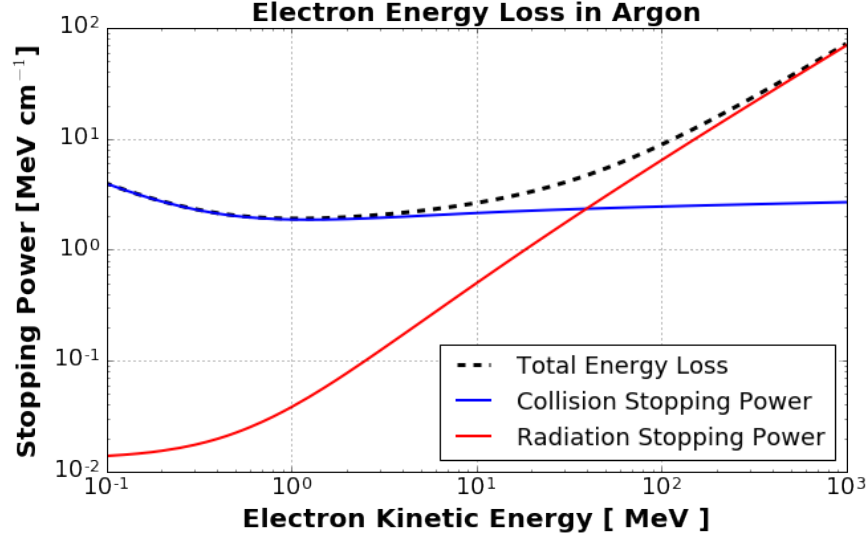


Figure 6.2: Energy loss for electrons in liquid argon computed through the NIST ESTAR [49] “unique materials” page (<https://physics.nist.gov/PhysRefData/Star/Text/ESTAR-u.html>) in which liquid argon was specified as having a density of 1.38 g/cm^3 and a mean excitation energy of 188 eV.

(positrons). High energy transfers, for which the bound electron can be approximated as free, tend to occur at lower energies. Moller scattering accounts for the indistinguishability between incident and target electrons. The term in square brackets of equation 6.1 for electrons and positrons becomes:

$$\frac{1}{2} \left[\ln \left(\frac{T}{I} \right)^2 + \ln \left(1 + \frac{\tau}{2} \right) + F^-(\tau) - \delta \right]$$

$$\frac{1}{2} \left[\ln \left(\frac{T}{I} \right)^2 + \ln \left(1 + \frac{\tau}{2} \right) + F^+(\tau) - \delta \right]$$

With $T = (\gamma - 1)m_e c^2$ and $\tau = T/m_e c^2$; F^+ and F^- appropriate for positrons and electrons respectively and expressed as:

$$F^-(\tau) = (1 - \beta^2) [1 + \tau^2/8 - (2\tau + 1) \ln(2)]$$

$$F^+(\tau) = 2 \ln(2) - (\beta^2/12) [23 + 14/(\tau + 2) + 10/(\tau + 2)^2 + 4/(\tau + 2)^3]$$

The difference between electrons and positrons in ionization energy loss according to the above equations is of order 5% in the 1-100 MeV energy range. These expressions and a much more

detailed discussion of the energy loss of electrons and positrons can be found in a review of the stopping power of electrons and positrons, found in the ICRU report 37 [50].

6.2.2 Bremsstrahlung Photon Production

Because bremsstrahlung photon production plays such an important role in the energy loss of electrons, we spend some time describing the characteristics of this physics process. Much of the information we report is obtained from reviews by H.W. Koch and J. W. Motz [51] and Yung-Su Tsai [52]. The experimentally relevant quantities related to bremsstrahlung photon production by electrons are the incident electron and outgoing photon energies, and the angle between the two particles. These quantities will be denoted by the variables E_0 and \vec{p}_0 , the incoming electron's energy and momentum respectively; E and \vec{p} , the same quantities for the outgoing electron; k and \vec{k} , the energy and momentum of the bremsstrahlung photon; and θ_0 , the angle between the incoming electron and outgoing photon's momenta. These quantities are illustrated in figure 6.3.

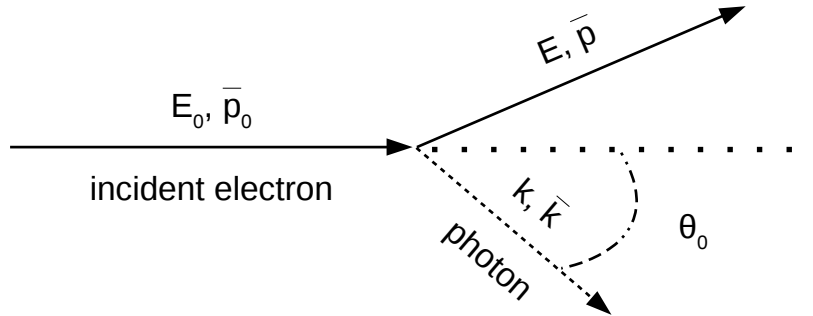


Figure 6.3: Diagram showing the variables used to denote the energy and momenta of the electron and photon involved in the bremsstrahlung interaction.

The cross-section dependence on the emitted photon energy and direction is such that production of low-energy, collinear photons is favored. Figure 3 of reference [52] (page 927) shows the cross section as a function of the energy transfer k for different incident electron energies. For energies above a few MeV, the cross-section scales roughly linearly with the inverse of the photon energy, until k reaches about 10% of the electron's total energy, at which point the rate drops even more rapidly. This favors the production of mostly low-energy bremsstrahlung photons.

Koch and Motz [51] show the dependence of the bremsstrahlung cross-section on the angle θ_0 at different incident electron energies and for different values of energy transferred to the outgoing

photon.

6.3 Photon Energy Loss

Photons beyond a few MeV predominantly lose energy via e^+e^- pair-production, leading to a cascade effect which produces electromagnetic (EM) showers of electrons and photons of successively lower energy. In the few MeV energy range Compton scattering (or incoherent scattering) dominates the energy loss, and this process is non-negligible up to a few tens of MeV. Figure 6.4 shows the cross-section for photons in liquid argon, measured in cm^{-1} as a function of the photon energy.

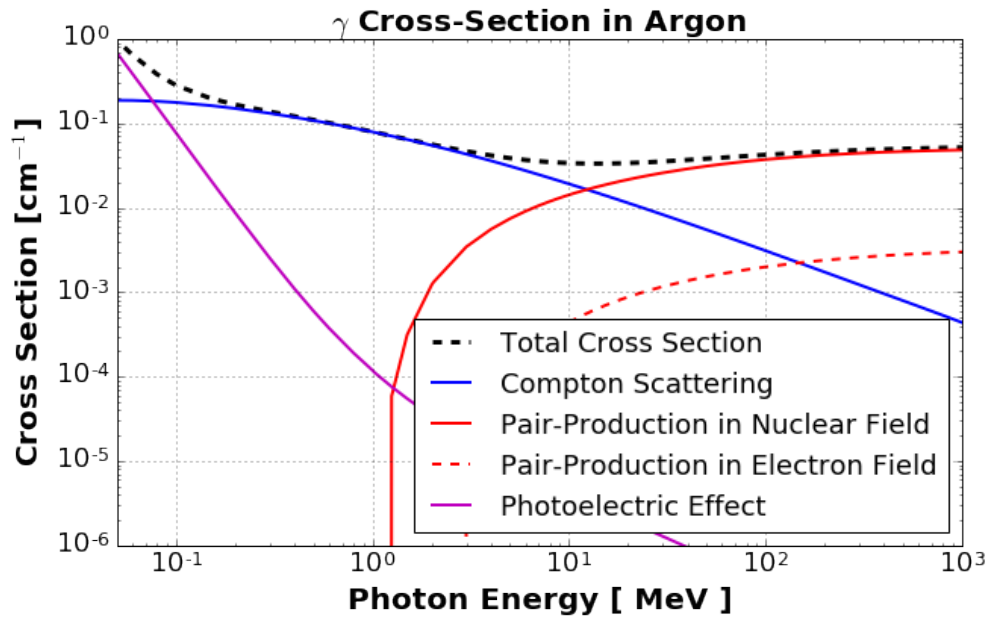


Figure 6.4: Cross section for photons in liquid argon obtained from NIST XCOM tables [53].

Contributions below a fraction of an MeV are largely due to the photo-electric effect, at which point Compton scattering and pair-production become dominant. Pair production can occur via the interaction with the material's nuclear or electron field, with the former dominating by over an order of magnitude.

6.3.1 Compton Scattering

Compton scattering describes the scattering of incident electrons on those present in the target material. It dominates at low energies and predominantly produces small energy transfers which

deposit small amounts of energy in the final stages of an EM shower.

6.3.2 Pair Production

The process $\gamma \rightarrow e^+ + e^-$ is only allowed, by energy and momentum conservation, if another particle is present in the interaction, meaning that this process occurs only for photons when traveling through a material. Pair production can be thought of as the inverse process as bremsstrahlung photon production. In this process a photon of energy k leads to the creation of electron pairs of energy E_+ and E_- such that $E_+ + E_- = k$. The cross-section for this process can be studied as a function of the fraction of the photon's energy transferred to one of the electrons created (denoted as ϵ). In the *Born approximation*¹ the cross-section [54] for argon as a function of ϵ is shown for different photon energies in figure 6.5. As the photon energy increases an asymmetric E_+ , E_- production becomes more likely. In a regime where the Born approximation does not hold an asymmetry in the kinematics of the electron and positron arises due to the fact that a low-energy positron is repelled, and a low-energy electron attracted by the nucleus. This leads to an enhancement of the cross-section for small E_- and depletion for small E_+ .

Similarly to the electron-photon angle for Bremsstrahlung, the average angle of an electron's momentum with respect to the initial photon direction is approximately given by $\theta \sim M_e c^2 / k$. The enhancement of forward-going e^+ / e^- pairs becomes less pronounced at lower energies.

6.3.3 Photon Radiation Length

A useful quantity used to characterize the energy loss of electrons and photons in a material is the “radiation length” X_0 defined as either the mean distance over which an electron loses $(e - 1) / e$ of its energy via bremsstrahlung, or equivalently 7/9 the mean free path for photon pair-production. The radiation length X_0 is given by the expression:

$$\frac{1}{X_0} = 4\alpha r_e^2 \frac{N_A}{A} \left\{ Z^2 [L_{rad} - f(Z)] + Z L'_{rad} \right\}. \quad (6.2)$$

For the case of argon ($A = 39.95$ g/mol, $Z = 18$) this gives $f(z) = 0.0204$, $L_{rad} = 4.252$, $L'_{rad} = 5.158$ giving $X_0 = 19.55$ cm²/g, or, at a density of 1.38 g/cm³, $X_0 = 14.167$ cm.

¹The Born approximation is defined by two assumptions. (1) relativistic kinematics such that $Z\alpha/\beta \ll 1$. (2) low enough electron energies so that screening effects can be neglected.

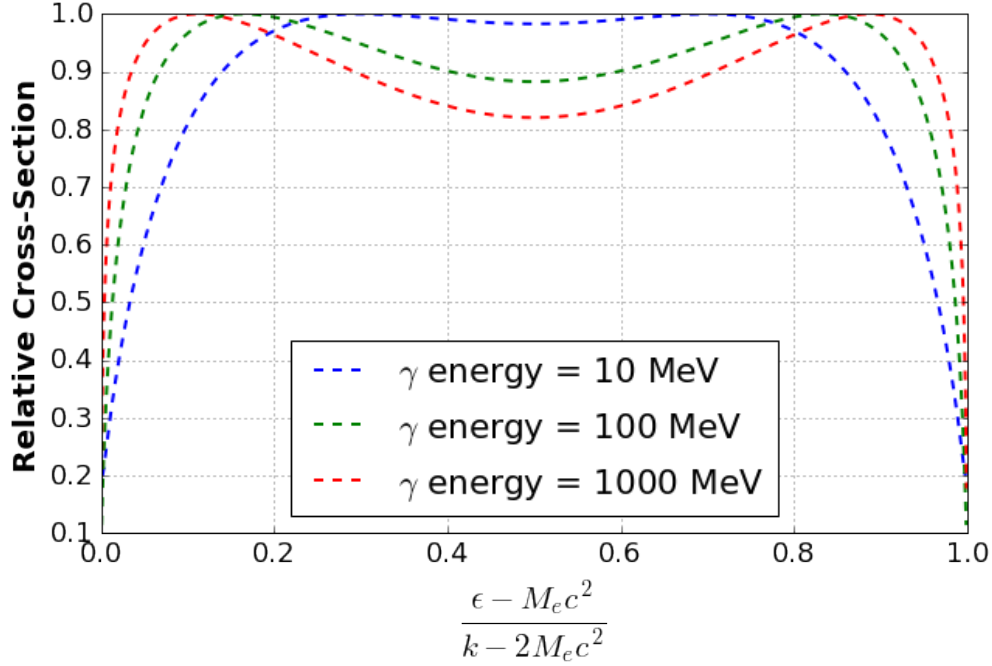


Figure 6.5: Pair production relative cross-section as a function of the fraction of the photon's energy transferred to either the electron or positron. The cross-section in the Born approximation is symmetric.

Figure 6.6 shows the total mean free path for photons in argon, as well as the individual contributions from pair-production and Compton scattering. The region between 10 and 100 MeV shows non-negligible contributions from both processes, and this is also the region in which the absorption length is largest, with photons traveling up to 30 cm on average before interacting. As the cross section asymptotes at high energy the mean free path approaches a value of roughly 19 cm. Overlayed in cyan are the definition of the radiation length calculated as 7/9 the mean free path at 10 GeV (solid), and the value computed with equation 6.2 (dashed line).

6.4 Summary and Implications for EM Reconstruction in LAr

EM showers are caused by the successive repetition of pair-production interactions followed by bremsstrahlung photon production. Energy is lost via ionization by electrons and positrons in the cascade. The small median angular deflections lead to a narrow cone of activity (contained within a *Moliere radius* of ~ 10 centimeters). The large conversion distance in argon causes EM showers to extend for considerable distances in the detector, while the high rate of compton-scattering in-

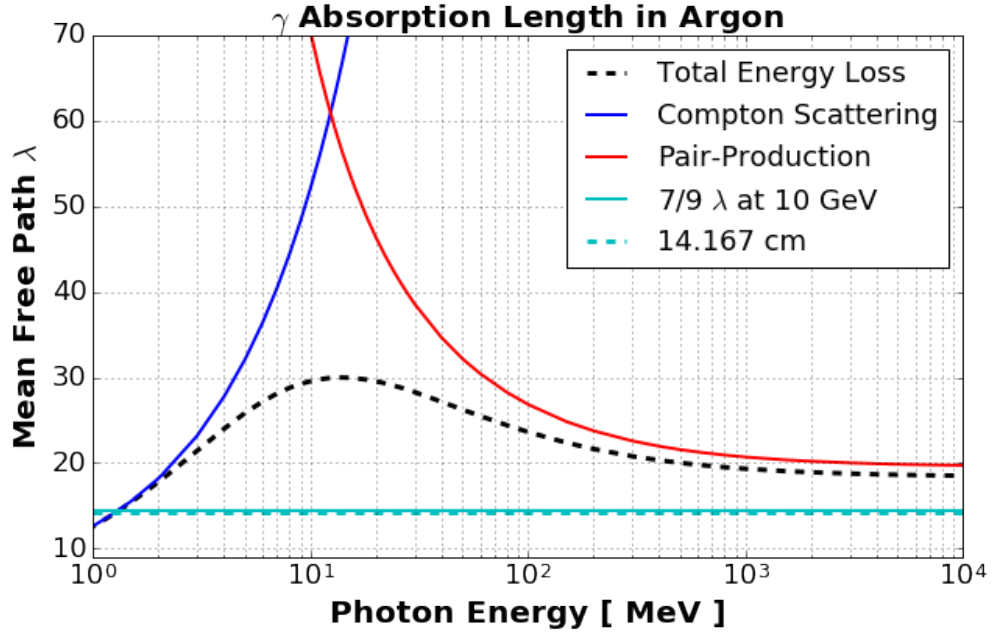


Figure 6.6: Inverse of the photon cross-section of figure 6.4 in units of cm.

interactions contributed mostly by lower energy photons produced as the shower loses energy lead to a significant amount of small energy depositions which may be difficult to detect, even in a high signal-to-noise environment. The ability to recover all energy deposited by EM showers impacts the energy reconstruction bias and resolution. An additional complication at energies of interest for this work comes from the stochastic nature of photon production at energies close to the critical energy. This leads to EM activity which is topologically challenging to identify and reconstruct.

Chapter 7

Measurement of Electromagnetic Backgrounds in a Surface LArTPC

The slow drift time of a time projection chamber is what causes cosmogenic backgrounds to be so problematic for a surface LArTPC detector. Cosmic ray muons, which are the dominant and most prominent source of cosmogenic backgrounds in the TPC, are not necessarily the largest problem when it comes to the reconstruction of EM activity. Energy deposited by δ -rays and bremsstrahlung photons induced by high-energy muons leads to potential backgrounds in the proximity of muon tracks which can mimic the signature of electromagnetic activity from neutrino interactions. Activity not correlated with cosmic-ray muons, such as argon spallation products, or cosmogenic neutrons entering the detector and scattering with the argon are potentially even more problematic. While cosmic-ray muons can be easily reconstructed due to their linear, well-recognizable imprint in the TPC, identifying and accounting for smaller energy deposits by these other backgrounds is more challenging. Having a data-driven measurement of these backgrounds is therefore essential in order to correctly account for their impact on neutrino analyses. In addition, spallation products and other activity in the few to tens of MeV energy range are particularly significant backgrounds for low energy physics measurements such as the study of neutrinos from galactic supernovae bursts.

In this chapter we perform a data-driven measurement of the rate of electromagnetic activity in the MicroBooNE surface LArTPC. For the purpose of this work, electromagnetic activity is a loose definition which encompasses any energy deposition not associated with cosmic-ray muons. The method employed for this study is outlined in section 7.1, results are presented in section 7.2.

A comparison of backgrounds to the expected rate of SNB neutrinos in section 7.3 completes this work. I would like to acknowledge useful discussions with John Beacom and Shirley Li on the topics of spallation backgrounds. Their previous work on this topic (see Ref. [55]) and interest in LArTPCs motivated me to work on this topic.

7.1 Methodology

For this study we are interested in measuring the energy spectrum and rate of interactions in the TPC produced by anything other than primary collision ionization due to cosmic-ray muons. Expecting a strong correlation between energy deposition in the TPC and proximity to cosmic-ray muons (primarily due to δ -rays and other bremsstrahlung activity) we are also interested in the spatial isolation of the measured backgrounds. We perform this analysis by identifying event by event all reconstructed cosmic-ray muons, ignoring their energy deposition, and clustering all remaining charge using a proximity-based clustering algorithm to isolate contiguous segments of charge deposition. Each cluster obtained by this procedure will then have an associated reconstructed energy and a measured *cumulative impact parameter* distance, referred to as IP , which denotes the cumulative two-dimensional distance between the charge in question and all identified cosmic-ray tracks in the event. Figure 7.1 shows a cartoon of the collection-plane view of a recorded cosmic event. Cosmic-ray muon tracks are denoted in red. The yellow hits denote an example of a background targeted by this analysis. Equation 7.1 describes how the quantity IP is computed.

$$IP = \sqrt{\left(\sum_{i=0}^{N_{track}} \frac{1}{r_i^2}\right)^{-1}} \quad (7.1)$$

We use 35,467 cosmic-ray data events, each having a recorded readout window of 3.2 ms, for a total exposure of 113.5 seconds. The background rates are measured in Hz / m^3 accounting for the exposure time of the dataset and volume of TPC scanned. We will study the background rate as a function of IP for values up to 70 cm. Each collection-plane view gives an image which spans the range [0,1036] cm in Z and [0,300] cm in Y . We use backgrounds identified in the range Z [150,880] and X [100,200] in order to minimally bias the measured IP for backgrounds found on the edges of the collection-plane event view. Note that a cut on the quantity X is not an actual

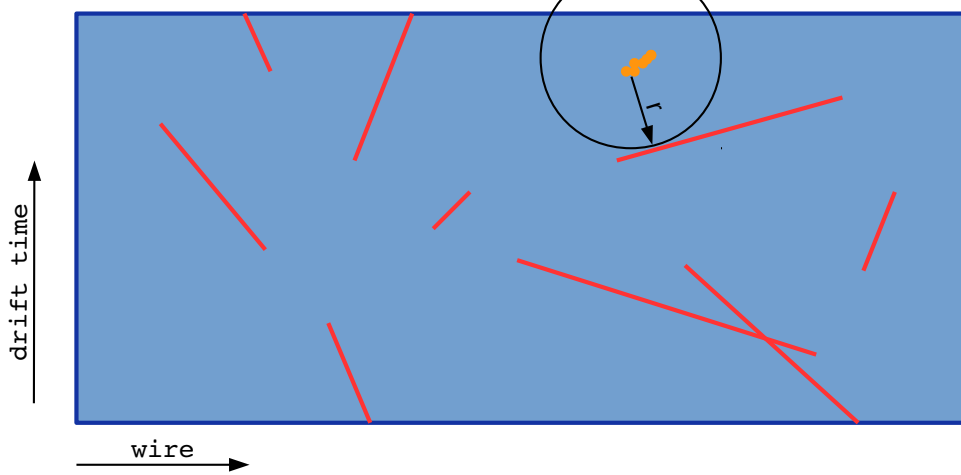


Figure 7.1: Cartoon showing an event display as seen from the collection-plane with overlaid reconstructed cosmic-muon tracks in red. An example identified background studied in this analysis is denoted as an isolated cluster of charge in orange. The radius r is used as shown in equation 7.1 to measure the cumulative impact parameter for this cluster, determining its weighted distance from nearby cosmic-ray muons.

spatial constrain on the energy deposition because the drift-time of clusters used in this analysis has not been corrected for.

The background rate dependence on the isolation of identified clusters is studied by cutting on IP . We note that the active volume coverage will decrease as different cuts on IP are applied. This loss of coverage must be accounted for in order to recover a correct rate in Hz / m^3 . We measure this correction factor by scanning the TPC volume over a large number of events, and for each point in the ZX plane measure the IP value by considering the cosmic-ray muons present in that event. The distribution of IP values (figure 7.2) shows the closest proximity to a cosmic muon track for the random points scanned in the TPC. From this distribution we can calculate the fraction of the TPC volume “visible” after applying different cuts on IP . This fraction, for a given value of IP , is given by:

$$F(x') = \frac{\int_{x=x'}^{\infty} \rho(x)}{\int_{x=0}^{\infty} \rho(x)} \quad (7.2)$$

With the distribution ρ given by figure 7.2. The function $F(r)$ is shown in figure 7.3. We use this function to correct for the loss of coverage due to the cut on IP .

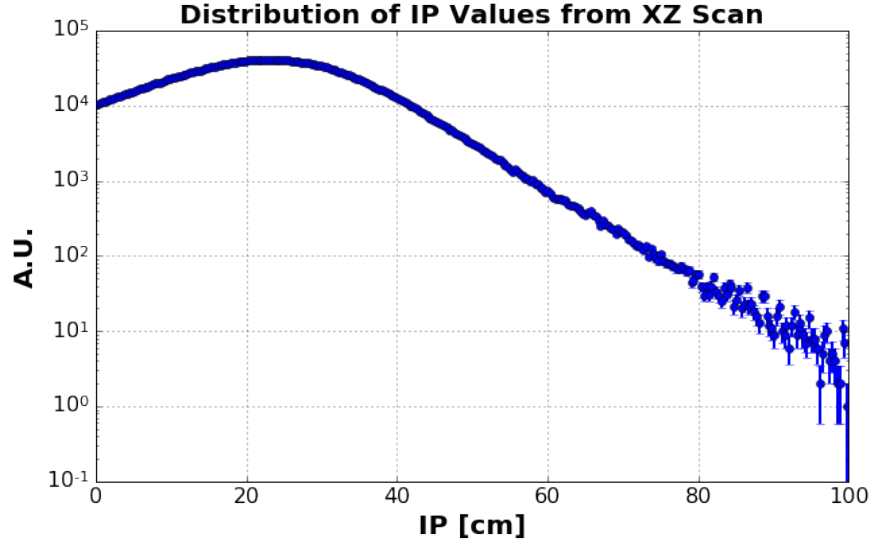


Figure 7.2: Distribution of IP values measured for a sample of cosmic events. For each event, points on a grid spaced 10 cm from each other are used to randomly sample the IP values across the TPC. The distribution peaks at roughly 20 cm, denoting the characteristic cumulative separation between any point in the TPC and the neighboring cosmic-muon tracks.

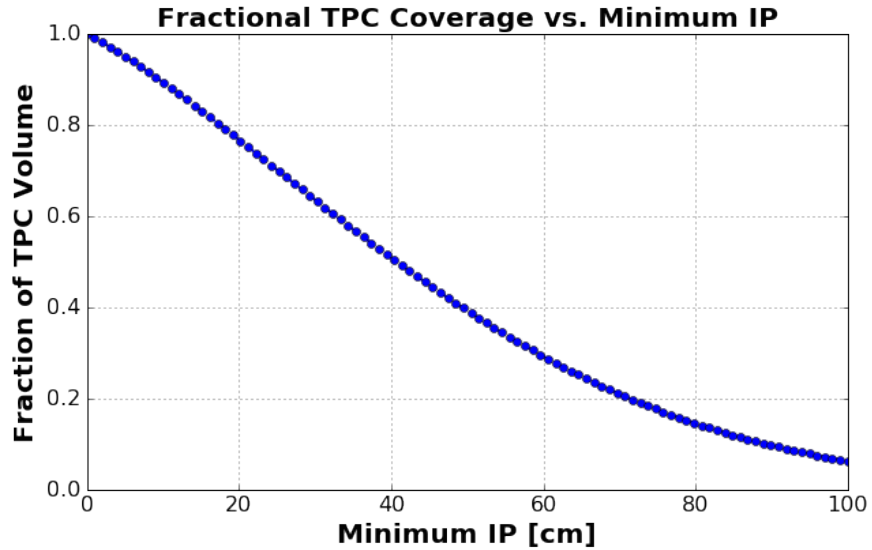


Figure 7.3: Fraction of visible TPC volume vs. minimum IP cut applied. This function, calculated from the distribution in figure 7.2 using equation 7.2, allows us to derive a volume correction factor to be applied when measuring background rates after cutting on the quantity IP .

7.2 Cosmogenic Background Rate Measurement

Figure 7.4 shows the rate of backgrounds as a function of their measured energy for different minimum IP cut values. In this figure, as any time a cut is applied on the quantity IP , a correction

factor is applied to account for the loss of fiducial volume due to the constraint of requiring a certain minimum IP value. This correction factor is given by $1/F(IP)$ with F defined in equation 7.2. In addition to a significant reduction in background rates, the energy spectrum becomes softer as the IP cut value is increased.

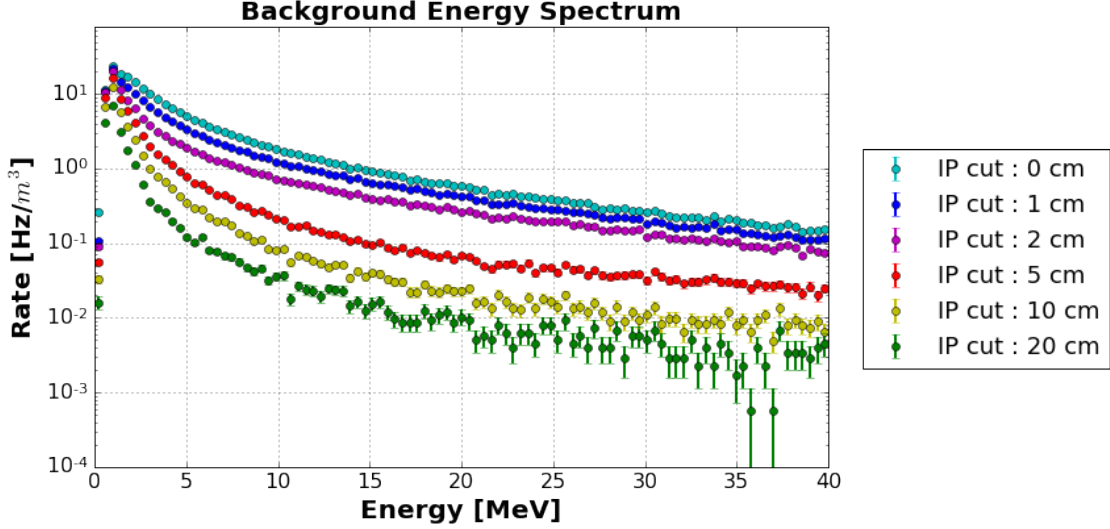


Figure 7.4: Energy spectrum of identified backgrounds for different cuts on the minimum IP value. A volume acceptance correction factor equal to $1/F(IP)$ is applied.

Figure 7.5 shows the radial distribution of backgrounds for different energy thresholds. The distributions are fit two a sum of two exponentials allowing the exponential decay scale and amplitudes to float separately. The data fit this function form well, as indicated by the χ^2 values for the fits are shown in the legend.

We show the values of the fitted exponential decay constants in figure 7.6. The fast exponential component, shown in blue, has a value of 10 to 6 cm across the energy range spanned, and seems to level off as the energy threshold is increased. The slow component (red scale on right hand side) is significantly smaller and comparable to the length-scale within the TPC. The measurement of this slow component is likely dominated by edge effects and we interpret this as a measure of an underlying flat background distribution.

We take the rate measured with an IP cut of 70 cm as an estimate for the the uniform cosmogenic backgrounds due to spallation products and cosmogenic neutrons, amongst others. The rate of this cosmogenic background as a function of energy threshold is shown in figure 7.7.

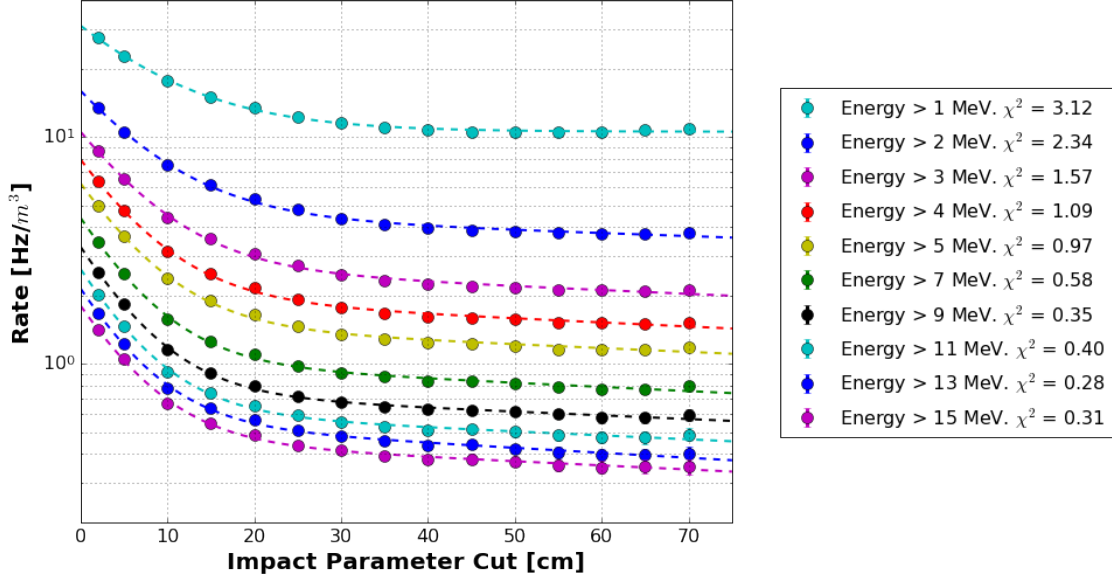


Figure 7.5: Rate of backgrounds in function of weighted radial distance to cosmic-ray muons in the event. Different distributions denote background rates for various energy thresholds. The distributions are fit to a sum of two exponentials to match the clearly noticeable fast component (associated with activity highly correlated with the muons, and the slow, more uniform component.

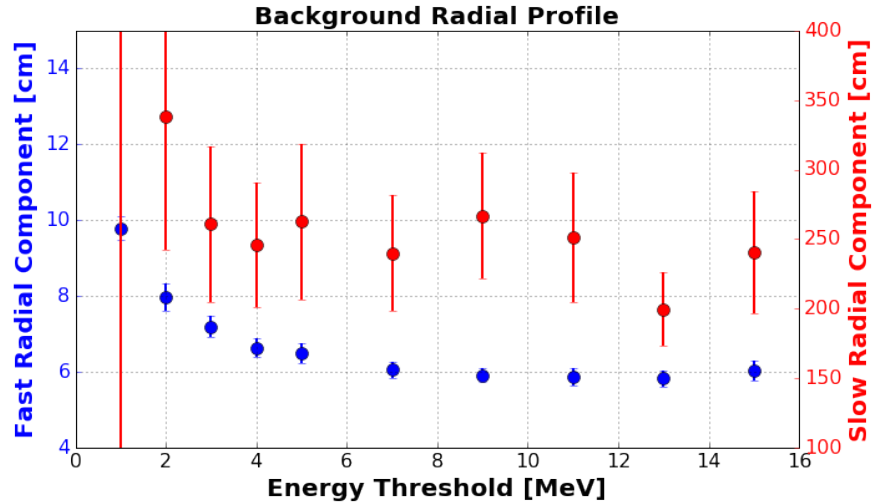


Figure 7.6: Measured radial decay constant for EM backgrounds. In blue is the fast component which after a few MeV of energy threshold appears to stabilize at ~ 6 Hz/ m^3 . In red is the slow component, with values of ~ 2 meters. This quantity matches the TPC size and is likely impacted by edge effects, suggesting that this background component is uniform.

7.3 Cosmic-Ray Backgrounds to Supernova Neutrinos Burst

Low energy backgrounds uncorrelated with nearby cosmic-ray muons can pose a significant challenge to the detection of neutrino interactions from supernovae neutrino bursts. In this section

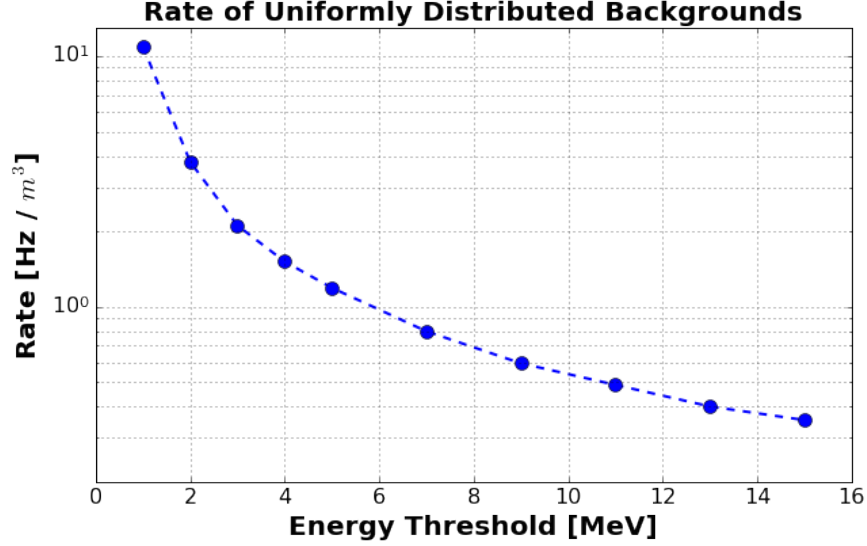


Figure 7.7: Rate of uniformly distributed backgrounds in function of the applied energy threshold. The measured rate comes from the fitted long exponential component in the radial background distribution of figure 7.5.

we compare the background rates measured in section 7 to the expected event rates for neutrinos from supernova bursts. As presented in section 3 galactic supernovae lead to a large flux of neutrinos of all flavors with approx. 10 MeV of energy of the duration of a few seconds. In liquid argon most neutrino interactions would occur through the charged current ν_e channel producing roughly 100 neutrino interactions per kiloton of mass. The time structure of the SNB neutrino flux varies significantly throughout the few second event duration, with a significantly large flux of electron neutrinos occurring in the first few ms following the collapse, in what is called the deleptonization burst. The time-profile of the integrated event rate for a simulated ¹ SNB is shown in figure 7.8. We take the peak rate of 1.4 Hz/m³ measured at about 20 ms, and the steady-state rate observed past 100 ms of 0.4 Hz/m³ (with 50% error-bars to indicate the fact that these are approximate) and overlay them on top of the measured background rate energy spectrum in figure 7.9. While these two data-points represent integrated fluxes, we draw them at the approximate median energy expected for ν_e neutrinos at their respective times. These energies are taken from the time- and energy-profile for a simulated SNB event used in the DUNE TDR. We find that a surface LArTPC

¹The event rate profile is taken from a 2D simulation for a 10 kpc SNB presented by Bronson Messer of the University of Tennessee at the ν ECLIPSE workshop held in August of 2017. Webpage: <https://sites.duke.edu/nueclipse/>. Fluxes and event rates differ significantly between different models. We assign error-bars of 50% to these rates.

would be able to identify SNB neutrinos from the prompt deleptonization burst. Identifying the neutrino flux associated with the subsequent SNB evolution would likely be possible statistically (after background subtraction), but identifying individual events may be challenging without an improved background mitigation strategy.

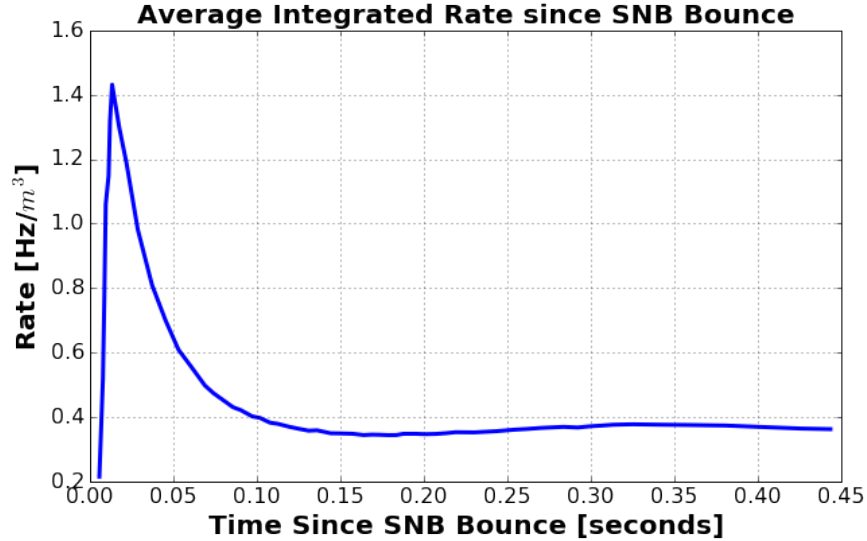


Figure 7.8: Integrated event rate as a function of time since supernova bounce measured as the total event count over the time since burst, in units of Hz/m^3 . The sharp peak at approximately 20 ms is due to the large flux of ν_e events produced during the deleptonization phase of the burst. At later times the integrated flux flattens out.

7.4 Conclusions

This chapter has presented the first measurement of low-energy cosmogenic backgrounds in a large-scale surface LArTPC. We measure a rate of uniform EM backgrounds which ranges from $10 \text{ Hz}/\text{m}^3$ at 1 MeV of energy threshold to $\sim 0.3 \text{ Hz}/\text{m}^3$ at 15 MeV. Additionally, we find that backgrounds which are correlated to cosmic-ray muon activity exhibit a radial exponential falloff with decay-constant of 6-8 cm. These measurements are valuable input to analyses which aim to reconstruct EM activity and can be used to estimate backgrounds and potential charge contamination which can impact energy reconstruction. This work is especially relevant to supernova studies because the energy range of neutrinos from supernovae is comparable to that of the backgrounds.

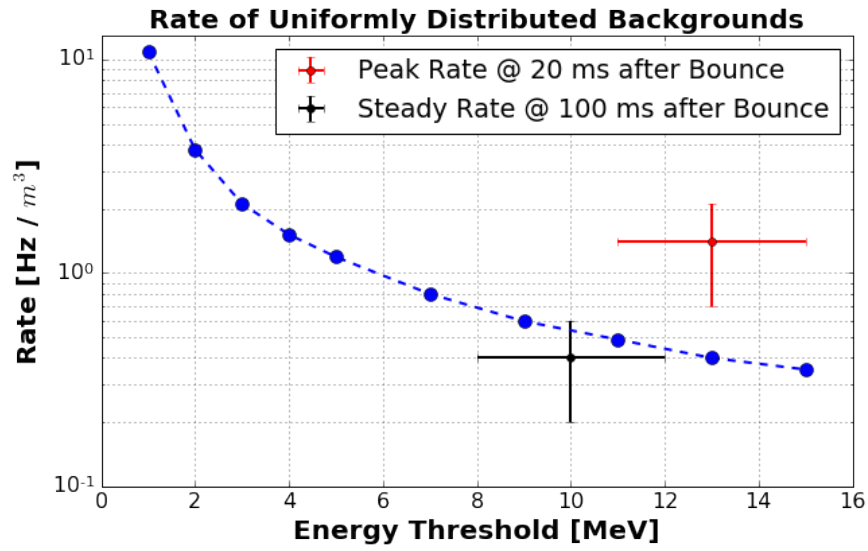


Figure 7.9: Rate of cosmic-muon uncorrelated backgrounds measured in MicroBooNE as a function of background energy with overlaid the rate of SNB events during the deleptonization burst (red) and the steady-state SNB flux (black). The SNB rates are approximate as they come from two specific simulations of the flux and energy time-profile

Chapter 8

Study of EM Activity in the 10-50 MeV range with Michel Electrons

Studying tens of MeV energy neutrinos provides an opportunity to investigate interesting research topics such as neutrino oscillations with stopped pion beams, or the measurement of astrophysical neutrinos from galactic supernovae bursts. As large-scale liquid argon time projection chamber (LArTPC) neutrino detectors become operational it is important to understand their response to electrons in the tens of MeV energy range. Furthermore, while EM activity in this energy range is below the 100 MeV to 1 GeV range at which current and upcoming oscillation experiments are being performed, backgrounds to these analyses will be impacted by activity at lower energies, and must therefore be understood. At these energies electrons exhibit a complex topology in liquid argon: the comparable amount of energy deposited as collision stopping power versus radiation via bremsstrahlung photon production causes them to manifest themselves as a short (~ 10 cm) track followed by several low energy (few MeV) photons which will travel up to tens of centimeters before depositing their energy. The stochastic nature of bremsstrahlung photon production implies that being able to identify and reconstruct the few MeV photons produced is essential in order to obtain an accurate measurement of the electron's energy. Sitting on the surface, the MicroBooNE detector is exposed to a large flux of Michel electrons produced by decay-at-rest cosmic-ray muons. A two-dimensional reconstruction technique was developed to tag Michel electrons based on the characteristic ionization Bragg peak of a stopping muon, and the spatial kink produced by the outgoing electron. The electron energy is reconstructed by integrating the ionization charge deposited

in the detector by the Michel electron and collected on the TPC wire planes. We produce two energy definitions, one which only measures the electron energy deposited via collision stopping power, and the second which includes the energy of reconstructed radiative photons. This work presents the first analysis of low energy electrons in a LArTPC which measures and addresses the impact of radiative energy loss on the electron energy reconstruction. With both definitions good agreement is seen between the measured Michel electron energy spectrum from data and simulation. Through a simulation study we notice an improvement of the electron energy resolution from above 30% to approximately 20% when we include the energy of reconstructed bremsstrahlung photons. Still, even when including radiative photons, a significant bias ($\sim 25\%$) in the measured energy remains, pointing to the challenge of tagging the far-reaching and low-energy photons produced.

The work presented in this chapter, once completed, was published in one of MicroBooNE's first publications, with myself as lead author. The citation for this work can be found in reference [56].

8.1 Electron and Photon Energy Loss at 0-50 MeV

A detailed treatment of energy loss in liquid argon for electrons and photons is presented in chapter 6. Here additional details focused on electrons and photons in the tens of MeV energy range are provided. Due to the overlap with the critical energy in argon (~ 40 MeV, see figure 6.2), energy loss for Michel electrons is non-trivial.

In the 0-50 MeV energy range electrons go from depositing almost all their energy as ionization, to releasing energy mostly through radiation. Because radiative contributions are stochastic, there is significant variation, event by event, on the amount of energy lost to the two different processes. Figures 8.1a and 8.1b show truth-level Geant4 studies where this effect is clearly visible. For a simulated sample of Michel electrons, in the left figure the primary ionization-only vs. total energy loss distribution is shown. On the right the distribution of the fractional energy lost to radiation is plotted for different ranges of true electron energy. The broad distributions observed clearly show that measuring the ionization-only energy deposited by electrons in this energy range is not sufficient to obtain good energy resolution.

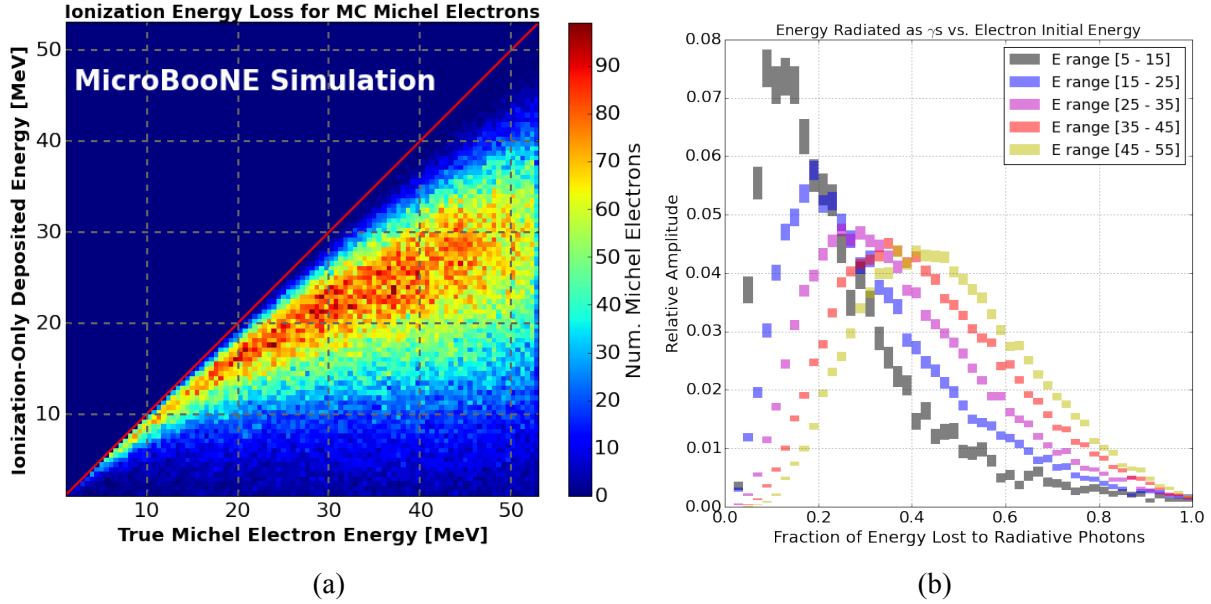


Figure 8.1: (a) Ionization energy loss vs total true Michel electron energy for a sample of simulated Michel electrons. (b) Distributions of the fraction of energy lost to radiation for a sample of Michel electrons. Both figures show truth-level information from the Geant4 simulation employed by MicroBooNE.

Identifying radiative photons is made challenging by their low energy and the relatively large radiation length in argon, which causes them to spread over a distance which is much larger than the total ionization segment produced by the primary electron's ionization. If a 30 MeV electron ranges out in ~ 15 cm, the total radiative energy lost can spread out to distances of up to a meter. This is shown quantitatively in figures 8.2a and 8.2b. The first has the energy spectrum of all bremsstrahlung photons produced over a sample of simulated Michel electrons. The spectrum is steeply falling, highlighting the important contributions coming from the lower-end of the energy spectrum. The second plot shows the spatial distribution of losses from radiative photons. The rectangular boxes are denoted by the total energy deposited by radiative photons contained within them. In order to recover most of the charge associated to radiative energy loss a considerable integration window must be used. This can prove challenging on a surface detector in a busy cosmic environment.

It is worth mentioning that muon capture at rest impacts the Michel electron energy spectrum. Figure 8.3 shows the spectrum for the free decay of μ^+ (a) vs. the bound decay of μ^- (b). Roughly 3/4 of all μ^- which stop in argon will be captured by an argon nucleus. When this occurs, the

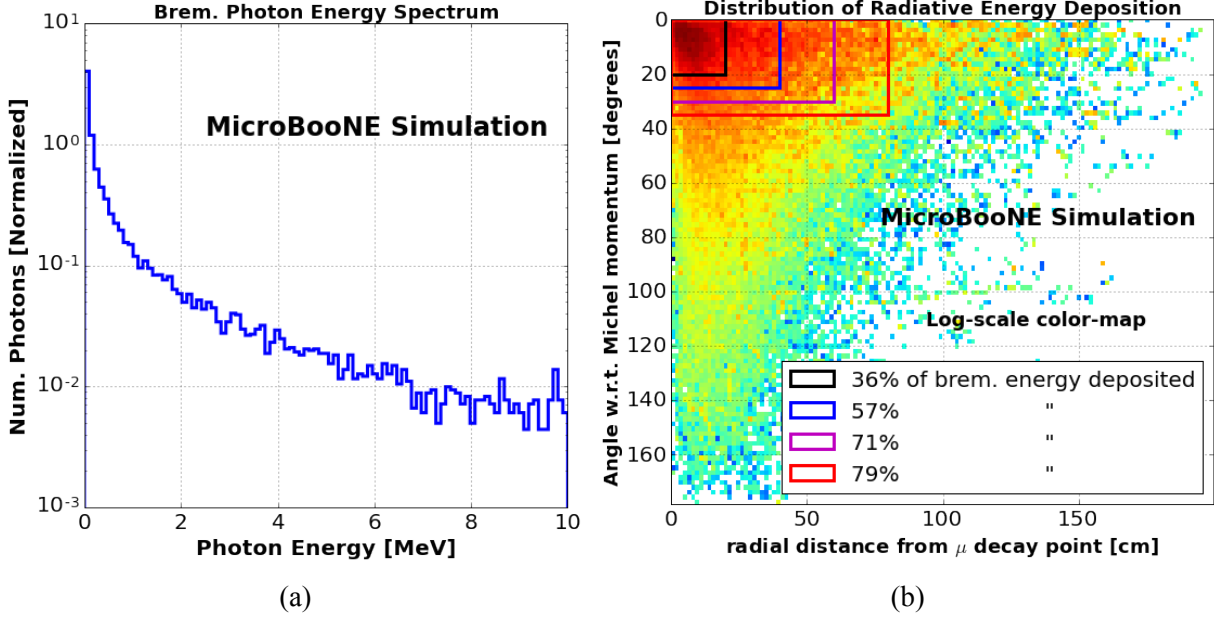


Figure 8.2: (a) Energy spectrum of bremsstrahlung photons produced by Michel electrons. (b) Spatial distribution of radiative energy loss only. Heat map represents amount of energy deposited, on a log-scale. The x-axis is the radial distance from the muon-decay point, and the y-axis is the angular separation from the electron's original 3D momentum direction. Rectangles are labeled by the total radiative energy loss they enclose.

orbital kinetic energy of the muon causes a shift and broadening of its energy.

The impact of radiative energy loss on the Michel energy spectrum is shown in figure 8.4. The red curve shows, from simulation, the Michel energy spectrum produced by cosmic-ray muons stopping in the MicroBooNE detector. The black curve shows the spectrum for the same events, when only primary-ionization energy loss is considered. The spectrum is considerably altered, peaking at roughly 20 MeV rather than 40-50 MeV. Moreover, the spectrum becomes significantly sharper. This is due to the fact that higher energy electrons will lose more energy to radiation than lower energy ones, sculpting the distribution.

8.2 Michel Electron Reconstruction

In this section we present the method by which we identify Michel electrons in the TPC. Michel electrons deposit charge over a region which spans tens of centimeters. With a drift velocity of $1.1 \text{ cm} / 10 \mu\text{s}$ the arrival time of the drifting electron is spread over hundreds of μs . This timescale is

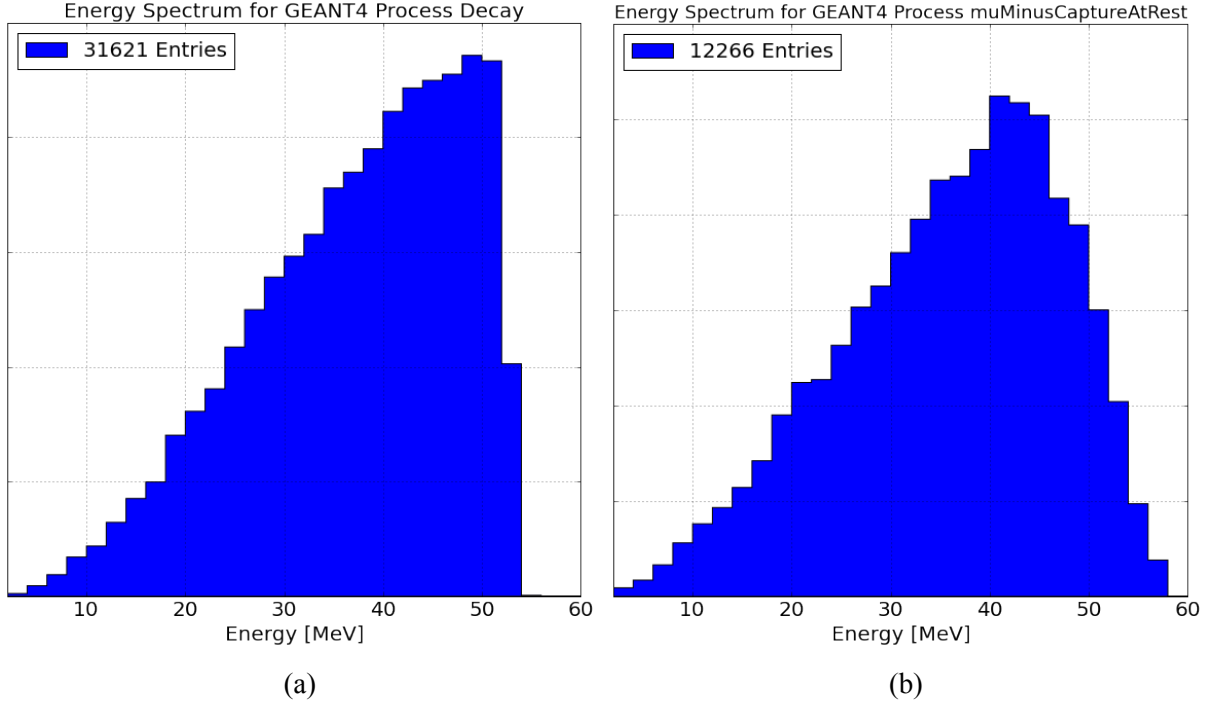


Figure 8.3: Energy spectrum for Michel electrons from the decay of free muons (a) and that of muon capture at rest (b). The orbital velocity of the muon causes a shift and broadening of the Michel energy spectrum.

much larger than the $2.2 \mu\text{s}$ muon lifetime and indicates that we cannot isolate and tag charge based on its arrival time on the sense-wires. Instead, we take advantage of the high-resolution topological and calorimetric information provided by the MicroBooNE TPC to search for signatures in the detector that are characteristic of a stopping muon producing a Michel electron.

Michel electrons from MicroBooNE cosmic data (data taken with the detector using a strobe trigger, in off-beam mode) are identified using an automated reconstruction chain of algorithms which relies on the output of the reconstruction described in appendix B. We note that the signal processing and deconvolution applied for this analysis correspond to an older version of the MicroBooNE reconstruction as that used in the remainder of this thesis, which leads to differences in calculated gains and calorimetric energy resolution. The analysis is performed in a self-consistent way with an independent calibration. As muons come to a stop, energy deposition along the particle's trajectory shows a characteristic rise, called the *Bragg peak*. Most Michel electrons produced by the decay will propagate in a direction different than that of the stopping muon. We use information about the position and density of the charge deposited within the TPC to identify the Bragg

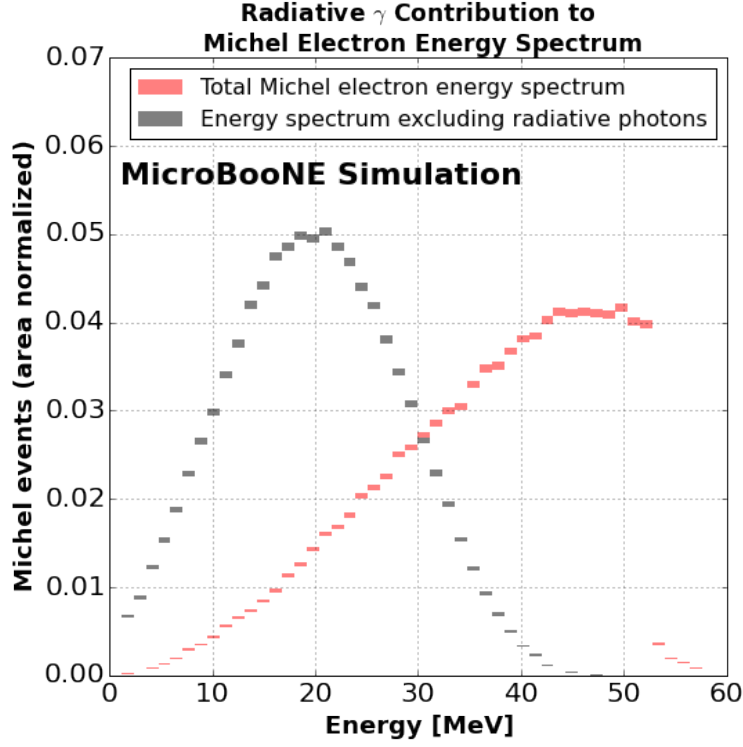


Figure 8.4: Michel electron energy spectrum obtained from MicroBooNE’s simulation of cosmic-ray interactions with (red) and without (blue) radiative contributions to the energy loss accounted for.

peak and the kink between the Michel electron and the stopping muon. An event display of a clearly identifiable Michel electron candidate can be seen in figure 8.5.

Charge clustered by the *pandora* cosmic-ray muon reconstruction [57] is used as an input to the stopping muon identification. Hits associated to each localized cluster are then sorted based on their spatial orientation, in order to obtain a profile of the muon’s charge deposition as it travels through the detector, which is smoothed by using a truncated mean algorithm. Given a spatially sorted list of 2D hits, the *truncated mean charge* of each hit is calculated by taking the charge of neighboring hits, removing the upper and lower tails of the distribution of charge for this subset of hits, and then computing the mean of the values remaining. For this work we include 8 hits on each side, and truncate the highest and lowest 25% of values.

A profile of the muon’s local linearity along the cluster is also calculated. The *local linearity* is a measure of the correlation of wire and time coordinates in a neighborhood of each reconstructed 2D hit. For each 2D reconstructed hit, the local linearity is given by the covariance of wire and

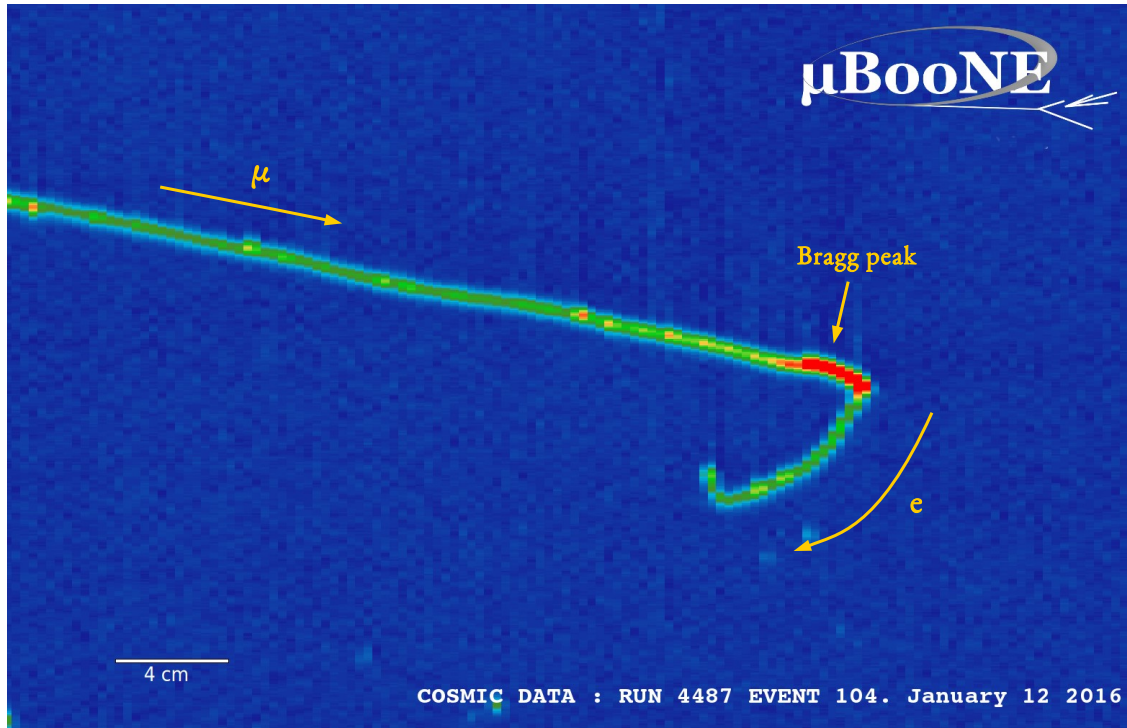


Figure 8.5: Event display showing raw data from a small region of the TPC volume from the collection plane where a candidate Michel electron was identified. The x axis shows the data along the beam direction (increasing wire-number to the right) and the y axis the drift-coordinate (increasing drift-time moving upwards). The scale bar applies to both the horizontal and vertical coordinates. The color coding denotes the amount of collected charge on each wire per time tick. In this display the muon candidate coming to a stop can be identified by the significant increase in charge deposited per unit distance at the Bragg peak. The outgoing Michel electron is distinguishable as the short track originating at the muon's stopping point and depositing charge for several centimeters in a different direction from that of the muon.

time coordinates calculated using the hit in question, and the five hits preceding and following it in the sorted muon cluster, divided by the product of the standard deviation of wire coordinates and that of time coordinates. A local linearity of one indicates perfect correlation for the selected hits, and thus a straight line-segment.

Figure 8.6 shows reconstructed hits for the same event in figure 8.5 with the calculated truncated mean and local linearity drawn in the bottom two panels of the image.

8.2.1 Bragg Peak and Spatial Kink Identification

As a muon comes to rest in the TPC and the density of deposited charge increases, the charge collected on each hit will increase as well. This will lead to a characteristic charge profile in which

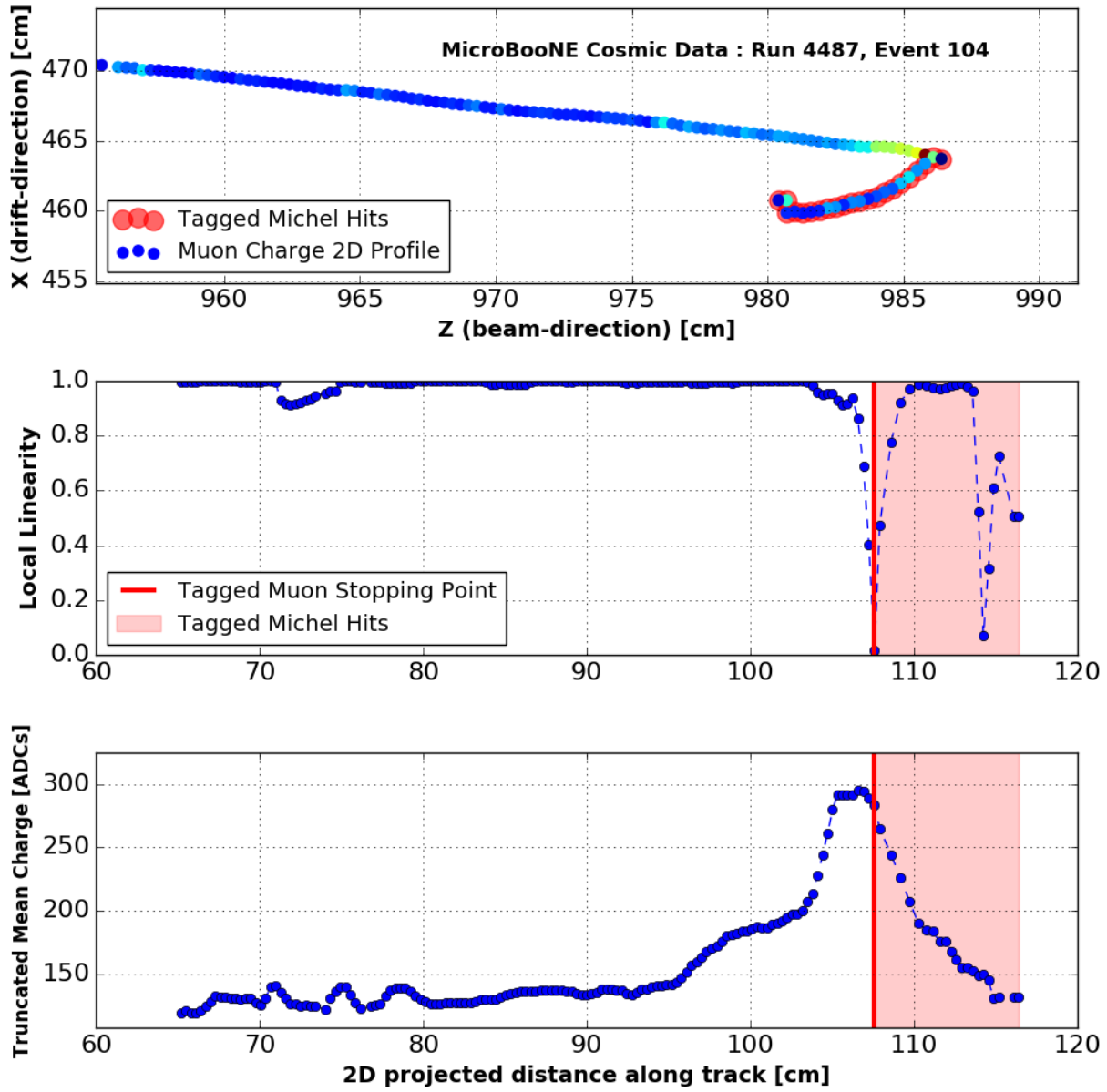


Figure 8.6: Event display showing hits associated with a tagged Michel electron candidate (top). The middle and bottom panels show the local linearity and truncated mean charge profiles calculated for the muon plus Michel electron cluster. The red vertical line indicates the location of the identified stopping point for the muon, and the region shaded in red represents the set of hits along the cluster identified as belonging to the candidate Michel electron. In the top panel, the 2D event display shows information in time vs. wire coordinates. Each hit is represented as a circle, with the color indicating the charge measured. Blue indicates lower charge. Hits that are outlined in red represent those associated with the tagged Michel electron.

a Bragg peak from the stopping muon can be identified. The hit with the largest truncated mean charge is identified as the approximate location of the Bragg peak. Subsequently we measure the

amount of charge deposited within the Bragg peak by integrating the truncated mean charge values in the last few cm up to the identified stopping point compared to that measured in the minimally ionizing particle (MIP) region of the muon to separate through-going from stopping muons. Finally, the hit with the largest charge within ~ 5 cm of the truncated mean charge maximum is reconstructed to be the 2D muon stopping location. Figure 8.7 shows how the truncated charge profile is used to identify the Bragg peak associated to the candidate Michel electron of figure 8.5.

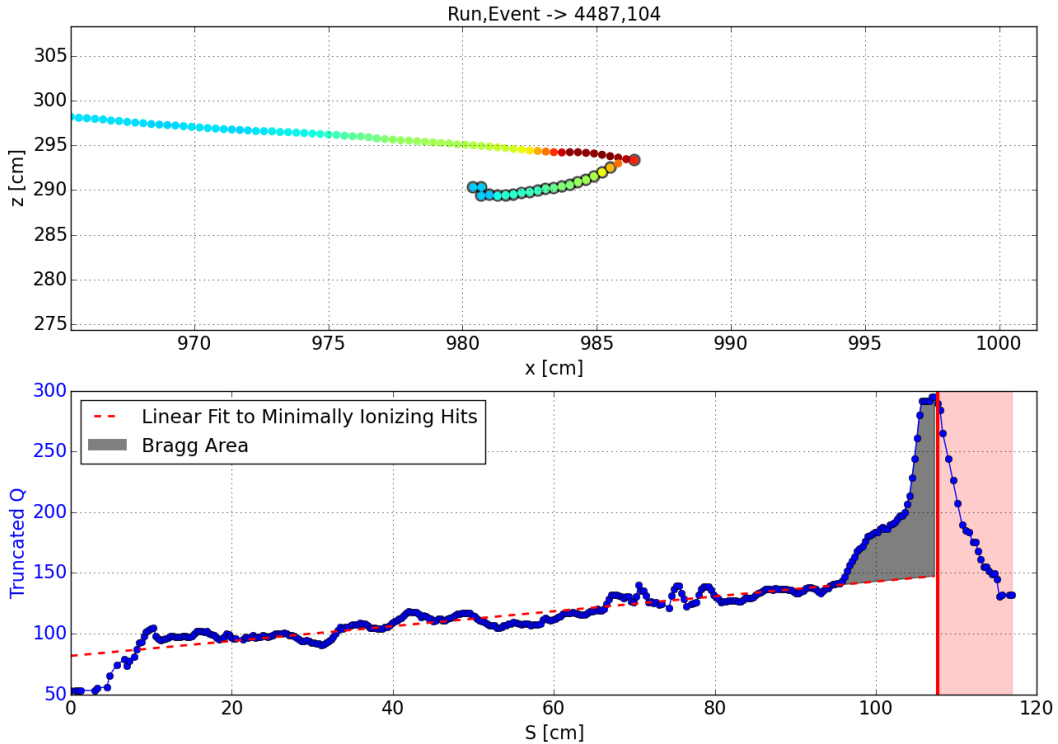


Figure 8.7: Event display of a reconstructed Michel electron. The bottom panel shows the charge profile along the muon's path. The fitted line indicates the expected MIP behavior, with the gray shaded area denoting the measured excess associated to the identified Bragg Peak.

In a similar fashion we scan the muon track searching for a significant kink in the 2D topology of the projected charge. The average local linearity is calculated for the five hits surrounding the identified muon stopping point location, and we require this value to be smaller than 0.8. If both a clear Bragg peak and a significant spatial kink are found, all hits sorted after the reconstructed muon stopping point are tagged as belonging to a candidate Michel electron. In order to further

enhance the sample purity a sequence of cuts on the candidate muon topology are applied: they require that at least 70% of hits have a measured local linearity greater than 0.9 and that the muon segment be at least 10 cm long. These cuts target the removal of muon tracks which are short and exhibit a large amount of scattering, which make the identification of Michel electrons more difficult.

8.2.2 Collecting Charge from Radiative Photons

A proximity-based charge-clustering algorithm will unavoidably miss any energy deposited by radiative photons. In order to attempt to recover this energy, we extend the search for charge associated with the Michel electron beyond that deposited via ionization. We begin by measuring a momentum direction for the Michel electron by fitting the charge deposited via ionization to a straight line. We then search for any charge deposited within an 80 cm distance (~ 3 photon absorption lengths) of the tagged muon stopping point and within a ~ 30 degree opening angle with respect to the reconstructed electron direction. These cuts are applied to information on the collection plane, which is a 2D projection of 3D charge deposition points. From a simulation study similar to that performed in figure 8.2b but in 2D, we expect 80% of all energy deposited by bremsstrahlung photons to be contained within this cut range. Charge identified within this cut region is split into individual reconstructed photons by isolating contiguous clusters of hits. An effective energy threshold of 1 MeV for any tagged radiative photon limits the ability to identify very small energy depositions. The measurement of this threshold value is obtained by studying the energy spectrum of tagged photons, presented further in this chapter, in section 8.5. Finally, we attempt to remove any tagged charge that may have been deposited by accidental cosmic ray muons. We do so by applying the following cuts:

- any reconstructed photon with more than 20 hits (~ 10 MeV) is excluded.
- reconstructed photons with 5 to 20 hits are required to have a local linearity smaller than 0.8. If additional charge not tagged as belonging to the Michel electron is found in a projected 2 cm radius of any of the photon's hits, the photon is considered to be too close to an external cosmic-ray and thus discarded.

Without applying these cuts we find that the attempt to improve the energy measurement by

including far-reaching radiative photons is hampered by the large amount of accidental cosmic activity crossing the event and mistakenly collected. For the case of Michel electrons the negative impact of incorrectly including charge deposited by other cosmic-ray interactions is particularly severe, given that just a few mis-identified hits can have a large impact on measuring the energy of a < 50 MeV electron. The first cut applied efficiently removes long muon tracks which cross the 80 cm, 30 degree cut region. The second removes smaller linear segments which may be due to activity in the proximity of cosmic-ray muons.

An example reconstructed events where two radiative photons are reconstructed is shown in figure 8.8.

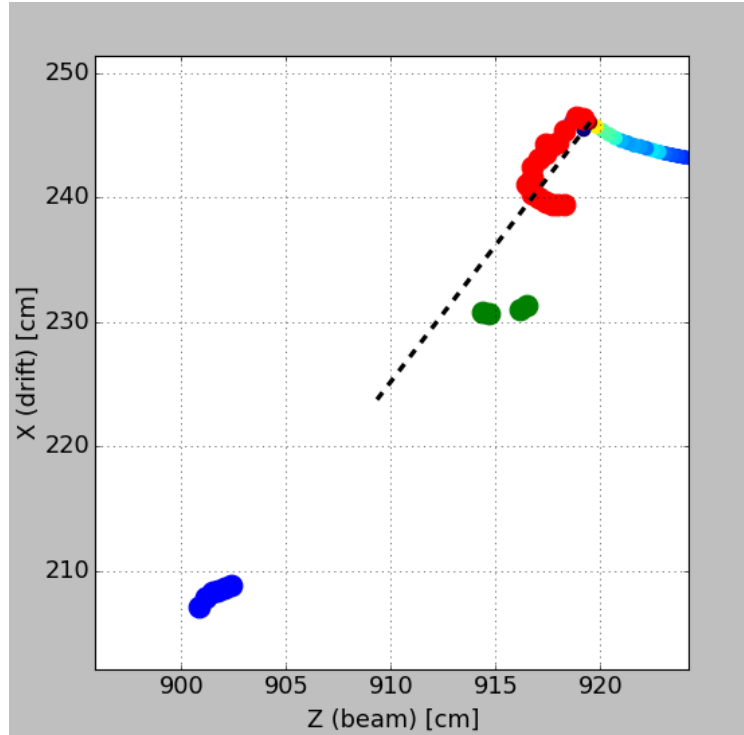


Figure 8.8: Michel electron candidate with two identified radiative photons. The muon, entering on the top-right of the image, decays into a Michel electron. The primary ionization-only energy deposited is shown in red. The black dashed line represents the fitted 2D direction of the Michel electron. Along this direction the two additional photons, in green and blue, are identified.

8.2.3 Selection Efficiency and Purity

The selection and reconstruction cuts applied above were tuned by visually inspecting their impact on data and simulation events and produce a pure sample of Michel electrons (80-90% purity) with a reconstruction efficiency of approximately 2%, which, given the large sample of cosmic data

available, is sufficient to provide the statistics necessary for this study. The efficiency is quantified by measuring the number of reconstructed Michel electrons over the total number of electrons simulated in a Monte Carlo cosmic-ray event sample. The sample purity is estimated by comparing the wire and time vertex position of reconstructed vs. true Michel electrons. Figure 8.9 shows the result of this comparison. The fraction of all reconstructed events within a given distance from a true Michel electron vertex allows to estimate the sample purity. For example, 80% of all reconstructed Michel electrons are within 3 cm of a true muon stopping point. This plot also shows the good vertex resolution, peaking at ~ 2 mm, below the wire-spacing. The low reconstruction efficiency is largely a consequence of the fact that we are only using 2D projected information to identify spatial and calorimetric features associated with the Michel electron topology. Backgrounds were studied by visually inspecting both data and MC events and were found to mostly consist of tagged EM activity from muons (delta-rays or bremsstrahlung photons) when such activity occurred close to the beginning or end of a muon track. A smaller subset of background events consisted of muon tracks which had undergone a large-angle scatter. Isolating background events in the simulation, we find their energy spectrum to be monotonically decreasing, with a low-end cutoff at ~ 10 MeV.

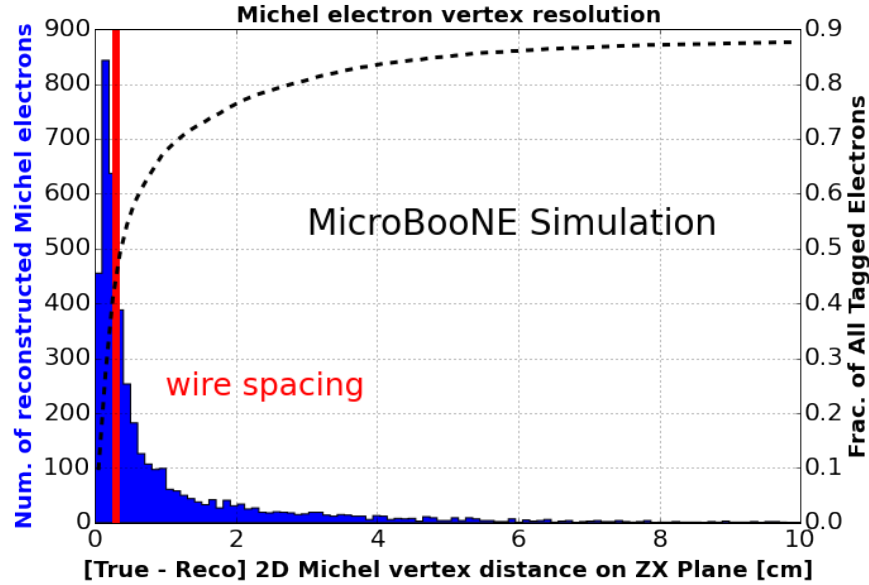


Figure 8.9: Vertex resolution for reconstructed Michel electrons from a Monte Carlo cosmic sample. The histogram shows the 2D distance on the ZX-plane (wire- and drift-coordinates) of reconstructed Michel electrons to the nearest true Michel electron location. The vertical red line indicates the 3 mm wire-spacing, and the dashed black curve quantifies the fraction of total reconstructed electrons with a 2D distance below a given value.

The low selection efficiency is largely due to the 2D reconstruction approach employed. The dependence of the selection efficiency on several variables is profiled: Michel electron energy, muon vertical momentum component, and muon-electron angle on the collection-plane. These studies are performed using simulated cosmic events and are based on truth information. The efficiency is measured as the ratio N_{reco}/N_{true} where N denotes the number of Michel electrons. Only reconstructed electrons falling within 3 cm in both X and Z of a true Michel electron are included in the numerator. The efficiency as a function of true Michel energy is shown in figure 8.10a. The efficiency is relatively flat after 25 MeV in energy. Figures 8.10b and 8.10c show the efficiency as a function of the muon's vertical momentum component and vs. the 2D angle, on the collection-plane, between the muon and Michel electron. There is significant variation in efficiency for these variables. Moreover, the efficiency is lowest for values which are most probable (as shown by the gray distributions for the variables) which leads to the overall low efficiency. The significant variation in efficiency for these two variables can be explained by the tagging technique required. Searching for a muon Bragg peak and Michel-muon kink is difficult when the muon is moving vertically downwards (covering only a few wires on the collection plane) and when the Michel electron and muon tracks are almost parallel.

8.3 Energy Reconstruction

To determine the reconstructed energy we perform a calorimetric measurement by integrating the total charge from hits associated to a Michel electron. A fixed calibration constant is applied to convert charge measured from reconstructed hits to MeV. This calibration accounts for the electronics of the collection-plane wires, the signal processing, as well as detector effects that convert the deposited energy into collected electrons on the wire planes.

The electronics gain (e^-/ADC) is obtained following the same procedure described in appendix C.2. Instead of relying on the stopping muon selection outlined, 3D stopping muon tracks are identified by requiring they be found to stop in proximity to one of the tagged Michel electrons. Because the Michel selection is performed in 2D, only (X,Z) position information is available to perform the matching. Tracks with an end-point within 2 cm of the identified 2D muon stopping point from the Michel reconstruction are selected. Tracks perpendicular to the beam direction (dot product

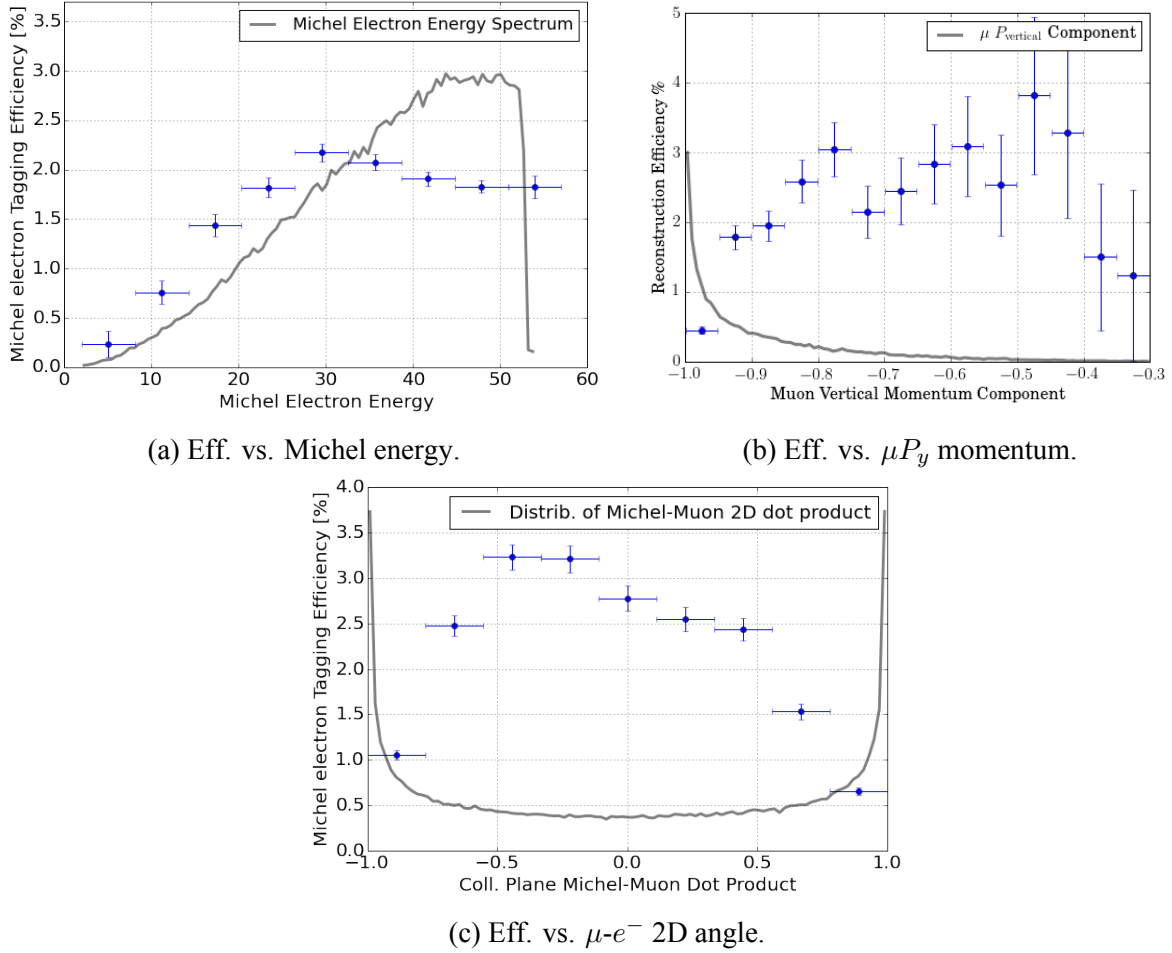


Figure 8.10: Reconstruction efficiencies for various variables. Blue points denote the selection efficiency, with statistical error bars, measured as the ratio of reconstructed Michel electrons with vertex within 3 cm of a true stopping muon. Grey curves denote the distribution of the variables against which the efficiency is calculated.

with the Z-direction smaller than 0.3) are ignored. This cut is motivated by the track-angle dependence of the calorimetry shown in figure C.15b. Additionally, space-points reconstructed outside of the range [400,800] cm are removed, to avoid regions of significant non-uniformities in the calorimetry, as seen in figure C.16.

The treatment of ion recombination is described in section C.4.1. From the simulation we estimate that the constant recombination correction factor of $R = 0.62$ contributes to a small, 2% smearing of the energy resolution for Michel electrons. The full dE/dx range (shaded area in figure C.17b) over which Michel electrons deposit energy is used to estimate a systematic for the

recombination correction applied. In this range, the recombination factor varies between 0.648 and 0.590, leading to a systematic of $1/2\Delta R/R = 4.7\%$.

Quenching by impurities is treated as discussed in section C.1.3. Space-charge effects, caused by the buildup of positive ions in the TPC, can lead to electric field distortions which in turn impact the calorimetry. A static space-charge simulation model, found to agree qualitatively with measurements from cosmic-ray data, shows that the impact on calorimetry throughout the detector volume leads to a smearing in the calorimetric energy measurement of less than 1% and is thus considered negligible for the purpose of this analysis. Finally, a 1.3% systematic uncertainty associated to the argon ionization energy W_{ion} (see sec. C.1.1) is taken into account. A detector-wide variation in response of order 6% is however found across the TPC, caused by variations in signal-response on different collection-plane wires, track-angle dependence, etc. This contributes to a smearing of the energy resolution.

The energy of a Michel electron in MeV is given by multiplying the reconstructed charge (e_{reco}^-) from hits associated with tagged Michel electrons by the calibration factor given by

$$\frac{E (MeV)}{e_{reco}^-} = 3.85_{-0.19}^{+0.21} \times 10^{-5}. \quad (8.1)$$

This corresponds to a $1_{-0.049}^{+0.055}$ fractional systematic uncertainty.

8.4 Effect of Radiative Photons on Energy Reconstruction: Monte Carlo Study

In this section we show the results of studying the impact of untagged radiative photons on the energy resolution by using a sample of simulated Michel electrons. We compare the reconstructed and true energy from the simulation under different scenarios.

We measure an energy-dependent fractional energy resolution by performing the following steps:

- Plot the reconstructed energy as a function of the true energy and fit to the function $E_{reco} = \alpha + \beta E_{MC}$.
- Correct the energy scale by calculating a corrected energy $E_{corrected} = \frac{E_{reco} - \alpha}{\beta}$.

- Binning in true energy to measure the fractional resolution by fitting the distribution $[E_{corrected} - E_{MC}]/E_{MC}$ to a Gaussian function. The σ from the fit gives a measure of the fractional energy resolution.

The value E_{reco} is measured employing the calorimetric conversion defined in equation 8.1. The slope β measures the bias between reconstructed and true energy introduced by the reconstruction algorithm. Both the energy bias and the energy resolution are important quantities and directly impact neutrino energy reconstruction for ν_e interactions.

This procedure will be applied to three different scenarios. First, we measure the fractional energy resolution for ionization-only energy deposited by Michel electrons. Next, we measure the energy resolution for the full Michel electron energy using two different definitions of reconstructed energy: one where only the reconstructed ionization energy is considered, and a second where additional energy tagged from radiative photons is also included. These three studies are presented below, and each is discussed in detail. The distributions of measured fractional resolution, binned in true energy and fitted to a gaussian is reported for all three studies in appendix D. The central regions of the distributions are modeled quite well by a gaussian (with measured $\chi^2/\text{d.o.f.} \sim 1$). We do not attempt to model the tails of the distribution. After the bias correction described above, the gaussian fits deviate from a mean of 0 roughly uniformly, and are generally within a few percent of this value.

Figure 8.11 shows the energy resolution obtained for the ionization-only energy deposited by Michel electrons. This measurement compares the true ionization-only deposited energy to the reconstructed ionization-only clustered energy. The correlation between true and reconstructed energy, quantified by the fitted line in figure 8.11 (a), shows that all ionization energy is correctly accounted for by the reconstruction procedure. The small positive bias (1 MeV) obtained from the fit is due to an over-clustering of charge near the muon decay point where the muon deposits a large amount of charge in its Bragg peak. The fractional energy resolution in figure 8.11 (b) can be interpreted as a measure of the calorimetric resolution, since it compares the measured and true value of the ionization energy that excludes any issue arising from the energy loss due to radiative photons. The improving resolution as a function of true energy is characteristic of what

one would expect for a calorimetric measurement. Ongoing studies in charge-estimation at the hit-reconstruction stage will likely improve the resolution obtained for this kind of measurement.

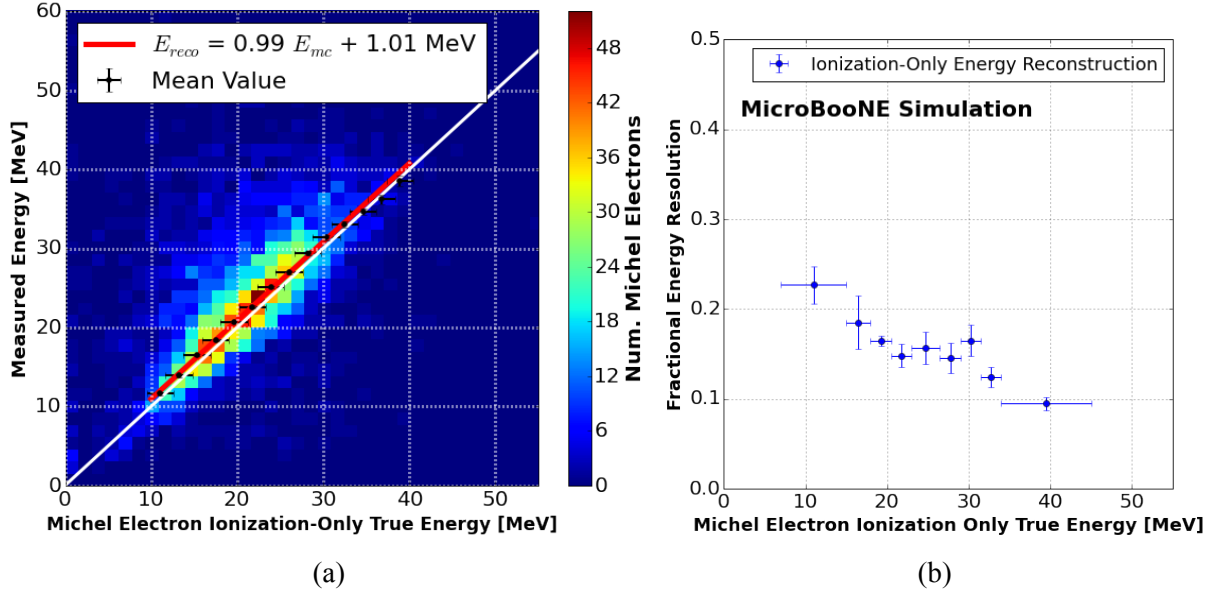


Figure 8.11: (a) reconstructed vs. true ionization-only Michel electron energy deposited. (b) fractional ionization-only energy resolution vs. true ionization-only Michel electron energy.

Figure 8.12 shows the same distributions, but now compares the reconstructed Michel electron energy measured excluding any charge deposited by radiative photons (ionization-only energy measurement) to the true Michel electron energy. Now we see a significant deficit of reconstructed energy, as well as a significant spread in the resolution. Furthermore, we notice that the fraction of collected energy decreases, on average, as the Michel energy increases, and that the distribution itself gets broader. At 50 MeV the reconstructed energy makes up only 60% of the total true energy implying a significant energy bias. This is consistent with what was shown in figure 8.1 and once again indicates how an ionization-only energy measurement would not achieve the best energy resolution.

Finally, in figure 8.13 we show the energy resolution obtained when we include the charge collected through tagged photons. The measured energy is now closer to the true one. Any remaining discrepancy comes from the inefficiency in including radiative photons. For example, at 50 MeV only 76% of the total energy is recovered, with missing energy attributable to photons under threshold and those mistakenly discarded in an attempt to remove charge from accidental cosmic rays, in addition to energy which escapes the TPC volume or lies beyond the 80 cm and

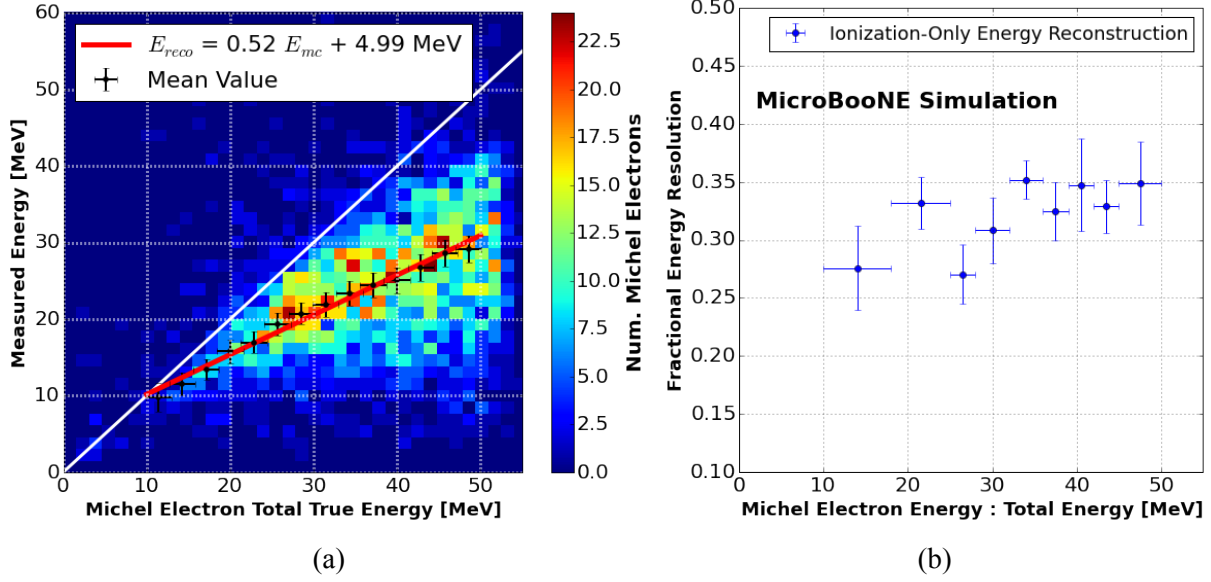


Figure 8.12: (a) reconstructed Michel electron ionization-only energy as a function of the true total Michel electron energy. (b) fractional energy resolution as a function of the true Michel electron energy. Error bars represent the uncertainty on the fit value.

30 degree cut values used. From a Monte Carlo study of the 2D hit reconstruction employed in this analysis we find that 15% of the energy deposited by photons is under the hit-reconstruction threshold and therefore escapes detection.

Figure 8.14 shows the overlay of the resolutions from the ionization-only energy measurement (blue squares) and that including the tagged photons (red circles). Tagging radiative photons improves the energy resolution from over 30% to 20%. There is also indication that the improvement is larger at higher energy, where radiative effects are more important. The effect of photon selection and reconstruction still dominates the resolution and bias, so any further improvement will require more efficient photon tagging. This will be challenging, since the presence of the cosmic rays in the detector (approximately at ground level) makes it hard to include all the associated energy without also integrating contributions from nearby cosmic rays.

8.5 Reconstructed Michel-Electron Energy Spectrum from Data

We finally present the results of the analysis chain described in Sections 8.2 and 8.3 applied to cosmic-ray data recorded by MicroBooNE in “off-beam” mode, when the Fermilab accelerator

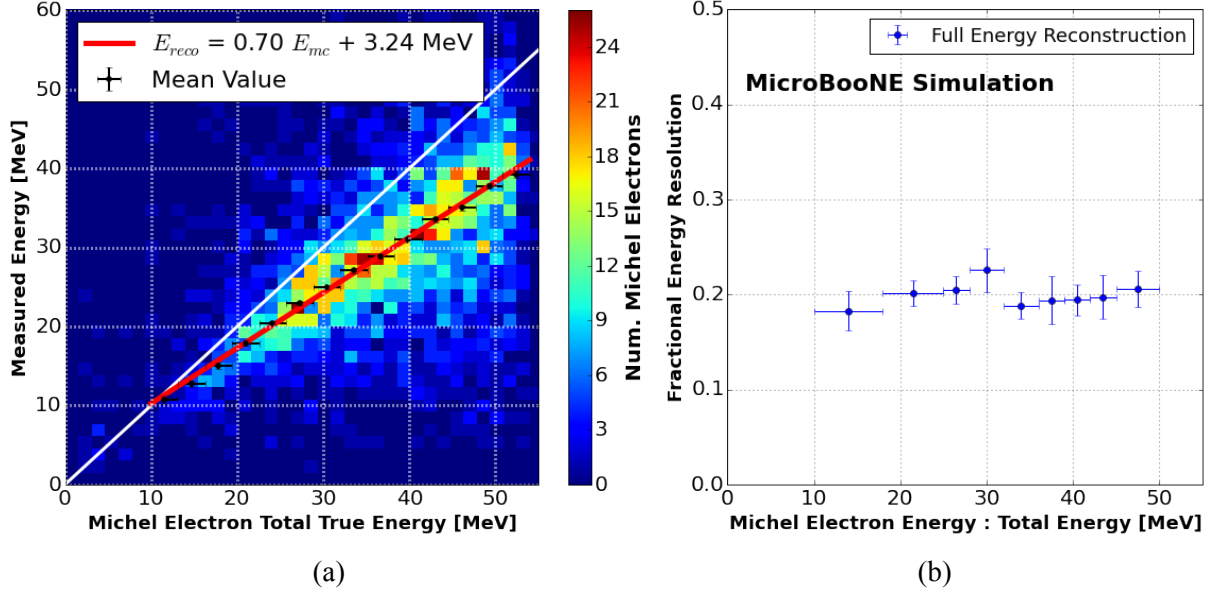


Figure 8.13: (a) reconstructed Michel electron energy as a function of the true Michel electron energy. (b) fractional energy resolution as a function of the true Michel electron energy. The reconstruction procedure to tag radiative photons (described in Sec. 8.2) attempts to collect energy deposited within 80 cm, and ~ 30 degrees of the muon stopping point in 2D.

complex was not providing neutrino beams.

We run the reconstruction chain on a sample of 5.44×10^5 triggered events (an event corresponds to a 4.8 ms readout of TPC data) and identify 1.4×10^4 candidate Michel electrons. Figure 8.15a shows the energy distribution for the ionization-only energy of tagged electrons. A measurement of the electron ionization spectrum was produced by the ICARUS T600 detector [40]. The two reconstructed spectra show good agreement. Figure 8.15b shows, for the same events, the reconstructed energy including charge deposited by tagged radiative photons. For both we compare the reconstructed energy spectrum from data to that obtained running over a sample of Monte Carlo simulated cosmic events. No correction for the energy-dependent efficiency is made, which is assumed to be the same for the data and simulation. While the overall reconstruction efficiency is low, it is largely impacted by the spatial orientation of the muon and Michel electron in the 2D collection-plane view and is relatively flat beyond 25 MeV.

By performing a χ^2 study of the data and simulation distributions we determine that the energy scale of the two distributions agree to within 3%. The study is described in appendix D. This quantity is compatible with the estimated $\sim 5\%$ systematic uncertainty associated with the calorimetric

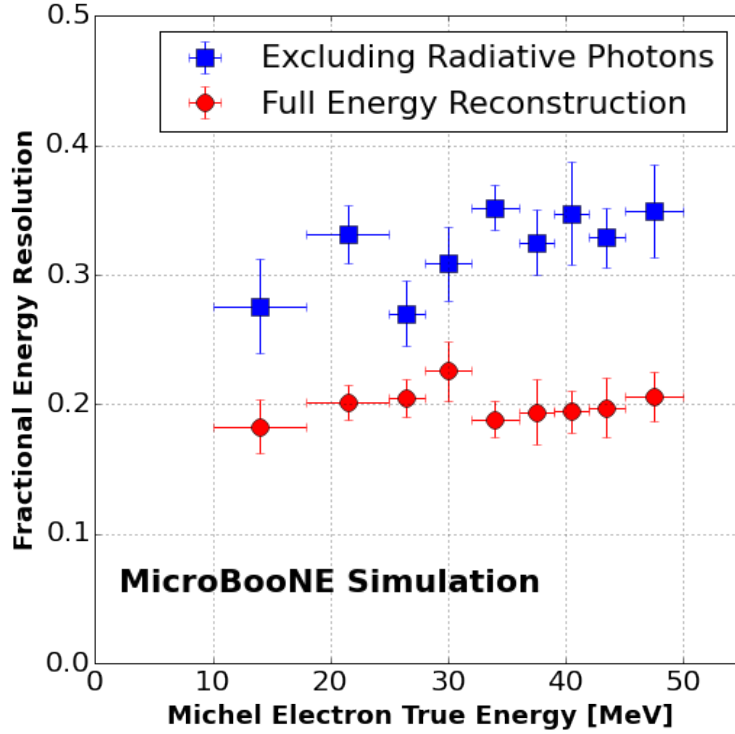


Figure 8.14: Fractional energy resolution as a function of the true Michel electron energy when using only the reconstructed ionization energy deposited (blue) vs. when including any measured energy deposited by radiative photons (red).

energy conversion (Eq. 8.1). The overall agreement between data and Monte Carlo indicates that our simulation is modeling the physics of muon decay and Michel electron propagation in liquid argon correctly. Furthermore, it allows to expand the conclusions of Sec. 8.4 to the data. For the ionization-only measurement the energy resolution in the range between 10 and 60 MeV is above 30%, and improves to about 20% when tagging of radiative photons is included. Including photons shifts the peak of the energy spectrum from ~ 20 to about 30 MeV. The energy bias measured in Sec. 8.4 changes from 60% to 76% of all electron energy recovered at 50 MeV of true electron energy. The decrease in energy-bias and shift in the peak of the energy spectrum are approximately consistent.

Both plots show a significant tail which extends beyond the end-point energy of Michel electrons for both data and Monte Carlo. This is due to tagged electrons for which charge from the stopping cosmic-ray muon is incorrectly included in the Michel energy, as well as any possible accidental charge from nearby muons.

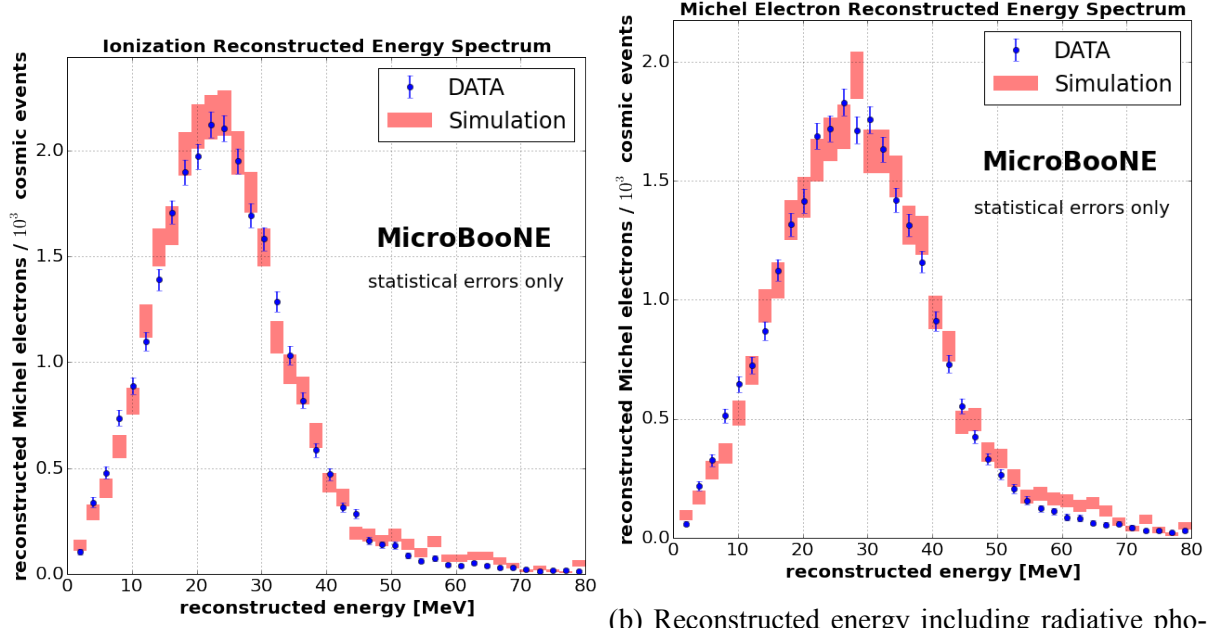


Figure 8.15: Reconstructed energy spectra for ionization-only (a) and total Michel electron energy (b) on data and simulation. Error bars represent statistical uncertainties only for both data and simulation.

Focusing on the contributions from radiative photons, the energy spectra of individually tagged Brem. photons is shown in figure 8.16. The spectra from data and simulation agree quite well except at the lowest energies: below ~ 1 MeV there is a deficit in the data, possibly caused by the impact of hit-thresholding at these energies. Another small deficit in the data is present at ~ 5 MeV. These discrepancies possibly contribute to a difference in the total Michel electron energy spectrum (figure 8.15b) observed at the tail of the distribution around 60 MeV.

8.6 Conclusions

Low-energy electrons play an important role in many physics studies addressing neutrino oscillations by using the LArTPC detector technology, and are a key ingredient to specific studies, such as the search of neutrino interactions from supernova bursts. We attempted to highlight the intricate nature of the propagation of such electrons in liquid argon and presented studies illustrating the significant impact of energy lost to radiative photons on the energy resolution.

The work presented here shows first results on Michel electron identification with the Mi-

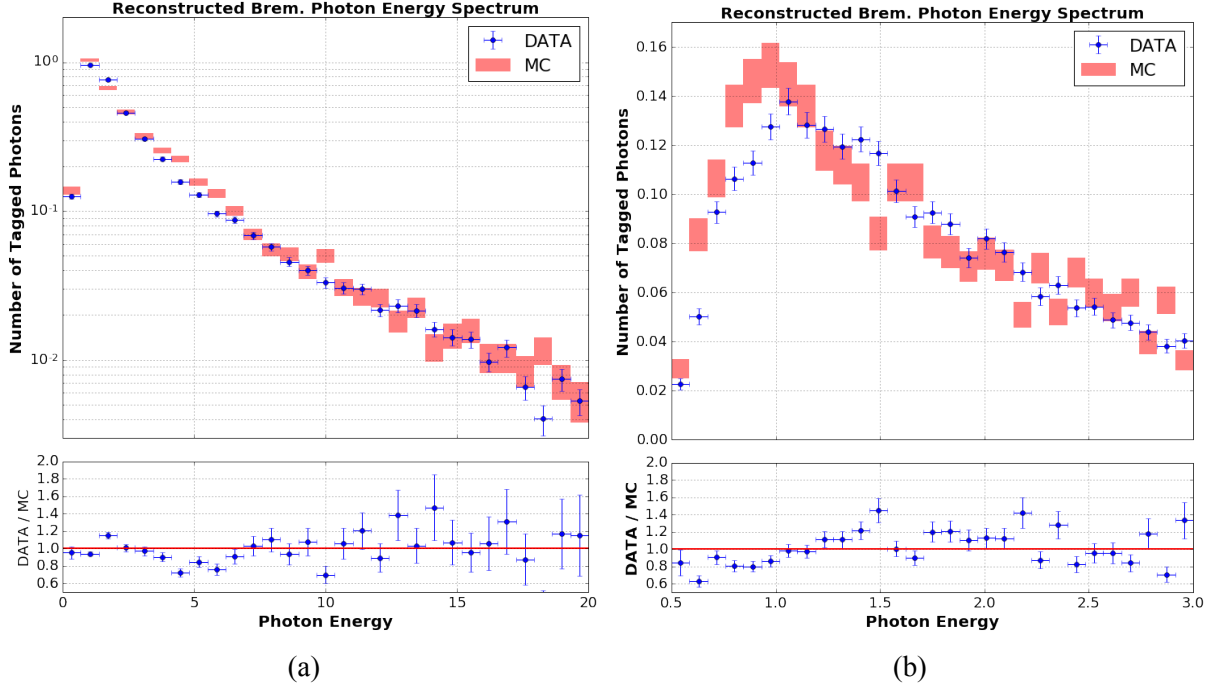


Figure 8.16: Energy spectrum of reconstructed radiative photons associated to tagged Michel electrons. Distributions are absolutely normalized. (a) Spectrum up to 20 MeV on log-scale. (b) Spectrum below 3 MeV on a linear scale. The distributions agree across most of the spectrum. The deficit in data with respect to the simulation at the lowest energies (below 1 MeV) indicate a possible difference in the impact of hit-thresholding in data vs. simulation.

croBooNE TPC employing a simple 2D reconstruction method. This is the first analysis which employs a fully automated reconstruction to study EM activity in a LArTPC neutrino detector. A sample of $\sim 14,000$ candidate Michel electrons was identified. The reconstructed energy spectrum when only ionization energy deposition is accounted for peaks at ~ 20 MeV and shows a significant energy deficit with respect to the true energy distribution. When we recover energy released by radiative photons, the spectrum's peak shifts to almost 30 MeV. While an improvement, this still falls well below the true energy spectrum cutoff at ~ 50 MeV. This work shows that we understand the performance of the MicroBooNE LArTPC as evidenced by the Monte Carlo reproducing the observed Michel electron energy spectrum. The reconstructed spectrum is considerably different from the true one, due to the challenge posed by identifying and successfully clustering energy deposited by radiative photons produced by low-energy electrons. We have shown that we can account for some of the missing energy by including tagged radiative photons, hence improving the energy reconstruction. The work presented in this chapter complements and expands on the first

study of Michel electrons produced by the ICARUS collaboration [40], going beyond a measurement of ionization-only energy loss and electron energy resolution, thus providing more realistic estimates of the attainable neutrino energy reconstruction accuracy and resolution. The reconstruction of the energy of Michel electrons can be improved by making full use of the 3D information available from LArTPC detectors. This is an essential step towards reaching the energy resolution required for future precision neutrino oscillation measurements.

Chapter 9

Selection and Reconstruction of π^0 Events from Charged Current ν_μ Interactions

Neutrino oscillation experiments rely on accurate neutrino energy reconstruction and flavor tagging in order to perform oscillation measurements. Studying π^0 interactions in MicroBooNE can help with both tasks. π^0 decay events provide a valuable sample of EM activity with which to study the biases and resolution associated to EM shower reconstruction. Additionally, interactions with final-state π^0 s are an important background to the ν_e appearance channel which accelerator-based experiments depend on for their measurements. Efforts which aim to study EM shower energy reconstruction and constrain the production of π^0 s in neutrino interaction can strengthen an oscillation analysis by reducing the systematic uncertainty associated with the determination of the neutrino energy and the rate of background events from misidentified topologies. This chapter presents an overview of π^0 production in neutrino interactions (9.1 9.2). The selection and reconstruction developed to identify CC π^0 interactions is described in section 9.3. Preliminary comparisons of distributions associated to the kinematics of π^0 s are presented, without efficiency corrections, along with a discussion on the next steps needed for this analysis to obtain cross-section measurements on argon. The subsequent chapter (10) focuses on the study of energy reconstruction for EM activity associated to the selected π^0 events, and the impact this has on ν_e energy reconstruction. A more detailed description of the EM shower reconstruction employed in this analysis is presented in appendix F.

9.1 Importance of π^0 Channels in ν Interactions.

Cross-section measurements for π^0 production on various targets in both NC and CC channels have been reported by various experiments over the past decade [58, 59, 60, 61, 62, 63, 64, 65]. The differences observed highlight the challenge faced in reconciling results obtained by different experiments, as well as between measurements in data and predictions from neutrino event generators. Reconciling these differences is difficult due to the impact different detector technologies have on identifying final states. The presence of final state interactions (FSI) and their dependence on the nuclear structure of the target material further complicate the ability to produce model-independent and detector-agnostic results. At present an experimentally validated modeling of pion production in $\mathcal{O}(\text{GeV})$ neutrino interactions capable of constraining the systematics associated to these channels to the degree needed for precision oscillation measurements is lacking. As a consequence, the neutrino physics community has argued for a strong research program aimed at expanding the experimental measurement landscape, focusing on providing results that are as model- and detector-independent as possible [66]. Detailed knowledge of neutrino interactions on argon will be essential in order to perform neutrino oscillation measurements with LArTPC detectors to a level of precision required to conclusively address the puzzle of sterile neutrino oscillations and measure δ_{CP} . The important role played by π^0 events in backgrounds to these analyses motivates a careful study of neutral pion production on $\nu - Ar$ interactions.

Strong motivation to constrain the rate of π^0 production in MicroBooNE exists as well. MiniBooNE's low energy excess' main background source is from NC π^0 events where one photon escapes detection and the event is reconstructed as a ν_e instead. While the mis-identified events from this channel in MiniBooNE will be smaller due to the electron/photon separation power of a LArTPC, it is still important to have a good understanding of the π^0 production rate in order to be able to properly constrain the magnitude of this background. Even though MiniBooNE and MicroBooNE share the same neutrino flux, the impact of FSI effects on the significantly different targets of carbon and argon will lead to differences in the production of this channel. A data-driven measurement of the neutrino interactions with π^0 s in the final state is therefore essential to properly measure, and assess the nature of, any possible excess of electron or photon events.

9.2 π^0 Production In Neutrino Interactions

Neutrino interactions with atomic nuclei lead to a wide range of final states, with significant dependence on neutrino energy. The current picture of neutrino interactions in the $\mathcal{O}(1)$ GeV energy range [67, 6] is complicated by the fact that at these energies neutrinos transition from probing individual nucleons in the atom to probing the quarks within them. Interactions with single nucleons can lead to Quasi-Elastic (QE) interactions in which the (anti-)neutrino interacts with a single neutron (proton) producing an outgoing lepton of the same flavor and proton (neutron). At slightly higher energies the struck nucleon can be excited into a resonant baryon state (N^*) which decays into a nucleon and pion. Such interactions are referred to as resonant pion production (RES) events. The resonance which is excited is typically the $\Delta(1232)$ [6]. At higher energies yet, interactions which probe the quarks within nucleons lead to the production of hadronic activity, possibly including one or more final state pions. Such interactions are referred to as Deep Inelastic Scattering (DIS) [68]. In addition, the complex environment within the nucleus further complicates the picture by adding dynamical freedom to the struck nuclei in the form of Fermi motion and nucleon-nucleon correlations [69]. Pions, the lightest mesons, are produced in RES and DIS interactions. Together with charged leptons from CC interactions and the struck nucleon they account for a significant portion of the total observable energy released by the interacting neutrino.

9.2.1 Final State Interactions

Final State Interactions, or FSI, have a significant impact on the observables in neutrino interactions. They are the product of re-interactions of particles produced in a neutrino interaction as they exit the nucleus. These interactions can be of many types (absorption, pion production, scattering, as shown in figure 9.1a) but all lead to one effect: they make it more difficult to reconstruct the incoming neutrino's energy using the reconstructed kinematics associated with observable final state particles. The impact on energy reconstruction is two-fold. First, FSI can produce or absorb particles not coming from the original interaction, leading an event to be classified differently than what it truly is. Second, scattering in the nucleus will change the kinematics of outgoing particles in a way that will smear the energy resolution.

9.2.2 Secondary π^0 Production in Neutrino Interactions

Particles produced in neutrino interactions can re-interact. Charged pions can undergo a process referred to as *charge exchange* in which the charged pion interacts with a nucleon in an argon atom to produce a π^0 and an outgoing nucleon which conserves the total charge:

$$\pi^+ + n \rightarrow \pi^0 + p \quad \text{or} \quad \pi^- + p \rightarrow \pi^0 + n \quad (9.1)$$

Interactions such as these can be a background to π^0 production in the neutrino interaction itself, specifically if the re-interacting pion does so shortly after having left the vertex. Figure 9.1b shows an example charge-exchange interaction in which a secondary vertex from which a proton and π^0 can be seen.

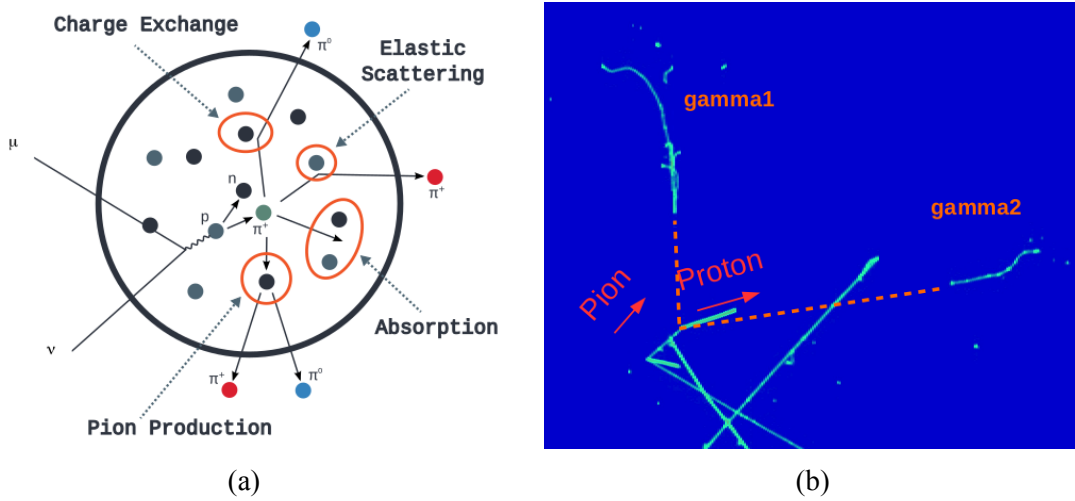


Figure 9.1: (a) Cartoon of the impact FSI can have on the observables produced in a neutrino interaction. Image taken from reference [66], by Tomasz Golan. (b) Charge-exchange interaction leading to a secondary π^0 associated with the neutrino interaction, but not produced within the nucleus.

9.2.3 π^0 Events from the BNB and their Kinematics

The short π^0 lifetime and the fact that virtually all decays ($> 98\%$) go to a $\gamma\gamma$ channel mean that π^0 interactions from neutrino interactions are identified by searching for two photons produced at the neutrino interaction vertex. The kinematics of the decay are such that from the reconstructed

γ s one can recover the π^0 invariant mass according to equation 9.2.

$$M_{\pi^0}^2 = 2p_{\gamma_1\mu}p_{\gamma_2}^\mu = 2E_{\gamma_1}E_{\gamma_2}[1 - \cos(\theta_1 + \theta_2)]$$

It is worth noting that π^0 s produced in neutrino interactions from the Booster Neutrino Beamline are generally low in momentum. This leads to γ s of low energy, which as presented before poses a challenge to the reconstruction. Figure 9.2 shows the energy distribution of photons from simulated BNB π^0 s in CC interactions. The two curves denote the lower- and higher-energy photon from each event. Reconstructing π^0 s by tagging both photons requires being able to efficiently reconstruct photons of 50-100 MeV of energy.

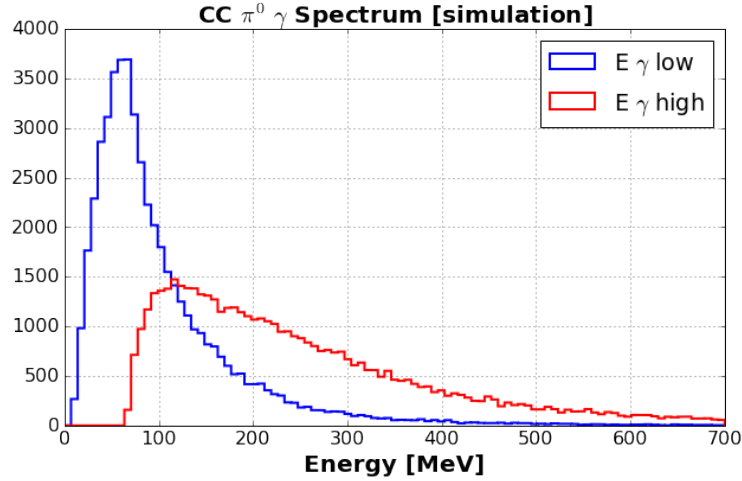


Figure 9.2: Photon spectrum from π^0 s produced in BNB CC interactions. The red curve denotes the higher-energy photon, the blue one the lower-energy one.

Reference [70] provides useful properties of kinematic relations for π^0 decays which can be derived from equation 9.2. We summarize those which can help understand this sample of EM showers and help guide their reconstruction. The $\gamma\gamma$ opening angle has a minimum value which depends on the π^0 energy, for which the relation is given by $\sin(\theta_{min}/2) = m_\pi/E_\pi$ with θ the $\gamma\gamma$ opening angle. The lab-frame distribution of photon energies is uniform and bound by the values $[(E_\pi - P_\pi)/2, (E_\pi + P_\pi)/2]$. The distribution of $\gamma\gamma$ opening angles for π^0 s of different energies is given by equation 9.2.

$$\frac{dN}{d\theta} = \frac{1}{4\beta\gamma} \frac{\cos \theta/2}{\sin^2 \theta/2} \frac{1}{\sqrt{\gamma^2 \sin^2 \theta/2 - 1}} \quad (9.2)$$

From these distributions we note that the $\gamma\gamma$ opening angle is almost always greater than 20 degrees for π^0 s of energy up to 700 MeV, which includes the vast majority of π^0 s produced in BNB neutrino interactions. The distribution of opening angles for a given π^0 energy exhibit sharp peaks at the minimum opening angle. This strong correlation can be leveraged when reconstructing the π^0 energy, if the opening angle can be precisely measured.

9.3 ν_μ Charge Current π^0 Interaction Selection and Reconstruction

The selection applied to neutrino data to identify π^0 candidates is composed of three stages. A first CC ν_μ selection aims to identify neutrino candidates producing a muon in the final state by relying on timing and TPC topology (and to a lesser degree on calorimetry). This selection performs an initial removal of cosmic-ray muons, followed by a secondary neutrino interaction reconstruction and provides a reconstructed 3D neutrino vertex and 3D muon candidate track. The second step involves running the γ reconstruction, summarized in this section and presented in more detail in appendix F. Finally, a π^0 selection on the output of such a reconstruction is applied. For the analysis presented in this work a final step is applied: data events from the selection are visually examined to identify those with π^0 candidates which have been reconstructed successfully. While the automated selection provides a sample of CC π^0 candidate which has a $\sim 70\%$ purity, a sizeable ($\sim 1/3$) fraction of events has at least one of the photon showers poorly reconstructed. We filter these events in order to produce a cleaner sample of γ showers which allows for a clearer interpretation of EM reconstruction studies. These reconstruction steps are presented in more detail below.

9.3.1 Selection of Neutrino Interactions

The neutrino selection applied for this analysis aims to identify muon tracks produced inside the TPC volume associated with ν_μ CC events. The challenge faced by the selection is the exclusion of cosmic-ray muons. Even with a software-trigger which requires the observation of light in-time with the 1.6 μs neutrino spill (see appendix A), most events (by a ratio of ~ 10 -to-1) contain no neutrino interaction within them. Furthermore, each event contains of order 10-20 cosmic-ray muons entering the TPC volume in the beam TPC readout window (2.3 ms). Achieving the additional factor of 100-to-1 removal of cosmic-ray contamination is the main task of the neutrino

selection. The selection outlined below is described in more detail in reference [71].

First, a series of steps are performed to remove cosmic-ray muons inconsistent with neutrino interactions. These cosmic-removal cuts are applied to the output of Pandora’s cosmic track reconstruction (*pandoraCosmic* [57]) and are described below:

1. **Geometric Tagging:** Reconstructed tracks found to enter and exit the detector (through-going) are removed.
2. **Out of Time Tracks:** Tracks which are partially found to lie outside of the beam-spill drift-window (before the trigger-time and after the trigger-time plus one drift-length) are removed. These tracks must have entered the TPC at a time which is inconsistent with the trigger-time.
3. **Anode-Cathode Piercing Tracks:** Tracks found to enter the detector at a time consistent with a reconstructed optical flash which is outside of the beam-spill are removed. For tracks which enter/exit the anode/cathode assessing this is possible simply by looking at the reconstructed time associated to the entering or exiting point. The cut therefore targets the removal of anode or cathode piercing tracks.
4. **Flash-Track Matching:** A flash-track matching stage is applied in which remaining reconstructed tracks are used to simulate the light-pattern expected on the PMTs. Tracks which are found to not be compatible with the PE spectrum observed on the PMTs for the selected beam-spill track are removed.

Charge remaining in the detector after this cosmic-removal stage is then run through Pandora’s pattern-recognition algorithms targeted to reconstruct neutrino interactions (*pandoraNu* [57]). A sequence of cuts relying on PMT and TPC information are then applied to identify ν_μ CC candidate events:

1. **Flash Timing and Amplitude Cut:** The software-trigger applies a minimum ~ 6.5 PE requirement for light produced in-time with the neutrino spill. An additional cut of 50 PE is applied for this selection: this has a negligible impact on signal CC events, and contributes to further suppress cosmic-ray backgrounds. A requirement that the largest flash of light reconstructed in the time-interval between 3.3 and 4.9 μs from the trigger-time be larger than 50 PE is applied.

2. **Vertex-Track Matching:** All reconstructed tracks are associated to 3D vertices which lie within 3 cm of either their start or end point. The number of tracks associated to the vertex is referred to as the multiplicity.
3. **Flash-Track Matching:** The largest flash in the beam-spill is compared to all tracks remaining in the event. If the track's Z position is found to be compatible with the flash extent in Z , the track is considered a possible muon candidate. For this to be the case the distance between the Z range of the track, and the Z range of the flash ¹ must be less than 70 cm.
4. **Muon TPC Cuts:** Different cuts are applied for events of different multiplicity. All reconstructed vertices are scanned. If they have associated 3D tracks, and if at least one of these tracks passes the flash-track matching cut, then one of the two below cuts are applied.
 - **Multiplicity == 1:** The selected track must be longer than 40 cm.
 - **Multiplicity >= 2:** The two longest tracks are selected. If the absolute value of the cosine for the angle between them is larger than 0.9, the candidate event is rejected. Additionally, for tracks with multiplicity equal to two, a cut aimed at removing Michel electron events is applied. If the shorter of the two tracks is below 30 cm, the event is removed if either the longest track is within 20 cm of the bottom of the TPC, or if its dE/dx profile is consistent with a stopping muon ².

If a vertex and the tracks associated pass these cuts, the vertex is denoted as the candidate neutrino interaction point, and the longest track associated to it as the muon candidate. After this stage in the selection 6,183 ν_μ CC candidate events are identified out of a total of ~ 525 thousand available from the 5E19 POT of unblinded BNB data. The purity of this selection is of order 60%.

9.3.2 EM Shower Reconstruction

There are three main challenges to the identification and reconstruction of $\mathcal{O}(100 \text{ MeV})$ electromagnetic activity in a LArTPC: (1) distinguishing charge deposited by track-like particles (muons,

¹The track Z range is given by the Z coordinates of its start- and end-points. The optical flash's Z extent is given by the mean and RMS of the charge-weighted PMT information associated to it.

²The exact requirement for this is an and of the following conditions: 1) the dE/dx measured for the track near the vertex be larger than that at the opposite end; 2) the dE/dx at the vertex be larger than 2.5 MeV/cm; 3) the dE/dx at the opposite end from the vertex be smaller than 4.0 MeV/cm.

protons, pions) from that produced by electrons and photons. (2) isolating the full extent of energy deposited by electrons or photons as they produce an EM cascade from the cosmic activity recorded in a “slow” surface detector. (3) developing a reconstruction approach capable of measuring EM activity over a range of energies across which the shower topology changes dramatically. Each category is further described, with examples of EM showers from the data, in appendix F.1. Figure 9.3 shows an example of a ν_μ CC interaction with four γ showers from two π^0 events which gives a sense for what EM interactions from these events look like in the TPC.

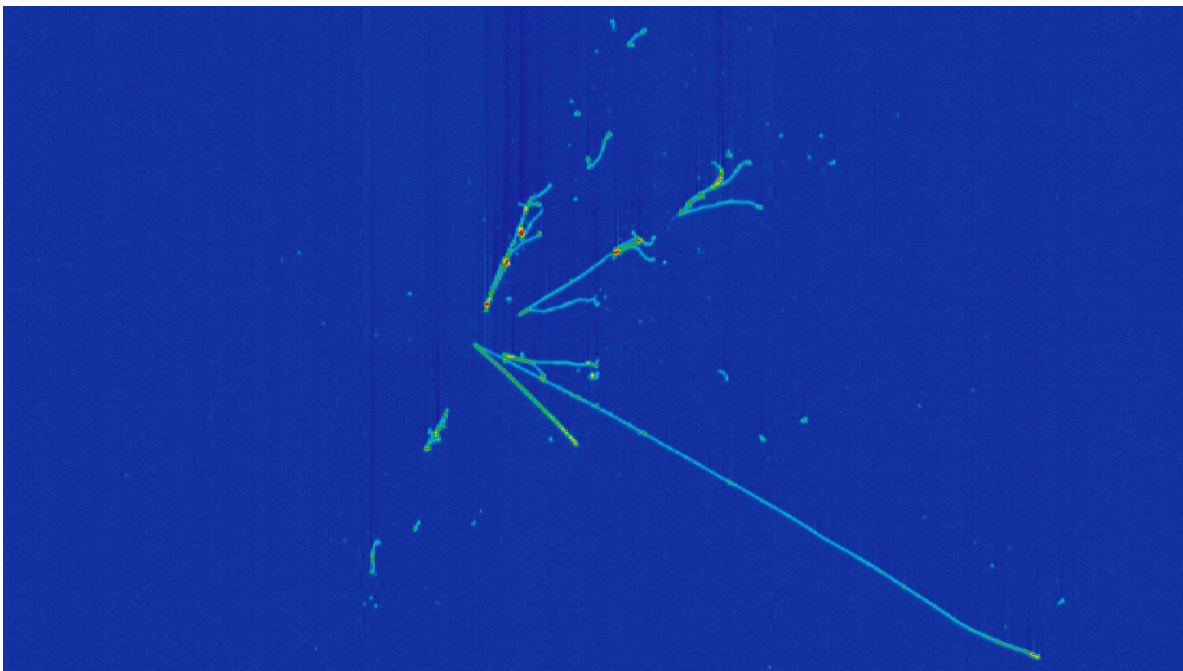


Figure 9.3: Event display of EM showers from a 2 π^0 CC ν_μ event. The stochastic and segmented nature of EM showers at these energies is clearly visible.

The reconstruction is performed in a staged approach, starting from reconstructed 2D quantities on each plane ³ to produce full three-dimensional reconstructed showers. The input to this stage of the reconstruction consists of 2D hits and information on the neutrino vertex location. Provided with this information, the reconstruction proceeds as follows:

1. **Track-Shower separation** Two-dimensional hits are classified as shower- or track-like. This step aims to “clean” each view of charge deposited not associated to the two photons by removing both charge from cosmic-ray activity as well as tracks produced in the neutrino

³Appendix B presents an overview of the generic 2D reconstruction performed on MicroBooNE data.

interaction. To perform this step we attempt to remove first charge deposited by cosmic-ray activity by measuring the spatial correlation of clusters with the reconstructed neutrino vertex. After this a series of metrics which aim to measure the degree of scattering of trajectories in the image are used to separate charge deposited by heavy charged particles (muons, pions, and protons) from electrons and photons. The metrics developed and cuts applied are described in appendix F.2.

2. **Two-dimensional clustering** Hits on each plane are merged in “clusters”, one per EM shower. At first, contiguous charge deposited via ionization is clustered via a proximity-based clustering algorithm in *photon clusters*. The photon clusters coordinates are converted in polar coordinates centered at the neutrino vertex, and are merged based on their angular and radial arrangement. Subsequently, the two largest clusters, separated by at least 15 degrees, are taken as the trunk of γ photons, and used to guide an additional clustering step aimed at collecting as much far-reaching charge as possible.
3. **Cross-Plane Matching** Pairs of clusters are matched across planes. This operation is performed by requiring that two clusters on separate planes must have hits which span overlapping intervals. One of the two clusters is required to be on the collection plane as charge from this plane will be used for the shower’s calorimetric energy reconstruction.
4. **Re-Clustering** A second clustering step is performed in order to tag charge which may have been ignored at the first pass. This is done by loosening the cuts on shower-track separation and focusing the inclusion of additional charge in the direction of the already identified γ s. At this step identified showers which are aligned in direction are merged, and the inclusion of additional charge expanded from an ROI of 2x2 meters to one of 4x4 surrounding the neutrino vertex.
5. **3D Shower Reconstruction** Information from merged clusters is used to reconstruct 3D showers. In this step a shower’s energy, position and momentum are computed. The γ direction is reconstructed by performing a charge-weighted vector sum of hit coordinates with respect to the neutrino vertex. The shower energy is computed by summing all the energy associated with collection-plane hits and applying the calorimetry described in appendix C.

The output of the reconstruction on the event shown in figure 9.3 is shown below in figure 9.4.

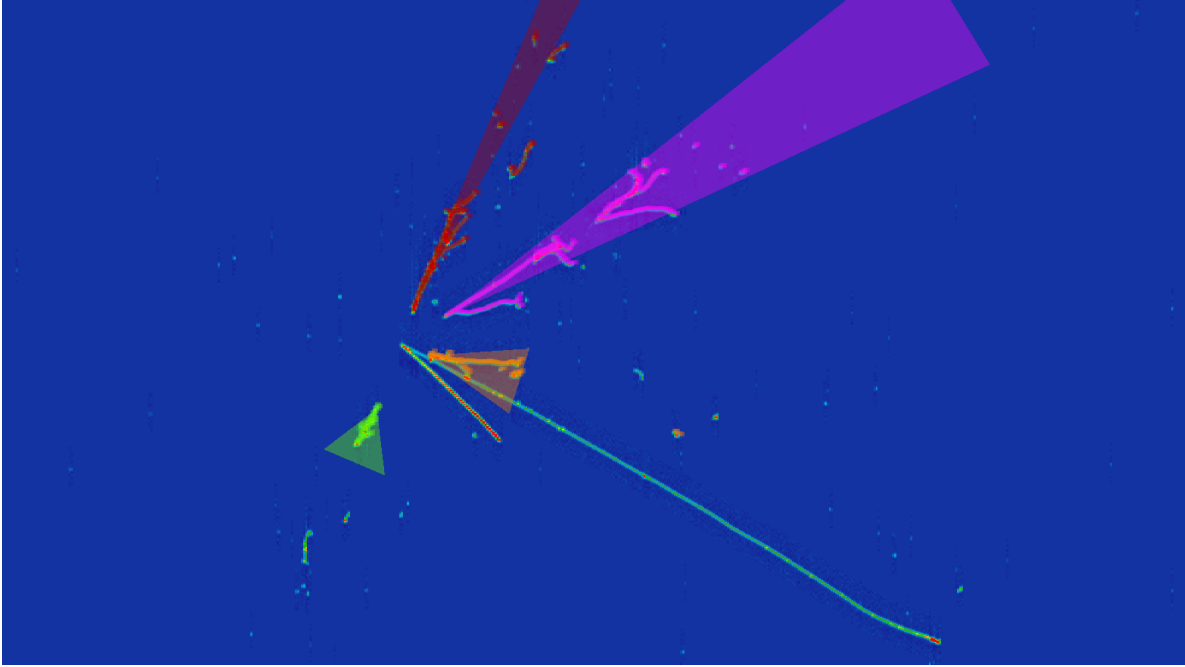


Figure 9.4: Event display of reconstructed EM showers from a $2 \pi^0$ CC ν_μ event. The four EM showers are reconstructed and represented in the image by triangles of different colors.

9.3.2.1 Shower Reconstruction Performance

The reconstruction performance is profiled in this section, with a focus on the quantities which have the most impact on the ability to identify π^0 events, and reconstruct their kinematics. These studies are performed on a simulated sample of CC $1\pi^0$ + cosmic events.

The efficiency for reconstructing γ showers is shown, as a function of the true γ energy deposited in the TPC, in figure F.11. Reconstructed-to-truth photon matching is performed by finding, for each true photon, the reconstructed shower with the most compatible 3D direction. The efficiency is shown for different requirements on the truth-reconstruction shower direction agreement. The significant energy dependence in the reconstruction efficiency is caused by the difficulty of reconstructing low energy EM showers due to the impact of hit-removal and the effort taken to ensure no low energy cosmogenic EM backgrounds are mistakenly identified as π^0 induced showers. While the reconstruction efficiency rises steeply and reaches 50% below 100 MeV, the considerable number of lower-energy γ showers from BNB π^0 events (see figure 9.2) is the main cause

for the overall low (an additional $\sim 30\%$ on top of the impact of the neutrino selection) CC π^0 selection efficiency, as estimated from simulation.

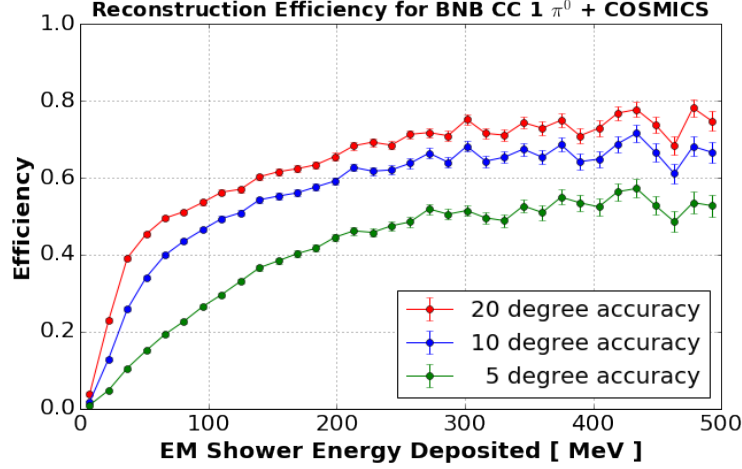


Figure 9.5: Reconstruction efficiency for photons from π^0 decay.

Because the reconstruction relies on the neutrino vertex to obtain the 3D shower direction, the angular resolution for reconstructed γ showers is quite accurate, with the mean, median, and truncated mean of the true-reconstructed angle difference values equal to 10.4, 5.0, and 3.0 degrees respectively. Finally, the energy reconstruction is profiled. The reconstructed vs. true γ energy is profiled to measure the reconstructed energy bias, as shown in figure 9.6. As a function of true energy, the truncated mean reconstructed energy is found, indicated by the red points in the figure. These points are then fit to a line, obtaining a slope of 0.79, indicating a bias of 21%.

Further studies of energy resolution are presented in appendix F.8.1, where the measured bias is corrected for and the fractional shower energy resolution measured. This is done by fitting the fractional energy resolution distribution to a Gaussian plus exponential tail distribution, to model the expected energy smearing and lossy processes which impact the reconstruction. These studies show a rather uniform energy resolution in the tens to 200 MeV photon energy, with a Gaussian smearing of $\sim 10\%$ and an exponential tail decay constant fit of $\sim 0.3-0.4$. The importance of lossy, non-gaussian smearing of the energy resolution on neutrino energy reconstruction is one of the significant aspects of EM shower reconstruction presented in this work.

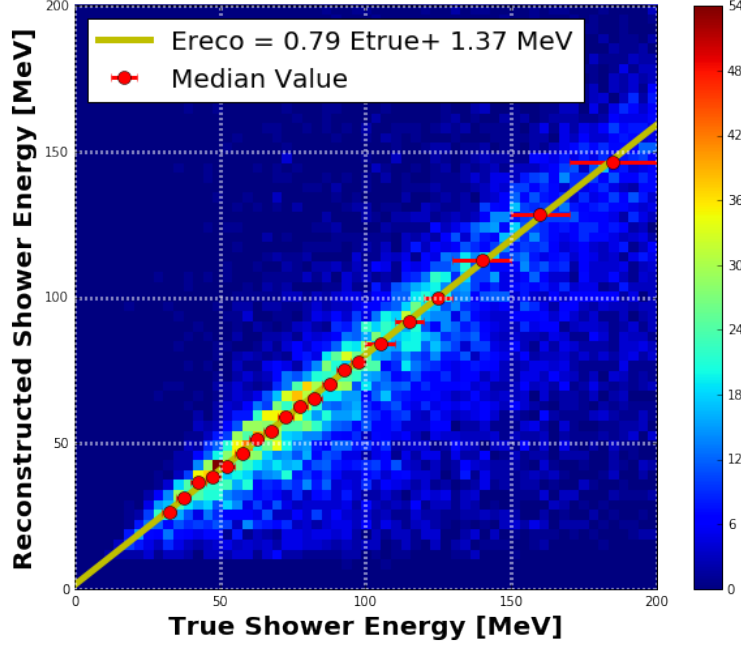


Figure 9.6: Reconstructed vs. true photon energy. Red points represent the obtained truncated mean of the distribution of reconstructed shower energies for each true energy bin. The yellow line is the result of a linear fit to the data-points.

9.3.3 π^0 Selection

This section describes the cuts applied to identify CC π^0 events, as well as the method by which the π^0 kinematics are reconstructed from the $\gamma\gamma$ pair's energies and angles.

All EM showers with less than 10 MeV of energy, and a conversion distance greater than 80 cm are ignored. Only events with two or three reconstructed EM showers which meet these requirements are considered. Events with four or more showers may indeed be CC π^0 interactions (some with two π^0 s in the final state) but often these events are associated with significant cosmic activity near the reconstructed neutrino vertex. The requirement of maximum three reconstructed showers therefore helps improve the purity of the selection. Other cuts applied are the following:

1. **20 degree minimum $\theta_{\gamma\gamma}$:** A minimum opening angle of 20 degrees is imposed for candidate photon pairs. This cut is motivated by the fact that for the energy spectrum of π^0 s expected, very few pions will produce a minimum opening angle smaller than this amount. Additional motivation is provided by the requirement imposed during the shower reconstruction 2D clustering step (F.4) that the two main photon clusters be separated by at least 15 degrees.

2. **4 cm maximum Impact Parameter:** A cut on the impact parameter ensures a degree of spatial correlation between the two photon showers. Because the reconstruction of 3D shower directions leverages significantly on the reconstructed vertex position, the impact on the selection is marginal. This cut primarily targets the removal of events with a poorly reconstructed vertex and/or shower direction.
3. **35 MeV minimum energy for larger shower:** A minimum energy on the larger of the two photon showers is imposed. The value, roughly half the minimum energy attainable by the higher energy photon ($M_{\pi^0}/4$) is partially meant to isolate background events (events with very small energy showers reconstructed) and partially aimed at removing entries where the π^0 kinematics and reconstructed mass would be significantly biased.

The impact of these cuts on the selection is described in table 9.1. By far the largest impact comes from the two-shower requirement, which removes $\sim 94\%$ of all events.

Table 9.1: Table evaluating Impact of Cuts on π^0 Selection.

Cut	5E19	ν selection	2 quality showers	angle, 35 MeV, and IP cuts
Events	525k	6,183	386	255

The 255 events left over in the sample are then visually inspected. They are split in signal and background categories. Signal events denote ones where a π^0 in the final state, produced at the neutrino interaction vertex, is recognizable. The breakdown for the selected events is shown in table 9.2:

Table 9.2: Breakdown of selected CC π^0 events broken down in various categories as determined by visual inspection.

Category	Events	Fraction
Total	255	1.00
Cosmic	40	0.16
ν other bkgd.	18	0.07
ν EM bkgd.	17	0.07
ν CC π^0	180	0.71
well reco'd	114	0.45

The selection produces a sample of ν_μ CC π^0 events with 70% purity. Of these events however, only $\sim 2/3$ are well-reconstructed. By this we mean that both photons have been correctly identified, even though not all the charge associated to them in the event may have been successfully clustered. In order to perform studies of EM shower development the 114 events identified as well-reconstructed π^0 candidates are selected. The following section explores in more detail the nature of the backgrounds selected.

9.3.3.1 π^0 Kinematics Reconstruction

The reconstructed photons associated with the π^0 decay can be used to measure its kinematics in a rather simple way: $E_{\pi^0} = E_{\gamma_1} + E_{\gamma_2}$ and $\vec{p}_{\pi^0} = \vec{p}_{\gamma_1} + \vec{p}_{\gamma_2}$. Two factors motivate us to explore alternative approaches to reconstructing the π^0 energy. The first is the fact that the $\gamma\gamma$ opening angle is strongly correlated to the π^0 energy, implying that use of this variable can potentially improve the accuracy of the energy reconstruction. The second is due to the non-gaussian energy resolution and biased energy measurement for photons caused by effects such as clustering and thresholding, discussed in detail in chapter 10. We re-arrange equation 9.2 as follows:

$$E_{\pi^0} = M_{\pi^0} \sqrt{\frac{2}{(1 - \alpha^2)(1 - \cos \theta_{\gamma\gamma})}} \quad (9.3)$$

with α denoting the energy asymmetry defined as $|E_1 - E_2|/(E_1 + E_2)$. The expression in eq. 9.3 makes use of the fact that the photons are known to originate from a π^0 decay and provides a measure of the energy which depends on the photon opening angle and the energy asymmetry α . This latter quantity, a unitless parameter which depends on the difference of the two photons' energies, helps mitigate some of the bias introduced on the reconstruction of each photon's energy. Figure 9.7 shows a comparison between the π^0 energy measured as the sum of the two photons' energies (blue), versus the resolution obtained with the energy definition of equation 9.3 (red). The FWHM of the distribution goes from ~ 0.5 to ~ 0.2 , and the distribution is rather symmetric, even without any additional bias correction applied.

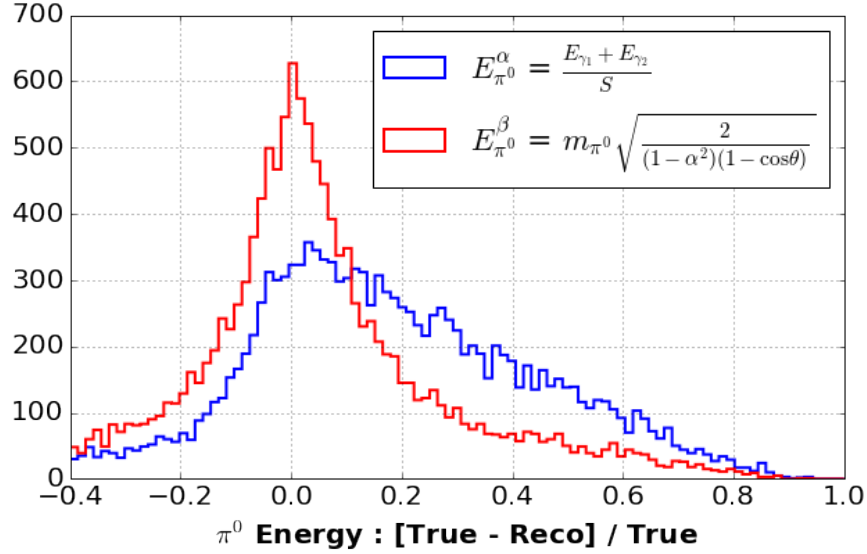


Figure 9.7: Fractional energy resolution computed on simulated CC π^0 + cosmic events with 1) in blue the π^0 energy defined as the sum of the two photon energies after accounting for a bias (S , equal to the slope of eq. F.5). 2) in red the same resolution using eq. 9.3.

9.3.4 Backgrounds To Selection

Examples of backgrounds from the selection on data are shown in figure 9.8. The displays show the hit-map surrounding the reconstructed neutrino interaction in black, the tagged vertex in red, and the reconstructed showers in orange and green. If a third shower was reconstructed in the event it appears as blue. The displays show: in figure 9.8a a cosmic-ray muon which has been “broken” in two tracks. EM activity surrounding the muon is tagged as γ s and mis-reconstructed as a π^0 . This category of background is the most common cosmic background. Figure 9.8b shows an event where a neutrino interaction has an incorrectly reconstructed vertex, which coincides with the conversion point of one of the two photons from a π^0 . This causes the shower reconstruction to fail, because it relies on the neutrino vertex for the charge-clustering stage. As a consequence the larger shower in the event is split in two. Figure 9.8c shows a neutrino interaction where EM activity by a $\mu \rightarrow e$ decay (green shower) is tagged as a π^0 photon. EM activity from muon decay caused by tracks from the interaction itself, or nearby cosmic poses a challenge to the selection due to the overlap between the Michel electron spectrum and the spectrum of the lower-energy photon produced by π^0 decay. Figure 9.8d shows an event where one of the photons from the charge-exchange interactions is split in two showers (orange and green) and selects as belonging to the

π^0 decay. Three photons are visible in this event. The one in blue is coming from the neutrino interaction, and a second photon from the interaction is present but was cut out from the image. Figure 9.8e shows an event where the neutrino vertex is well reconstructed and the two photons correctly identified. The photon shown in orange, however, overlaps a track and their charge is summed together incorrectly counting towards the photon's total energy.

9.3.5 Data-Simulation Comparisons of π^0 Kinematics

The selection presented in this section is applied to events from simulation and data. As described previously, a final filtering stage is applied to the data by visually inspecting reconstructed events to remove those cases in which the selected event does not contain a correctly identified CC π^0 event. The simulation employed consists of a sample of 50,000 CC ν_μ $1 \pi^0$ BNB interactions. No final visual inspection is applied to this already pure sample. For the distributions below, a final cut is applied on the ratio of the mass reconstructed after-to-before the containment energy correction. This ratio is required to be below 1.5, bringing the total number of entries to 100. Comparisons of reconstructed distributions for data and simulation are shown. Figures 9.9 and 9.10 show the reconstructed mass and conversion distance, respectively. Agreement in the energy scale in the former indicates good agreement on the π^0 energy reconstruction and photon energy loss modeling. A more quantitative discussion of these effects is presented in chapter 10. The measured conversion distance shows agreement between data and simulation, also pointing to a correct modeling of photon energy loss in the simulation.

Figure 9.11 provides comparisons of kinematic distributions related to π^0 production in neutrino interactions and are therefore of interest for the study of pion production and FSI modeling. Because the impact of the selection applied to produce events in data and simulation has not been accounted for, it is not possible to take these distributions as is to produce comparisons to the output of generators. Energies are not corrected to account for the biases observed. The agreement seen in the data and MC distributions can allow us to claim that overall broad agreement is seen, within the large statistical uncertainties present in the data.

9.3.6 Towards a Cross-Section Measurement

The performance of the reconstruction chain described in this chapter is such that ν_μ CC interactions from the BNB with a π^0 in the final state can be selected with good purity and reasonable effi-

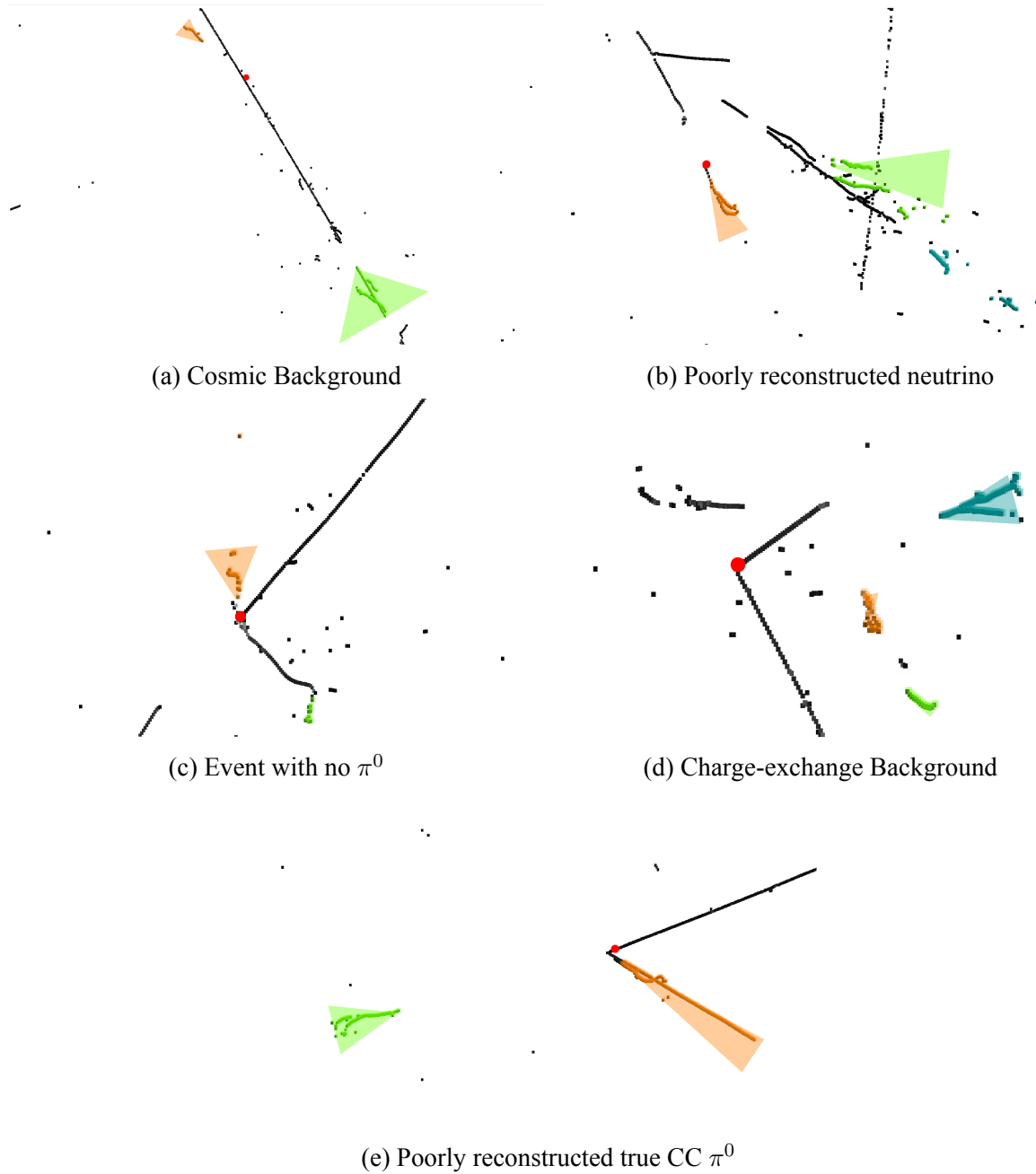


Figure 9.8: Backgrounds to CC π^0 selection. Black marks denote reconstructed hits. The red dot represents the reconstructed neutrino vertex. Orange, green, and blue cones, with the associated hits, represent the reconstructed showers.

ciency. This selection is currently being used to perform an integrated cross-section measurement for this channel. Systematics associated to the neutrino selection and other aspects not pertaining to the topic of this work are currently being studied. More work is required in order to bring the selection and reconstruction to a state where a larger fraction of selected events not only have a π^0

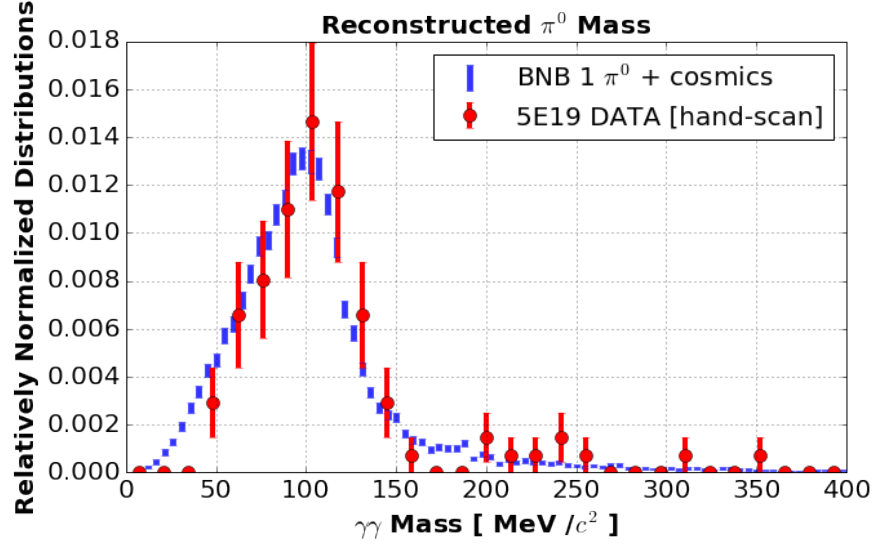


Figure 9.9: Comparison of reconstructed π^0 mass for data and simulated events. No energy reconstruction bias correction is applied, causing the shift from the known mass of 135 MeV. A more quantitative discussion of the bias, and thorough comparison of data and simulation are provided in chapter 10.

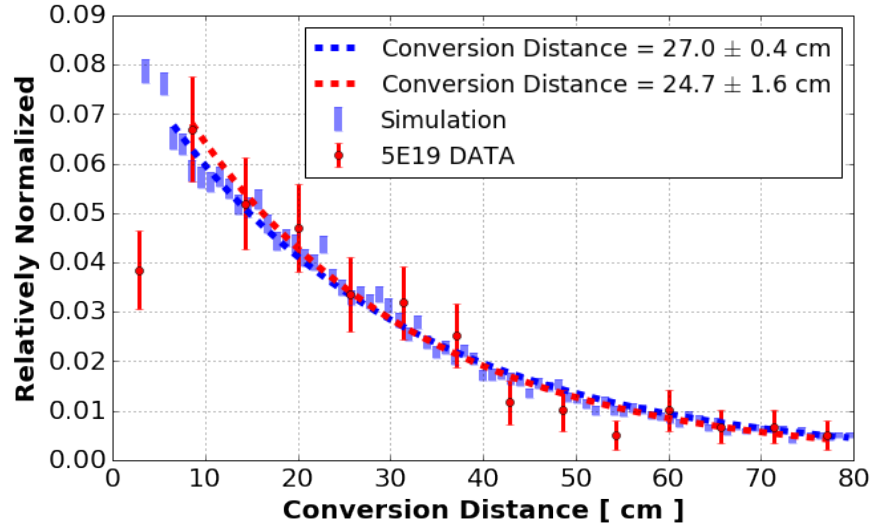


Figure 9.10: Reconstructed conversion distance for photons from data and simulation.

in the final state, but have both photons from that π^0 be correctly identified and reconstructed. The main limitation to this currently lies in the performance of the track-shower separation reconstruction step. While the current implementation allows for a significant removal of non-EM induced charged in the vicinity of the neutrino interaction, further improvements in removing EM activity deposited by uncorrelated cosmic-ray activity, as well as in dealing with confusing topologies due

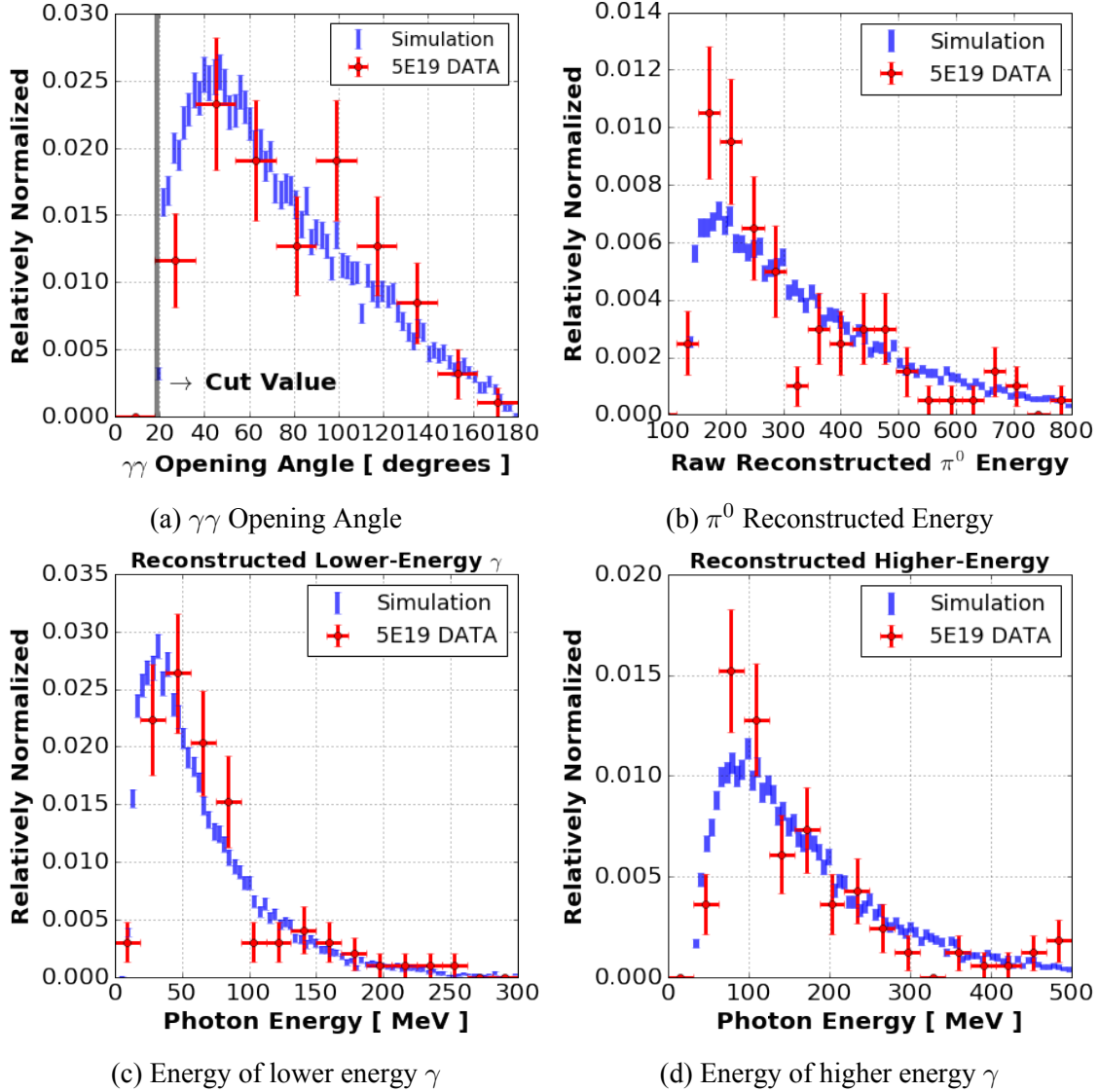


Figure 9.11: Data-MC comparisons of reconstructed kinematic distributions for (a) $\gamma\gamma$ opening angle, (b) π^0 energy, measured as defined in eq. 9.3, (c) lower energy photon and (d) higher energy photon energies. The distributions of the lower and higher energy photon energies shown are not corrected for energy biases.

to 2D overlap of particle energy deposition is needed. A reconstruction approach that relies more heavily on 3D topological information for this reconstruction step would be able to achieve this. The limitations of the current selection and reconstruction motivated the final “visual-scanning” stage applied in the selection. We have shown that it is possible to reconstruct the π^0 kinematics with high accuracy. This will allow to perform differential (in π^0 energy, for example) cross-sections and other studies which are crucial in order to get to the bottom of the nuclear physics

which has a strong impact on systematics related to oscillation analyses. The preliminary agreement between data and simulation of figures 9.9, and 9.10 are a promising step towards this goal. Finalizing the selection such that it does not rely on visual inspection of the tagged events will allow to have better control of the selection biases and allow to make conclusive claims on FSI and other effects in argon.

Chapter 10

Studies of EM Shower Energy

Reconstruction with π^0 induced Photons

This chapter contains two sections. The first (10.1) explores the causes for an observed bias in the measured energy of EM showers from π^0 s obtained from the selection of chapter 9. This is found to be due to the incomplete collection of charge deposited in the TPC due to thresholding effects and charge-clustering in the reconstruction. The impact of these effects is measured in the simulation, and this measurement is compared to the reconstruction applied to data. We show that the sources of bias in measuring the shower energy are understood and can therefore be accounted for in the calibration. The second section (10.2) of this chapter is dedicated to a more detailed study of energy loss in EM showers from photons produced in π^0 decays. We bypass the clustering stage of the automated EM shower reconstruction, performing this task manually, in order to better quantify the intrinsic limitations of EM shower reconstruction in LArTPC detectors. The reconstructed photons obtained in this manner allow additional studies which profile the energy loss of EM showers in data.

In both sections presented here we stress the impact that lossy processes have on the energy reconstruction of EM activity caused by the particular nature of how electrons and photons lose energy as they propagate and on the impact of detector and reconstruction effects. These effects lead to biases in the energy reconstruction and an asymmetry in the reconstructed minus true energy distribution. In order to account and model these effects we choose to employ a Gaussian plus exponential distribution (described in appendix G) to study the energy reconstruction bias and res-

olution. Neglecting the impact of the asymmetry of the energy reconstruction can have significant consequences for the systematics of the neutrino energy reconstruction.

10.1 Study of Energy Reconstruction Biases in EM Shower Reconstruction

Biases in the energy reconstruction of EM activity must be understood in order to be correctly accounted for. In this section results from simulation are used to quantify the impact of lossy processes in EM shower reconstruction, and these are compared to measurements of the reconstructed π^0 mass in data. We conclude this section by commenting on the impact these effects have on the non-Gaussian nature of the smearing of the energy resolution.

10.1.1 Thresholding

MicroBooNE's signal-to-noise ratio on the collection plane allows for low detection thresholds for signals on the TPC wires. The TPC signal reconstruction has been optimized to be efficient at collecting signals from MIP-like energy deposition on the Anode-plane wires, while not creating spurious hits from detector electronics noise. EM showers will, as they cascade, produce very low energy photons which may lead to local energy depositions smaller than the applied threshold. This will cause a certain fraction of the initial photon's energy to go undetected, and contribute to a bias in the reconstructed shower energy. Figure 10.1 shows the energy spectrum of reconstructed one-hit clusters associated with γ showers. A hit-threshold of 0.27 MeV is measured from this distribution.

We estimate the impact of this effect by studying the output of MicroBooNE's reconstruction on simulated EM shower events. For these events, we integrate the true energy associated to reconstructed hits on the collection plane, and compare this amount to the true total photon energy. The difference between these quantities is a measure of the energy bias attributable to thresholding. Figure 10.2 shows the fraction of charge recovered, after hit thresholding is accounted for, for showers of different energies. The distributions are fit to a Gaussian plus exponential distribution [87], to better model the biased impact of thresholding on calorimetric energy reconstruction. A discussion of this function is presented in appendix G. We note that the fraction of energy lost

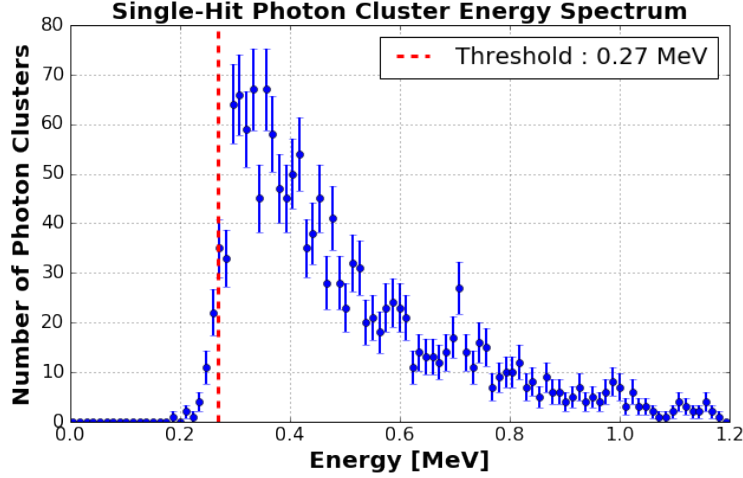


Figure 10.1: Energy spectrum for one-hit reconstructed photon-clusters associated with γ EM showers. The distribution has a sharp turn-on at ~ 0.3 MeV, while the true photon distribution continues to grow at lower energies. The hit-threshold is measured to be 0.27 MeV, which is the value at which half the peak-value is reached in the sharp up-rise.

to hit thresholding is fairly independent of shower energy. The fitted Gaussian gives a mean of approximately 93%, with a width of 3-6%. The average energy loss across the entire distribution, accounting for entries in the tail, is $\sim 86\%$. The impact of hit thresholding on the reconstructed π^0 mass is similar, causing a bias of 8% in the peak which shifts from 135 to 124 MeV.

10.1.2 Clustering

In this section we rely on the clustering approach described in appendix F and apply it to a sample of simulated π^0 events in order to evaluate the impact of charge-clustering on γ energy reconstruction, the bias in the energy measurement which this leads to, as well as the impact on the reconstructed π^0 mass.

For each reconstructed shower we measure the ratio of true energy associated to the clustered hits to the true energy deposited by the γ in the TPC volume. The distribution of this ratio is shown in figure 10.3. The Gaussian plus exponential fit returns a mean of 89% and 6% Gaussian width, with an exponential constant of 0.3, indicating that roughly 50% of entries are not fully modeled by the Gaussian distribution. The median of the distribution at 81% indicates that approximately 20% of the shower energy is lost due to clustering. As for hit-thresholding, the dependence of clustering on photon energy is studied. A variation of $\sim 5\%$ on the fitted mean μ is observed in a 50-200 MeV energy range, with higher charge-collection efficiency of 92% at 50 MeV compared to 88%

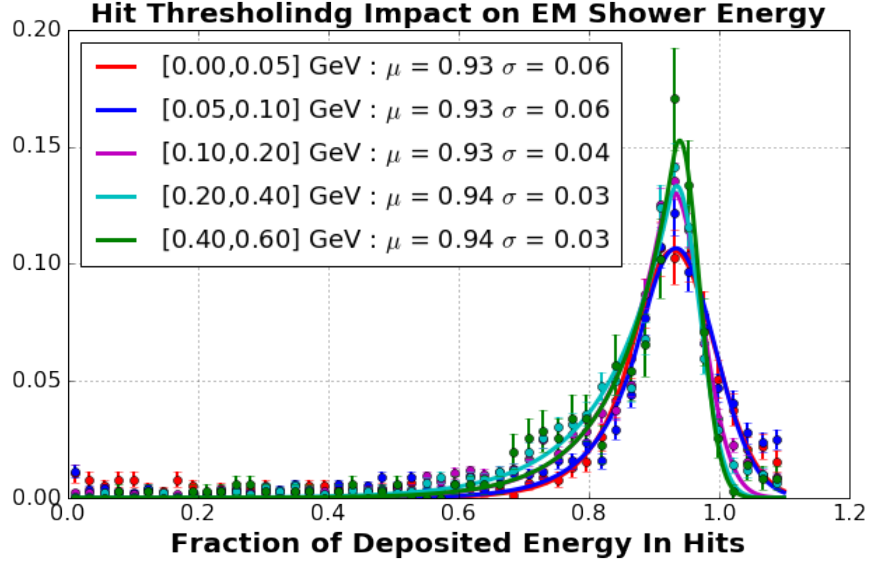


Figure 10.2: Impact of hit thresholding on energy collected from EM showers in the TPC. Simulated EM shower events are binned according to the fraction of energy which they deposit associated with reconstructed hits. The missing energy therefore measures the impact of hit-thresholding. Different distributions are for showers of different energy. Data is fitted to a Gaussian plus exponential negative tail.

at 200 MeV. The impact of energy containment was accounted for. The impact of clustering on the reconstructed mass in a full CC $\pi^0 \nu_\mu$ + cosmics simulation can be seen in figure 10.4.

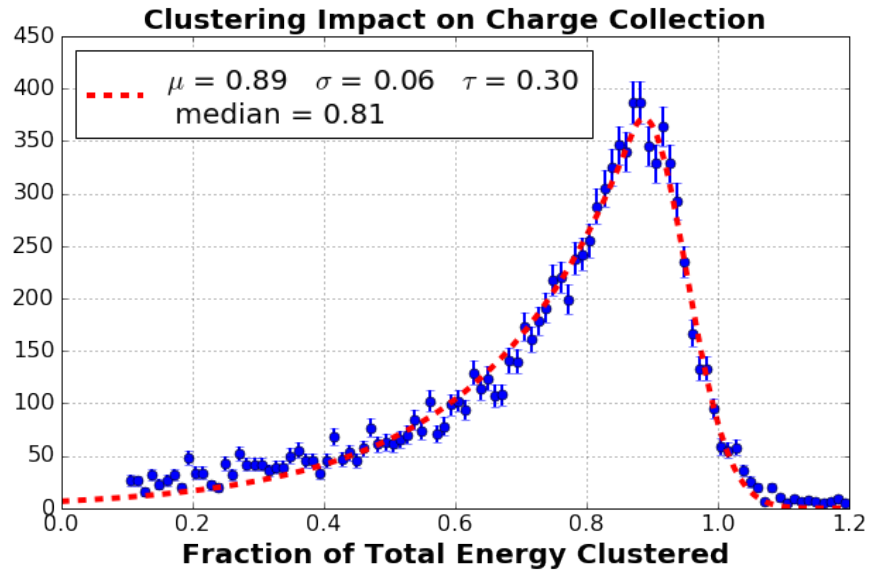


Figure 10.3: Fraction of energy associated to hits selected by the reconstruction as belonging to a γ over the true energy deposited within the TPC. Study performed on photons from a single π^0 simulation. The distribution is fit to a Gaussian plus negative exponential tail function.

The additional bias introduced by charge-clustering on the reconstructed energy shifts the reconstructed mass from a peak of 124 to 105 MeV (roughly 14% additional bias on the true value). The largest impact however is on the negative tail of the distribution. The exponential tail of the Gaussian plus exponential fit shifts from encompassing roughly 30% of all entries when only hit-thresholding is considered, to approximately 60% in the case of clustering. The median shifts from 121 MeV to 97 MeV, an added bias of $\sim 18\%$.

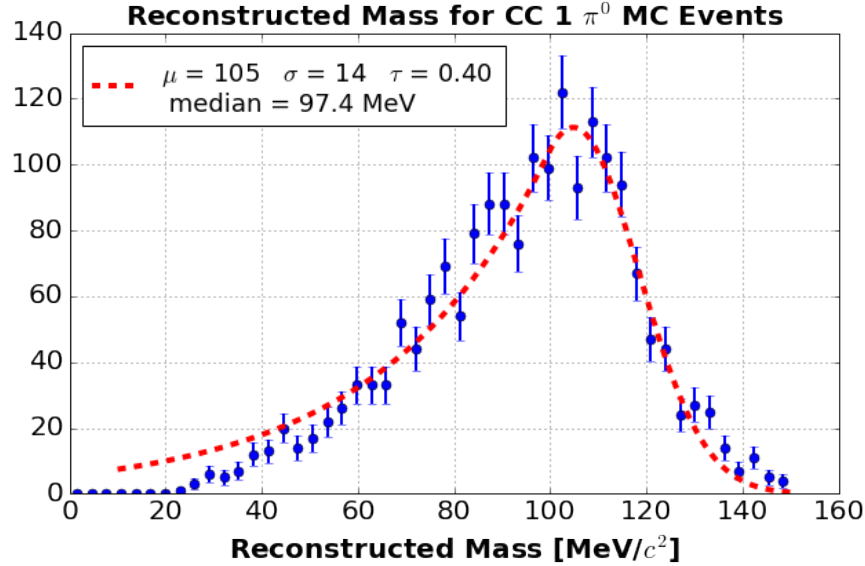


Figure 10.4: Mass distribution from simulated CC 1 π^0 events plus cosmics on which the π^0 selection of sec. 9 is applied, in addition to a cut on the difference between the true and reconstructed photon direction for both γ s, which must be below 5 degrees. The distribution is fit to a Gaussian plus negative exponential tail function.

10.1.3 Bias Correction

We find that the energy reconstruction for EM showers presented in this work is associated with a bias contributed by thresholding and clustering effects. The first account for a bias of approximately 7%, with a further 14% due to clustering. Thresholding is found to not be dependent on the shower energy, and causes little smearing in the recovered energy. Clustering, on the other hand, has a more significant impact on the energy resolution. The reconstructed π^0 mass spectra obtained from data and our simulation are shown in figure 10.5 before any energy correction is applied.

When accounting for the measured bias in the simulation, as quantified by the fitted mean of the gaussian in figure 10.4, as well as the statistical error on the fitted mean from the data, and the

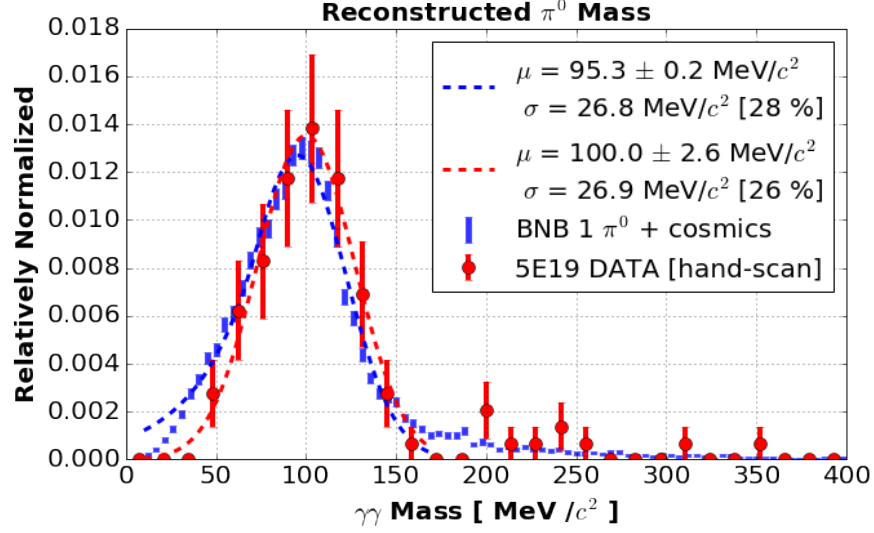


Figure 10.5: Data (red) and simulation (blue) overlay of reconstructed π^0 mass distribution. Data events come from the neutrino plus π^0 selection described in sec. 9 with a final hand-selection step. Simulation is obtained from a sample of true CC π^0 events with simulated cosmic overlays. No quality cuts are applied to the simulated sample.

systematic uncertainty associated with the calorimetric energy reconstruction obtained in section C, we recover a π^0 mass of:

$$M(\pi^0)_{\text{corrected}} = 128.7 \pm 3.3 \text{ (stat.)} \pm 4.0 \text{ (syst.) MeV}/c^2. \quad (10.1)$$

The reconstructed value falls within error of the true π^0 mass. The difference between the true value and the reconstructed one is of the same order of the difference between the data and monte carlo, and is of order 5%. The deficit in the simulation with respect to the data is predominantly caused by the fact that the simulated π^0 distribution has no hand-selection stage applied which removes events with poorly reconstructed π^0 s, which tend to push the mass distribution to lower values. Requiring that both photons be reconstructed within 20, 10, and 5 degrees of truth, and applying the same fits leads to values of μ of 97.2, 97.5, and 99.3 MeV respectively, largely alleviating the tension between data and simulation.

10.1.4 Non-Gaussian Energy Smearing

The same effects which contribute to biasing the shower energy measurement play the dominant role in smearing the energy resolution. The nature of these effects produce a non-gaussian smearing

of the energy resolution, as was shown in section F.8.1. This has motivated the use of a gaussian plus exponential function to fit the fractional energy resolution and reconstructed π^0 mass peak distributions. The significant fraction of events not modeled by the gaussian alone (30% from the impact of hit-thresholding, and 60% for the full impact of clustering plus hit-thresholding) will play an important role in the energy reconstruction of ν_e events.

10.2 Hand Clustering

In order to study in more detail the impact of charge-clustering on the reconstruction of EM showers in a surface LArTPC we apply a second reconstruction technique to selected π^0 events which substitutes the automated clustering (F.4) and matching (F.5) with a human hit-tagging step which selects reconstructed hits on different planes associated with the same EM shower, and which can then be fed to the 3D shower reconstruction algorithms described in sec. F.7. The input to this reconstruction approach consists of events selected from the CC π^0 selection described in sec. 9.3 as well as a sample of hand-scanned neutrino interactions which contain a π^0 in the final state. For these events the π^0 decay point is also reconstructed by tagging the location of the interaction vertex on two different planes. This allows to obtain accurate vertex information even for those events from the neutrino selection where the vertex may have been incorrectly tagged, and additionally allows to reconstruct EM showers from π^0 s produced in charge-exchange interactions. A study of the tagging accuracy for π^0 vertices done comparing the tagged vertex location to the true neutrino interaction point in CC π^0 simulated events allows us to estimate the vertex resolution to be of order 0.9-1 cm.

Unlike for EM showers reconstructed following the procedures of sec. F, no cuts are applied during the shower reconstruction steps. Additionally, the minimum opening angle, maximum conversion distance, and maximum IP cuts imposed are also not applied here. When reconstructing π^0 candidates from events with four EM showers we study all three shower-pair combinations and choose the combination which minimizes the reconstructed π^0 mass obtained from the two shower-pairs in the event ¹.

¹The bias in the reconstructed mass obtained due to an under-estimation of the EM shower energies is accounted for by minimizing the difference of the masses reconstructed by the two EM shower pairs to the peak of the reconstructed π^0 mass obtained with events in which a single π^0 is present

The reconstructed π^0 mass for the 223 candidate events obtained via the human hit-tagging reconstruction is shown in figure 10.6. The deficit with respect to the true π^0 mass is substantially smaller than that obtained for the automated reconstruction, heavily impacted by charge clustering, of figure 10.5.

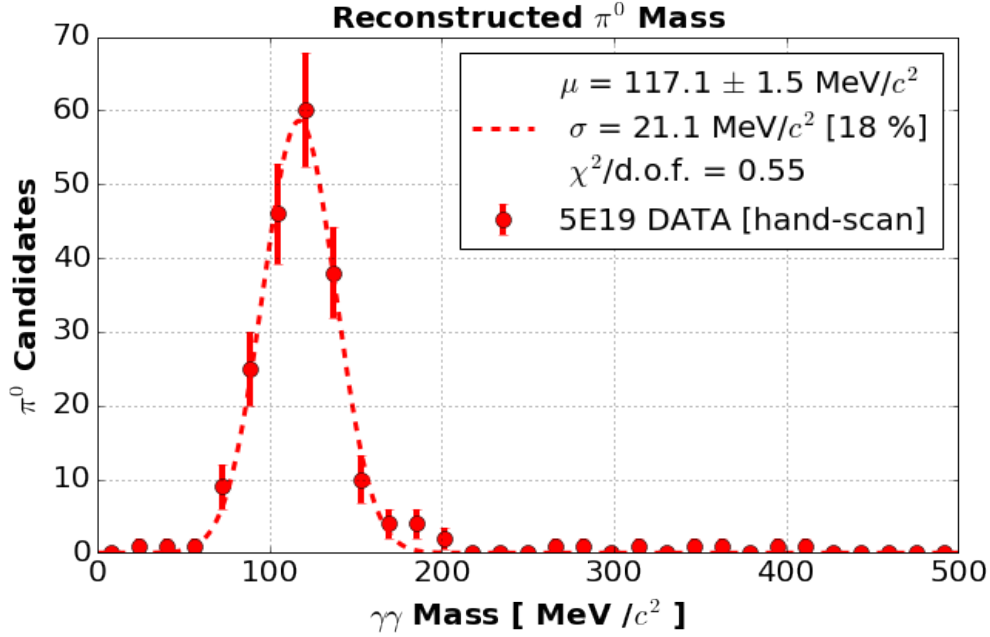


Figure 10.6: Hand-clustered π^0 mass from ν_μ CC events. Distribution is fit to a Gaussian.

When no containment correction is applied, the zoomed-in mass distribution shows similar features to those observed when studying the impact of hit-thresholding (figure 10.7). The distribution is fit to a gaussian plus exponential, from which we obtain a gaussian resolution of 13%.

For the γ showers obtained from this sample we show the measured conversion distance in figure 10.8. The exponential fit of 23 ± 2 cm, obtained by fitting the data in the range 10-80 cm, is in agreement with the expected absorption length for γ s in argon shown in figure 6.6, which ranges from 26 to 20 cm in the energy range 50-200 MeV. The fact that the fit result gives a smaller conversion distance, closer to the theoretical value, than what obtained in figure 9.10 is due to the bias introduced in the automated reconstruction by the occasional removal of charge at the start of the shower formation from the track-shower hit-removal reconstruction step.

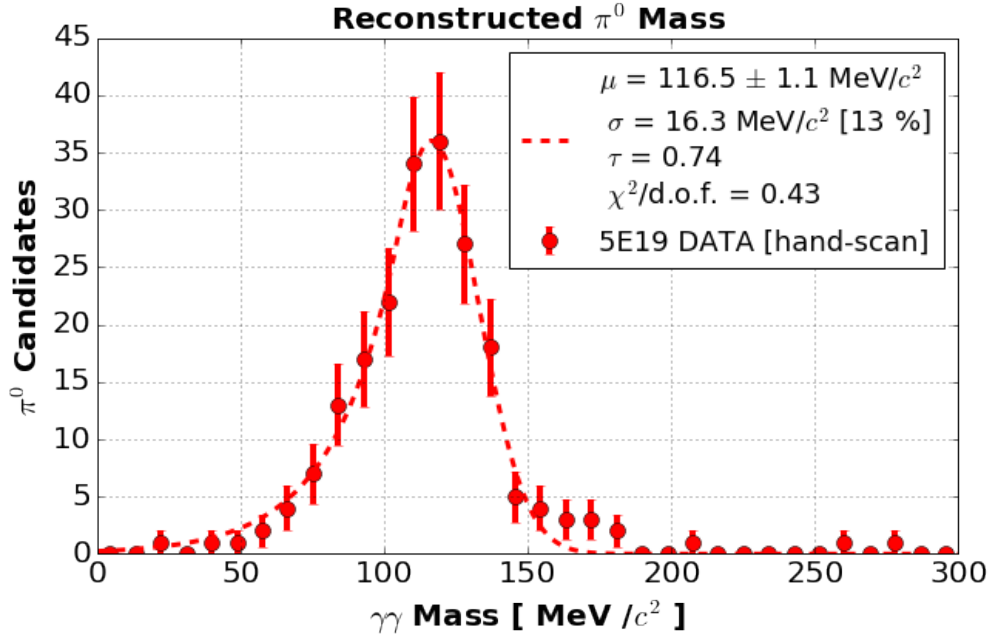


Figure 10.7: Reconstructed π^0 mass distribution, with no containment correction, fit to a Gaussian plus exponential distribution.

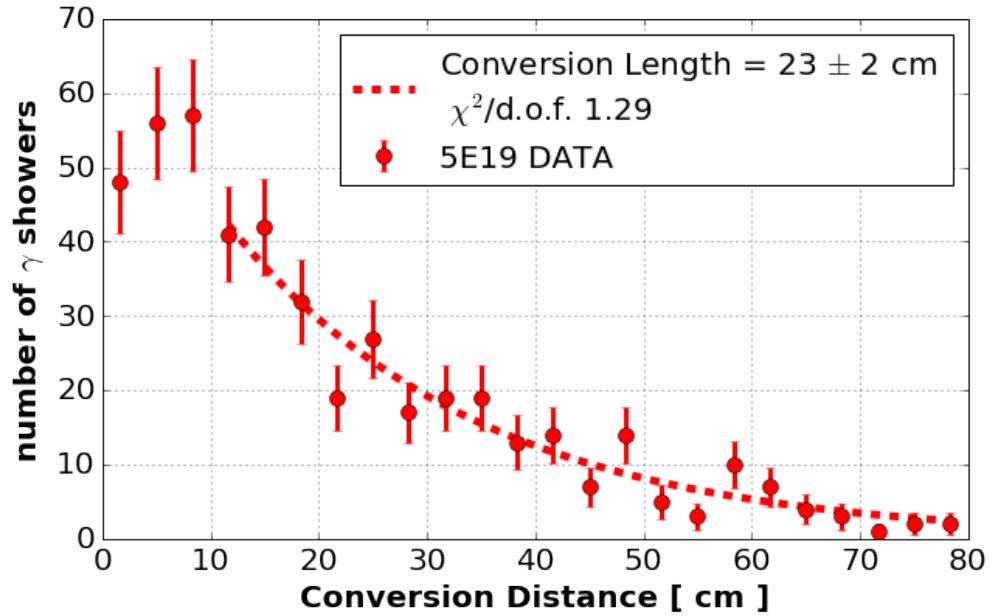


Figure 10.8: Conversion distance for reconstructed γ showers.

10.2.1 Accounting for Missing Energy

The measured π^0 mass of figure 10.7 obtained from the gaussian component of the fit is still deficient compared to the true value of 134.98 MeV. While the hand-tagging applied to reconstruct

the γ showers was meant to remove the impact of clustering on estimating the γ energy, any effect due to hit thresholding would still be present. In section 10.1.1 a bias in measuring the γ energy of 8% was attributed to hit-thresholding effects. Accounting for this additional bias we obtain a measurement of the π^0 mass of:

$$M_{\pi^0} = 126.9 \pm 1.2 \text{ (stat.)} \pm 4.0 \text{ (syst.) MeV.} \quad (10.2)$$

Accounting for the second major cause for energy bias after clustering, the reconstructed mass value now falls, within uncertainty, close to the true value. The residual 2% discrepancy can be attributed to effects not considered such as missing energy from unresponsive wires, and a residual bias caused by deficiencies in the hand-clustering applied.

10.2.2 Additional Studies of the Energy of π^0 EM Showers

The hand-reconstructed photons obtained from the π^0 sample presented in this section are used to profile their radial and energy distributions. This presents a data-driven measurement of the development of EM showers in argon. The sample of “hand-reconstructed” photons largely overcomes the issue of charge-clustering, but is still impacted by several effects which introduce biases in the measurements shown. These need to be carefully considered when interpreting such results. We outline these effects in the following points:

1. Only energy associated to reconstructed hits is used to measure the photon energy, implying that hit-thresholding biases in the energy measurement are still present.
2. Shower containment corrections are not applied, meaning that escaping charge is not accounted for in the following studies.
3. Dead wires impact the energy measurement and radial profile of EM showers. This is also not accounted for. The fact that dead-wire regions are uncorrelated with the position of the photon showers means that on average their presence will not impact the radial profiles shown.

We study the EM showers in the sample by measuring the radial profile of their energy deposition, and the spectrum of individual photons which make up each EM shower.

EM Shower Radial profile The radial profile of each EM shower can be studied by measuring the fraction of all energy associated to it as a function of the integration radius R . For this study we select the subset of showers which are measured to have a containment distance greater than one meter. We study the radial profile of photons as a function of the radial distance from the photon conversion point (EM shower start point) in figure 10.9, and as a function of the reconstructed neutrino vertex in figure 10.10. These studies are performed in bins of reconstructed shower energy. The data points shown indicate the median fraction of shower energy collected for different integration radii. The error bars represent the spread in fractional containment. These intervals are asymmetric due to the asymmetric nature of the distributions and are built by requiring that they include half the entries above (below) the median for the upper (lower) error bars.

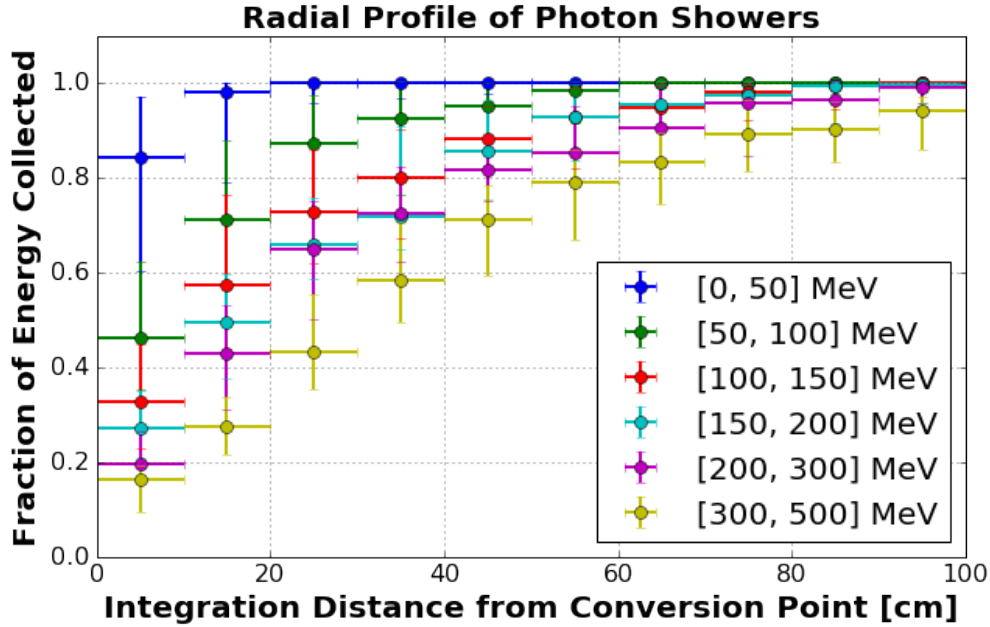


Figure 10.9: Fractional containment of reconstructed shower energy for showers in different energy ranges. For showers of a given energy, the median fraction of charge contained within a certain radius is calculated. The denominator in this fraction is the total charge associated to the shower as obtained from the hand-clustering step. The error bars represent the spread in fractional containment. These intervals are asymmetric due to the asymmetric nature of the distributions and are built by requiring that they include half the entries above (below) the median for the upper (lower) error bars.

The π^0 reconstructed mass distribution can provide us with a quantitative estimate of the impact of a radial integration cut on the shower energy bias (peak location) and resolution (distribution width). We calculate the π^0 mass using the reconstructed opening angle, and the energy associated

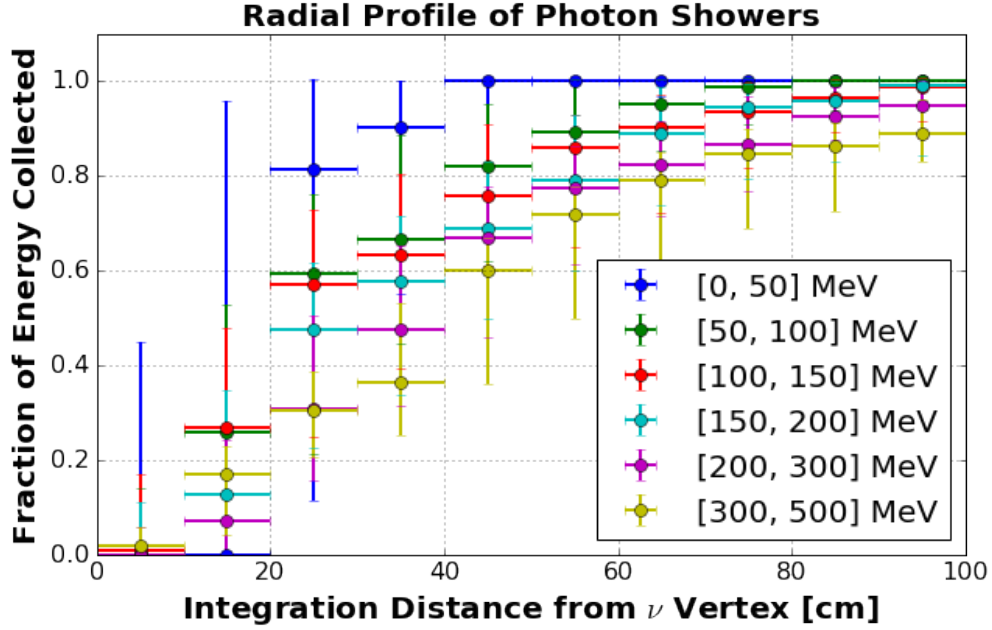


Figure 10.10: Same as figure 10.9, but now measuring the radial integration distance starting from the neutrino interaction vertex, rather than the reconstructed showering point.

with each shower up to an integration distance R . The reconstructed mass values obtained are used to estimate the bias in energy, quantified by the fractional difference between the median reconstructed mass and the true π^0 mass, and the spread in the π^0 distribution, measured as the symmetric interval surrounding the median reconstructed value necessary to contain 50% of entries, over the median. The bias and resolution as a function of different intergration radii are shown in figure 10.11.

Shower Photon Energy Spectra Each reconstructed EM γ shower manifests itself in the detector as a cascade of successively lower energy electrons and positrons. The energy spectrum of these individual electrons and positrons will provide useful in addressing the impact of energy thresholds which may be applied to the reconstructed individual electrons. Figure 10.12 shows hits from an example EM shower from the data divided in individual electron/positron clusters. For each an energy is measured integrating the charge associated with the cluster's hits. Each reconstructed cluster represents a contiguous portion of deposited energy.

Figure 10.13 shows the energy spectrum of individual clusters reconstructed from the sample of hand-reconstructed π^0 events. The larger figure shows the spectrum up to 30 MeV on a log-

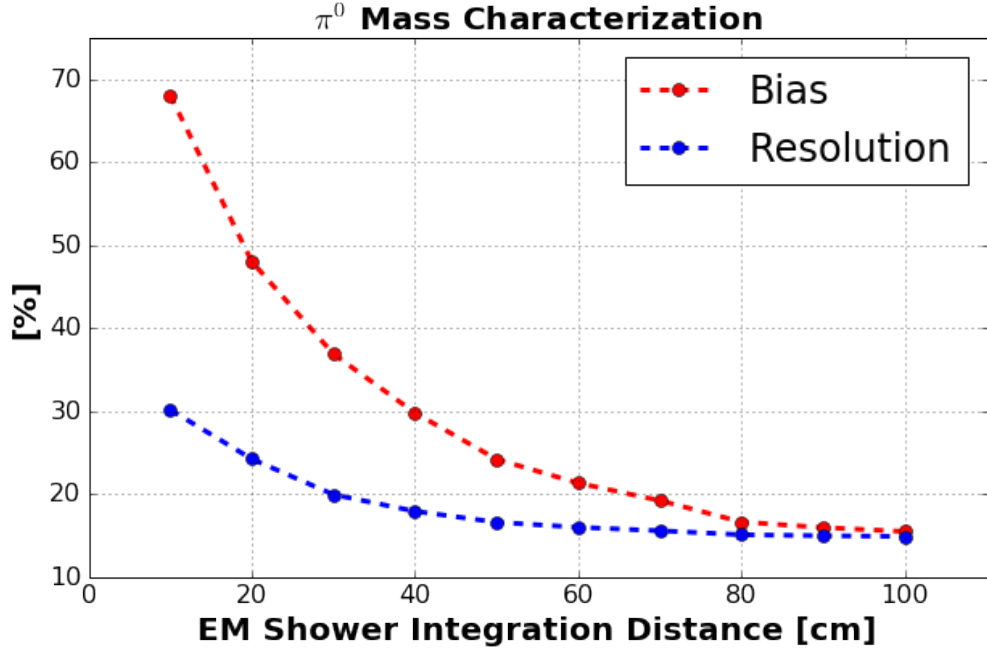


Figure 10.11: Measured bias and resolution on the reconstructed π^0 mass as a function of the total integration radius R for EM shower energy reconstruction. The bias is given by the percent difference between the median reconstructed mass and the true value. The resolution is given by the width of the interval surrounding the median which contains 50% of all entries, divided by the median itself.

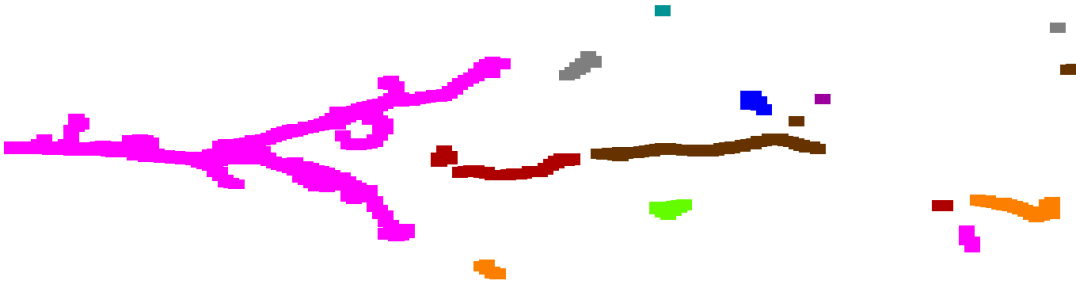


Figure 10.12: Example of reconstructed γ subdivided in individual photon-clusters.

scale, while the insert in the top-right focuses on the 0-3 MeV region, and is drawn on a linear scale. The cutoff at ~ 0.3 MeV is due to hit-thresholding. Three rapidly falling populations are found, one falling off rapidly up to ~ 0.6 MeV, the next going up to ~ 4 MeV, followed by a slower declining distribution. The low-energy and high-energy portions of the spectrum are fit to

exponentials separately in figure 10.14.

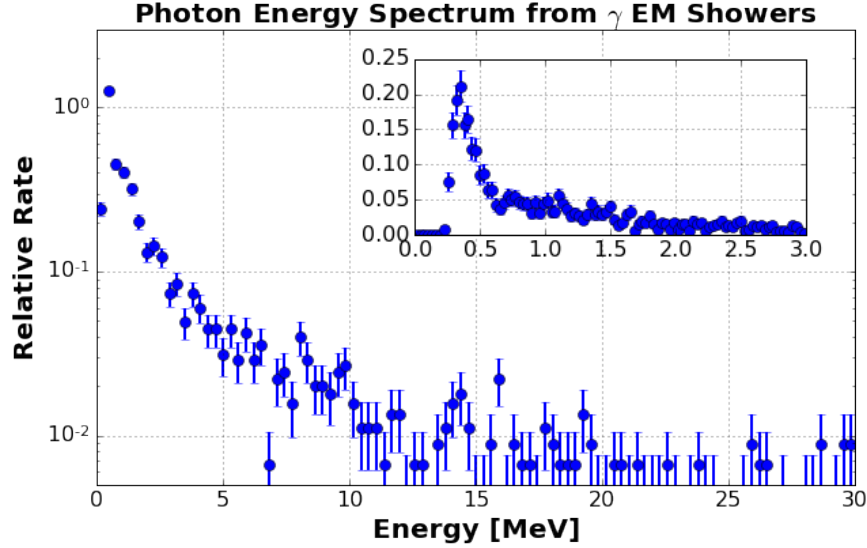


Figure 10.13: Energy spectrum of individual photons in reconstructed EM showers.

The energy spectra and exponential fits shown in figure 10.14 along with their residuals model the data reasonably well. The three exponential constants we obtain are $\tau_0 = 0.1 \pm 0.01$ MeV, $\tau_1 = 1.28 \pm 0.13$ or 1.06 ± 0.14 MeV from the fit in the lower and higher energy subsets respectively, and $\tau_2 = 7.8 \pm 1.5$ MeV for the highest energy portion of the spectrum. The fits to τ_1 from the lower and higher energy spectra agree within the uncertainties on the fit.

As was done for the integration radius R , the fraction of energy recovered for each EM shower is measured as the threshold on the minimum photon cluster energy is increased. Figure 10.15 shows the fraction of total EM shower energy collected as the threshold is increased. Data points represent the median value for showers in the various energy ranges, and the error-bars represent the asymmetric interval which contains 50% of all showers.

As before, we rely on the reconstructed π^0 mass distribution to extract a quantitative measure of the impact of different photon-cluster energy thresholds on the width and bias. Figure 10.16 shows the change in bias and mass-peak resolution as the threshold is increased up to 10 MeV. We note that while the π^0 mass width does not change significantly, the bias goes from roughly 13% to $\sim 23\%$.

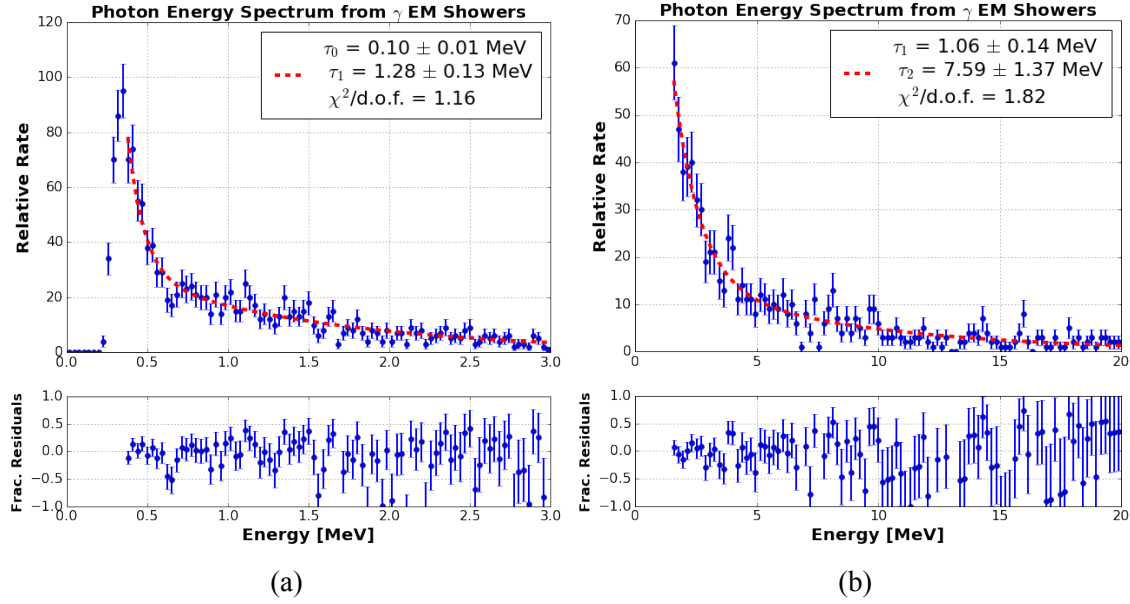


Figure 10.14: Fitted energy spectrum of individual photons from EM showers.

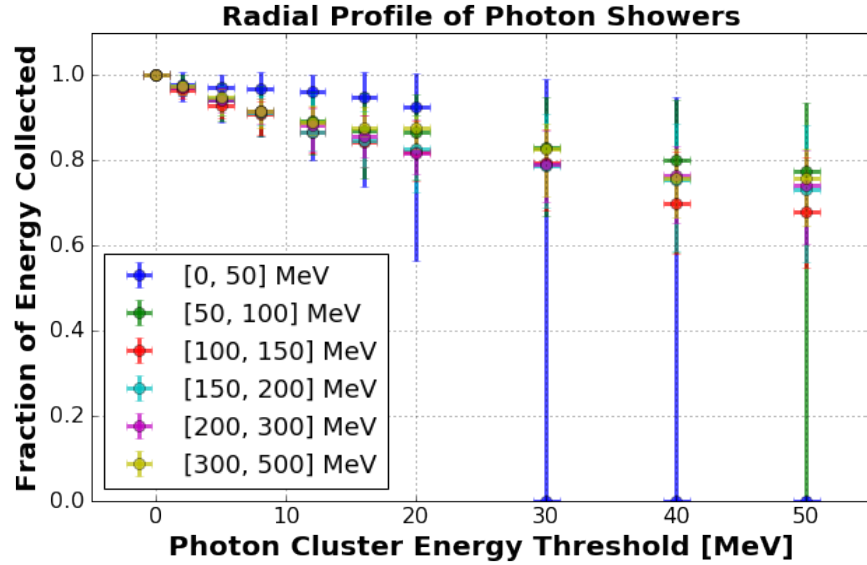


Figure 10.15: Fraction of energy energy collected for EM showers vs. photon energy threshold.

10.3 Conclusions

In this chapter we have explored the biases and smearing which affect the energy reconstruction of EM activity in LAr by studying a sample of photons from π^0 decay. We find good agreement between data and simulation within the limitations presented throughout the chapter. Simulation studies indicate that the impact of a ~ 0.3 MeV hit-reconstruction threshold on biasing the energy

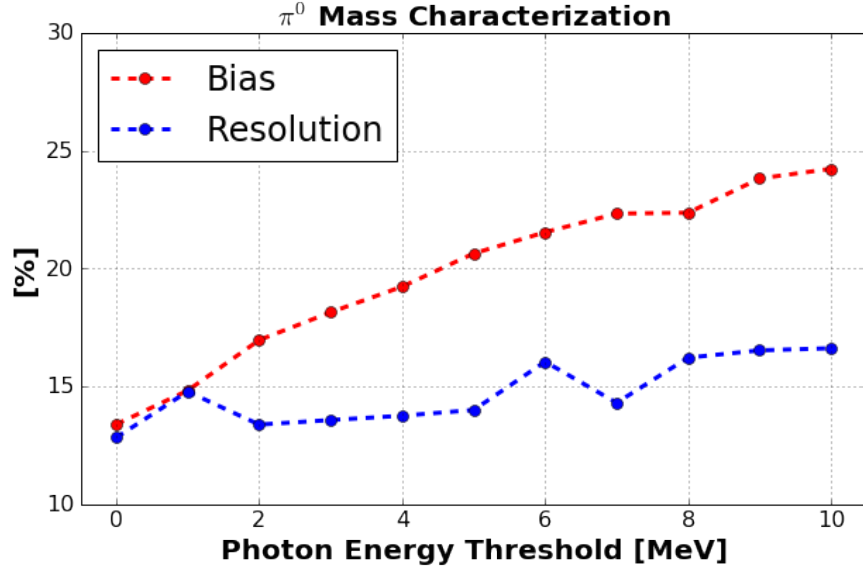


Figure 10.16: Bias and resolution on reconstructed mass vs. photon threshold.

measurement is of order $\sim 8\%$, with a smaller impact on the energy resolution ($\sim 3\%$). The impact of clustering, as performed for this analysis, has a more pronounced effect on both the bias and resolution for EM shower reconstruction, and brings the overall bias in the reconstructed mass to $\sim 23\%$.

The same sources of energy bias are the main contributors to a loss in energy resolution. Due to their nature they lead to significant non-gaussian smearing, which we have modeled using a gaussian plus exponential fit. The biased and non-gaussian nature of the calorimetric energy reconstruction of EM showers will impact energy reconstruction for ν_e interactions. Currently such effects are not being accounted for in simulation studies of ν_e oscillation sensitivity measurements such as [28] or [39].

By largely bypassing the impact of clustering on the reconstruction we are able to profile the energy loss of photons in LAr and measure the impact of various effects on their energy reconstruction. This study produces a π^0 mass distribution with a bias of 13% and an 18% gaussian resolution, a significant improvement to that obtained through the fully-automated reconstruction due to the lack of smearing from clustering. We find that hit-thresholding accounts for almost the total deficit in energy observed, with a residual 2.5% contributed by secondary effects such as energy lost due to dead-wires. The energy spectrum of individual electrons and positrons produced in EM showers is measured, and the impact of a radial and energy cut on the shower reconstruction

measured by studying the bias and resolution of the obtained π^0 mass-peak.

The accurate estimation of energy bias in EM shower reconstruction depends on a precise calorimetry. Uncertainties on the calorimetry which impact EM shower energy reconstruction are discussed in appendix C. A 3% systematic in the electronics gain, (section C.2), and the impact of ion recombination on EM energy deposition (section C.4) are the current limitations to obtaining EM shower energy measurements with higher accuracy. Concerning the impact of ion recombination, a lack of measurements specific to EM activity (specifically for electrons below 1 MeV) requires to trust models built on energy loss from muons and protons at $\mathcal{O}(1)$ GeV. A more precise calorimetry and more sophisticated recombination model specific to low-energy electrons are needed to push the level of energy calibration and bias measurement to be of order 1%. Progress can be made by performing additional dedicated studies of muon energy loss focusing on the impact of angular dependence. We additionally suggest the impact of recombination for low-energy electrons be directly measured.

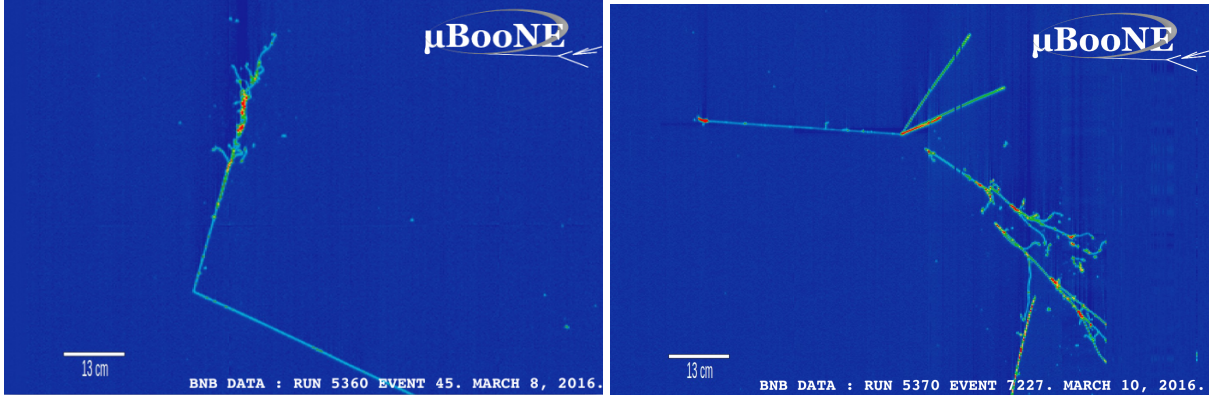
Chapter 11

Calorimetric Separation of Electrons and Photons

The ability to perform accurate particle identification is one of the strengths of the LArTPC technology. The separation of electron and photon electromagnetic showers is essential in order to carry out the accelerator-based neutrino oscillation programs which aim to search for sterile neutrinos and measure the oscillation parameters θ_{23} , $|\Delta m_{13}^2|$, and δ_{CP} . In the past, photon EM showers from π^0 decay have been the largest background to $\nu_\mu \rightarrow \nu_e$ appearance searches. LArTPC detectors can rely on their high-resolution imaging capability to separate the two. This chapter presents results from the study of the energy-dependence of the calorimetric mis-identification rate of photons as electrons from a sample of $\sim 50\text{-}300$ MeV γ showers. This is the first such study of its kind in liquid argon and can be used to better estimate the mis-identification rate of photons as electrons in the MicroBooNE LEE analysis as well as for future studies with the SBN and DUNE experiments.

Electrons and photons have two characteristics which distinguish one from the other. The first is topological: electrons begin to ionize the material which they traverse immediately after being produced, while photons will travel undisturbed until undergoing Compton scattering or pair-production. The 14 cm radiation length in argon means that photons, unlike electrons, will exhibit a visible gap between the neutrino interaction vertex and EM shower start point. The second distinguishing feature is calorimetric: photons which undergo pair-production (the majority above

10 MeV) will produce an e^+ and e^- which will both ionize the argon, each depositing roughly 2 MeV/cm of energy before showering. If the e^+/e^- pair is boosted, the trajectories of the electron and positron will overlap, leading to an average energy deposition double that of a minimally ionizing electron. In this text the calorimetry information obtained from the initial few centimeters of the shower development will be referred to simply as dE/dx . Figure 11.1 shows example event displays for a candidate electron neutrino interaction producing an electron shower, and a candidate neutrino interaction with two photons in the final state. The distinction between electrons and photons is clearly visible thanks to the spatially separated vertex for the two photons. It is worth noting that in order to observe a vertex displacement additional final state particles (protons, muons, charged pions) must be produced in the interaction.



(a) Electron from candidate ν_e interaction.

(b) $\gamma\gamma$ pair from candidate neutrino interaction.

Figure 11.1

A first demonstration of the separation power for electrons and photons using calorimetry was performed by the ArgoNeut collaboration [72]. In this analysis electromagnetic interactions produced by neutrino interactions in the NuMI beamline at Fermilab are separated in an electron and photon sample based on vertex displacement; their dE/dx , as measured in the first four centimeters of propagation is then analyzed to show the viability of this technique. This section presents a measurement of the dE/dx from candidate gamma showers from π^0 decay in CC neutrino interactions in MicroBooNE. One focus of this study is the evaluation of the ability to separate electrons and photons calorimetrically at low EM shower energies (at ~ 100 MeV and above) as this is an important energy range for the study of the MiniBooNE Low Energy Excess in MicroBooNE.

11.1 Limitations to Calorimetric e/γ Separation

There are two main limitations to separating electrons and photons via their characteristic dE/dx .

1. Photons which Compton scatter providing the outgoing electron with most of their energy will appear as a single minimally ionizing electron, thus calorimetrically indistinguishable from electrons. From figure 6.4 one can deduce that Compton scattering becomes less and less prominent compared to pair-production as the photon energy increases. The two cross-sections are equal at ~ 10 MeV and the Compton scattering cross section becomes one order of magnitude smaller than that for pair-production at ~ 100 MeV.
2. The kinematics of the e^+/e^- from pair-production may hamper the ability to reconstruct the $2x$ MIP dE/dx characteristic of photons. Asymmetric e^+/e^- events where the two electrons are either moving in different directions, or have significantly different energies, may cause a lack in the characteristic overlap of two minimally ionizing electrons. Figure 11.2 shows an example photon tagged in data with a discernible asymmetry in the e^- and e^+ produced, which are visible as separate tracks starting from a common origin.

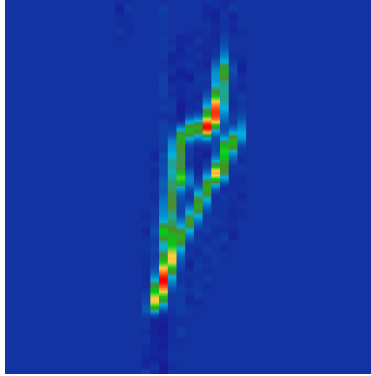
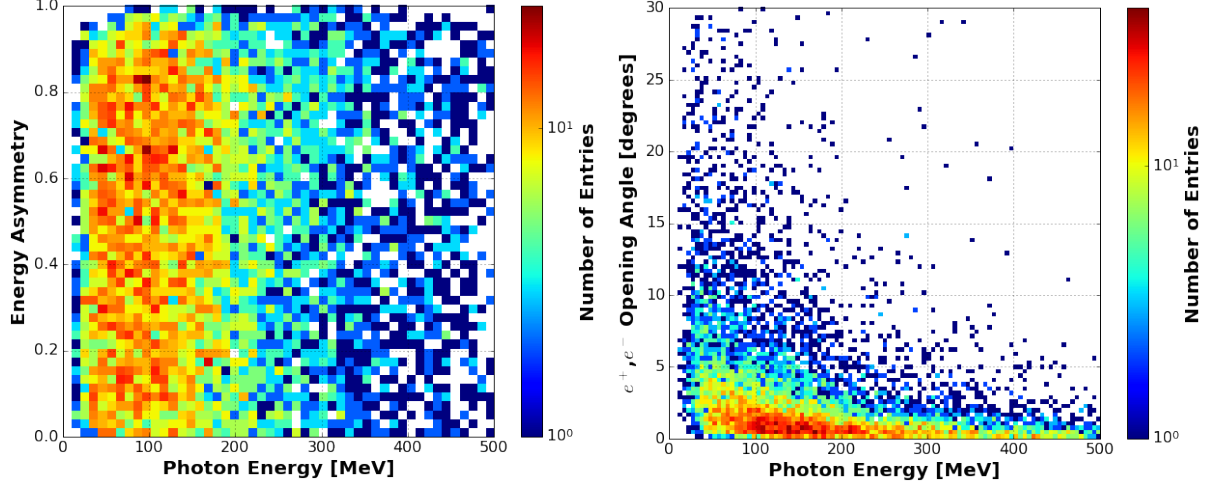


Figure 11.2: Asymmetric $\gamma \rightarrow e^+e^-$ from data where the electron and positron can be seen as separate tracks. The image shown is a $\sim 10 \times 10$ cm region of the collection-plane.

Figure 11.3 shows distributions for the pair-production asymmetry (quantified as the difference in energy of the e^+ or e^- electrons over the sum of their energy) vs. the γ energy (left) and the e^+/e^- pair opening angle vs. γ energy (right). The energy asymmetry of the decay (a) shows a rather uniform distribution independent of the photon energy (consistent with what seen in figure 6.5 of section 6.3.2) indicating that even at high photon energies a signif-

icant number of e^+/e^- pairs will have an energetically asymmetric decay. The distribution of e^+/e^- opening angles shows some energy dependence, but the vast majority of decays are very boosted with opening angles of ~ 3 degrees.



(a) Asymmetry of e^+/e^- energies from pair-production (E_{pair}^{MIN}) vs. photon energy. (b) Opening angle of electron-positron pair vs. photon energy.

Figure 11.3: Distributions of pair-production asymmetry vs. photon energy from a sample of photons from BNB π^0 decays. Geant4 truth-level information is used.

11.2 Truth Studies of Photon dE/dx

A sample of simulated photons from π^0 decay is used to study the dE/dx distribution expected to be reconstructed. For each γ the dE/dx is reconstructed as follows:

1. The true photon conversion point is tagged as the location of the photon's first energy deposition point (according to Geant4 truth-level information).
2. All reconstructed hits within a fixed 3D distance (*integration radius* R) of the start point are tagged.
3. The charge of the selected hits is separated in 3 millimeter segments, such that all hits with a distance from the start point between x and $x + 3$ mm is summed together in the same bin.
4. The median value of the above defined binned data is taken as the characteristic dE/dx of the shower. The distance dx is computed using the true shower 3D direction to calculate the wire pitch.

In the above procedure, the variable R can be varied. Using a value of $R = 5$ cm we obtain a dE/dx distribution for photons as shown in figure 11.4

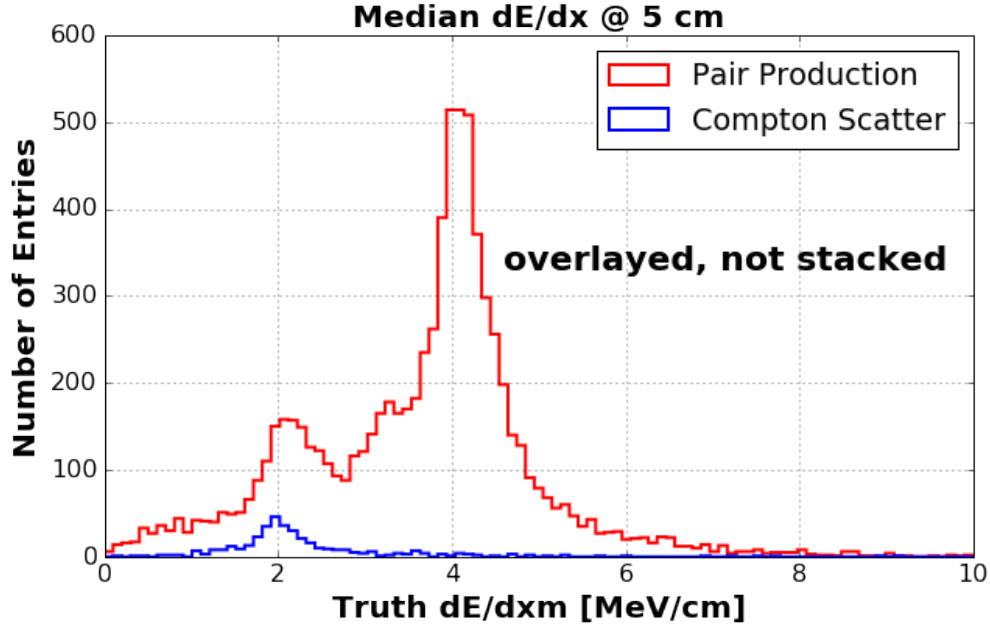


Figure 11.4: Measured dE/dx based on the true γ start point and direction separated in contributions from pair-production (red) and Compton-scatter (blue) events. The distributions are overlayed, not stacked.

Pair-production and Compton-scatter events are well separated at 2 and 4 MeV/cm respectively, but there is a significant contribution of pair-production photons in the 2 MeV/cm peak. We aim to investigate the nature of this peak, focusing on the possibility that it may be due to asymmetric pair-production decays.

Figure 11.5 shows the measured dE/dx as a function of the energy of the smaller of the electron-positron pair electrons (a), and the angle between the electron and positron (b). It is evident that the population of pair-production photons with a dE/dx near 2 MeV/cm is caused by energetically asymmetric decays which lead to an electron or positron with less than 20 MeV of energy. This low energy electron, traveling a short distance and possibly scattering, causes a mis-reconstruction of the photon's dE/dx .

The dependence of the measured dE/dx on the photon total energy is shown in figure 11.6 from which we observe that contributions to a reconstructed dE/dx of ~ 2 MeV/cm is largely caused by lower energy (< 200 MeV) showers, which are more likely to produce an electron from an e^+/e^-

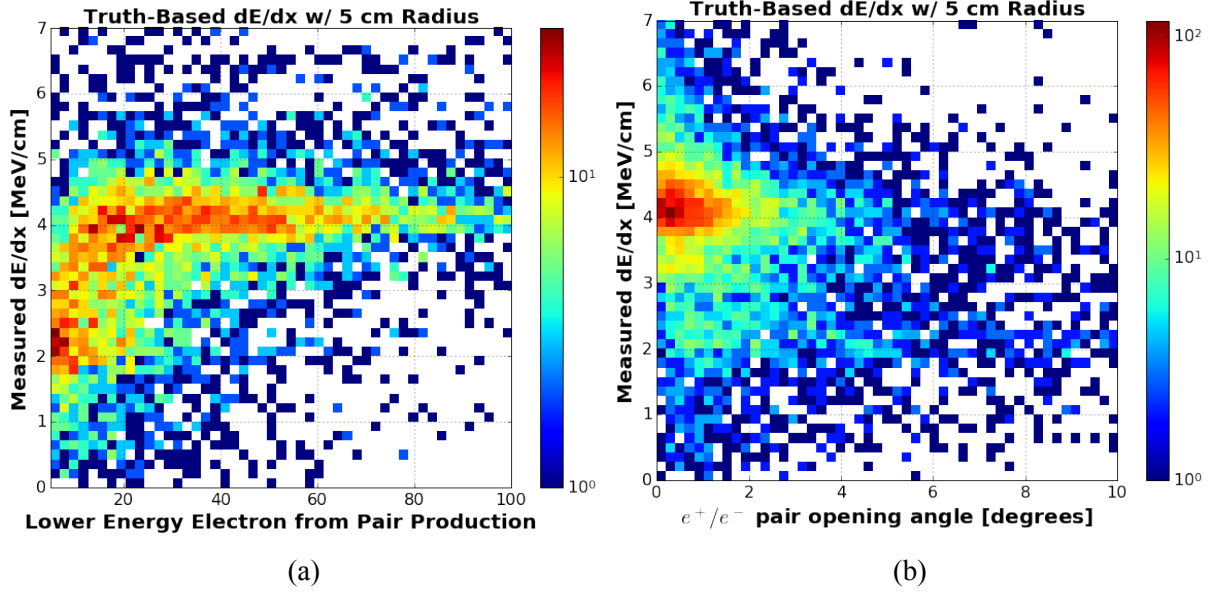


Figure 11.5: (a) dE/dx vs. E_{pair}^{MIN} for pair-production photons. (b) dE/dx vs. e^+/e^- opening angle (degrees) for pair-production photons.

pair with very low energy.

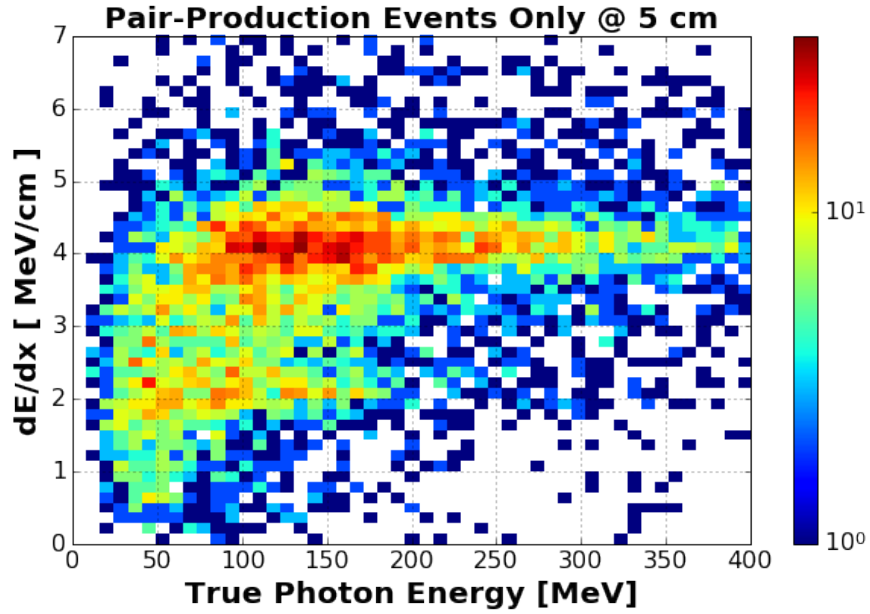


Figure 11.6: Measured dE/dx as a function of the photon's energy when a 5 cm integration window is used.

A shorter integration distance should cause fewer of the very asymmetric electrons to range out, thus decreasing the number of showers with a measured dE/dx of 2 MeV/cm. We study the

reconstructed dE/dx for the same sample of photons varying the integration distance from two to five centimeters, in one centimeter steps. The dE/dx spectrum obtained is reported in figure 11.7. From this study we can see that the contribution to the peak at 2 MeV/cm becomes smaller as the integration window is shrunk. At the same time, no loss in sharpness can be noticed for the peak at 4 MeV/cm.

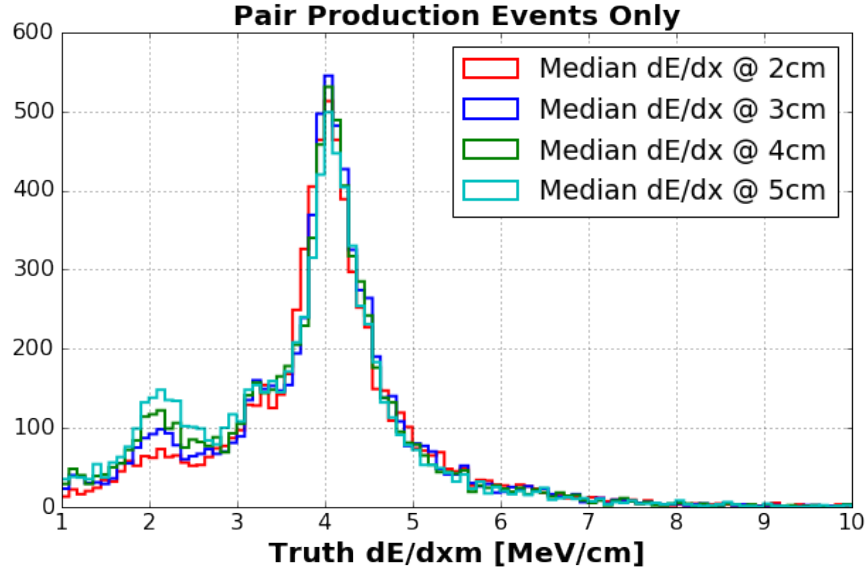


Figure 11.7: Measured dE/dx based on the true γ start point and direction for integration distances of 2,3,4, and 5 cm. The contribution to the peak at 2 MeV/cm decreases as the integration window is shortened, while the resolution in the peak at 4 MeV/cm does not get worse.

11.3 Measurement of dE/dx in data

We study the dE/dx for photons from the data using the sample of hand-clustered photons described in sec 10.2. The same algorithm described above is applied to this sample for two different values of the integration radius: 2 and 4 cm. For reconstructed data events we apply the following additional cuts: all showers considered must have a reconstructed start point at least 20 wires (~ 7 centimeters) away from any non-responsive collection-plane wire. This ensures that we are not using a segment of the γ energy deposition which is too distant from the true starting position. Figure 11.8 shows the dE/dx reconstructed for a 4 (left) and 2 (right) cm integration radius. We observe, as we did in the simulation, a significant reduction of entries below 3 MeV/cm for a shorter integration radius. Overall we see an additional improvement across the entire range

plotted. The fact that the relative strength of the peak at 2 MeV/cm is more significant than in figures 11.4 and 11.7 is caused by the fact that we are using the reconstructed, rather than true start point, as well as due to the lower energy distribution of events in this sample compared to that from simulation.

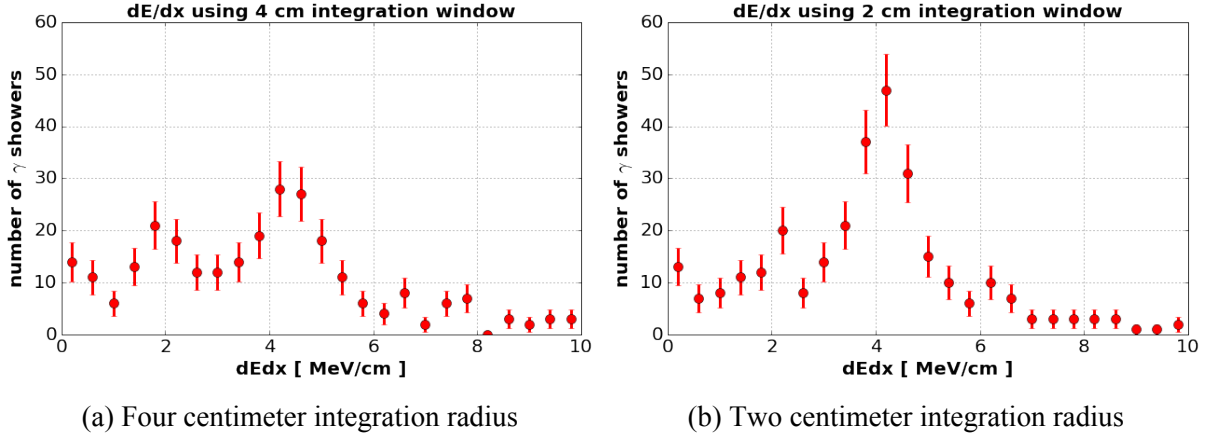


Figure 11.8: dE/dx for hand-clustered photons (see sec. 10.2 with two different integration radii: 4 cm (left) and 2 cm (right)). Showers with a reconstructed start point within 7 cm of a dead-wire on the collection plane are removed from the sample. For these plots a cut requiring that the minimum reconstructed shower energy of 50 MeV is applied.

A study of the energy-dependence of the dE/dx measured for photons is performed. For a given minimum energy threshold on the photon energy, the ratio of dE/dx values falling in the 1-3 MeV range (x1 MIP) to the total entries in the $(1 - 3) \cup (3 - 5)$ MeV ranges (x1 and x2 MIP) is measured. This ratio, as a function of minimum photon energy, is plotted in figure 11.9. The fraction of photons reconstructed with a ~ 2 MeV/cm dE/dx falls from $\sim 30\%$ when no energy cut is applied, to $\sim 15\%$ at 180 MeV minimum energy. The ratio appears to stabilize after this point, although the low statistics make it difficult to make strong conclusions for the highest energies.

11.4 Conclusions

We have analyzed the calorimetry associated to low energy (~ 100 MeV) photons from the MicroBooNE LArTPC in order to study the capability of using dE/dx to perform particle identification and separate electrons from photons. Our study shows that we are able to reconstruct the characteristic 2x MIP dE/dx associated with photons both in data and simulation.

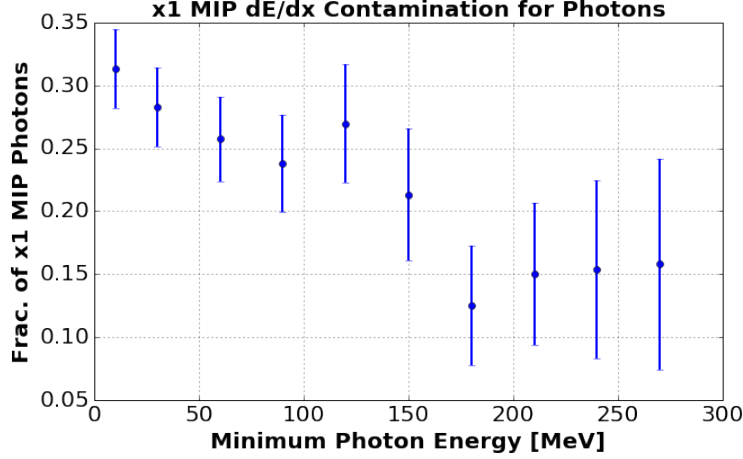


Figure 11.9: Contamination of x1 MIP-like reconstructed photons as a function of minimum photon energy cut. The y-axis denotes the ratio of photons with a reconstructed dE/dx in the 1-3 MeV range over the total entries in the $(1 - 3) \cup (3 - 5)$ ranges.

Studying low energy photons we have identified that energetically asymmetric decays of the photon to an e^+/e^- can hamper the ability to identify photons via calorimetry. At these energies energetically asymmetric decays play a role that is dominant, compared to that of Compton scattering, to the inefficiency of separating electrons and photons calorimetrically in a LArTPC. We find that for EM showers of 100-200 MeV of energy a shorter integration distance for the measurement of dE/dx allows to maximize the calorimetric separation power for electrons and photons by reducing the photon background below 3 MeV/cm. Furthermore we have shown that, for the reconstruction technique employed in this analysis, the contamination of electron-like dE/dx values is energy-dependent, with lower-energy photons contributing a larger fraction of the total mis-id fraction.

Chapter 12

Conclusions

This thesis has presented a study of EM interactions in liquid argon which serves the purpose of providing insights for the development of current and future analyses aimed at making precision measurements of neutrino oscillations. A series of measurements of EM activity over an energy range spanning $\mathcal{O}(1)$ to a few hundred MeV were performed with the MicroBooNE LArTPC focused on addressing different aspects of how EM activity and EM shower topology impact neutrino energy reconstruction and background rejection. The results from these studies are summarized below.

A first measurement of EM-like backgrounds in a surface LArTPC in the 1-15 MeV energy range has been performed by analyzing cosmic data events. Charge deposited in the detector not associated with cosmic-ray muons is identified and the spatial correlation of such backgrounds with nearby muons profiled. We find that at all energies such backgrounds can be described by two populations: one highly correlated with cosmic-ray muons with a radial exponential falloff of 6-8 cm, and a second consisting of a population uniformly distributed in the detector. For this second population we measure an energy-dependent rate of $\sim 10 \text{ Hz/m}^3$ for backgrounds greater than 1 MeV of energy, and $\sim 0.3 \text{ Hz/m}^3$ at 15 MeV. The radial dependence of backgrounds spatially correlated with muons can be employed to perfect the removal of cosmogenic backgrounds to neutrino analyses. We compare the measured rate of uniformly distributed backgrounds to the predicted rate of supernova burst neutrinos for a typical SNB event at a distance of 10 kilo-parsec and find that the rate of SNB neutrinos for the prompt neutronization of the supernova is above that of background by a factor of ~ 2 , while the steady state ν_e event rate is comparable to that of

background events.

Michel electrons from the decay-at-rest of cosmic-ray muons are reconstructed and their energy is studied. These electrons, of up to 60 MeV of energy, present a complex topology due to the similar contributions to energy loss from collision stopping power and bremsstrahlung radiation. Due to the stochastic nature of radiative energy loss recovering the full energy deposited by these electrons is necessary in order to obtain good energy resolution. By profiling the reconstruction on simulated cosmic-rays in the MicroBooNE detector we are able to show that even via the simple 2D reconstruction technique developed for this work an attempt to tag radiative photons of more than 1 MeV of energy up to a distance of 80 cm from the muon decay point improves the energy resolution from over 30% to roughly 20%. Data-simulation comparisons of the reconstructed Michel electron energy spectrum show good agreement (to within 3%) indicating that the simulation is properly modeling the propagation of tens of MeV electrons in argon. We note that even though the attempt to recover radiative charge shifts the reconstructed Michel electron energy spectrum closer to its true shape, a significant deficit in reconstructed energy is still present. Approximately 70% of the full energy is recovered, with roughly equal amounts lost due to thresholding effects from low-energy depositions and clustering of far-reaching photons. This work presents the first measurement and characterization of radiative charge from electrons in the 0-60 MeV energy range in liquid argon. The results obtained can provide valuable input to studies of energy reconstruction for ν_e interactions in LAr which produce tens of MeV electrons, such as from stopped pion beams and supernovae.

In order to study EM activity at higher energies a selection for ν_μ charged current events with a π^0 in the final state was developed. Photons produced by the π^0 decay are reconstructed and the π^0 mass reconstructed. The invariant mass provides a calibration tool with which to study in data the impact of EM topology on EM energy reconstruction in the $\mathcal{O}(100)$ MeV energy range. The reconstruction produces a mass distribution which peaks at 100.0 MeV/c² with a width obtained from a Gaussian fit of 26.9 MeV/c². From simulation studies the bias is found to be due to the impact of hit-thresholding and charge-clustering which account for a shift of 8 and 14% respectively. Accounting for the bias from simulation results in a corrected reconstructed mass of 128.7 ± 3.3 (stat.) ± 4.0 (syst.) MeV/c². Additional studies of π^0 induced photons produced by hand-selecting reconstructed 2D hits and thus avoiding the impact of deficiencies in the recon-

struction due to clustering lead to a reconstructed mass of $117.1 \text{ MeV}/c^2$ with a narrower Gaussian width of 18%. The deficit in reconstructed energy agrees, to a couple of percent, with the impact of hit-thresholding. The agreement between simulation and data obtained with this studies, of order 5% and within the systematic uncertainties estimated for the energy reconstruction provide additional support for the correct treatment of electron and photon energy losses in the simulation. To improve the level of agreement we suggest more detailed measurements of ion recombination be performed for electrons and photons in liquid argon.

A final study of particle discrimination between electrons and photons via their calorimetric energy profile was presented. Because photons from π^0 decay have been the major source of background to ν_e appearance oscillation experiments at the $\mathcal{O}(1) \text{ GeV}$ neutrino energy, the ability of LArTPC detectors to provide electron/photon separation is an important factor which has motivated the employment of this detector technology for future precision oscillation experiments. While demonstrating in MicroBooNE the ability to isolate photons via calorimetry, this work has for the first time studied the energy-dependence of the calorimetric mis-identification of photons as electrons in the 50-300 MeV energy range. We find that the rate of mis-identified events decreases as the photon energy increases and via simulation studies identify that the main cause for his mis-identification is due to energetically asymmetric photon pair-production into an electron-positron pair. The results obtained in this study can benefit ν_e appearance experiments in two ways: first we have shown that the calorimetric separation of photons from electrons benefits from a different reconstruction approaches at different energies, and second the rate of mis-identified photons measured in data can be used to better account for background rates.

Liquid Argon Time Projection Chamber detectors are and will be playing an important role in neutrino oscillation experiments in the coming decade. Throughout this thesis we have presented results from various studies of electromagnetic interactions in liquid argon, focusing on the impact of electron and photon energy loss on energy reconstruction, and providing data-driven studies of EM backgrounds to ν_e measurements. Work presented in this thesis can be used to guide analysis strategies, reconstruction approaches, and design principles for upcoming detectors.

Bibliography

- [1] Francis Halzen and Alan D. Martin, *Quarks and Leptons: An Introductory Course in Modern Particle Physics*, 1984.
- [2] Super-Kamiokande Collaboration, *Evidence for Oscillation of Atmospheric Neutrinos*, Phys. Rev. Lett. **81** (1998), 1562.
- [3] SNO Collaboration, *Measurement of the Rate of $\nu_e + d \rightarrow p + p + e^-$ Interactions Produced by 8B Solar Neutrinos at the Sudbury Neutrino Observatory*, Phys. Rev. Lett. **87** (2001), 071301.
- [4] SNO Collaboration, *Direct Evidence for Neutrino Flavor Transformation from Neutral-Current Interactions in the Sudbury Neutrino Observatory*, Phys. Rev. Lett. **89** (2002), 011301.
- [5] Andre de Gouvea, *2004 TASI Lectures on Neutrino Physics*, NUHEP-TH/04-17, arXiv:0411274.
- [6] K.A. Olive et al., Particle Data Group, *Chin. Phys. C*, **38** (2014) 090001.
- [7] DayaBay Collaboration, *Measurement of electron antineutrino oscillation based on 1230 days of operation of the Daya Bay experiment*, Phys. Rev. D **95**, 072006 (2017), arXiv:1610.04802
- [8] Double Chooz Collaboration, *Improved measurements of the neutrino mixing angle θ_{13} with the Double Chooz detector*, J. High Energy Physics (2014) 2014:86, arXiv:1406.7763.
- [9] Soo-Bong Kim, *New results from RENO and prospects with RENO-50*, 2014, arXiv:1412.2199.
- [10] NoVA Collaboration, *Measurement of the neutrino mixing angle θ_{23} in NOvA*, Phys. Rev. Lett. **118** (2017), 151802. arXiv:1701:05891.

- [11] T2K Collaboration, *Measurement of neutrino and antineutrino oscillations by the T2K experiment including a new additional sample of ν_e interactions at the far detector*, arXiv:1707.01048 [hep-ex].
- [12] NOvA Collaboration, *Constraints on Oscillation Parameters from ν_e Appearance and ν_μ Disappearance in NOvA*, Phys. Rev. Lett. **118** (2017) 231801. arXiv:1703.03328.
- [13] W. Buchmuller, R. D. Pecei, T. Yanagida, *Leptogenesis As the Origin of Matter*, DESY 05-031, February 2005, arXiv:0502169.
- [14] C. L. Cowan, F. Reines, F. B. Harrison, H. W. Kruse, and A. D. McGuire, *Detection of the Free Neutrino: A Confirmation*, Science **124** (1956) 3212.
- [15] ALEPH, DELPHI, L3, OPAL, and SLD Collaborations, and LEP Electroweak Working Group, and SLD Electroweak Group, and SLD Heavy Flavour Group, *Phys. Reports*, **427**, 257 (2006).
- [16] K. Nakamura, et al. (Particle Data Group), JPG **37**, 075021 (2010) (URL: <http://pdg.lbl.gov>)
- [17] IceCube Collaboration, *Searches for Sterile Neutrinos with the IceCube Detector*, Phys. Rev. Lett., **117** (2016) 071801, arXiv:1605.01990.
- [18] NOvA Collaboration, *Search for active-sterile neutrino mixing using neutral-current interactions in NOvA*, FERMILAB-PUB-17-198-ND, arXiv:1706.04592
- [19] Daya Bay and MINOS Collaborations, *Limits on Active to Sterile Neutrino Oscillations from Disappearance Searches in the MINOS, Daya Bay, and Bugey-3 Experiments*, Phys. Rev. Lett., **117** (2016) 151801, arXiv:1607.01177
- [20] J. Conrad, and M. Shaevitz, *Sterile Neutrinos: An Introduction to Experiments*, arXiv:1609.07803.
- [21] C. Giunti and M Lavaden, *Statistical Sigifnicance of the Gallium Anomaly*, Phys. Rev. C, **83** (2011) 065504, arXiv:1006.3244.
- [22] Daya Bay Collaboration, *Evolution of the Reactor Antineutrino Flux and Spectrum at Daya Bay*, Phys. Rev. Lett. **118**, (2017) 251801 arXiv:1704.01082.

- [23] PROSPECT Collaboration, *The PROSPECT Physics Program*, Journal of Physics G, **43** (2016) 11, arXiv:1512.02202
- [24] J. Conrad, W. Louis, M. Shaevitz, *The LSND and MiniBooNE Oscillation Searches at High Δm^2* , Ann. Rev. Nucl. Part. Sci. **63** (2013) pp. 45-67.
- [25] LSND Collaboration, *Evidence for Neutrino Oscillations from the Observation of Electron Anti-neutrinos in a Muon Anti-Neutrino Beam*, Phys. Rev. D **64** (2001), 112007. arXiv:0104049.
- [26] *Celebrating the Neutrino*, No. 2, 1997. Los Alamos National Laboratory.
- [27] MiniBooNE Collaboration, *Improved Search for $\bar{\nu}_\mu \rightarrow \bar{\nu}_e$ Oscillations in the MiniBooNE Experiment*, Phys. Rev. Lett. **110** (2013), 161801. arXiv:1303.2588.
- [28] R. Acciarri et. al., *A Proposal for a Three Detector Short-Baseline Neutrino Oscillation Program in the Fermilab Booster Neutrino Beam*. arXiv:1503.01520 [hep-ex].
- [29] D. Kaleko, *MicroBooNE: The Search For The MiniBooNE Low Energy Excess*, FERMILAB-THESIS-2017-12.
- [30] D. Freedman, *Coherent Effects of a Weak Neutral Current*, Phys. Rev. D, **9** (1974), 5 pp. 1389-1392.
- [31] K. Hirata et al., *Observation of a Neutrino Burst from the Supernova SN 1987a*, Phys.Rev.Lett., **58** (1987), pp. 1490–1493.
- [32] R. Bionta et al., *Observation of a Neutrino Burst in Coincidence with Supernova SN 1987a in the Large Magellanic Cloud*, Phys. Rev. Lett., **58** (1987), p. 1494.
- [33] E. N. Alexeyev, L. N. Alexeyeva, L. V. Krivosheina, V. I. Volchenko, *Detection of the Neutrino Signal from SN 1987A Using the INR Baksan Underground Scintillation Telescope*, ESO Workshop on the SN 1987A, Garching, Federal Republic of Germany, July 6-8, 1987, Proceedings (A88-35301 14-90). Garching, Federal Republic of Germany, European Southern Observatory, 1987, p. 237-247; Discussion, p. 247.

- [34] K. Scholberg, *Supernova Signatures of Neutrino Mass Ordering*, <https://arxiv.org/abs/1707.06384> [hep-ex].
- [35] A. Beck, et al., *SNOwGLOBES : SuperNova Observatories with GLOBES*, version 1.1 (March 11, 2013), https://github.com/SNOwGLOBES/snowglobes/blob/master/doc/snowglobes_1.1.pdf.
- [36] R. S. Raghavan, *Inverse β^- decay of ^{40}Ar : A new approach for observing MeV neutrinos from laboratory and astrophysical sources*, Phys. Rev. D, **37** (1986), pp. 2088-2091.
- [37] M. Bhattacharya, et. al, *Neutrino absorption efficiency of an ^{40}Ar detector from the β decay of ^{40}Ti* , Phys. Rev. C, **58** (1998), 6 pp. 3677-3687.
- [38] M. Bhattacharya, C. D. Goodman, A. Garcia, *Weak-Interaction strength from charge-exchange reactions versus β decay in the $A=40$ isoquintet*, Phys. Rec. C **80** (2009), 055501.
- [39] R. Acciarri et. al, DUNE Collaboration, *Long-Baseline Neutrino Facility (LBNF) and Deep Underground Neutrino Experiment (DUNE) Conceptual Design Report. Volume 2: The Physics Program for DUNE at LBNF*, arXiv:1512.06148 [hep-ex].
- [40] S. Amoruso et al., ICARUS Collaboration, *Measurement of the mu decay spectrum with the ICARUS liquid argon TPC*, European Physics Journal C **33** (2004) pp. 233-241. [hep-ex/0311040].
- [41] W. J. Willis, V. Radeka, *Liquid argon ionization chambers as total absorption detector*, Nuclear Instruments and Methods **120** (1974) 221.
- [42] C. Rubbia, *The Liquid-Argon Time projection Chamber: a new concept for Neutrino Detector*, CERN-EP/77-08, 1977.
- [43] G. De Geronimo, et al., *Front-End ASIC for a Liquid Argon TPC*, IEEE Transactions on Nuclear Science, **58**, 3 (2011) pp. 1376-1385.
- [44] D. Caratelli for the MicroBooNE Collaboration, *Noise Dependence on Temperature and LAr Fill Level in the MicroBooNE Time Projection Chamber*, MICROBOONE-NOTE-1001-TECH

- [45] Dennis Barak, Beau Harrison, and Adam Watts, Fermilab Accelerator Division, Operations Department, *Concepts Rookie Book*, December 2013, http://operations.fnal.gov/rookie_books/concepts.pdf.
- [46] Dennis Barak, Beau Harrison, and Adam Watts, Fermilab Accelerator Division, Operations Department, *LINAC Rookie Book: RIL*, October 2015, http://operations.fnal.gov/rookie_books/RIL.pdf.
- [47] Michelle Gattuso, *MiniBooNE Mini-Rookie Book*, August 2002, http://operations.fnal.gov/rookie_books/MiniBooNE_v1.pdf.
- [48] MiniBooNE Collaboration (Aguilar-Arevalo A.A. et al.), *The Neutrino Flux Prediction at MiniBooNE*, Phys. Rev. D **79** (2009) 072002. arXiv:0806:1449 [hep-ex].
- [49] M.J. Berger, J.S. Coursey, M.A. Zucker, and J. Chang, *ESTAR, PSTAR, and ASTAR: Computer Programs for Calculating Stopping-Power and Range Tables for Electrons, Protons, and Helium Ions* (version 1.2.3), (2005), [<http://physics.nist.gov/Star>, retrieved Feb. 24, 2017].
- [50] *Stopping Power for Electrons and Positrons*, ICRU Report No. 37 (1984).
- [51] H.W. Koch and J. W. Motz, *Bremsstrahlung Cross-Section Formulas and Related Data*, Review of Modern Physics, **31**, 4 (1959) pp. 920-955.
- [52] Yung-Su Tsai, *Pair-production and bremsstrahlung of charged leptons*, Review of Modern Physics, **46**, 4 (1974) pp. 815-851.
- [53] M.J. Berger et al., *XCOM: Photon Cross Section Database (version 1.5)*, (2010), [<http://physics.nist.gov/xcom>, retrieved Feb. 24, 2017].
- [54] W. Heither, *The Quantum Theory of Radiation*, 1954.
- [55] Shirley W. Li and John F. Beacom, *Spallation Backgrounds in Super-Kamiokande Are Made in Muon-Induced Showers*, Phys.Rev. D **91** **10** (2015), 105005, arXiv:1503:04823.
- [56] R. Acciarri, et al., MicroBooNE Collaboration, *Michel electron reconstruction using cosmic-ray data from the MicroBooNE LArTPC*, JINST **12** P09014 (2017) arXiv:1708.03135 [hep-ex].

- [57] R. Acciarri, et al., MicroBooNE Collaboration, *The Pandora multi-algorithm approach to automated pattern recognition of cosmic-ray muon and neutrino events in the MicroBooNE detector*, arXiv:1708.03135 [hep-ex].
- [58] C. Mariani et al., T2K collaboration, Phys. Rev. D **83**, 054023 (2011).
- [59] S. Nakayama et al., T2K collaboration, Phys. Lett. B **619**, 255 (2005).
- [60] T. Le et al., MINER ν A collaboration, Phys. Lett. B **749**, 130 (2015).
- [61] O. Altinok, al., MINER ν A collaboration, arXiv:1708.03723.
- [62] A. A. Aguilar-Arevalo et al., MiniBooNE collaboration, Phys. Rev. D **83** 052009 (2011).
- [63] A. A. Aguilar-Arevalo et al., MiniBooNE collaboration, Phys. Rev. D **81** 013005 (2010).
- [64] C. T. Kullenberg, et al., NOMAD collaboration, Phys. Lett. B **682**, 177 (2009).
- [65] Y. Kurimoto et al., SciBooNE collaboration, Phys. Rev. D **81**, 033004 (2010).
- [66] L. Alvarez-Ruso, et al., *NuSTEC White Paper: Status and Challenges of Neutrino-Nucleus Scattering*, arXiv:1706.03621.
- [67] J.A. Formaggio and G.P. Zeller, *From eV to EeV: Neutrino Cross Sections Across Energy Scales*, Rev. Mod. Phys. **84**, 1307 (2012), arXiv:1305.7513.
- [68] Conrad, J. M., M. S. Shaevitz, and T. Bolton, 1998, Rev. Mod. Phys. **70**, 1341. arXiv:970705 [hep-ex].
- [69] O. Hen, et al., *Nucleon-Nucleon Correlations, Short-lived Excitations, and the Quarks Within*, arXiv:1611.09748, [nucl-ex].
- [70] K. McDonald, Princeton University, *Neutral Pion Decay*, September 15, 1976 (updated June 13, 2013), <http://www.physics.princeton.edu/~mcdonald/examples/piondecay.pdf>.
- [71] MicroBooNE Collaboration, *Selection and kinematic properties of numu charged-current inclusive events in 5E19 POT of MicroBooNE data*, MICROBOONE-NOTE-1010-PUB,

July 4th, 2016. <https://www-microboone.fnal.gov/publications/publicnotes/MICROBOONE-NOTE-1010-PUB.pdf>.

- [72] R. Acciarri, et al., ArgoNeut Collaboration, *First Observation of Low Energy Electron Neutrinos in a Liquid Argon Time Projection Chamber*, Phys. Rev. D **95**, 072005 (2017). arXiv:1610:04102 [hep-ex].
- [73] MicroBooNE Collaboration, *Determination of muon momentum in the MicroBooNE LArTPC using an improved model of multiple Coulomb scattering*, arXiv:1703.06187.
- [74] ICARUS Collaboration, *Muon momentum measurement in ICARUS-T600 LAr-TPC via multiple scattering in few-GeV range*, JINST **12** (2017) arXiv:1612.07715.
- [75] MicroBooNE Collaboration, *Noise Characterization and Filtering in the MicroBooNE Liquid Argon TPC*, JINST, **12** P08003 (2017) arXiv:1705:07341 [physics.ins-det].
- [76] R. Acciarri et al., ArgoNeuT Collaboration, *A study of electron recombination using highly ionizing particles in the ArgoNeuT Liquid Argon TPC*, JINST **8** (2013) P08005 arXiv:1306.1712 [hep-ex].
- [77]
- [78] Table 289: Muons in Liquid Argon (Ar). http://pdg.lbl.gov/2012/AtomicNuclearProperties/MUON_ELOSS_TABLES/muonloss_289.pdf
- [79] MicroBooNE Collaboration, *Cosmic Shielding Studies at MicroBooNE*, MICROBOONE-NOTE-1005-PUB, May 30th, 2016. <https://www-microboone.fnal.gov/publications/publicnotes/MICROBOONE-NOTE-1005-PUB.pdf>.
- [80] MicroBooNE Collaboration, *Establishing a Pure Sample of Side-Piercing Through-Going Cosmic-Ray Muons for LArTPC Calibration in MicroBooNE*, MICROBOONE-NOTE-1028-PUB, July 22nd, 2017. <https://www-microboone.fnal.gov/publications/publicnotes/MICROBOONE-NOTE-1028-PUB.pdf>.

- [81] MicroBooNE Collaboration, *Study of Space Charge Effects in MicroBooNE*, MICROBOONE-NOTE-1018-PUB, November 29th, 2016. <https://www-microboone.fnal.gov/publications/publicnotes/MICROBOONE-NOTE-1018-PUB.pdf>
- [82] MicroBooNE Collaboration, *Measurement of the Electronegative Contaminants and Drift Electron Lifetime in the MicroBooNE Experiment*, MICROBOONE-NOTE-1003-PUB, May 19th, 2016. <https://www-microboone.fnal.gov/publications/publicnotes/MICROBOONE-NOTE-1003-PUB.pdf>.
- [83] MicroBooNE Collaboration, *A Measurement of the Attenuation of Drifting Electrons in the MicroBooNE LArTPC*, MICROBOONE-NOTE-1026-PUB, August 30th, 2017. <https://www-microboone.fnal.gov/publications/publicnotes/MICROBOONE-NOTE-1026-PUB.pdf>.
- [84] P. Agnes, et al., DarkSide Collaboration, *Simulation of argon response and light detection in the DarkSide-50 dual phase TPC*, arXiv:1707:05630 [physics.ins-det].
- [85] M. Miyajima, T. Takahashi, S. Konno, T. Hamada. *Average energy deposited per ion pair in liquid argon*. Physical Review A, **9**, 3 (1974).
- [86] M. Miyajima, et al., *Erratum: Average energy deposited per ion pair in liquid argon*. Physical Review A, **10**, 4 (1974).
- [87] Souvik Das, *A Simple Alternative to the Crystal Ball Function*, <http://home.fnal.gov/~souvik/GaussExp/GaussExp.pdf>.

Appendix A

Beam Trigger

Due to the low cross section for neutrinos to interact, most beam spills reaching the detector are “empty”, meaning that no neutrino interaction has actually occurred in the TPC. Given the neutrino cross-section, beam flux and intensity, and detector volume, roughly one in six hundred beam spills (0.16%) will lead to a neutrino interaction in the TPC. Recording all spills in the detector leads to a very inefficient use of resources. Because scintillation light reaches the PMT array within tens of nanoseconds, it can be used to identify activity in the detector coincident with the $1.6 \mu\text{s}$ beam-spill and allow to avoid triggering on the vast majority of empty beam-spills. Given the 5 kHz cosmic-ray flux constantly entering the detector, a random coincidence of cosmic activity in time with the beam will occur ($1.6 \mu\text{s} \times 5 \text{ kHz}$) roughly 0.8% of the time. This means that even after imposing a requirement of light activity in coincidence with the beam-spill, roughly one in six (0.16% vs. 0.8%) recorded events will contain a neutrino interaction.

A decision on whether to record an event or not based on light information in time-coincidence with the beam is made by the DAQ after the PMT and TPC event data have been recorded. This decision can be made “on the fly” because of the relatively simple format of the PMT data and relatively long time between consecutive triggers (0.1 ms). The algorithm employed for this task is described below.

Software Trigger Algorithm : A decision on whether to save an event or not is made, given the waveforms of the high-gain channel of each PMT, based on two quantities: the number of PMT channels above a set threshold (multiplicity) and the summed ADC value of all PMTs above

threshold (PHMAX_{sum}). These two quantities are calculated tick-by-tick in the time-interval which defines the beam-spill. If at any point in this interval the trigger condition is met, the event is saved. For each PMT, the PHMAX at each tick is calculated as follows:

1. The derivative of the PMT waveform is computed such that $WF^*(i) = WF(i + \phi) - WF(i)$. The phase offset ϕ is set to 3 to match the rise time of the shaper.
2. A threshold (DISC3) is set such that:

$$PHMAX(i) \begin{cases} WF^*(i), & \text{if } WF^*(i) \geq DISC3 \\ 0, & \text{otherwise} \end{cases}$$

The value of DISC3 is set to 10 ADC.

3. The value of PHMAX is updated for up to 7 ticks, and a given value of PHMAX is preserved for a time interval referred to as the “trigger width” set to 6 time-ticks (about 100 ns).

Figure A.1 shows an example raw PMT waveform, the differential waveform $WF^*(i)$, and the value of PHMAX.

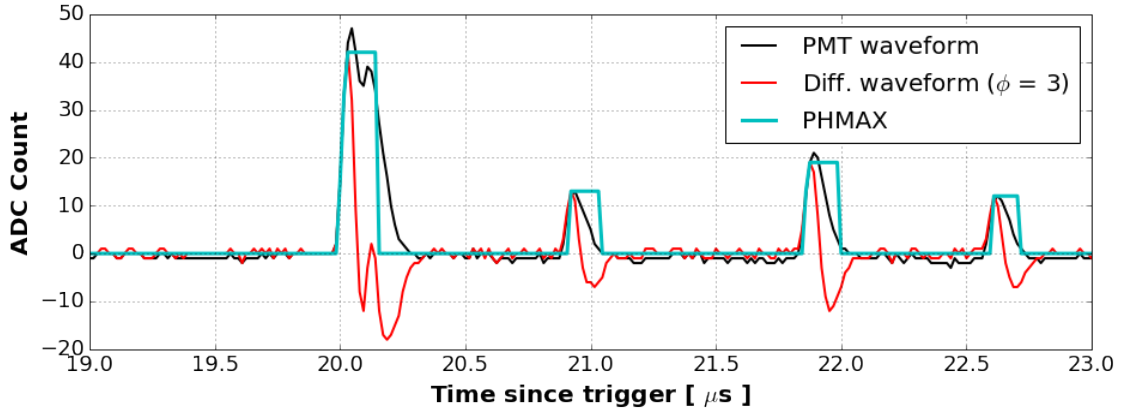


Figure A.1: Example showing PHMAX calculation for the waveform from a single PMT. The raw waveform (black), differential waveform (red) and PHMAX vector are shown overlayed. A discriminator threshold DISC3 of 10 ADC is applied and the PHMAX value is updated for up to 7 time-ticks since first firing and preserved for a time interval referred to as the “trigger width” set to 6 ticks.

The PHMAX_{sum} waveform is obtained by summing the individual PHMAX waveforms of each PMT, with an example shown in figure A.2.

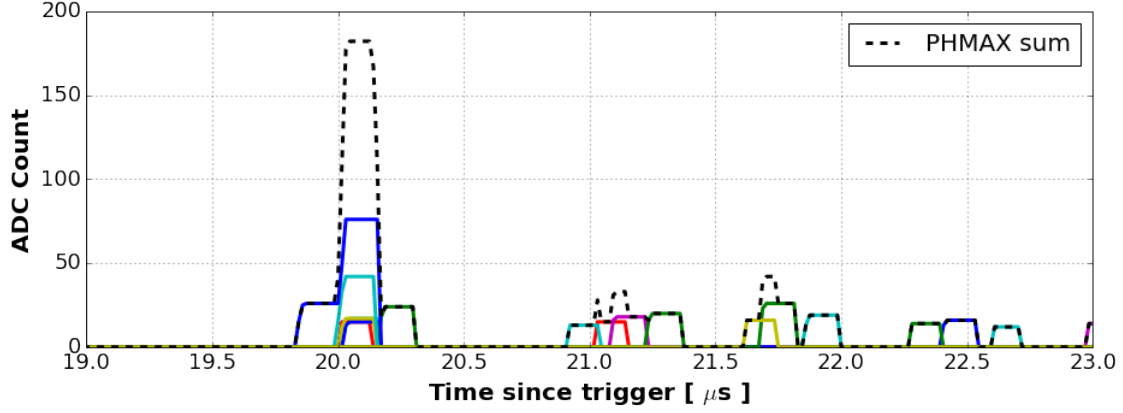


Figure A.2: Example PHMAX sum calculation from several input PMT waveforms. The PHMAX waveform for various PMTs are shown with different solid colors, and the total PHMAX sum resulting from these individual waveforms is overlayed in the black dashed line.

The goal in deciding the trigger configuration is to apply thresholds as low as possible while maintaining the data rates within manageable levels for the resources allocated to the experiment. In order to identify the trigger configuration to be used for data taking a scan of the variables PHMAX sum and multiplicity was performed. The time-interval over which to apply the trigger condition depends on the duration of the beam-spill. Given the significant difference in beam-spill duration for the BNB ($1.6 \mu\text{s}$) vs. NuMI ($9.6 \mu\text{s}$) the trigger configuration for the two beams was optimized separately. Figure A.3 shows the software-trigger passing rate for as a function of the PHMAX sum threshold for a fixed multiplicity of 1 for the BNB and NuMI respectively. Because of the six time longer beam-spill the probability of passing the trigger condition for the same thresholds for NuMI is always larger than that for the BNB. Both distributions show a significant fall off in the passing rate after a threshold of a few PE is applied. This is due to the suppression of the high-rate SPE noise constantly impacting the PMT system. After a few PE in threshold cosmic-rays become the dominant source of light produced in the detector, leading to a more gradual decrease in the passing rate.

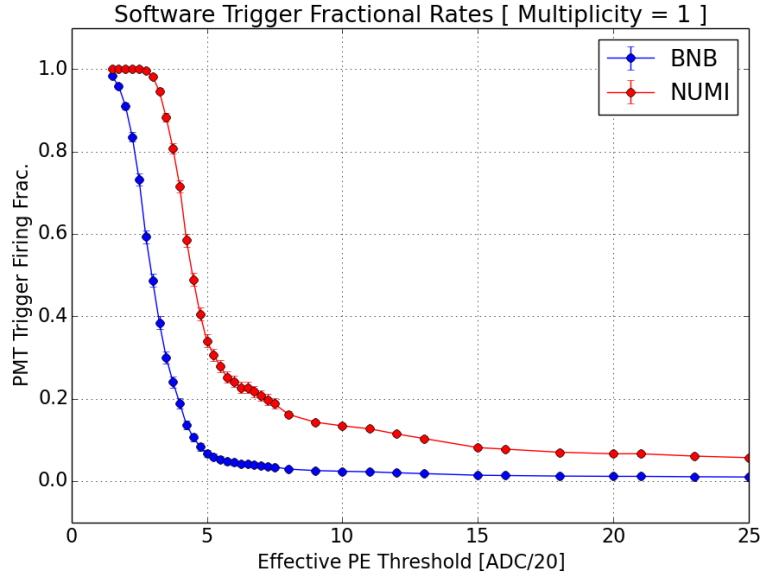


Figure A.3: Software trigger passing rate for BNB (blue) and NuMI (red) applied on a time window set to match the beam-spill width of the two beams. The passing rate was measured in off-beam mode (cosmics dominate the triggering rate even with a software-trigger applied).

The final software-trigger configuration for the BNB is set to a threshold of $PHMAX = 130$ (6.5 PE) with multiplicity 1.

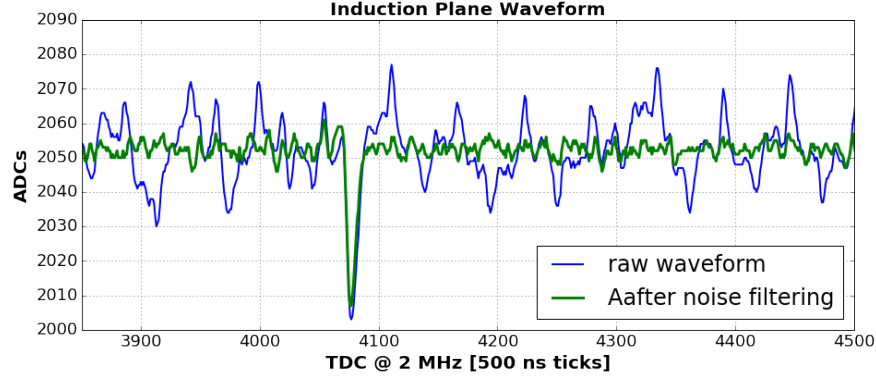
Appendix B

TPC Signal Reconstruction

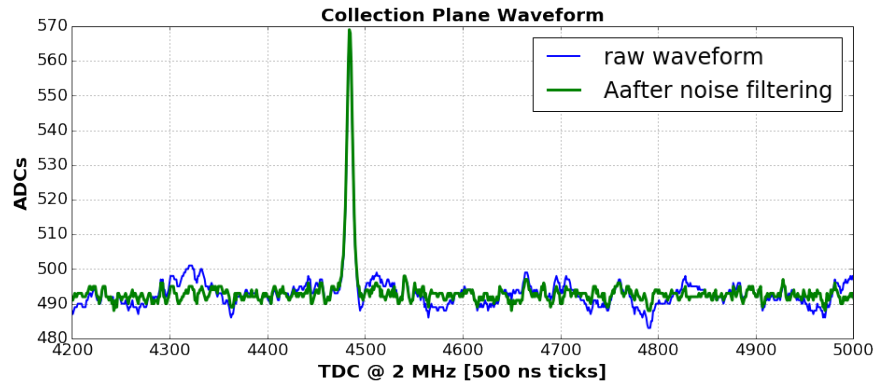
This chapter presents the low-level reconstruction applied to TPC signals. This stage of the reconstruction involves two steps: (1) raw signals from each channel are processed through a signal-processing stage which involves noise-removal and deconvolution; (2) pulses of charge associated to energy deposition, denoted as *hits*, are reconstructed via a hit-finding algorithm which fits identified regions of interest on each waveform to a Gaussian. The first step is described in section B.1, followed by the second in section B.2.

B.1 TPC Signal Processing

Raw TPC signals from each plane are processed through a software frequency-domain filter aimed at removing various sources of noise observed in the TPC and described in detail in reference [75]. While the MicroBooNE TPC wires have low nominal noise levels, a series of artifacts which are either intermittent in time, or impact specific malfunctioning channels lead to instances in which noise levels begin to impair the ability to recover true signals. The removal of these features is the focus of such a filtering stage. The implementation of noise-filtering is particularly important on induction plane wires affected more strongly by spurious noise features and with an overall lower signal-to-noise. Figure B.1 shows an example waveform from an induction plane (a) and the collection plane (b) before and after noise-filtering in blue and green respectively. The signal is faithfully preserved, while the noise is suppressed in both instances.



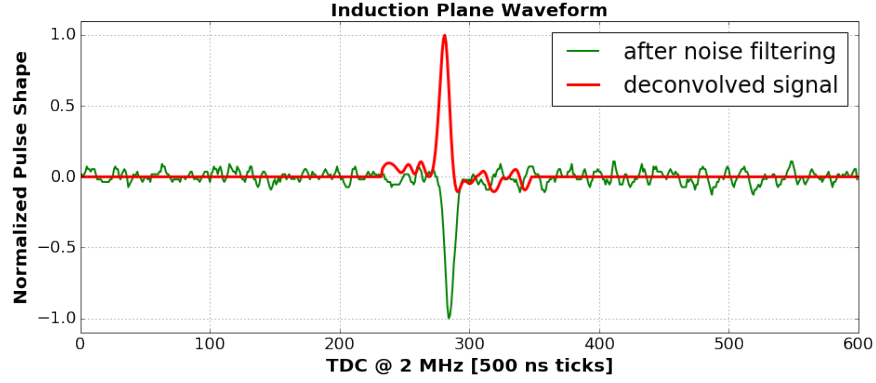
(a) Induction-plane signal before (blue) and after (green) noise-filtering is applied.



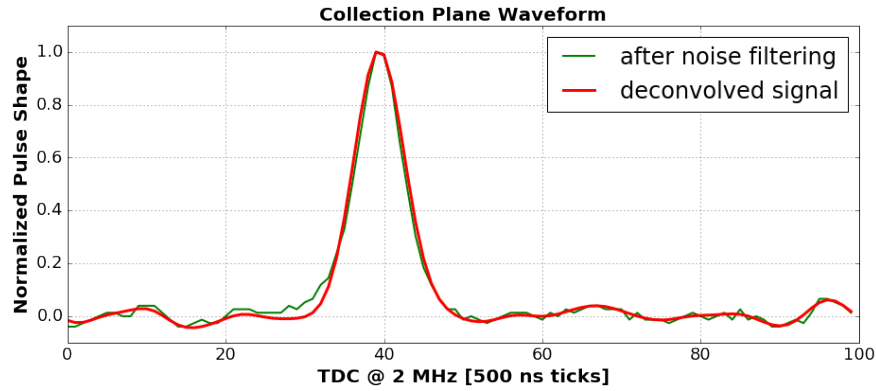
(b) Collection-plane signal before (blue) and after (green) noise-filtering is applied.

Figure B.1: TPC signals before and after noise-removal.

A subsequent reconstruction step is applied to first identify Regions of Interest (ROIs) associated with TPC signals, and subsequently deconvolve the localized pulses. The deconvolution step aims to remove the impact of the signal shaping induced by both the electronics and the field response in the TPC, in order to recover the original profile of charge drifting pass or being collected on a wire. Figure B.2 shows the impact of deconvolution on the same TPC signals. The deconvolution applied aims to recover the expected Gaussian distribution of drifting charge. The impact on induction-plane wires is substantial, while relatively minor on the unipolar collection-plane.



(a) Noise-filtered (green) and deconvolved (red) signal from an induction-plane wire.



(b) Noise-filtered (green) and deconvolved (red) signal from a collection-plane wire.

Figure B.2: TPC signals before and after deconvolution.

B.2 Hit Finding

The final stage in the reconstruction of one-dimensional signals is referred to as “hit-finding”. Identified ROIs are fit to one or multiple Gaussians. Figure B.3 shows a small region of the collection-plane with two intersecting cosmic-ray muons. The waveforms shown in the image are from the wires surrounding the intersection of the signals. Each reconstructed hit is associated with a time, defined as the mean of the Gaussian fit, and RMS, given by the Gaussian width. The charge associated to each pulse is quantified by the hit integral, defined as the integral of the Gaussian fit to the waveform.

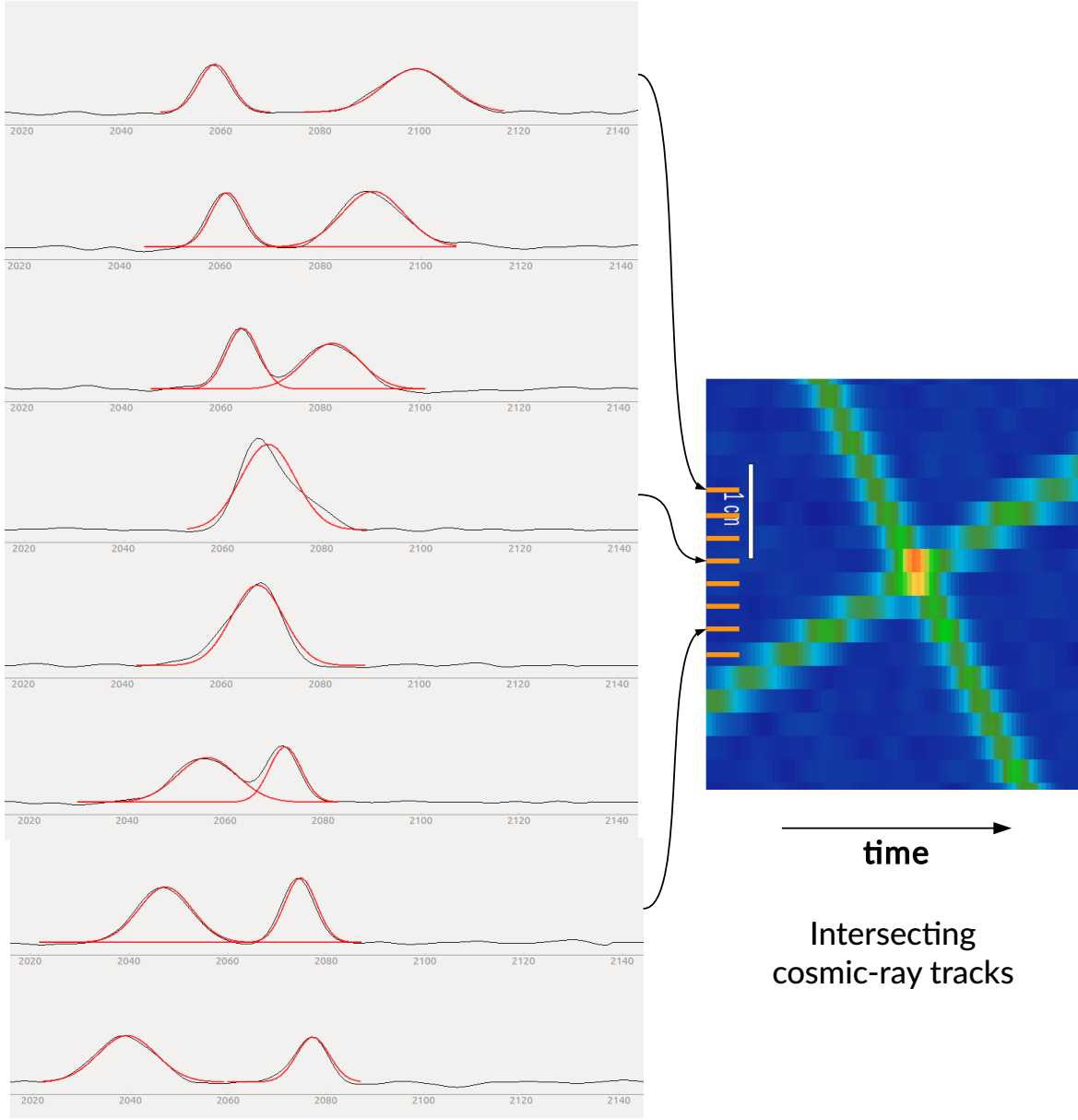


Figure B.3: Left: the red curves in the diagram represent the Gaussian fits to the underlying waveforms used in the hit reconstruction. The units of the x-axes are in 500 ns time-ticks. The consecutive waveforms shown are taken from neighboring wires surrounding the intersection of two cosmic-ray muons, for which the deconvolved wire signal is visible in the image on the right.

Reconstructed hits are then passed down to higher-level reconstruction routines which perform 2D and 3D pattern recognition to identify topologies associated with particle energy deposition in order to reconstruct their kinematic quantities.

Appendix C

Detector Energy Calibration

This chapter describes the detector energy calibration and is divided in four sections. The first presents the various physics effects which occur in the detector volume responsible for translating deposited energy into charge collected by the TPC sense-wires. These are the effects of argon ionization, ion recombination, and electron attenuation. Each is discussed in section C.1 and their impact on signal formation quantified from previous or in-situ measurements, along with an associated systematic uncertainty. Section C.2 presents the calibration of the detector's energy response performed using samples of stopping muons. Section C.3 presents measurements of detector response variations in position across the TPC and particle propagation direction with respect to the wire-plane orientation. These measurements will be used to normalize the response across the detector volume. Finally, the last section (C.4) addresses aspects of the energy calibration specific to EM showers.

C.1 Ionization Energy Loss and Signal Formation

Charged particles traversing a material lose energy by ionizing and exciting atoms within that material. Excitation, which causes electrons to move to a higher atomic orbital, manifests itself primarily as emission of light. Ionization produces a trail of charge which maps out the charged particle's path. Ionization electrons can then re-interact with nearby positive argon ions, or be absorbed by impurities as they drift in the detector, leading to an effective quenching of the collected signal. The production rate of ionization electrons, and loss due to such effects must be properly

accounted for in order to correctly calibrate the detector. Equation C.1 parametrizes the transformation from energy lost (ΔE) to charge collected on TPC wires (ΔQ). W_{ioni} measures the average energy expended per ion pair. R measures the quenching due to ion recombination. The last term accounts for the signal loss due to electron absorption by impurities, and depends on the drift time t of the electrons. This section presents the measurements obtained for these values, either from MicroBooNE data or external results, and the associated estimated systematic uncertainties.

$$\Delta Q = \Delta E \times W_{\text{ioni}} \times \frac{1}{R} \times e^{-t/\tau}. \quad (\text{C.1})$$

C.1.1 Ionization Energy W_{ioni}

The average energy expended per ion pair created, W_{ioni} , depends on the complex electron cloud structure surrounding the nucleus. The value of W_{ioni} has been determined experimentally [85] by measuring 0.976 MeV electrons from a ^{207}Bi source in a liquid argon chamber at high electric field (up to 20 kV/cm) with calibrated electronics, and determined to be equal to $23.6 \pm 0.3 \text{ eV}/e^-$.

C.1.2 Ion Recombination

Recombination is the process by which ionized electrons are attracted by the positive ions produced along a particle's trajectory to re-form neutral argon atoms, which leads to a reduction of the number of drifting electrons. Its magnitude depends on the local ion density and amount of time ions spend in close proximity. In this analysis we model the effects of recombination according to the treatment and results obtained by the ArgoNeuT experiment [76]. The recombination factor R is defined as

$$dQ \times \frac{W_{\text{ioni}}}{e^-} = dE \times R \left(\frac{dE}{dx}, E_{\text{field}} \right). \quad (\text{C.2})$$

where dQ denotes the amount of ionization charge and dE the amount of energy deposited over some distance. dE/dx is the local energy deposition per unit distance and is the observable used to account for ion density. E_{field} is the magnitude of the electric field (273 V/cm for MicroBooNE) which impacts the length of time ions are close enough for them to recombine. ArgoNeuT makes use of the Modified Box Model [76] to convert from charge to energy:

$$\frac{dE}{dx} = \frac{e^{\beta \times \frac{W_{\text{ioni}}}{e^-} \frac{dQ}{dx}} - \alpha}{\beta}. \quad (\text{C.3})$$

Given equations C.2 and C.3, we can express the recombination factor R as

$$R = \frac{\ln\left(\frac{dE}{dx} \times \beta + \alpha\right)}{\frac{dE}{dx} \times \beta}, \quad (\text{C.4})$$

with the constants α and β given by

$$\begin{aligned} \alpha &= 0.93 \pm 0.02, \\ k_b &= 0.212 \pm 0.002 \left[\frac{\text{g} \times \text{kV}}{\text{MeV} \times \text{cm}^3} \right], \\ \beta &= \frac{k_b}{\rho [\text{g/cm}^3] \times E_{\text{field}} [\text{kV/cm}]} = 0.562 [\text{cm/MeV}], \end{aligned} \quad (\text{C.5})$$

with ρ denoting the density of liquid argon and E_{field} the strength of the electric field in the TPC. The values of α and k_b come from ArgoNeuT's results. Figure C.1 shows the recombination factor R calculated using the Modified Box recombination model, as a function of dE/dx .

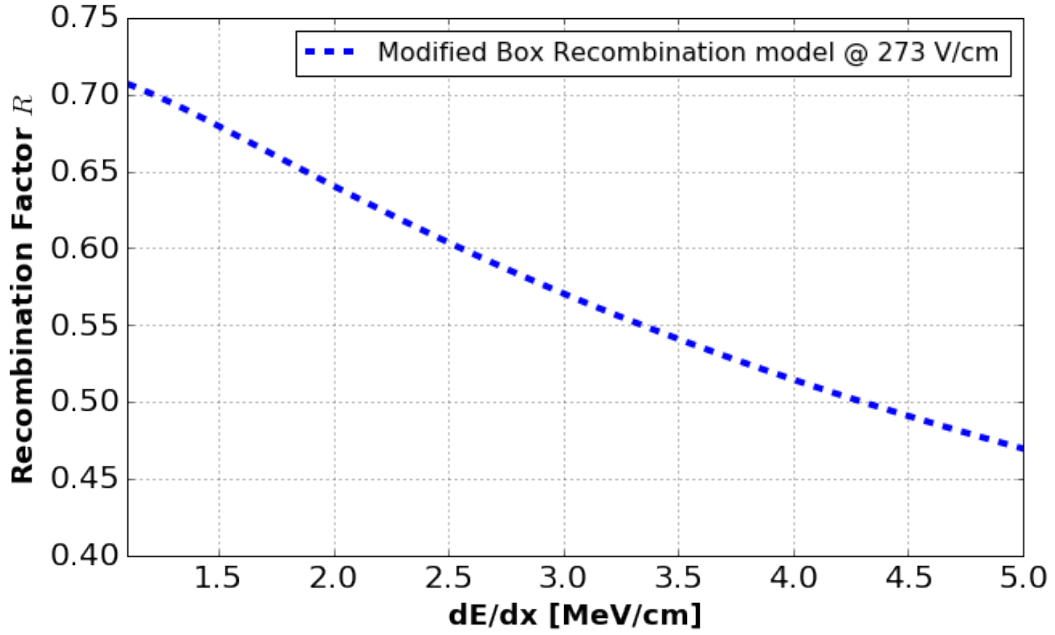


Figure C.1: Recombination factor measured according to eq. C.5 as a function of dE/dx for an electric field of 273 V/cm.

The uncertainty on R for MIP-like energy deposition associated to the error on the model parameters α and β is 1.5%.

While the Modified Box recombination parametrization adopted by the ArgoNeuT collaboration is driven by an underlying physical model, it is not the only such parametrization devised. The Birks model of recombination, used by the ICARUS collaboration [77], presents an alternative form for recombination, while depending on the same observables of electric field and dE/dx . The two models differ primarily at high energy loss density (dE/dx) and are virtually identical in the ~ 2 MeV/cm energy loss regime of interest for electrons, photons, and minimally ionizing muons. For an energy loss of 2 MeV/cm, at MicroBooNE's electric field, the variation in recombination factor for the two models is of order 0.05% and thus presents a negligible systematic.

The MicroBooNE electric field is known to less than one percent (272.5 ± 0.4 V/cm) and has an impact on the recombination factor, at a dE/dx of 2 MeV/cm of 0.08% which is negligible.

C.1.3 Electron Absorption by Impurities

Impurities in the argon can absorb drifting electrons as they travel from their production location towards the anode-plane wires. Assuming a uniform concentration of these impurities, the impact on signal quenching can be modeled by an exponential probability for ions to be absorbed defined by a characteristic lifetime τ such that

$$Q = Q_0 \times e^{-t_{drift}/\tau} \quad (C.6)$$

With Q_0 denoting the ionization charge originally produced, τ the measured electron lifetime, and t_{drift} the drift-time for the ionization cloud, which is related to the energy deposition drift-coordinate location by the drift-velocity ($v_{drift} = 0.1114$ cm/ μ s). The low concentration of impurities measured by the MicroBooNE argon filtration system [82] causes the impact of ion absorption to have a relatively minor contribution on the drift-dependent calorimetric response in the TPC. A preliminary measurement of the electron lifetime [83] shows that during nominal operations the ratio of charge collected at the anode to charge deposited at the cathode (maximal drift-distance) is greater than 0.95, corresponding to an electron lifetime greater than 45 ms.

C.2 Absolute Energy Calibration With Stopping Cosmic-Ray Muons

In order to calibrate the detector's TPC wire response we need a source of known energy deposition. Cosmic-ray muons offer a convenient source for this calibration. Given the well-known energy deposition profile of muons traveling in liquid argon, for a given point along a track we can use information on a track's residual range reconstructed using spatial-information to extract the true expected energy deposition at that location. Fig. C.2 shows the dE/dx vs. residual range (RR) profile for muons in liquid argon. The red curve shows the average energy loss per unit distance. In blue is the most probable value (MPV) of the energy loss distribution. The difference between these quantities is due to the skewed energy loss distribution which follows a Landau-Vavilov function and is referred to as the straddling function. While the average energy loss per unit distance is independent of the distance traveled by the particle, the shape of the straddling function varies, causing the MPV to be thickness dependent. This dependence goes as $a + b \log(\eta)$ with η the thickness. This effect is shown in figure C.2 by the different blue curves showing the energy-dependent MPV for different thickness values.

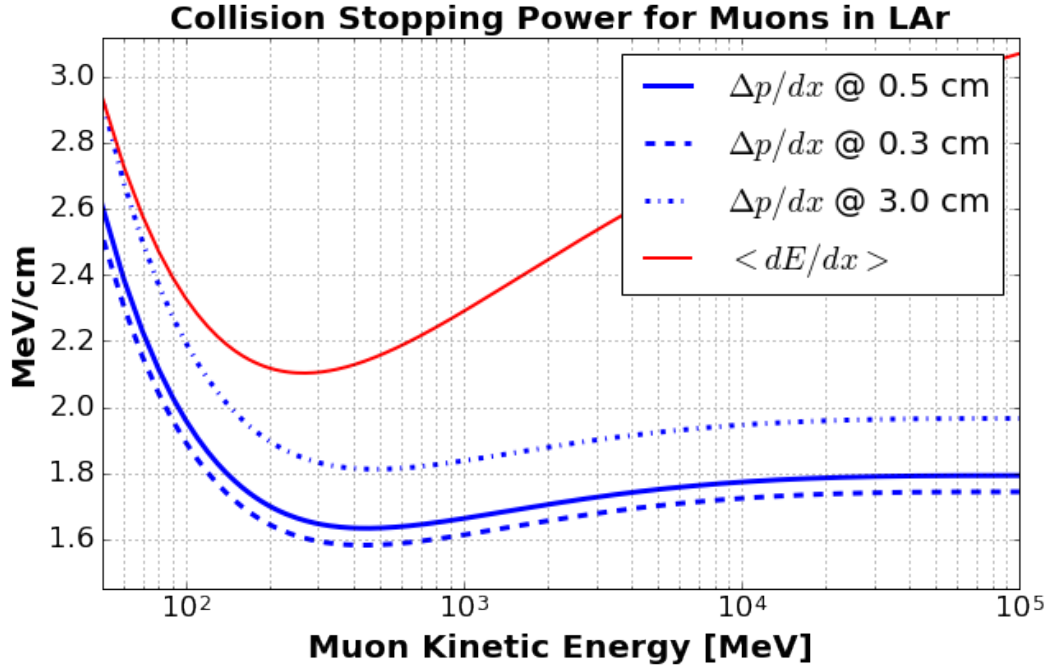


Figure C.2: Energy loss for muons in argon. Blue data-points represent the MPV energy loss for different thickness values. In red is the average energy loss.

The MPV's dependence on thickness has a significant impact on the calibration performed in this analysis. This is particularly true for a calibration with cosmic-ray muons, which span a wide range of angles with respect to the sense wire direction, resulting effectively in a wide distribution of thickness values contributing to the measured energy loss. As shown in figure C.3, the MPV value expected for tracks traversing the detector at different angles (pitch) with respect to a wire-plane varies substantially. The overall variation is of order 10%. If this effect is not correctly accounted for, the absolute energy calibration will therefore suffer by a systematic error of order 10%.

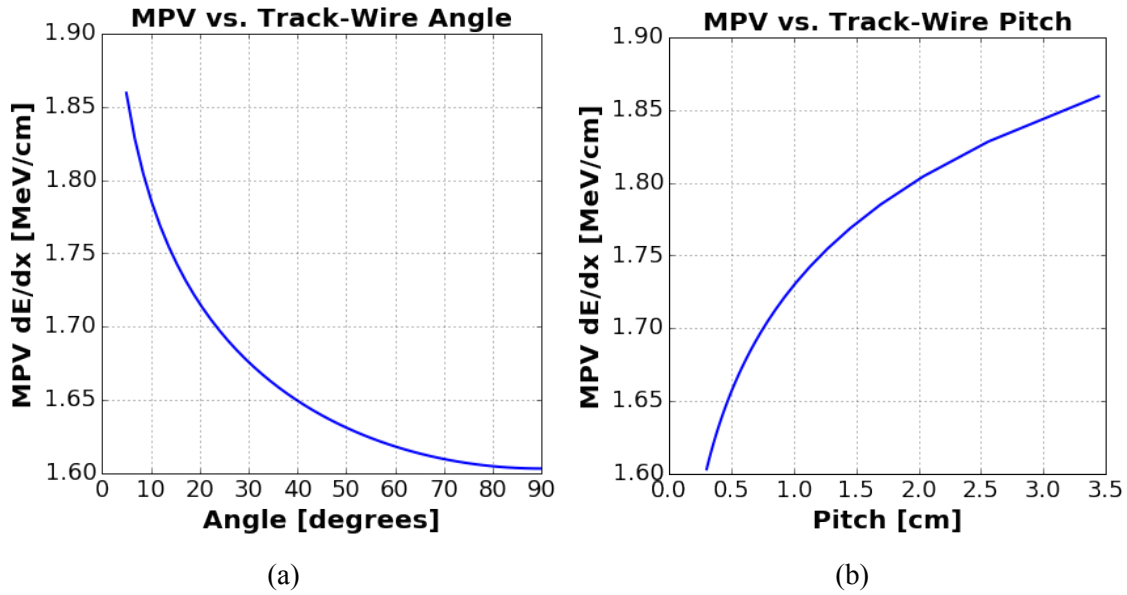


Figure C.3: (a) MPV vs. angle between wire direction and track-direction. (b) MPV vs. track-wire pitch. These curves are produced for muons of 266 MeV of kinetic energy, the point at which they are minimally ionizing.

C.2.1 Stopping Muon Energy Loss Profiling

We dedicate this section to describe how, given a reconstructed 3D track, we obtain a profile of the reconstructed calorimetry information in a way that can allow us to identify and isolate stopping muon tracks.

For each reconstructed track a calorimetry reconstruction module is run tasked with measuring, for all 3D points along the track, the quantities of dQ/dx in ADC per cm and residual range, in cm. The measured dQ/dx uses the charge measured from reconstructed hits (see chapter B), and accounts for the separation between neighboring wires in the direction of propagation of the track.

Fig. C.4 shows the profile of dQ/dx vs. RR for a well reconstructed stopping muon track. Red dots represent the measured dQ/dx along the track. One can observe that while the characteristic Bragg-peak at low RR is noticeable, there is a lot of jitter in the plotted points, partially due to the impact of extra energy from possible δ -rays, partially to the Landau nature of the distribution of energy deposition, as well as from any reconstruction artifacts introduced.

Profiling with an algorithm a stopping muon from the raw dQ/dx charge is difficult. To overcome this the quantity of truncated local dQ/dx ($TLdQdx$) is employed. This quantity is computed by averaging, in a neighborhood of each point, the local dQ/dx values after removing values which fluctuate significantly from the local median. The precise definition of how this metric is computed is described in the following section C.2.2. Fig C.4 shows in blue the profile obtained when using the computed $TLdQdx$. The significantly smoother distribution will allow for a much simpler algorithmic recognition of stopping muons which relies on the identification of the Bragg peak. We note that the $TLdQdx$ metric is biased with respect to the true measured charge along the track. While this metric provides an ideal way to identify stopping muons, the raw dQ/dx will be used to calibrate the detector response.

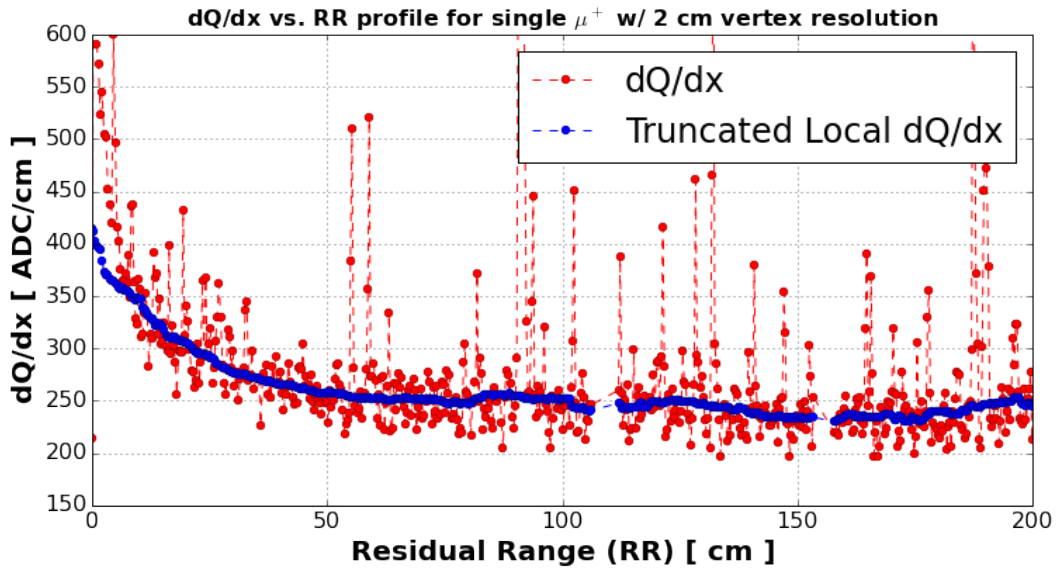


Figure C.4: dQ/dx vs. RR profile for a well reconstructed stopping muon from simulation. Red points denote the raw dQ/dx measured in ADC/cm from the calorimetry reconstruction module. Blue points denote the measured $TLdQdx$.

C.2.2 Truncated Local dQ/dx

The truncated dQ/dx is computed given measured dQ/dx and RR values as follows:

1. For each dQ/dx value, a list of neighboring dQ/dx values $dqdx_v$ is produced, selecting points within a RR range of 10 cm.
2. The median and rms of $dqdx_v$ values are calculated.
3. A subset of values from the $dqdx_v$ list is selected, requiring that they fall within the range $[\text{median}-\text{rms}, \text{median}+\text{rms}]$.
4. The average of this sub-sample is taken as the truncated local dQ/dx .

The code in which this function is implemented can be found at the following URL: <https://github.com/davidc1/CaraTool/blob/master/3DMichel/TruncMean.cxx>.

C.2.3 Parametrization of Muon Energy Loss Profile

Given the profiled $TLdQdx$ we next develop a series of metrics aimed at identifying stopping muons. We design metrics that measure the relative amplitude of charge associated with the muon's Bragg peak with respect to energy deposited in the MIP region. This relative measurement is important as it allows us not to depend on the absolute calorimetry, which may introduce a bias in the stopping muon selection in data vs. MC.

Each muon's profile is separated in three RR ranges: $[0,50]$, $[50,100]$, and $[100,150]$ cm. The 100 to 150 cm range, expected to be very uniform, is used to measure an approximate value for the MIP dQ/dx for this track. The $TLdQdx$ values measured are then normalized to the obtained MIP measure. Figure C.5 show the same track as in Fig. C.4, normalized by the measured MIP response, and split in the three sections of interest.

Based on the normalized $TLdQdx$ we next calculate the following quantities:

1. BA0: the MIP-subtracted integral under the normalized $TLdQdx$ profile in the RR range of 0-50 cm (red shaded region in Fig. C.5).
2. BA1: the MIP-subtracted integral under the normalized $TLdQdx$ profile in the RR range of 50-100 cm (purple shaded region in Fig. C.5).

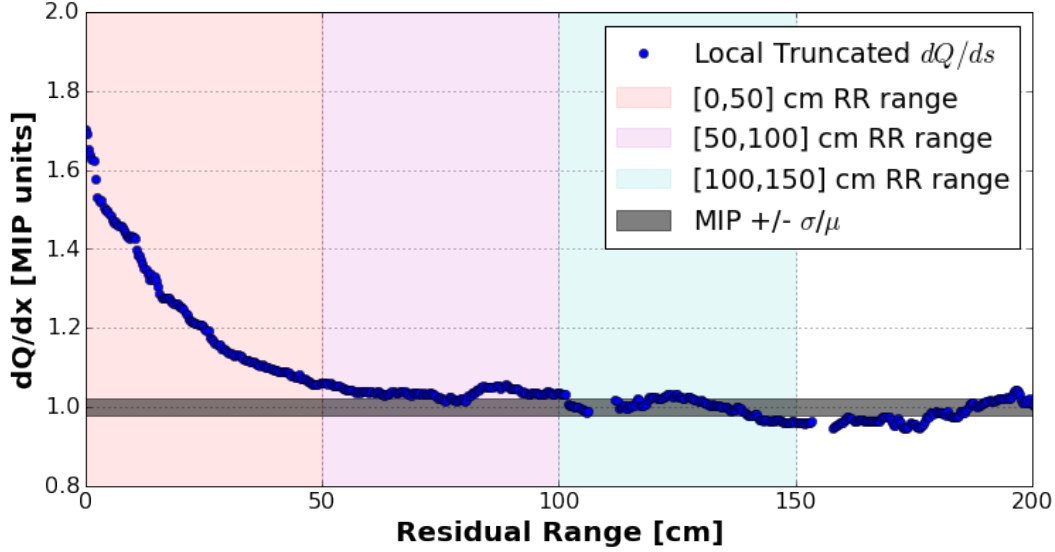


Figure C.5: dQ/dx vs. RR profile for a well reconstructed stopping muon from simulation. The blue points denote the measured $TLdQdx$. The $TLdQdx$ is normalized to the MIP $TLdQdx$ calculated by finding the average $TLdQdx$ in the $[100,150]$ cm RR interval. The width of the grey line at $y=1$ is given by the standard deviation of the $TLdQdx$ in the $[100,150]$ cm RR interval.

3. Y_0 : The intercept on the y-axis at $= 0$ from a quadratic polynomial fit to the normalized $TLdQdx$ vs. RR performed for RR values < 50 cm.

These three metrics are expected to help us separate stopping muon tracks which present a well-reconstructed Bragg peak, from through-going muons or otherwise broken tracks. We expect, qualitatively, $BA0$ to be large, while $BA1$ should be small as the track profile in the range $[50,100]$ cm is still relatively flat. The intercept obtained from the quadratic fit will further help us separate tracks by measuring to some degree the shape of the Bragg peak profile.

In order to obtain selection cuts we produce distributions of $BA0$, $BA1$, and Y_0 . These are shown in figures C.6(a), (b), and (c) respectively. These distributions are obtained from a sample of all reconstructed tracks (blue) and well-reconstructed stopping muon tracks which end within 2 cm of the true muon end-point (red).

C.2.4 Selection of Stopping Muons

Our goal is to obtain a high-statistics, pure sample of reconstructed stopping-muon tracks with well reconstructed calorimetry information. This will allow us to build a dE/dx vs. RR profile from which to extract a calibration constant to go from ADC to collected e^- on the wires.

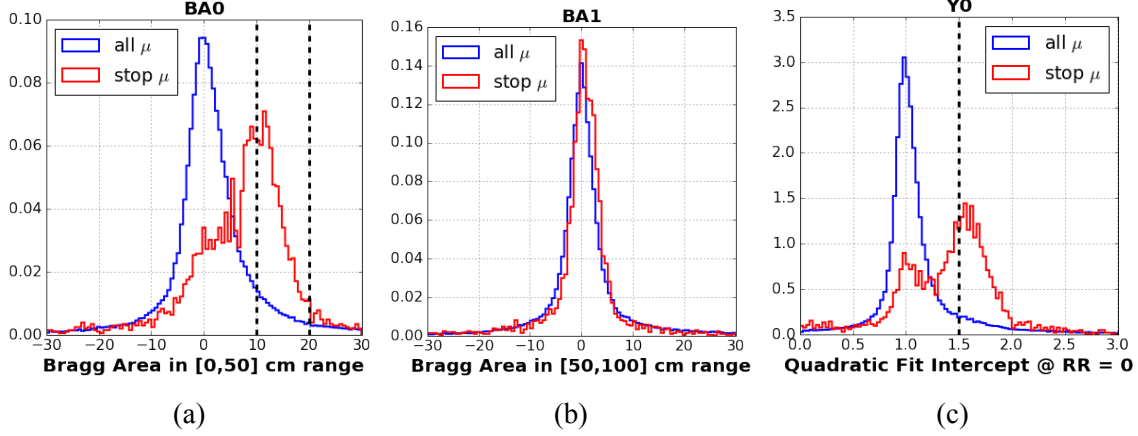


Figure C.6: (a) BA0 and (b) BA1 distributions in MIP units calculated in the [0,50] and [50,100] cm RR ranges, respectively. (c) Y_0 distribution. In blue we show distributions for all tracks longer than 150 cm which stop at a Z coordinate > 500 cm. In red we show the subset of tracks with reconstructed end-point within 3 cm of a true stopping muon location. Black vertical lines show cuts applied which will be described in sec. C.2.4.

To obtain this sample we use 3D tracks reconstructed with the `pandoraCosmic` tracking algorithm. Cuts are studied on a sample of Corsika-simulated cosmics. A sample of 19,000 cosmic simulated events is used. We list and describe the cuts in the following bullet-points:

1. Only tracks which stop at $z > 500$ cm are selected. This ensures the tracks come from a region which has a rather uniform response. All reconstructed tracks with length larger than 150 cm are selected. This is to ensure that the track is long enough to be able to profile the dQ/dx vs. RR .
2. Tracks which end below $Y_{stop} = -98$ cm are excluded: these are most likely exiting tracks. The value of -98 rather than -116 (the detector boundary) is motivated by the impact of space-charge (see figure C.7 (c)).
3. To account ADC-truncation artifacts tracks with end-points in $X < -40$ and > 290 cm are removed. Tracks exiting the front and end of the TPC ($Z < 10$ and > 1020) are removed. Tracks ending in the dead-wire region $Z > 697$ and $Z < 740$ are removed (see figures C.7 (b,d)).
4. Tracks exiting the anode and cathode are removed. This is done by matching all tracks to the nearest flash in time assuming the track-time. Tracks with a flash within $14 \mu s$ are removed.

The cut value is based on the distributions of figure C.7 (a).

5. The following cuts are applied to separate stopping muons with calorimetry: $BA0 > 10$ and < 20 (Fig. C.6(a)). $Y_0 > 1.5$ and < 2.0 (Fig. C.6(c)).

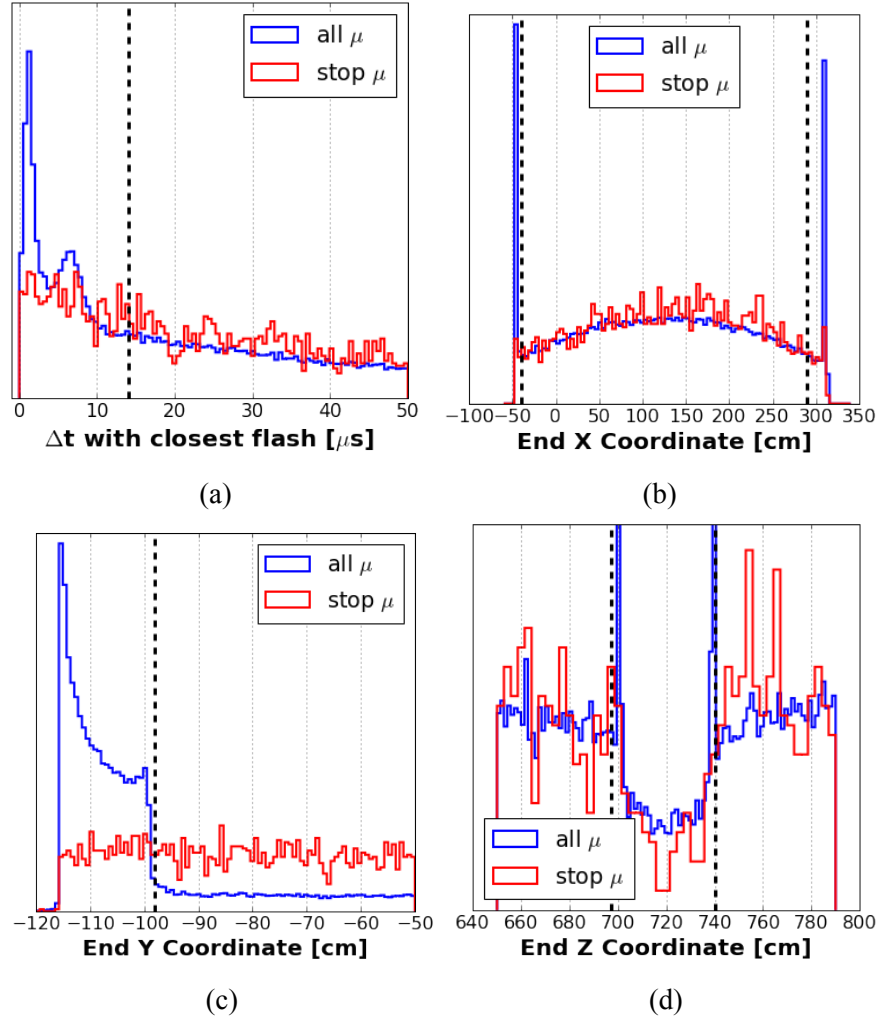


Figure C.7: (a) Time difference between reconstructed track time using the track end-point assuming it exits the anode or cathode and the nearest reconstructed optical flash time. In blue is the distribution for all tracks, with two peaks at 2 and 7 μ due to anode- and cathode-crossing tracks respectively. In red is the distribution for true stopping muons. (b) End x-coordinate for reconstructed tracks. Spikes at $x = -50$ and 300 are due to the ADC truncation performed in the reconstruction. These tracks, while exiting the detector, may be mistaken as stopping and are excluded. (c) End Y coordinate. Tracks which exit the bottom of the detector are removed. The cut is placed at $Y = -98$ cm to account for space charge. (d) Track which have a reconstructed end Z position in a region affected by dead-wires are excluded.

In the table below we list the impact of these cuts on the purity and efficiency of selecting stopping muons. The purity is measured by calculating the fraction of selected reconstructed tracks with an end-point within 10 cm of a true muon stopping point in the same event. This distance is calculated in the 2D YZ projection. The x-coordinate is excluded as no t_0 reconstruction for the selected tracks is performed and this quantity is thus offset with respect to the true drift-coordinate position.

Table C.1: Table presenting the performance of the selection as various cuts are applied.

cut	total tracks	stop muons	stop μ /event	purity [%]
1) Length > 150 cm	92k	4,596	0.24	4.99
2) $Y_{stop} > -98$ cm	31k	3,761	0.20	11.77
3) Z and X end-point cuts	17k	3,297	0.17	19.17
4) $\Delta t > 14 \mu s$	4,321	2,393	0.13	55.38
5) Bragg Peak cuts	669	623	0.03	93.1

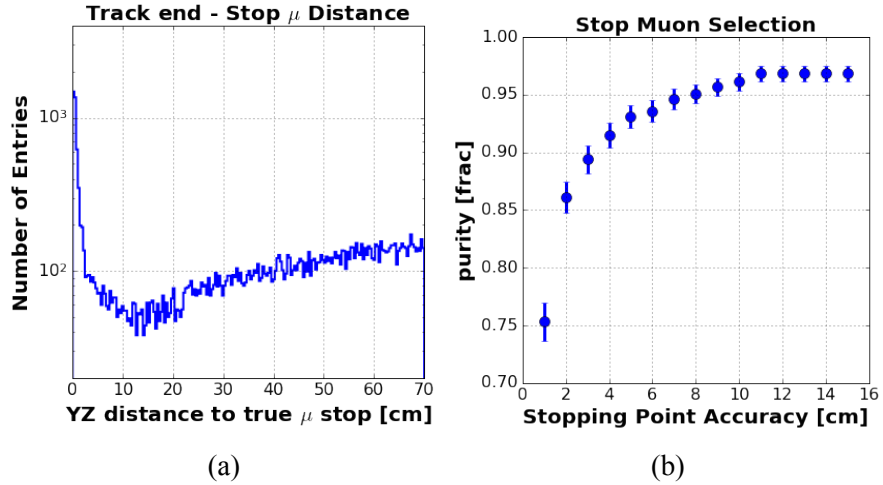


Figure C.8: (a) Separation, measured in 2D with YZ coordinates, between all reconstructed track end-points and true muon stopping points in the detector. (b) Purity of selection after applying the cuts of table C.1 as the requirement on the distance between reconstructed end-point and true stopping point is varied.

After applying these cuts we obtain a sample of well-reconstructed stopping muon tracks with a purity of more than 90% with approximately 1 reconstructed track for every 30 cosmic events.

C.2.5 Gain Extraction

The same selection performed in simulation is applied to reconstructed tracks from data. The only cut applied differently is the dt cut to remove tracks exiting from the anode and cathode. A cut value of $30 \mu s$ is applied, justified by the different distribution of dt values. The distribution of uncalibrated dQ/dx vs. residual range for selected tracks from data is shown in figure C.9.

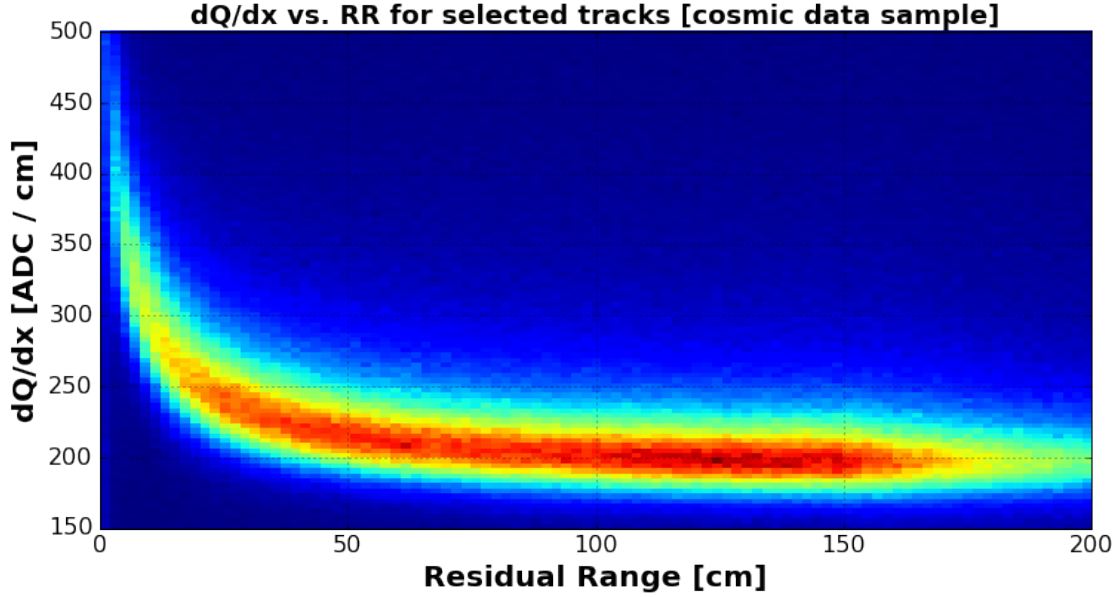


Figure C.9: Measured dQ/dx vs residual range for tracks selected from data cosmic events.

To obtain a measurement of the gain a minimization of the measured MPV dE/dx compared to the theoretical value is performed by varying the applied electronics gain. Data points are required to come from tracks with reconstructed pitch values in the range 0.3-0.4 cm, and the theoretical MPV value is computed for a pitch of 0.35 cm. The variable which is minimized is the χ^2 as defined in equation C.7.

$$\chi^2 = \frac{1}{N} \frac{(\text{MPV theory} - \text{MPV measured (gain)})^2}{\sigma^2} \quad (\text{C.7})$$

The uncertainty σ of equation C.7 is contributed by the uncertainty of the best-fit MPV value, in addition to systematic effects, described below.

Treatment of Systematic Uncertainties The following sources of systematic uncertainty are considered. **Non-uniformities** by limiting the selection to $Z > 500$ cm we have isolated the most

significant variations in response on collection-plane wires due to shorted and other malfunctioning wires. Remaining position-dependent variations due to space-charge and lifetime are minor and cause an overall smearing of the calorimetric response and are not expected to bias the measurement. **Recombination** A systematic of 1.5% is assigned to the recombination correction applied to account for the 1σ uncertainties on the fit parameters for the Modified Box model applied in this analysis. The small uncertainty on the measured electric field in MicroBooNE has a negligible impact on the recombination correction. **Methodology** A 1% systematic is applied to account for the $\sim 1\%$ fluctuations in dE/dx values measured for simulation at large residual range. **Vertex Resolution** Because the calibration is performed at large residual range, where there is relatively small variation in the MPV value, vertex resolution has a negligible impact on the extracted gain.

The χ^2 as a function of applied gain is shown in figure C.10. The best-fit value is $239.8^{+1.8}_{-1.9} e^-/\text{ADC}$.

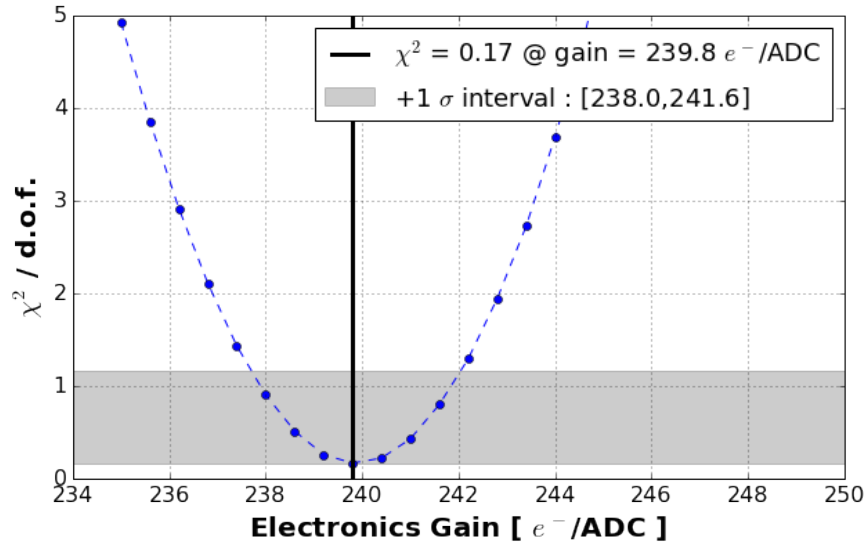


Figure C.10: χ^2 minimization employed to obtain the electronics gain extraction.

Examples of the extracted MPV value at different values of residual range, for the best-fit gain of $239.8 e^-/\text{ADC}$ are shown in figure C.11.

A comparison of extracted MPV values in data to theory is shown in figure C.12. The gray shaded area shows the range of values where minimization of residuals of measured MPV to theory was performed. The fitted MPV values exhibit fluctuations of order 2%. A kinetic-energy dependent bias is visible in data, where at lower energies the measured MPV is slightly larger

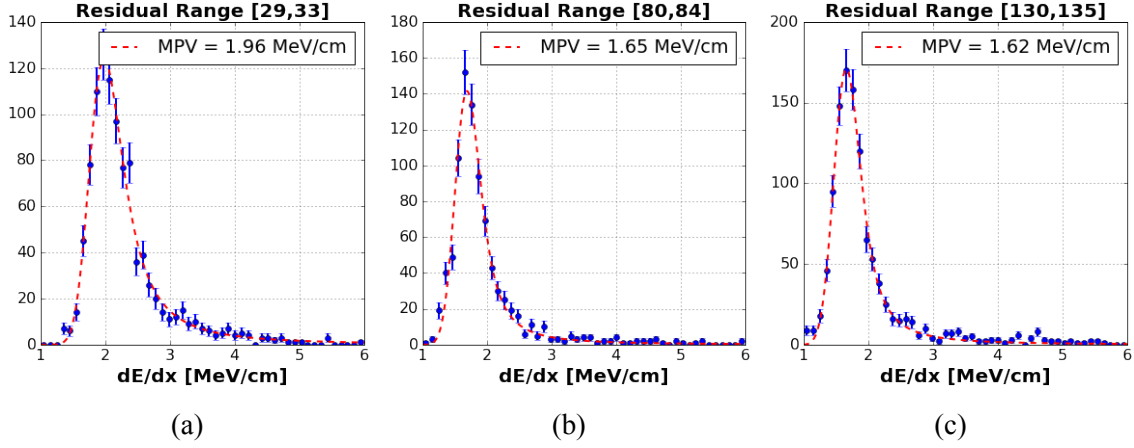


Figure C.11: Landau convolved with Gaussian fit to dE/dx distribution at residual range values of 29-33, 80-84, and 130-135 cm.

then that in the MIP region. This $\sim 3\%$ difference could be attributable to biases introduced by the selection, or a percent-level inconsistency in the recombination model applied in this analysis.

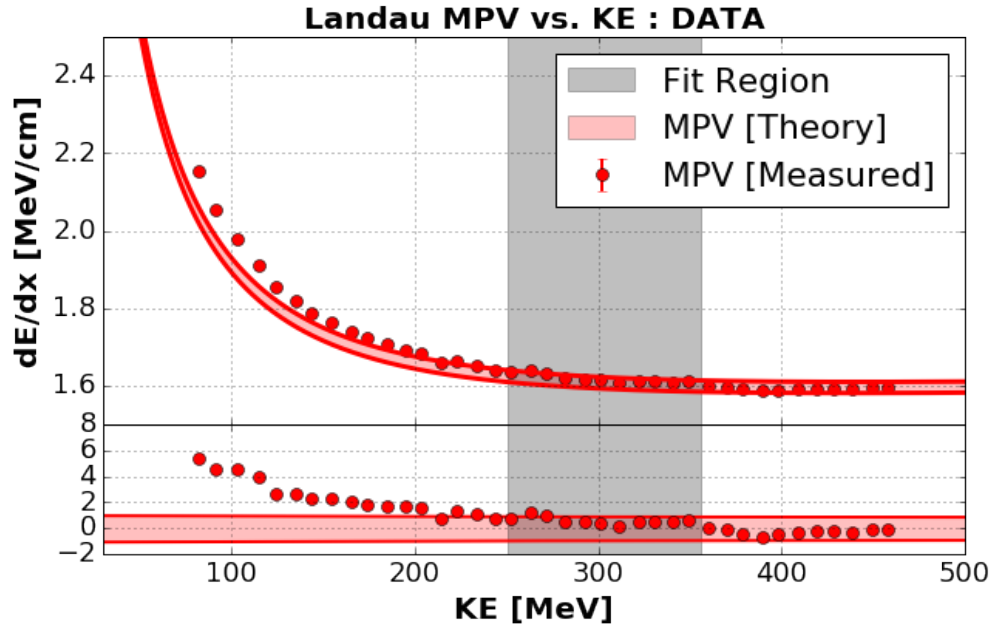


Figure C.12: Measured MPV vs kinetic energy for tracks selected from data, compared to theoretical values. The shaded red region denote the expected MPV for thickness values in the range 0.3-0.4 cm. The gray shaded region represents the values of residual ranges in which the minimization employed to extract a gain was performed. The bottom plot in the figure shows residuals, in percentage values.

We compare the energy reconstructed through calorimetry and range for selected tracks. This comparison is shown in figure C.13. The distribution peaks at 1.03, providing a data-driven vali-

dition to the gain extracted, to within 3%. The range-based muon energy measurement has been validated to be accurate to within 1% in simulation.

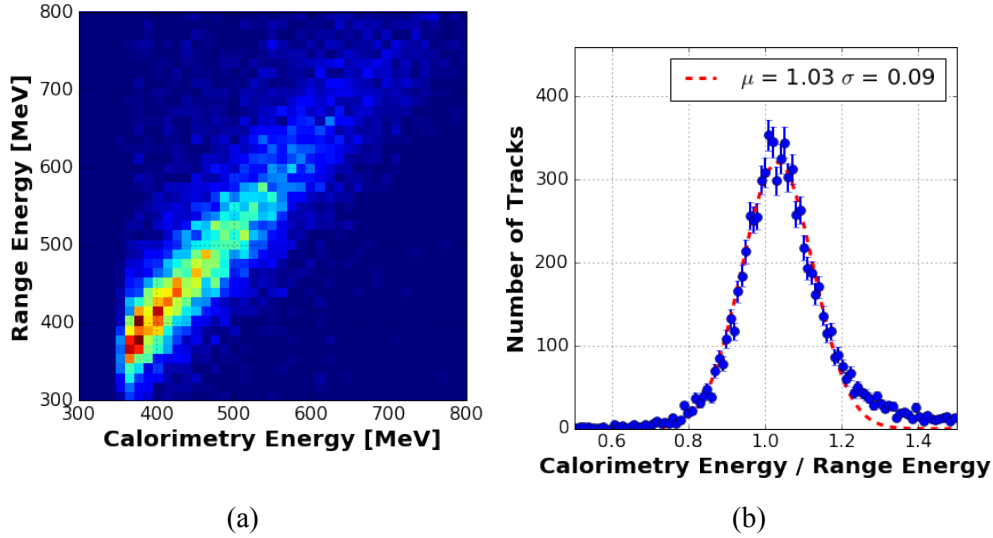


Figure C.13: Calorimetry-based energy vs. range-based energy for selected stopping muons from data. The calorimetry-based gain is computed by employing the extracted gain of $239.8 \text{ } e^-/\text{ADC}$.

C.2.6 Angular Dependence of Most Probable Value

As discussed previously the MPV of an energy loss distribution varies depending on the thickness of material traversed. In a LArTPC this results in an angular, or pitch dependence due to the preferential direction of each wire-plane. We measure the pitch-dependence of the extracted MPV and compare the obtained values to the theoretical expectation. To perform this study we restrict ourselves to tracks which are predominantly perpendicular to the drift-direction, in order to exclude the impact of signal-processing on the calorimetry extracted for pulses which are significantly stretched in time. Selected tracks must be at angles in the range 70-110 degrees with respect to the drift direction. Figure C.14 shows this measurement. Other than for one data point at a pitch of ~ 0.8 , the trend observed in data matches what expected: larger pitch values correspond to larger MPV. While overall the trend expected from theory is observed, there is significant deviation at larger pitch values. The overall discrepancies are of order 3%.

The measured gain of $239.8^{+1.8}_{-1.9} \text{ } e^-/\text{ADC}$ accounts for uncertainties associated to the recombination model and method employed to extract the gain. We additionally account for a systematic

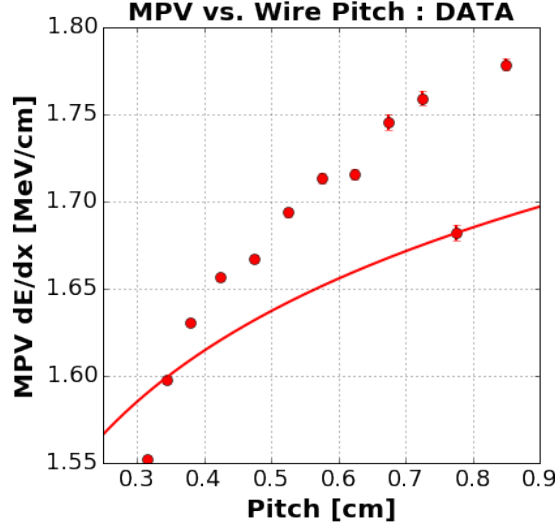


Figure C.14: Angular dependence of MPV in simulation (a) and data (b) compared to theory.

uncertainty of 3% attributable to the 3% offset observed in calorimetric vs. range-based energy measurement (figure C.13), as well as the overall discrepancy in MPV vs. pitch (figure C.14) caused by higher order angular effects which impact the calorimetry. The measured gain with full systematic uncertainty is

$$\frac{e^-}{\text{ADC}} = 239.8 \pm 7.4 = 239.8 \times [1 \pm 0.031]. \quad (\text{C.8})$$

C.3 Calibration of Non-Uniformities in Detector Response

Nonuniformities in the detector response can lead to a misreconstruction of energy deposited in the TPC and a smearing of the calorimetric energy resolution. In this section we identify and discuss the primary sources of detector response non-uniformities in MicroBooNE's LArTPC and perform studies to estimate their impact, and correct for these effects when appropriate.

We identify two causes for nonuniformities in the detector response. The first is caused by the underlying physics of energy deposition and transport of ions in the detector, while the second is introduced by signal-formation and reconstruction effects such as response variation across TPC channels and reconstruction artifacts. It is important to note that while a LArTPC is a total-absorbing calorimeter, it is a biased one. A wire's orientation with respect to the direction of a traversing particle causes a variation in response which impacts the calorimetry.

The main sources of response variation across the detector caused by physics effects are space-charge and ion-absorption. The space-charge effect consists of the accumulation of positive argon ions (which drift a factor of 10^3 times slower than electrons). This build-up of ions distorts the local electric field, which leads to position-dependent variations in the drift time and recombination across the detector. Preliminary work on modeling the space-charge effect in MicroBooNE can be found in reference [81], which shows qualitative agreement with measurements from data. Electron absorption by impurities is proportional to the drift time, and thus manifests itself as an X -coordinate dependent effect.

Response variations due to signal processing and reconstruction artifacts are largely caused by the variation in field response near the anode-plane wires caused by unresponse, mis-configured, and otherwise damaged TPC wires. Variations in the bias voltage applied to TPC wires impacts the shape of signals on all wires in their proximity.

A source of through-going cosmic muons for which reconstructed T_0 information is available [80] allows to recover X , Y , Z , and dQ/dx information associated to energy deposition along their trajectory. This information is used to build calibration maps which span the 3D detector volume. Through going cosmic-ray muons cover a range of energy between ~ 1 and 10 GeV [79], which leads to a variation in MPV dE/dx of approximately 5%. For each TPC cell we measure the truncated mean value of the dQ/dx distribution, which closely maps the MPV value. Combined with the high-statistics sample which guarantees uniform coverage in muon energy across the various cells allows us to obtain a highly uniform sample of energy deposition ideal to correct for detector response variation.

Maps of the variation in response measured across the TPC are shown in figures C.15a and C.16 as a function of X vs. Y and Z vs. Y respectively. The increase in dQ/dx close to $X \sim 250$ in figure C.15a is due to buildup of positive ions near the cathode-plane). The stripes and bands visible in figure C.16 are due to variation in the field response in different regions of the there anode planes.

The variation in response as a function of track direction, measured by the Y and Z components of the track momentum, is shown in figure C.15b. Tracks moving towards the collection plane exhibit stretched waveforms which, when run through the uniform signal processing, cause a

mischaracterization of the energy deposited associated with them. This is the cause for the severe variation in response for entries at small P_z . It is worth noting that while for tracks it may be easy to account for this effect, for EM showers, where the direction associated with the fuzzy energy deposition points is not easy to recover, this is more challenging.

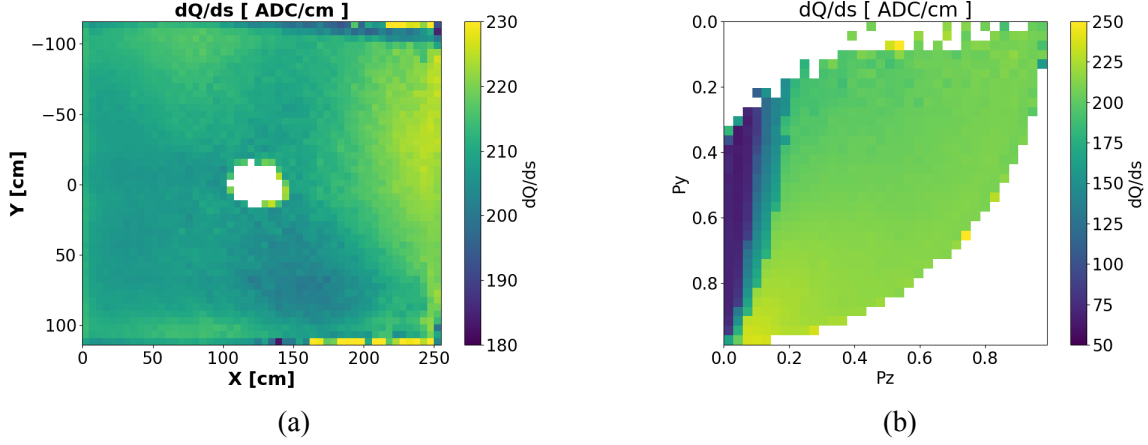


Figure C.15: (a) Response variation as a function of X and Y in the detector. Note that the top of the TPC is on the bottom of the image. The white region is due to a lack of statistics which prevent a reliable measurement of dQ/dx . (b) Response variation as a function of track direction. P_y and P_z are the components of momentum of the track.

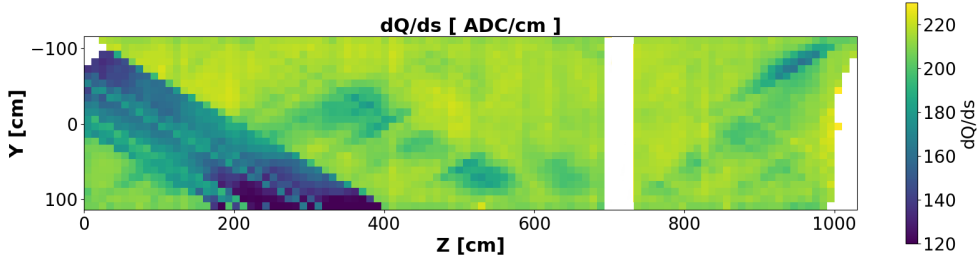


Figure C.16: Response variation as a function of Z and Y in the detector. Note that the top of the TPC is on the bottom of the image. The white region is due to a lack of statistics which prevent a reliable measurement of dQ/dx . The white region close to $Z = 700$ cm is caused by a 30 cm gap in the working collection-plane channels.

C.4 Energy Calibration for EM Showers

Section C.2 of this chapter focused on deriving calibration constants which allow to convert recorded signal amplitudes in ADC to collected charge in units of electrons e^- . This section presents the

additional steps required to go from collected charge to total deposited energy for EM activity produced by electrons and photons. Of the three physics effects presented in Sec. C.1, the argon ionization energy (W_{ioni}) and absorption of electrons by impurities are independent of the specific type of particle which leads to the energy deposition, and no further discussion is required. Ion recombination, depending on the density of energy loss (dE/dx), is impacted by the particle type and its kinetic energy. This section is dedicated to studying how to properly account for ion recombination when reconstructing the energy of electrons and photons.

Calorimetric energy reconstruction for charge deposited by ionization from tracks accounts for ion recombination by measuring the dE/dx deposited along the track on each wire, and then calculating the appropriate recombination correction factor. This is possible because for long and linear tracks measuring both dE and dx can be done precisely. For EM activity where energy is deposited over multiple electron/positron ionization segments which constantly branch out and curve significantly, measuring dx segment-by-segment is challenging. On the other hand, unlike heavier mass particles such as muons and protons, the range of energy loss for electrons is fairly uniform over a wide range of kinetic energies, and deviations from MIP-like energy deposition become significant only once the electron's kinetic energy is very small. These two observations make it reasonable to investigate the option of applying a single recombination correction to the total collected charge associated to each reconstructed EM shower, rather than a hit-by-hit correction. We define an *effective recombination factor*, R_e , which measures the impact of recombination on the total energy deposited by an EM shower. This quantity is defined as in eq. C.9

$$R_e = \frac{Q_{\text{ionization}} \times W_{\text{ioni}}}{E_{\text{deposited}}}. \quad (\text{C.9})$$

The remainder of this section is dedicated to studying the appropriate values of R_e to be used to correct for the impact of ion recombination, and validate the simulation of ion recombination in MicroBooNE when it is used as input to the choice of R_e .

C.4.1 Recombination For Continuous Collision Stopping Power Energy Loss by Electrons

Electrons depositing energy via collision stopping power exhibit a relatively constant dE/dx up until they reach very low momentum, as can be seen in fig. C.17a. In an energy range between ~ 1 MeV and 60 MeV (of interest for Michel electrons) the average dE/dx varies in the range 1.9

to 2.7 MeV/cm. The recombination factor extracted from the Modified Box model in this range varies from ~ 0.59 to ~ 0.65 , as illustrated by the grey band in figure C.17b, with $R = 0.62$ at the mid-point of 2.3 MeV/cm. We take this value of R as a reasonable estimate for the effective recombination correction to be applied to reconstructing the energy deposited by electrons in the 1-60 MeV energy range.

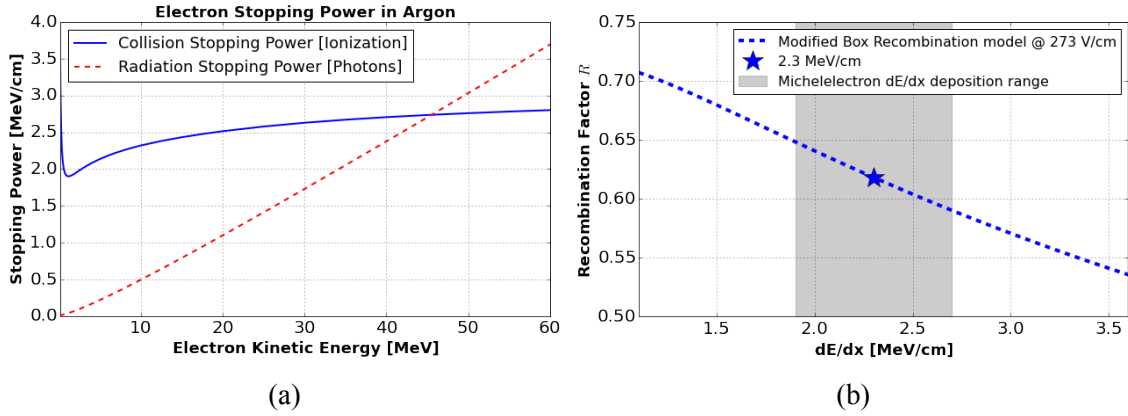


Figure C.17: (a) Energy loss from NIST ESTAR [49] for electrons in the Michel electron energy range. (b) Recombination, according to the Modified Box model, as a function of dE/dx at MicroBooNE's electric field.

C.4.2 Recombination Correction For EM Showers

Energy loss by EM showers of up to several hundred MeV covers a wide range of dE/dx stopping power. At high energies electrons ionize argon at a higher rate, and the many low-energy electrons and positrons produced in an EM shower will show contributions to energy loss from their Bragg peak. These higher dE/dx contributions will lead to an enhancement of the ion recombination effect. This section presents an overview and validation of the simulation of recombination for MicroBooNE, followed by a study of the impact of recombination on tens to hundreds of MeV γ showers which will be used for the energy calibration.

Simulation of Ion Recombination MicroBooNE simulates ion recombination as part of its detector simulation once Geant4 particle propagation has taken place. Each Geant4 particle is tracked through its path in the detector as it loses energy in steps (G4Step) which are associated with a starting and ending position, and energy lost along the way. The energy lost (dE) and step-length (dx) are used to compute the recombination factor according to equation C.5. Figure C.18 shows the

applied recombination factor vs. the kinetic energy of simulated particles produced in the propagation of 1 MeV electrons (left) and photons (right). The simulation shows to match what expected from the analytical Modified Box model, which is overlayed in black. The significant difference between electrons and photons in coverage on the R vs. K.E. plots is due to the fact that while the electron loses energy continuously following its Bragg peak curve, photons at this energy Compton scatter producing many very low energy electrons (0-100 keV) which ionize heavily and cause a lowering in the effective recombination factor. The large population of entries in both plots associated with a K.E. of 0 and at recombination factor of ~ 0.1 are associated with electrons and positrons at the very end of their Geant propagation. Even though the energy of these electrons is very small (below 250 keV of kinetic energy) they are produced copiously and contribute $\sim 6\%$ of the total energy lost by EM showers of a few hundred MeV, according to the simulation. The validation of the recombination model applied at these energies is done by comparing the R factor vs. K.E. from the simulation to results obtained by the DarkSide dark matter experiment [84], a LArTPC operating at 200 V/cm in similar conditions to MicroBooNE. The comparison shows good agreement, allowing us to validate the implementation of the recombination model at these very low energies.

Choice of Recombination Correction Factor for EM Showers Energy loss in EM showers is induced by MIP-like energy deposition of higher-energy electrons which contribute recombination factors of $\sim R = 0.6$, as well as very low energy electrons with R in the range 0.1-0.5. The effective recombination (R_e , defined in eq. C.9) is found to be very uniform across a broad range of γ shower energies (tens to hundreds of MeV), peaking at 0.572 with a FWHM of 0.018. This value of R_e is significantly impacted by the contributions to energy deposited by very low kinetic energy electrons which contribute values of $R \sim 0.1$ but which are, due to their very low energy (~ 0.1 MeV), likely not to be detected. Focusing on charge deposited above threshold, the measured value of R_e is shown in figure C.19a as a function of γ energy for a sample of simulated photons, and the distribution for all photons is in figure C.19b. By only considering charge above threshold, the effective recombination correction has shifted from 0.572 to 0.596 (4.2% difference). The distribution is still very uniform, with a FWHM of 0.017 (2.8% spread). We conclude that the use of a single value of R_e to account for ion recombination is well motivated. A value of $R_e = 0.596$

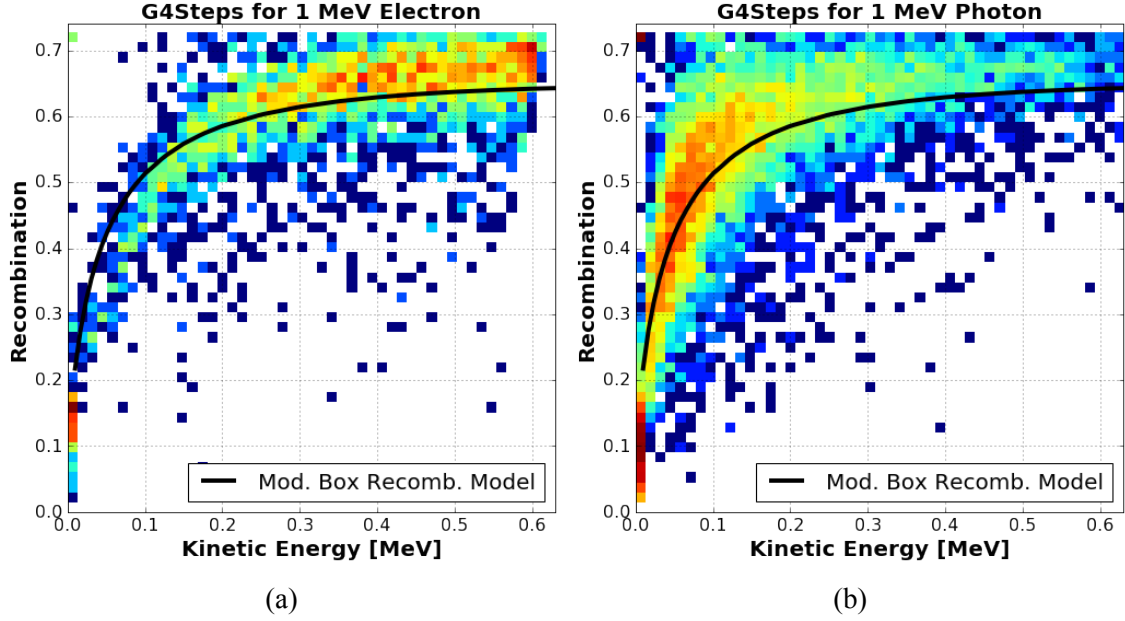


Figure C.18: Output of MicroBooNE recombination simulation. Heat maps are made up by the kinetic energy and simulated recombination factor for all Geant4 steps for a sample of one hundred 1 MeV electrons (a) and 1 MeV photons (b). The overlaid black lines are the recombination model as a function of electron kinetic energy calculated by using NIST tables to obtain the average dE/dx at each value of kinetic energy, and equation C.5 to calculate the appropriate recombination correction.

is used in this analysis to correct for the impact of recombination on the charge deposited above threshold.

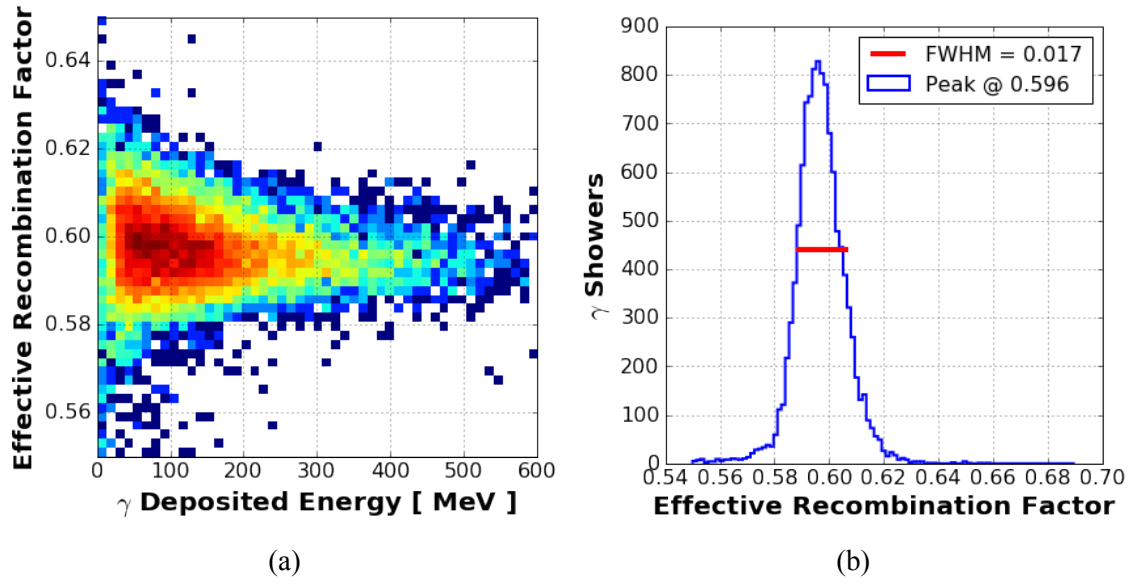


Figure C.19: (a) R_e for a sample of simulated single photon showers of different energies. The value of R_e is calculated using information from charge which is above detection threshold (~ 0.3 MeV). (b) distribution of R_e for the same sample of simulated photons. The peak of the distribution and FWHM range, shown as a red horizontal line, are reported.

Appendix D

Michel Electron Reconstruction: Supplemental Material

Section 8.4 provides a study of energy resolution as a function of true energy. This study is performed by measuring the fractional energy difference, after applying an energy correction, and fitting the resulting distribution to a Gaussian. Here we report the distributions and Gaussian fits obtained in bins of true energy.

Data-MC Energy Spectrum Comparison We quantify through a χ^2 measurement the level of agreement between the reconstructed energy spectra for data and MC. We are particularly interested on studying how the χ^2 varies as the constant energy reconstruction factor is varied. To perform this study, we calculate a χ^2 difference between the data and MC spectra as we vary the constant energy conversion factor of Eq. 8.1 by a constant amount. The value of χ^2 is calculated as follows:

$$\frac{\Delta\chi^2}{\text{d.o.f.}} = \frac{1}{B} \sum_{i=0}^{i=B} \frac{(N_i^{\text{MC}} - \alpha N_i^{\text{RC}})^2}{(N_i^{\text{MC}} + \alpha N_i^{\text{RC}})}, \quad (\text{D.1})$$

With α a normalization term such that the two spectra are area-normalized ($\alpha = \text{total MC entries} / \text{total RC entries}$). B is the total number of bins used (we use the same binning as in Fig. 8.15, but only consider bins up to 50 MeV to ignore data/MC disagreements in the tail of the distribution).

We calculate this quantity as we vary the constant calorimetric energy conversion applied to data, by a factor f between 0.8 and 1.2. The distribution of χ^2 vs. f will indicate if there is a

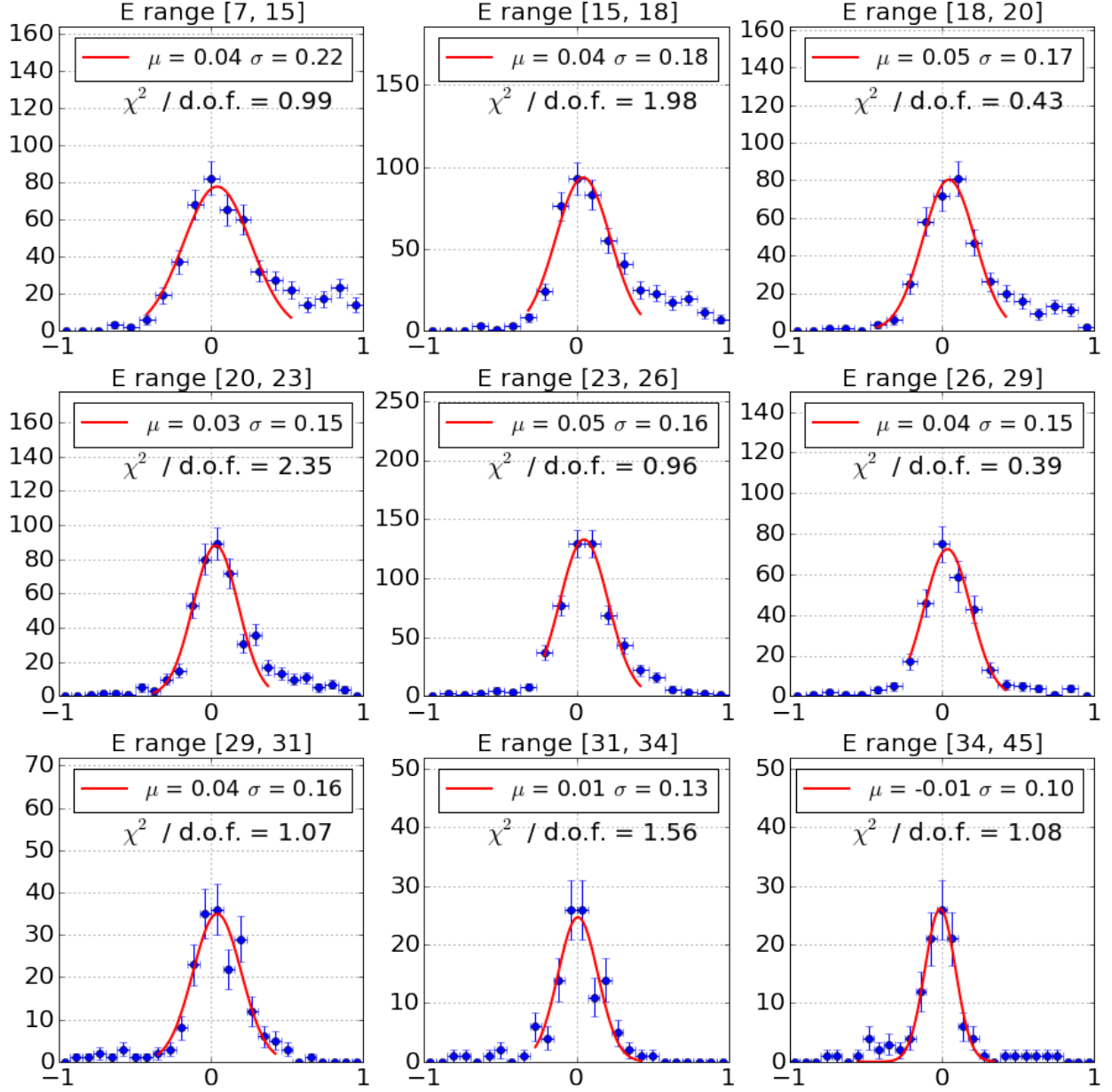


Figure D.1: Measurement of fractional energy resolution in bins of true energy associated to the energy resolution measurement for ionization-only energy loss associated to figure 8.11.

systematic offset between the two energy spectra. The obtained χ^2 as a function of the constant correction f is shown in Fig. D.4. The distribution for the ionization-only energy spectrum (blue) is relatively flat around $f = 1$ with a minimum at ~ 1.03 and the 1σ ($+1\chi^2$) falling between ~ 0.98 and ~ 1.05 . For the full energy spectrum (red) we see a minimum at ~ 1.03 and 1σ band encompassing values in the range ~ 1.01 and ~ 1.07 .

We conclude from this study that our energy reconstruction for data and MC agree to within

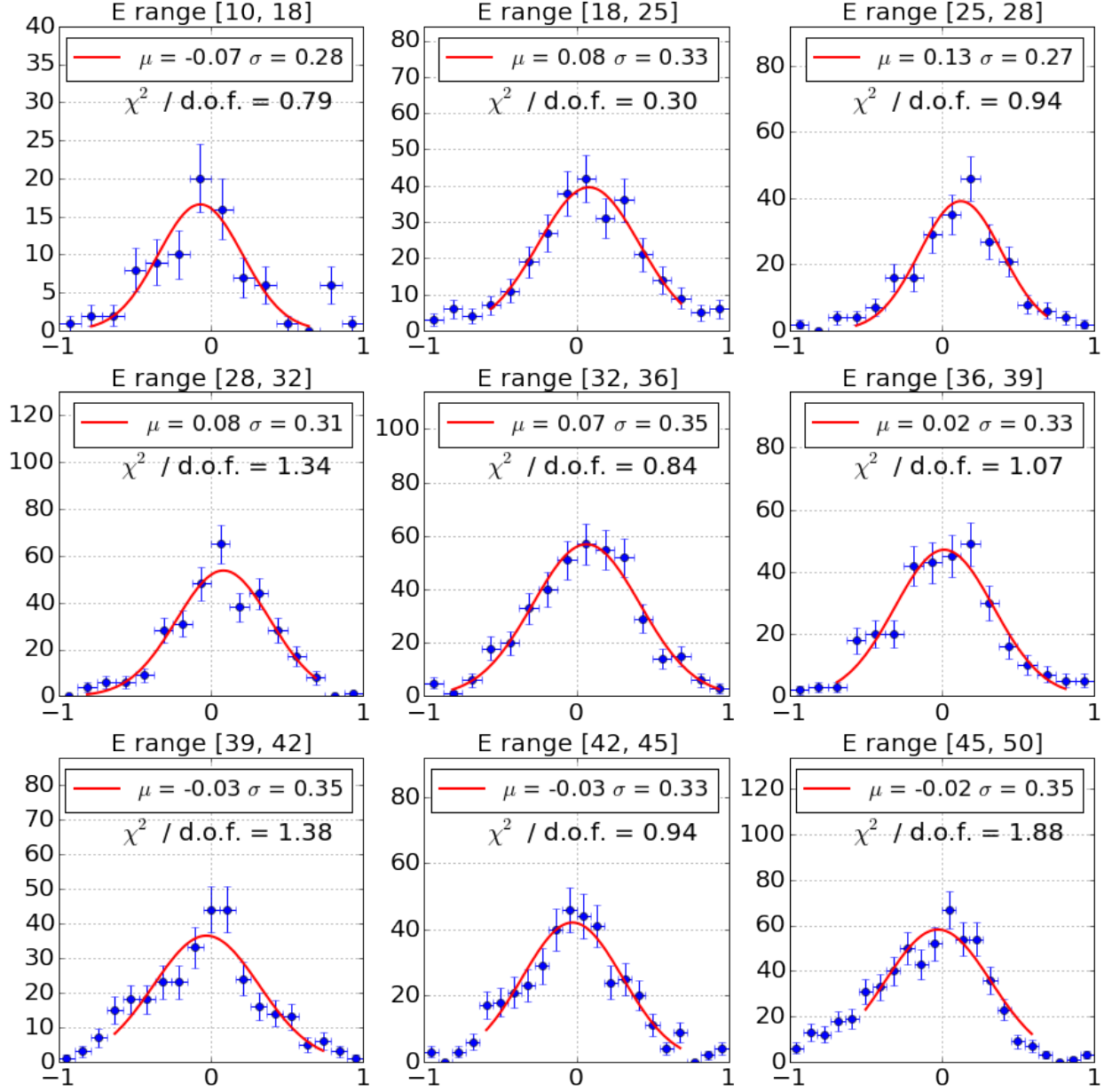


Figure D.2: Measurement of fractional energy resolution in bins of true energy associated to the energy resolution measurement for the total Michel electron energy, with a definition of reconstructed energy which includes only ionization energy loss. These distributions are associated to figure 8.12.

$\sim 3\%$, within the estimated systematic uncertainty of Eq. 8.1.

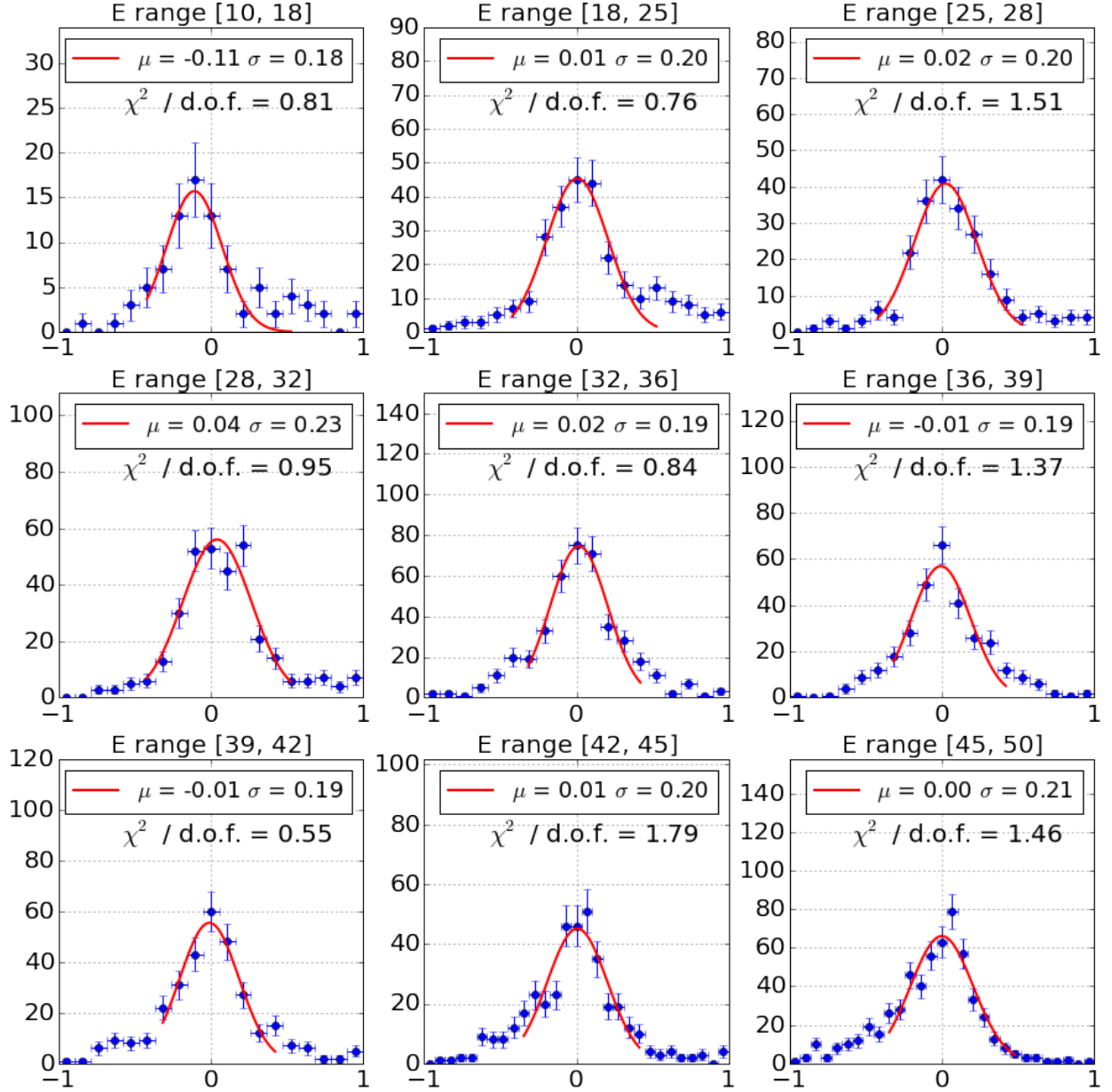


Figure D.3: Measurement of fractional energy resolution in bins of true energy associated to the energy resolution measurement for the total Michel electron energy, with a definition of reconstructed energy which includes any charge tagged in radiative photons. These distributions are associated to the results of figure 8.13.

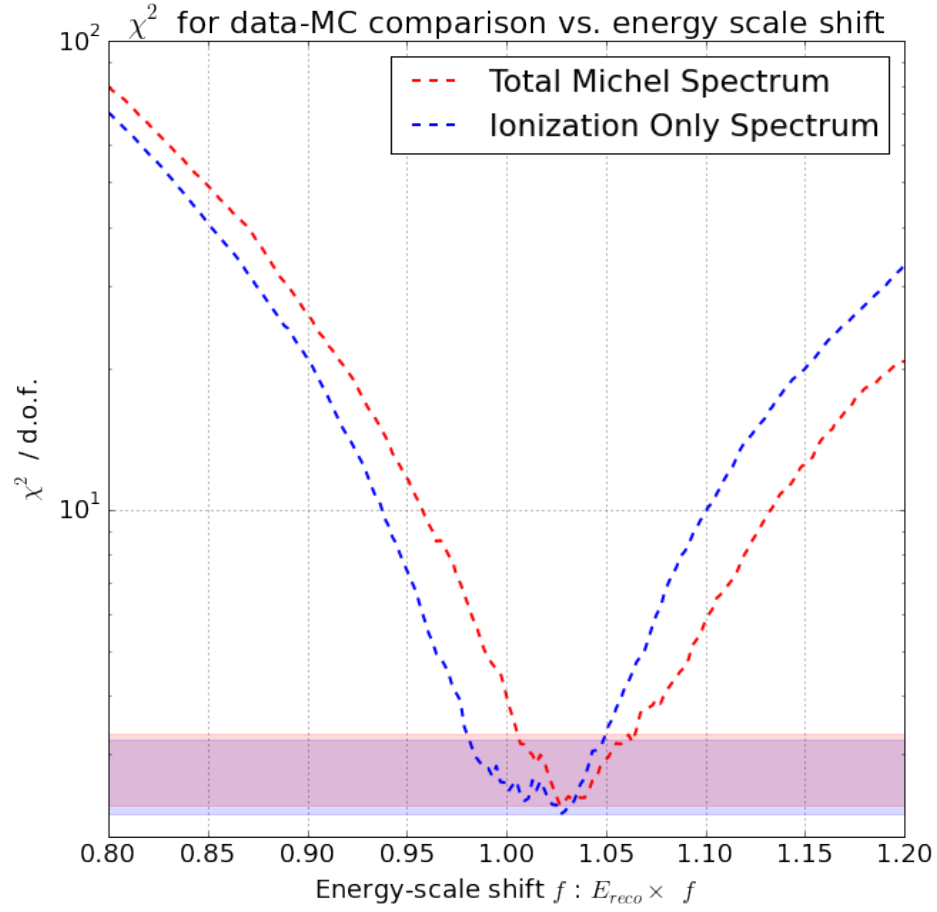


Figure D.4: Distribution of χ^2 computed vs. the energy correction factor f . The results for the ionization-only energy spectrum are shown in blue, and those for the full energy reconstruction in red. The red and blue bands show a band of width equal to one unit of χ^2 starting from the minimum value for each distribution.

Appendix E

Track-Shower Separation

E.1 Cosmic Removal

Cosmic-removal algorithms attempt to remove hits from clusters which are found to be uncorrelated with the neutrino interaction. These algorithms rely heavily on the reconstructed neutrino vertex in order to determine if a given cluster is consistent with a particle that has originated at that location. All Cosmic-removal algorithms make use of *Pandora* pattern-recognition algorithms employed to identify cosmic tracks [57]. The four algorithms, described in this section, effectively remove the vast majority of cosmic-induced charge in the ROI surrounding the neutrino interaction.

ROI Removal algorithm The first step in cosmic removal consists of removing all clusters which have even a single hit outside of the ROI. Figure E.1 shows an example event where this algorithm effectively removes almost all the charge associated with cosmic-ray muons. Many neutrino-induced tracks are often removed at this step. Occasionally branches of EM showers which exit the pre-defined 2m x 2m ROI are also excluded. Unless the γ first pair-converts beyond the ROI, in which case locating it and reconstructing it would be difficult in any circumstance, only a subset of charge from the shower is removed via this algorithm. We can hope to recover this lost charge at a later stage in the reconstruction.

Vertex-Slope Correlation algorithm Clusters associated with cosmic-ray muons and other activity are not, unless by chance, correlated with the neutrino interaction vertex. The Vertex Slope

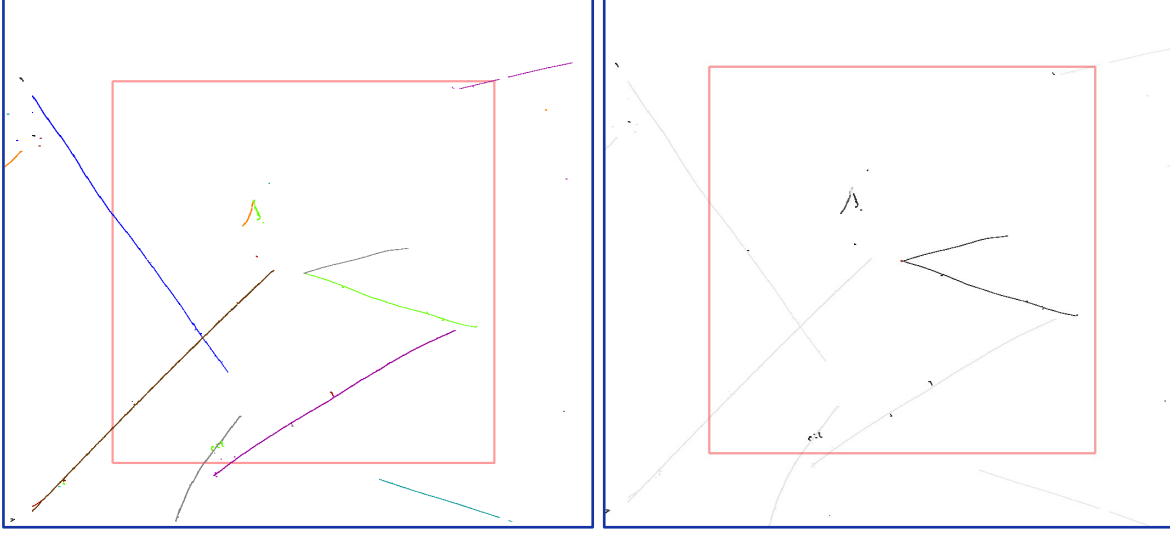


Figure E.1: Example event before/after the ROI removal algorithm. Left: event centered around the 2m x 2m ROI, with different reconstructed clusters labeled by different colors. Right: Same image after hit removal. Hits in gray indicate hits from clusters found to cross or be external to the ROI which are removed.

Correlation algorithm calculates the best-fit 2D line to each cluster and uses it to measure an impact parameter with respect to the vertex to determine if the cluster is associated with the vertex.

A minimum of ten hits is required for a cluster to be removed. For that cluster the best-fit 2D line is found, along with the error on the measured slope. The IP with respect to the vertex is measured for the best-fit line, as well as when varying the slope by \pm the measured error. Clusters are removed by cutting on the smallest IP obtained. The cut values were obtained by studying the distribution of measured IP s for a sample of single-particle π^0 events compared to a cosmic MC sample. The cut on the IP , seen in Fig. E.2, was chosen to be a function of the number of hits in the cluster: $IP > 80 \times e^{-\frac{N-10}{30}} + 5$.

Vertex-Angle Correlation algorithm Cosmic-ray muons passing coincidentally very close to the vertex will not be removed by the Vertex-Slope Correlation algorithm. These cosmic-rays, however, while intersecting the vertex will have both end-points far away from the vertex. To isolate these remaining cosmic-rays for each cluster we identify the two end-point hits in the cluster and measure the angle they form with the vertex. Clusters which pass close to the vertex but are

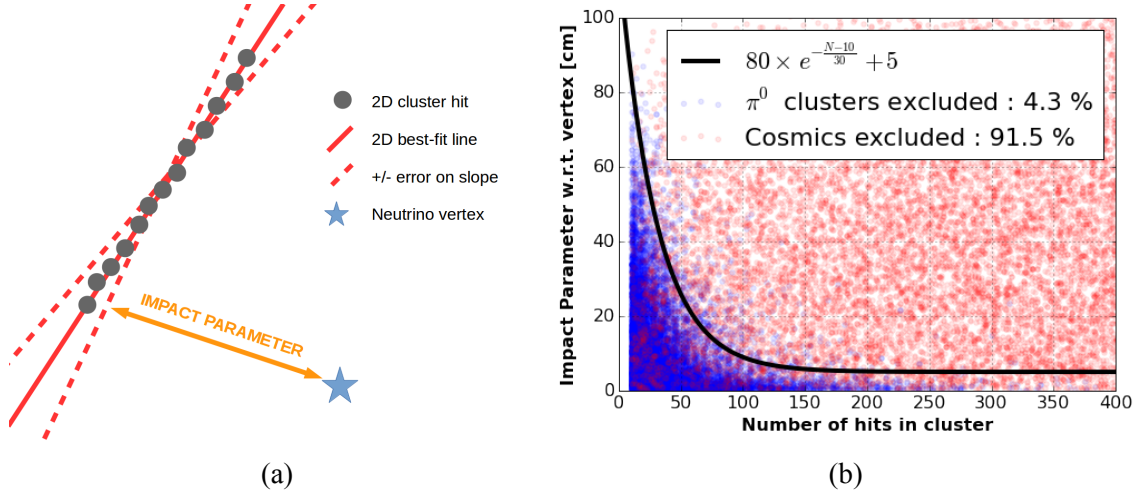


Figure E.2: (a) Schematic describing how the IP is calculated given the best-fit line to the cluster. The smallest IP value obtained when varying the fit within the slope's measured error is used. (b) Measured minimum IP for single π^0 s (blue) and cosmic clusters as a function of the number of hits in the cluster.

uncorrelated will have the end-points on opposite sides of the vertex and thus produce a large measured angle. The smaller the IP , the larger the expected angle. We thus cut on the correlation between these two variables, as shown in Fig. E.3. Clusters with less than ten hits are ignored by this algorithm. If the measured angle is larger than 160 degrees, the cluster is removed regardless of the measured IP .

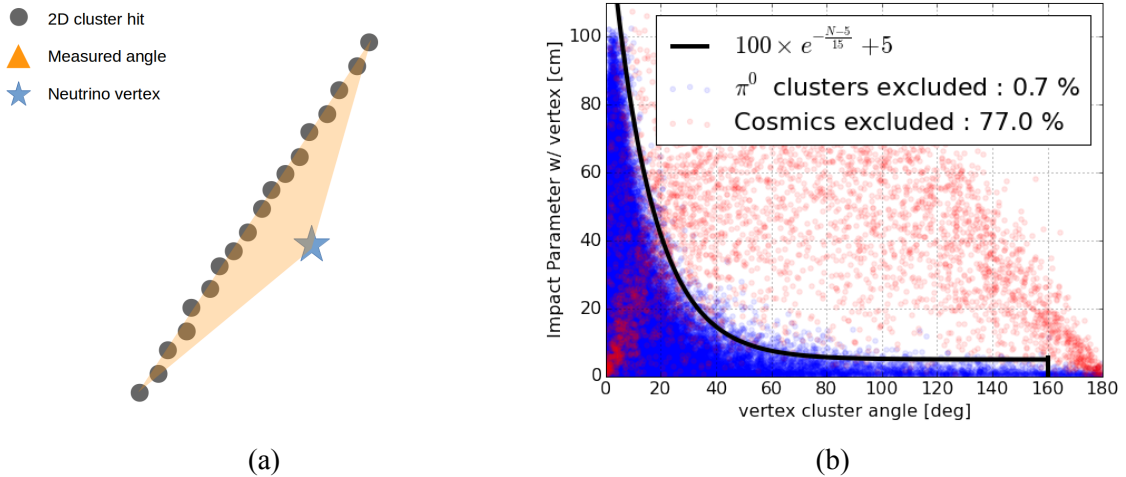


Figure E.3: (a) Schematic showing how the angle formed by the cluster's end-points and the vertex is defined. (b) Measured IP as a function of the angle centered at the vertex connecting the end-points of each cluster.

Delta-Ray Removal algorithm The final step in the removal of cosmic-induced hits targets delta-rays and other EM activity correlated with cosmic-ray muons. A cluster is targeted as a delta-ray if it has less than 50 hits, a minimum distance from a previously removed cosmic cluster less than 1 cm, and a maximum distance less than 15 cm.

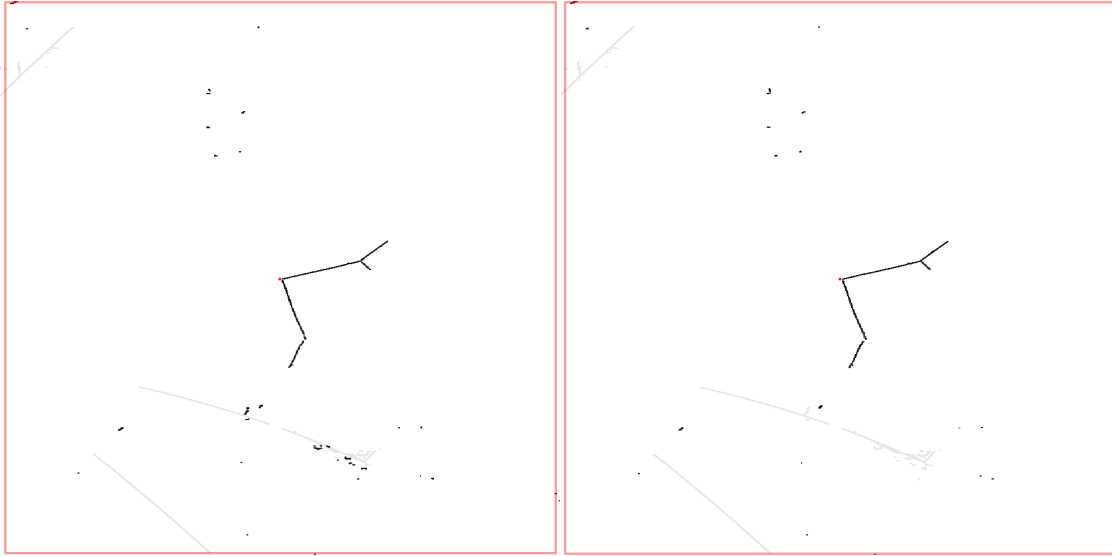


Figure E.4: Example event before/after delta-ray removal. The many small clusters surrounding the cosmic muon crossing the ROI below the vertex are removed in the right-hand-side image.

This algorithm is very important in making sure that small clusters of charge produced by delta-rays, which can mimic EM activity, are removed. Removing these small clusters is important in order to obtain lower detection thresholds for small γ showers which deposit a few tens of MeV of energy in the TPC.

E.1.1 Neutrino Track Removal

The separation of of charge associated with the neutrino interaction between track-like and shower-like clusters relies on two features that distinguish muon, pion, and proton tracks exiting the neutrino interaction with respect to photons produced in a π^0 decay:

1. Clusters from tracks will exhibit a larger linearity than γ s, because of both the smaller amount of scattering which these particles undergo, as well as because of the lack of the production of a cascade of e^+/e^- pairs due to γ pair-conversion.

2. Clusters produced by tracks will originate in close proximity to the vertex, while photon clusters will (usually) be displaced given the large radiation length (14 cm) in argon.

When quantifying the linearity of a cluster we rely on two metrics described in detail below.

Truncated Local Linearity The TLL metric aims to measure the linearity of a cluster accounting for a possible slow curvature of the hits in the cluster due to effects which may bend the track such as multiple Coulomb scattering or detector effects such as space-charge distortions. The TLL quantity is calculated by measuring, for each hit in the cluster, the linearity of hits in a local neighborhood of the hit, and finding the average of the distribution of the computed values after the tails of the distribution have been truncated. This metric is more effective at separating tracks from showers because it is able to assign a high degree of linearity to tracks from muons and pions which bend, while still penalizing fuzzy clusters from EM showers. A visual representation of how the TLL metric is computed can be found in Fig. E.5(a).

Summed Square Variance The SSV metric measures the residuals of the 2D hit coordinates to their best fit line, accounting for the degrees of freedom (number of hits) in the cluster. This metric returns a high linearity measure for clusters which are very straight and exhibit very small curvature or bending, and is ideal for identifying small proton clusters. A schematic view of how the SSV is computed is shown in Fig. E.5(b).

Vertex Proximity Removal algorithm As a first step, we remove clusters that originate close to the vertex applying a fairly aggressive cut on the TLL variable ($TLL < 0.2$). By requiring that all clusters removed at this stage start in close proximity to the vertex (within 3.5 cm) we are selecting hits associated to tracks which do not have a noticeable gap separating them from the vertex, as is the case for hits from photons. The cut on the TLL quantity is to ensure that very obviously shower-like clusters are kept, in order to preserve those photons which may pair-convert within a few cm of the vertex. A minimum of 8 hits is required for a cluster to be removed at this stage. Figure E.6 shows the impact of this cut on a sample of single π^0 s and a CC 0 π^0 sample.

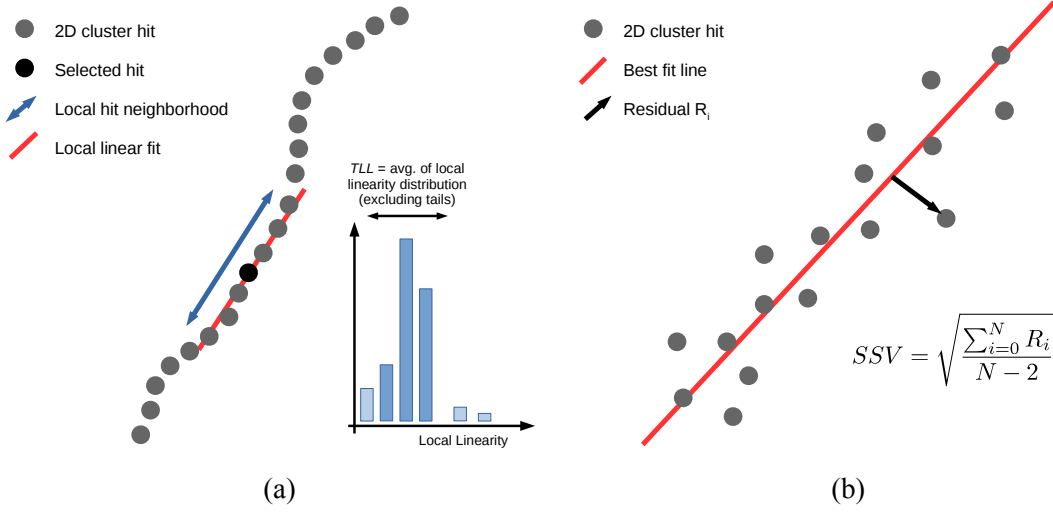


Figure E.5: Schematic of how the (a) TLL and (b) SSV metrics are computed for the hits in a cluster.

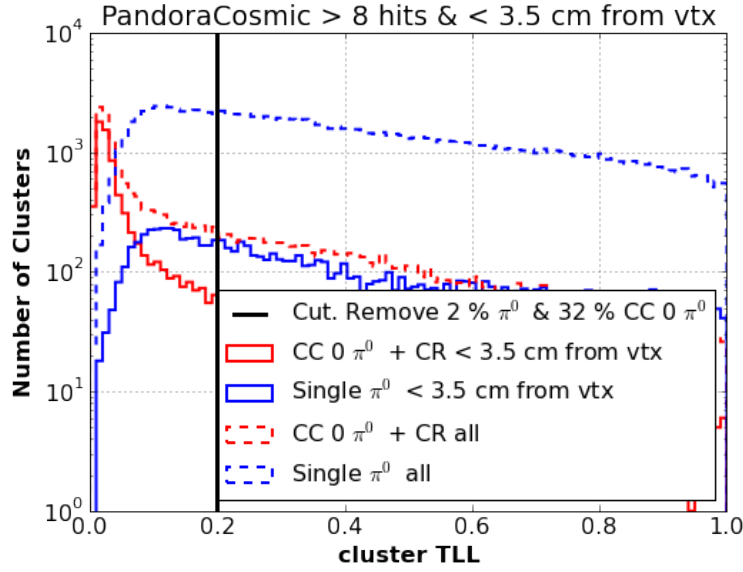


Figure E.6: Impact of the Vertex Proximity algorithm on pandoraCosmic clusters from a sample of single π^0 (blue) and CC 0 π^0 + cosmics events (red). Dashed distributions show the overall TLL distributions for the two samples, solid lines show the subset of clusters from each sample within 3.5 cm of the vertex. The cut value at 0.2 in TLL removes 36% of the total clusters in the CC 0 π^0 left after cosmic-removal, and only 2% of clusters in the single π^0 sample.

Linear Removal algorithm At this stage, we target the removal of clusters which exhibit a high level of linearity. Two metrics for linearity are used to separate track-like from shower-like clusters:

1. the TLL quantity, which quantifies the local-linearity of hits in a cluster, best suited for longer muon or pion clusters which may scatter and exhibit some degree of curvature while

still maintaining a linear profile.

2. the SSV quantity, which measures the absolute linearity of an entire cluster and can best distinguish small clusters from protons (very straight due to the few and small angular scatters) from low-energy electrons which exhibit a larger amount of curvature.

Removing long μ/π tracks The TLL metric allows to separate EM-induced from track-induced clusters by accounting for the possibly high amount of curvature observed in longer tracks. To identify cut values for the TLL metric we take samples of single-particle π^0 and muons and study the measured TLL as a function of the number of hits in the cluster, as well as the overall slope of the cluster in the time vs. wire 2D projection of a TPC wire-plane. Fig. E.7 shows the distributions obtained as well as the cut values chosen. We note that the significant variation in the TLL as a function of the slope is due to the fact that at high slope values, when the cluster extends predominantly in the drift-direction, the reconstruction of individual hits is sub-optimal, affecting the reconstruction position of each hit and thus the measured linearity. Because of the slope-dependent TLL value measured, for clusters with a slope smaller than 1 we cut as indicated by the black line in Fig. E.7(a) and for clusters with a slope larger than 1 we cut as shown in Fig. E.7(b).

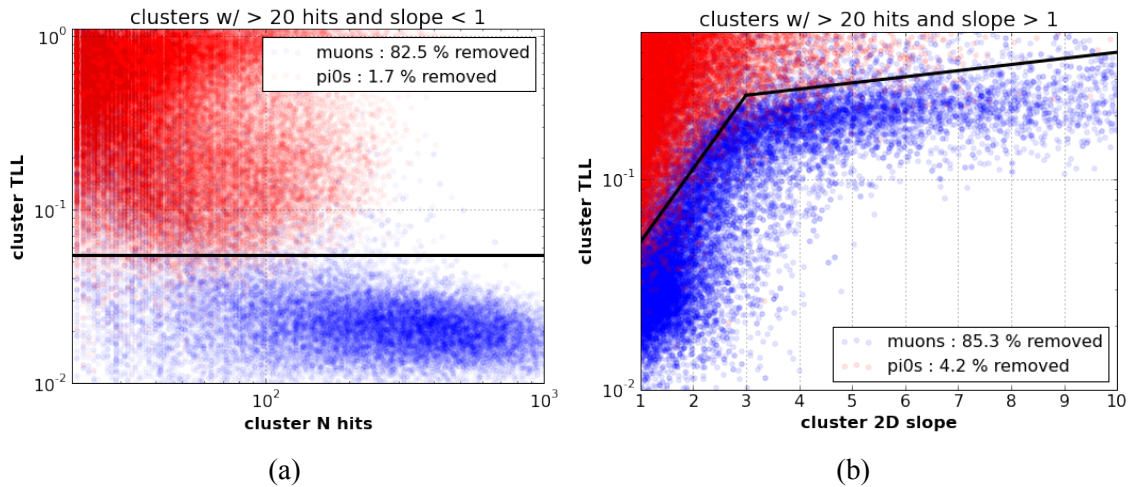


Figure E.7: (a) TLL vs. number of hits for π^0 and muon clusters. (b) TLL vs 2D cluster slope. Black lines denote cut values chosen. The slope measured in (b) is computed from a representation in which the drift-coordinate is along y and the wire-coordinate along x. A high slope value therefore indicates clusters mostly parallel to the drift-direction.

Removing short proton-induced tracks To target proton clusters we apply a cut on the SSV metric, removing any cluster with a value < 0.06 which also have a maximum distance from the reconstructed vertex smaller than 10 cm. The impact of this cut is shown in Fig. E.8.

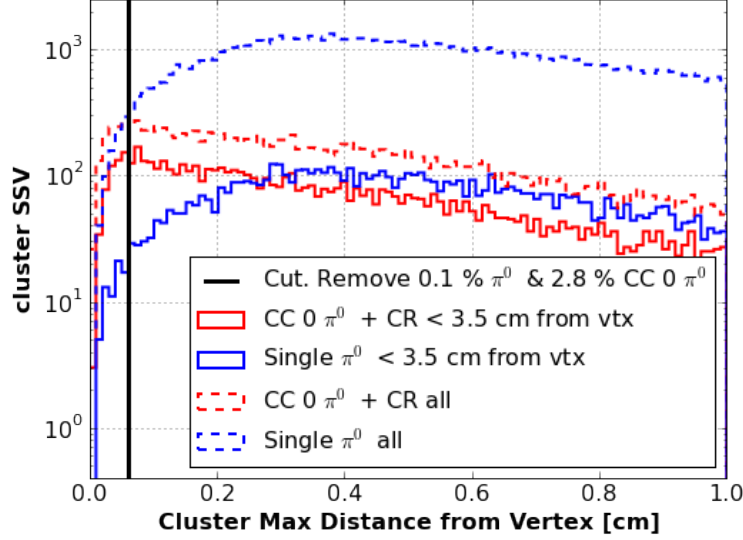


Figure E.8: Impact of the SSV cut in the Pandora Linear algorithm on a sample of single π^0 (blue) and CC 0 π^0 + cosmics events (red). Dashed distributions show the overall SSV distributions for the two samples, solid lines show the subset of clusters from each sample within 3.5 cm of the vertex. The cut value at 0.06 in SSV removes 3% of the total clusters in the CC 0 π^0 left after cosmic-removal, and virtually no clusters in the single π^0 sample.

Track Delta-Ray Removal algorithm As in the cosmic-removal stage, we attempt to identify delta-rays associated with previously removed tracks. The algorithm is functionally identical to that used in the cosmic-ray removal stage, but the cuts applied are more conservative, in order to preserve hits from photons which are produced in close proximity to the neutrino-induced tracks and may otherwise be accidentally removed at this stage. We remove clusters if they have less than 20 hits, and have a closest distance to a removed track of less than 1 cm, and a maximum distance of no more than 4.5 cm.

Re-Clustering To correct possible reconstruction errors due to the *Pandora* reconstruction algorithms, we take any charge which remains at this point and apply a simple proximity-based clustering algorithm to re-cluster charge present in the ROI. Similar cuts to those applied previously making use of the TLL and SSV metrics are then applied.

Appendix F

$\pi^0 \rightarrow \gamma\gamma$ Shower Reconstruction: Supplemental Material

This chapter summarizes the reconstruction techniques employed to identify electromagnetic showers from photons produced in the decay of neutral pions (π^0) which originate from charged current (CC) ν_μ interactions, and reconstruct their kinematic properties. A more detailed discussion of the algorithms developed for the reconstruction is provided in appendices E and F.

The reconstruction is performed in a staged approach, starting from reconstructed 2D quantities on each plane ¹ to produce full three-dimensional reconstructed showers. The input to this stage of the reconstruction consists of 2D hits and information on the neutrino vertex location. Provided with this information, the reconstruction proceeds as follows:

1. Track-Shower separation. Two-dimensional hits are classified as shower- or track-like. This step aims to “clean” each view of charge deposited not associated to the two photons by removing both charge from cosmic-ray activity as well as tracks produced in the neutrino interaction. This step is described in section F.2.
2. Two-dimensional clustering. Hits on each plane are merged in “clusters”, one per EM shower. The clustering algorithm employed is described in Sec. F.4.
3. Clusters are matched across planes. Combining information from multiple planes enables the reconstruction of 3D information associated to each shower. Matching is described in

¹Chapter B presents an overview of the generic 2D reconstruction performed on MicroBooNE data.

Sec. F.5.

4. A second clustering step is performed in order to tag charge which may have been ignored at the first pass. This procedure is described in section F.6.
5. Information from merged clusters is used to reconstruct 3D showers. In this step a shower's energy, position and momentum are computed. The procedure followed is presented in Sec. F.7.

Before the details of the reconstruction are presented, a description of the challenges of reconstructing $\mathcal{O}(100)$ MeV EM showers in a surface LArTPC are presented in section F.1

F.1 Challenges of Reconstructing $\mathcal{O}(100)$ MeV Photons in a Surface LArTPC

There are three main challenges to the identification and reconstruction of $\mathcal{O}(100)$ MeV electromagnetic activity in a LArTPC: (1) distinguishing charge deposited by track-like particles (muons, protons, pions) from that produced by electrons and photons. (2) isolating the full extent of energy deposited by electrons or photons as they produce an EM cascade from the cosmic activity recorded in a “slow” surface detector. (3) developing a reconstruction approach capable of measuring EM activity over a range of energies across which the shower topology changes dramatically. Each category is further described below, with examples of EM showers from the data.

Track-Shower Separation Unlike at higher energies where radiative energy loss induces the formation of broad, fully developed EM showers, at energies of up to a few hundred MeV energy loss to photons appears more sparse, causing γ showers to manifest themselves as a collection of several scattering but fairly linear track-like ionization segments. Figure F.1a shows a candidate neutrino interaction with a final state π^0 in which the γ showers appear as wavy track-like segments surrounded by smaller energy deposition photons, rather than fully developed EM showers. This fact makes the topological discrimination of photons and electrons from other tracks more challenging at these energies.

Charge-Collection and Clustering Unlike for tracks where energy loss is continuous, EM showers develop stochastically. This means that collecting the full energy deposited by an EM shower is necessary in order to measure its energy accurately. Recovering the full charge deposited is challenging due to the significant extent of the shower and the unavoidable presence of

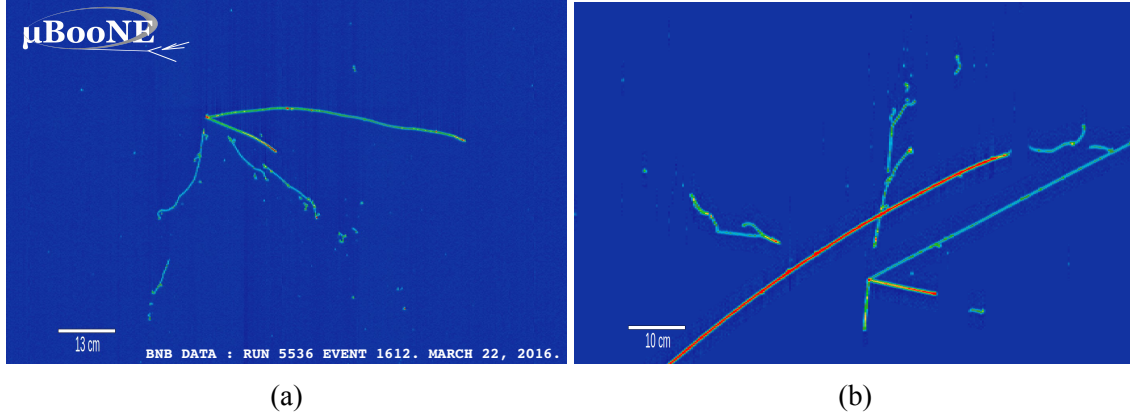


Figure F.1: (a) Event display of candidate CC π^0 neutrino interaction in which the two photons manifest themselves as fairly linear track-like segments of ionization energy deposition. (b) Example of EM shower with overlying cosmic activity caused by the slow drift-time in LAr.

overlapping cosmic activity super-imposed on the EM shower in a surface detector. For a detector the size of MicroBooNE, containment of charge in the TPC active volume also hampers the ability to fully recover the energy deposited by EM showers. Additionally, specific sections of the detector which are non-responsive contribute an additional loss of detector coverage. The stochastic nature of radiative energy loss implies that extrapolating the expected behavior of the EM shower in these regions is not as easy as for tracks. Figure F.2 shows the significant extent (over two meters in length in this example) and sparse nature of EM showers in LAr. Figure F.1b shows a similar event where the presence of overlying cosmic activity may confuse the reconstruction. An additional challenge is posed by the energy deposited below threshold by very low energy photons produced in EM showers, which must be accounted for.

Topological Variation The widely different appearance of EM activity at a few tens of MeV versus several hundred MeV, caused by the relative proximity to the critical energy of LAr, makes it challenging to develop a comprehensive reconstruction approach. π^0 s of a few hundred MeV will decay, often asymmetrically, in two photons which will span this entire energy range, making this a serious concern for the reconstruction of CC π^0 neutrino interactions. Figure F.2 is a great example of this behavior: the significant EM shower which propagates from the vertex is accompanied by a second, much smaller photon, visible towards the top of the image at the end of one of the tracks branching from the vertex. Reconstructing both these widely different photons is necessary in order to reconstruct the π^0 which produced them. Figure F.3 shows three very different examples of EM

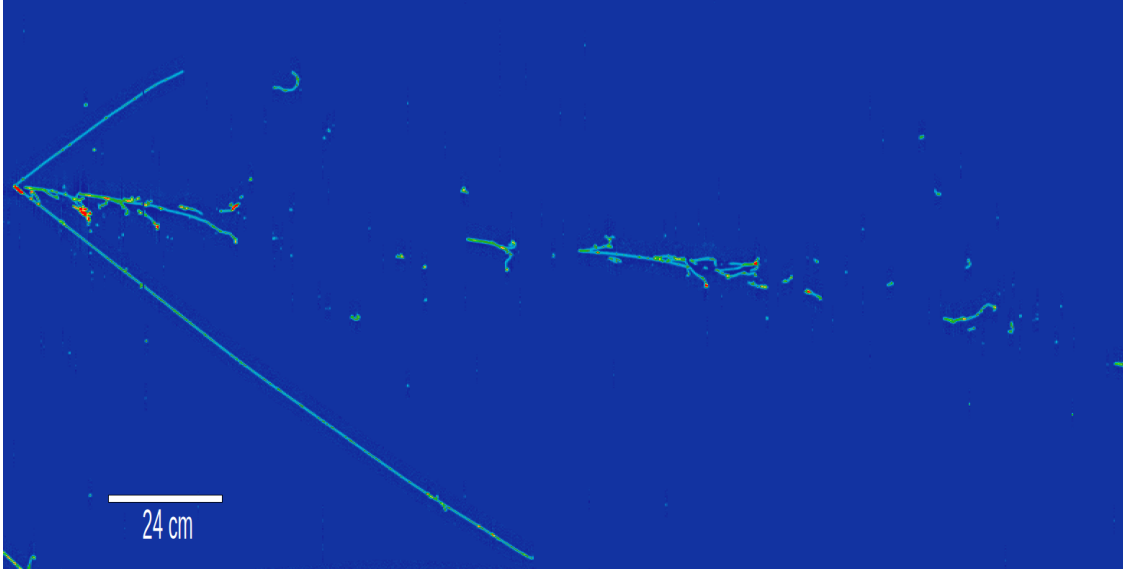


Figure F.2: Event display of candidate CC π^0 neutrino interaction showing the significant extent and sparse nature of $\mathcal{O}(100 \text{ MeV})$ EM showers in LAr.

activity in LAr across a wide range of energies.

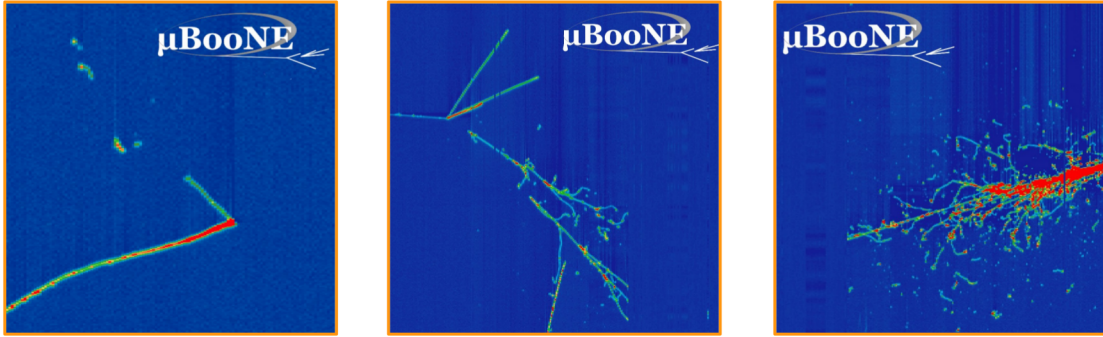


Figure F.3: Examples of EM activity: left, a Michel electron; center, photons from a beam π^0 ; right, a cosmic high energy shower.

F.2 Track-Shower Separation

This section presents the reconstruction chain denoted as *hit removal*, or *track-shower separation*, which aims to isolate charge deposited by γ s produced via π^0 -decay in ν_μ charged current (CC) interactions. The approach taken relies on a neutrino event-selection to have identified neutrino candidates within an event, and makes use of the reconstructed neutrino vertex to help perform the removal of cosmic- and track-induced hits in the event. The aim of this step in the recon-

struction chain is to isolate hits from π^0 decays in order to facilitate the downstream clustering and shower-reconstruction stages. By providing the clustering and 3D shower reconstruction algorithms “clean” images which are stripped of all charge except for that deposited by the γ showers, we are able to make these tasks simpler and more efficient.

Hit-removal is performed by a modularized chain of algorithms in which a decision whether hits should be removed is taken on a cluster-by-cluster basis. This operation is performed on each plane separately. The sequence of algorithms employed are split in two distinct categories: those which aim to remove charge from cosmic-induced tracks, which are uncorrelated with the neutrino interaction, and those which are produced by tracks (from muons, pions, and protons) in the neutrino interaction itself. These two steps are referred to as *Cosmic Removal* and *Neutrino Track Removal*. The full chain of algorithms employed is described in appendix E. A summary with examples and a final profiling of the performance is provided here.

A *Region of Interest* (ROI) is used in this analysis to help isolate charge associated with the π^0 decay. The ROI is defined by a 2x2 meter square surrounding the reconstructed 2D neutrino vertex on each plane. At this stage in the reconstruction all charge external to the ROI is ignored. The removal of cosmic-ray activity and charge from tracks produced in the neutrino interaction is targeted separately in order to take advantage of different characteristics the two exhibit. For the cosmic-removal stage the correlation of clusters with the vertex allows to isolate cosmic-induced muons. The removal of tracks produced in the neutrino interaction is targeted by cuts which aim to identify the degree of linearity of reconstructed clusters. Two metrics which aim to account for the scattering of trajectories for different particles are constructed to quantify the degree of linearity of a cluster. These metrics are referred to as *Truncated Local Linearity* (*TLL*) and *Summed Square Variance* (*SSV*) and are defined in appendix E. The fact that photons, unlike tracks, are separated from the neutrino vertex, is also leveraged in the neutrino-track removal stage. To test the performance of the hit-removal reconstruction step various simulated samples are employed: single π^0 events, BNB CC ν_μ interactions with zero, and one π^0 in the final state, and cosmic events.

Fig. F.4 shows the impact of hit-removal on these samples. The algorithm is able to remove over 90% of charge from cosmic-only and BNB CC 0 π^0 + cosmic events while only removing approximately 16% of the charge from simulated π^0 s.

The impact on each sample is measured quantitatively in figure F.1, where the average fraction

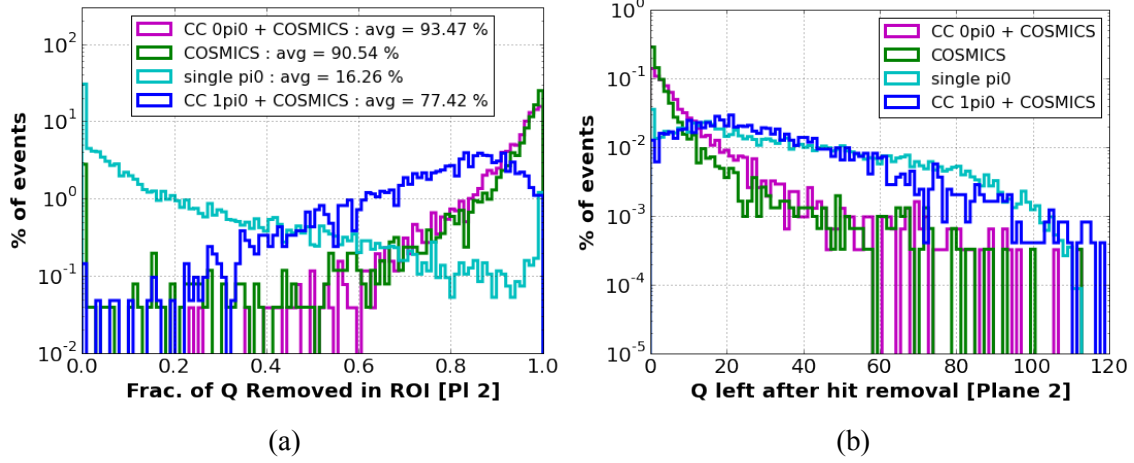


Figure F.4: (a) Fraction of charge remaining in the ROI for different samples. (b) Absolute amount of charge in (ADCs) after hit-removal. Both plots are produced using collection-plane ROIs.

of charge removed for each sample is reported.

Table F.1: Table evaluating performance of hit-removal on various samples.

Sample	single π^0	CC 0 π^0	CC 1 π^0	CC 0 π^0 + CR	CC 1 π^0 + CR	CR
Frac. Removed	16.3	89.6	60.6	93.3	79.1	91.2

F.3 Two-Dimensional Clustering and 3D Shower Reconstruction

Provided with reconstructed 2D hits associated to EM activity from each plane a series of algorithms is employed to cluster photons from π^0 in each TPC wire-plane, and subsequently match charge across planes in order to reconstruct 3D kinematic variables associated to the γ showers. The steps involved in this reconstruction sequence are briefly described below, and treated in more detail in appendix F.

F.4 Two Dimensional Clustering

This reconstruction stage is tasked with separating hits on each plane into clusters, one for each of the two γ s produced by the π^0 . Hits identified as shower-like in the hit-removal reconstruction stage are clustered via a proximity clustering algorithm into what we refer to as “photon-clusters”,

as shown in Fig. F.5. These proximity-based clusters are used as the input to the γ clustering stage. Provided this input, two algorithms are applied to reconstruct the two γ s.

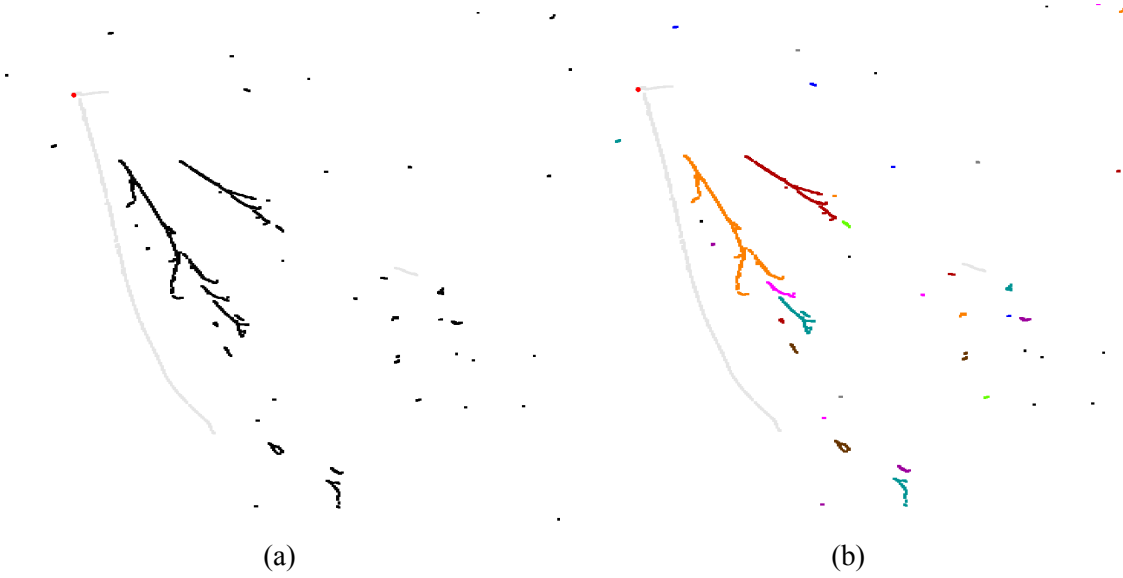


Figure F.5: Example of reconstructed information from a simulated BNB event provided as input to the 2D clustering stage. (a) Neutrino interaction reconstructed hits after hit-removal. Hits in black are those kept after hit-removal is applied. The red dot represents the neutrino vertex. (b) Hits split into proximity-based clusters, labeled by different colors. We will refer to each of these clusters as “photon-clusters”.

F.4.1 Polar Coordinate Merging

Individual photon-clusters are merged according to their polar-coordinate orientation with respect to the neutrino vertex. For each photon-cluster we compute an angle and angle-span. The first is the charge-weighted direction of the hits in the cluster, and the second the range of angles encompassing all hits in it. A start point and end-point are also reconstructed, corresponding to the (r, θ) coordinates of the hit closest and furthest away from the vertex respectively. The radial distance between these two points is referred to as the cluster length. These quantities are used to determine whether to merge two photon clusters or not according to the following cuts:

1. Given a pair of clusters, the upstream one (the cluster with smaller start-point radius) must have more charge than the downstream one for the two to be merged.
2. A down-stream cluster must have its reconstructed angle θ within the angle-span of the larger upstream one.

3. The distance between the two clusters, measured as the radial separation between the upstream end-point and the downstream start-point, must be smaller than the total length of the larger upstream photon-cluster.

This procedure is repeated on each plane separately until an iteration is reached in which no clusters are merged.

F.4.2 Vertex Aligned Merging

The second algorithm specifically aims at clustering photon-clusters under the assumption that two γ EM showers from a π^0 decay are present in the event. The first action taken is to identify, in each plane, the two clusters with the largest amount of charge. These are taken as the trunk of the two γ showers in the event. These two clusters must be separated in polar angle θ by at least 15 degrees. Once these two clusters are identified, all remaining photon-clusters in the event are scanned to determine if they should be merged with a γ cluster. A smaller cluster is merged if:

1. It is within 12 degrees of the closest γ cluster, but more than 15 degrees away from the second γ cluster.
2. The radial distance between the γ cluster end-point and the small cluster's start-point is less than three times the radial length of the γ cluster.

This procedure is repeated separately on each plane until an iteration is reached in which no more clusters are merged.

Figure F.6 shows the same event from Fig. F.5, after these two merging algorithms have been applied.

F.5 Cluster Matching

After clusters have been merged on each plane separately, a cross-plane matching algorithm is applied to associate clusters belonging to the same γ . Due to the difficulty of finding a photon which is well-clustered on all three planes, we require that matching be done exclusively between a pair of clusters on two planes. We further demand that one of the two clusters must lie on the collection

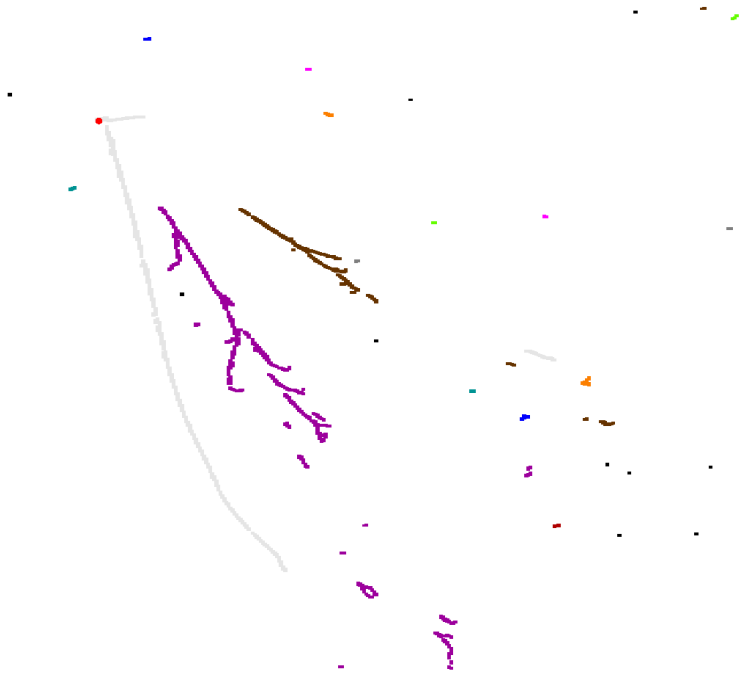


Figure F.6: Simulated CC π^0 interaction after the 2D clustering reconstruction stage. Two large clusters, corresponding to the two γ s are visible in purple and brown. Several smaller photon-clusters remain in the event.

plane, as this will provide us with the best information with which to perform calorimetry and measure the γ 's energy. Finally, only clusters which have at least ten reconstructed hits associated to it will be considered. The matching algorithm applied calculates the overlap in time of pairs of (Y,V) and (Y,U) plane clusters and assigns a score based on this overlap. Cluster-pairs with the highest score are then merged. The figure of merit devised as the overlap score is denoted IoU , for intersection over unity, and is defined as the time-interval common to the two clusters over the union of the two cluster's time interval. A minimum IoU of 0.25 is required to match two clusters, and clusters are matched in order of their score: if a cluster has a match with two or more clusters, the pair with the largest score is chosen. The matching continues until no cluster-pairs with a match above the cut value remain. Fig. F.7 shows the output of cluster-matching for an example simulated event.

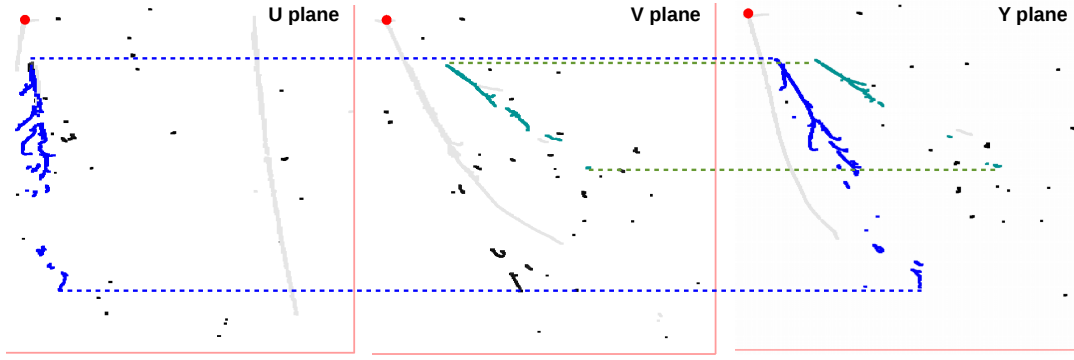


Figure F.7: Example output of IoU matching algorithm. Three-plane view of the same event, with vertical axis time-aligned across the three planes. The red dot denotes the vertex, and colored clusters denote matched cluster-pairs. Red lines denote the edge of the 2x2 meter ROI surrounding each vertex.

F.6 Photon Re-Clustering

The hit-removal and clustering stages described above will unavoidably miss some of the energy deposited by photons. In order to mitigate the impact of under-clustering on energy reconstruction, a second clustering stage is applied at this point in the reconstruction. This consists of two different steps: an attempt to merge together separate clusters which are aligned and thus probably associated to the same photon, as well as an attempt to include charge previously excluded from the event.

F.6.1 Aligned Shower Merging

After clusters are matched across planes, an attempt is made to merge together clusters on the collection plane which are aligned in direction. The reason for doing so at this stage in the reconstruction (after cluster matching) is to ensure that a more complete clustering result on the collection plane does not inhibit a match with a cluster on either induction plane due to a worse IoU score. If collection-plane clusters from different match results are found to be within 15 degrees of each other, they are merged in the same shower. The induction-plane cluster matched to the most upstream of the two collection-plane clusters being merged is retained as the sole matched cluster, and no merging is performed on either induction plane.

F.6.2 Photon Tagging

Because at the hit-removal and 2D clustering stages a significant portion of charge deposited by the γ showers may be excluded, we apply a re-clustering step which aims to identify any charge in the event which was not included at the original clustering stage. New photon-clusters can be added more inclusively at this stage because now their correlation with existing showers can be tested based on their angular orientation in the event, with less stringent cuts applied to the cluster size, linearity, or distance from the vertex.

First, charge from the event is clustered, using the same proximity-based clustering algorithm employed previously, in photon-clusters. All charge in a 4x4 meter ROI surrounding the neutrino vertex (double the size of the ROI used previously) are used in this clustering stage. Proximity-based clusters obtained in this way are then filtered by requiring they have less than 100 total hits, and have a maximum truncated local linearity (TLL) of 0.06. A photon-cluster is then added to an existing shower's collection-plane cluster if:

1. the photon-cluster has less than half the number of hits associated with the shower's collection-plane cluster.
2. The angle between the 2D slope of the photon-cluster and the shower is less than 50 degrees.
3. An isosceles triangle extending 150 cm from the shower's start-point in the shower direction, and with an opening angle of 40 degrees is created. Photon-clusters which are fully contained, or start within the triangle are associated with the shower.

Figure F.8 shows an example where a significant amount of shower energy is successfully recovered after the re-clustering stage is applied.

F.7 Shower Reconstruction

Finally, pairs of clusters on two planes are used to reconstruct 3D showers. Specifically, this reconstruction stage aims to measure the γ 's 3D start point and direction, as well as its energy. The reconstruction is modularized in a series of algorithms, which are described in the following sub-sections.

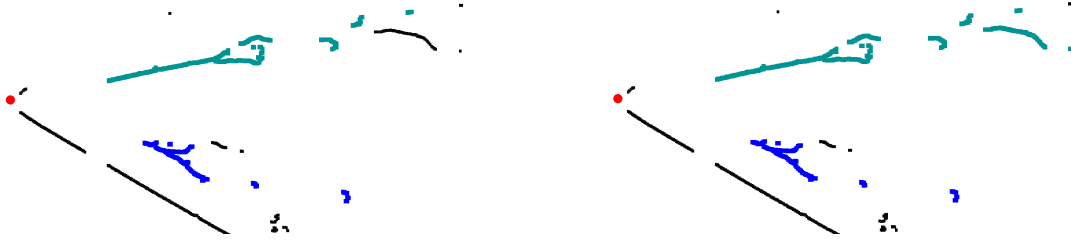


Figure F.8: Example of charge re-clustering. Top: event before re-clustering. Bottom: after re-clustering is applied. The green shower has a significant amount of energy deposited added back to improve the energy reconstruction. Some energy deposited by the blue shower is however not successfully re-clustered.

F.7.1 Direction Reconstruction

The 3D direction of a shower is reconstructed by transforming the two 2D directions reconstructed for the pair of matched clusters into 3D coordinates. The 2D direction on each plane is calculated by measuring the charge-weighted 2D direction with respect to the vertex location of all hits associated with the γ on a given plane, according to Eq. F.1:

$$\begin{aligned} w_{dir} &= \frac{1}{\sum_{i=0}^{N_{hits}} Q_i} \times \sum_{i=0}^{N_{hits}} Q_i (w_i - w_{vtx}) \\ t_{dir} &= \frac{1}{\sum_{i=0}^{N_{hits}} Q_i} \times \sum_{i=0}^{N_{hits}} Q_i (t_i - t_{vtx}) \end{aligned} \quad (F.1)$$

F.7.2 3D Start Point Reconstruction

The 3D start point is reconstructed by taking the Y-plane reconstructed 2D start-point and projecting it onto the reconstructed 3D direction to recover the missing y coordinate. This is done in practice by finding the (Y,Z) intersection point between the two wires associated to (1) the 2D collection-plane start point and (2) the induction-plane wire associated to the collection-plane start-point projected on the shower's 3D direction. The X coordinate is reconstructed from the time-tick associated to the start-point on the collection-plane.

F.7.3 Energy Reconstruction

The shower energy is reconstructed by integrating all charge associated with the collection-plane hits belonging to the γ shower, and converting this quantity to MeV by applying the constant

calorimetric energy conversion of equation C.8 derived and discussed in section C.2.

F.7.4 Detector Response Non Uniformity Correction

The variation in response across the TPC volume is accounted for by correcting for spatial non uniformities in detector response according to the measurements obtained in section C.3. Each reconstructed collection-plane hit associated with a shower is assigned a 3D position with X and Z coordinates from the drift and wire information of the hit, and Y obtained by extending the shower start point in the direction of the reconstructed shower momentum for a distance equal to the 3D distance separating the hit in question to the shower start point. Provided with the XYZ charge coordinate, the corrected charge is given by

$$Q_{corr}(xyz) = Q \times \frac{Q_{TPC}}{Q(xyz)} \quad (F.2)$$

Where Q_{TPC} is the median detector response across the entire detector and $Q(xyz)$ is the response measured in the voxel which contains the xyz point.

F.7.5 Shower Containment Correction

The fact that neutrino interactions are uniformly distributed in the detector volume, combined with the ~ 25 centimeter conversion distance of photons means that a considerable number of photons from π^0 decay will deposit some fraction of their energy outside of the detector volume, causing it to go undetected. In order to account for this when reconstructing the photon energy we study, for a sample of γ showers from simulated π^0 decays, the fraction of shower energy deposited in the detector volume as a function of the observable r : the 3D distance between the showering point (where the photon converts) and the TPC boundary in the shower's direction. This distribution is shown in figure F.9. Black points represent the measured truncated mean for each vertical slice in r , with error bars denoting the standard deviation on the distribution. The red line is the result of a fourth order polynomial fit to these points, expressed in equation F.3. While the containment correction does not do much to improve the energy resolution for photons which convert close to the detector boundary, as indicated by the large spread in the distribution, it does help recover the correct energy scale for the reconstructed photons. Using a sample of BNB-induced π^0 events to estimate this correction is essential because the fraction of energy contained

as a function of r in figure F.9 depends significantly on the energy spectrum of the showers.

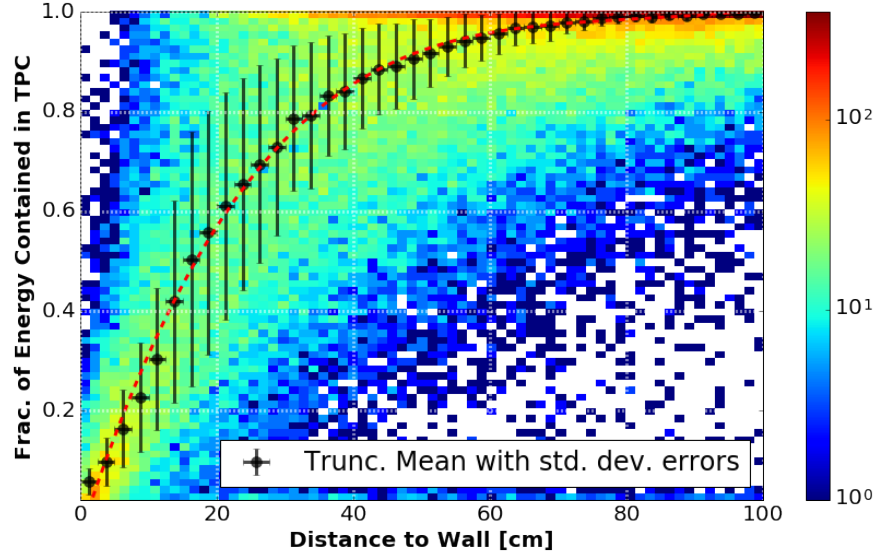


Figure F.9: Heatmap showing the fraction of energy deposited within the TPC over the total shower energy as a function of the 3D distance between the photon conversion point and the TPC boundary, measured in the direction of the photon’s momentum. Black points denote the truncated mean value obtained from each vertical slice, and the error bars indicate the spread in the underlying distribution. The red line is a fourth order polynomial fit to the points, expressed in equation F.3. Heatmap scale is logarithmic.

$$f = -1.039E - 8 \times r^4 + 4.34E - 6 \times r^3 - 6.47E - 4 \times r^2 + 4.224E - 2 \times r - 4.999E - 2 \quad (\text{F.3})$$

F.8 Shower Quality Filters

Throughout the shower-reconstruction chain a sequence of quality checks are applied to avoid reconstructing showers which are probably not associated to a true γ from a π^0 decay from the neutrino interaction vertex. Showers are excluded from the reconstruction chain if:

- No reconstructed 2D start-point is associated to the collection-plane clusters.
- The reconstructed 3D start point is found to lie outside of the TPC volume.
- The reconstructed 3D direction projected on the collection-plane, and the charge-weighted 2D vector computed on the collection-plane by performing a charge-weighted vector sum

connecting each cluster's 2D hit to the 2D start-point cluster coordinates disagree in angular direction by more than 25 degrees. This cut is effective at removing showers associated with charge uncorrelated with the neutrino vertex, such as from Michel electrons or other activity which happens to fall within the 2x2 meter ROI.

Fig. F.10 shows the same example event of figures F.5, F.6, and F.7 after the shower reconstruction chain described is run.

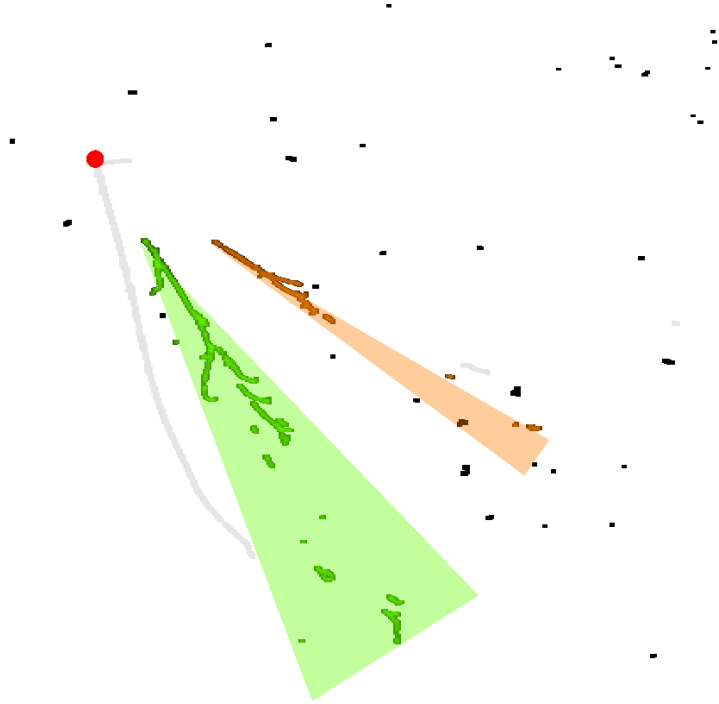


Figure F.10: Example event displaying reconstructed showers associated to the two γ s from the π^0 decay. The showers, shown as green and orange cones are overlayed on hits with corresponding colors associated to the two showers on the collection plane. The cones displayed are associated with a length and opening angle calculated from the hits associated to the shower, but these quantities are not used at any point in our reconstruction.

F.8.1 Shower Reconstruction Performance

The reconstruction performance is profiled in this section, with a focus on the quantities which have the most impact on the ability to identify π^0 events, and reconstruct their kinematics. These studies are performed on a simulated sample of CC $1\pi^0$ + cosmic events.

The efficiency for reconstructing γ showers is shown, as a function of the true γ energy deposited in the TPC, in figure F.11. Beacuse each event has two true γ s from a π^0 decay and a variable number of reconstructed photons, reconstructed-to-truth photon matching is performed by finding, for each true photon, the reconstructed shower with the most compatible 3D direction. The reconstruction efficiency is defined as follows:

$$\frac{\text{reconstructed showers with 3D direction within } \theta \text{ degrees of truth}}{\text{total photon showers at a given energy}} \quad (\text{F.4})$$

The efficiency is shown for a minimum 3D angle agreement of 20, 10, and 5 degrees.

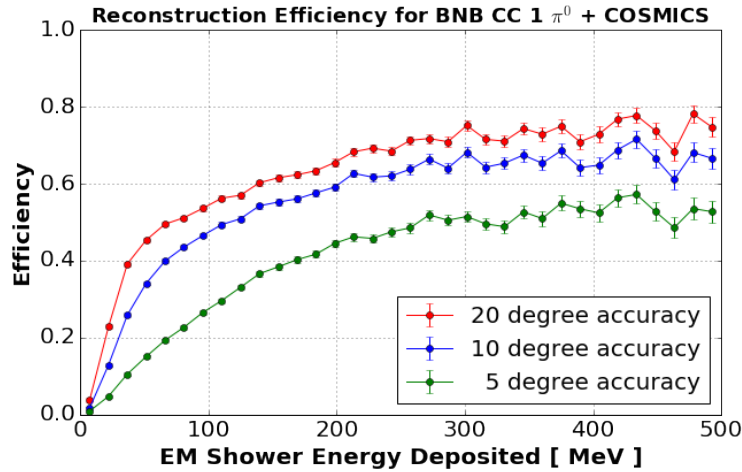


Figure F.11: Reconstruction efficiency for photons from π^0 decay.

The angular resolution, measured as the difference in 3D angle between the true shower direction and the direction of the most compatible reconstructed 3D shower is shown in figure F.12. The mean, median, and truncated mean of the distribution are reported.

Finally, the energy reconstruction is profiled. First the reconstructed vs. true γ energy is profiled to measure the reconstructed energy bias, as shown in figure F.13. As a function of true energy, the truncated mean reconstructed energy is found, indicated by the red points in the figure. These points are then fit to a line, obtaining a slope of 0.79, indicating a bias of 21%.

The measured bias is used to convert the reconstructed energy to a corrected energy:

$$E_{corr} = \frac{E_{reco} - \alpha}{\beta} \quad (\text{F.5})$$

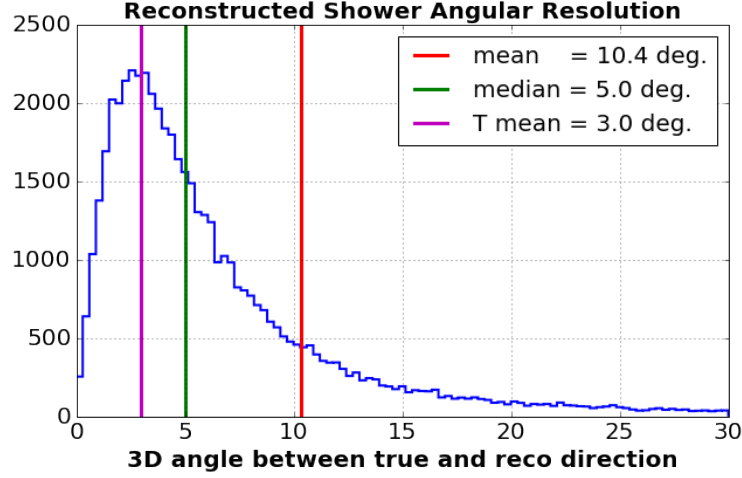


Figure F.12: Angular resolution for reconstructed γ showers.

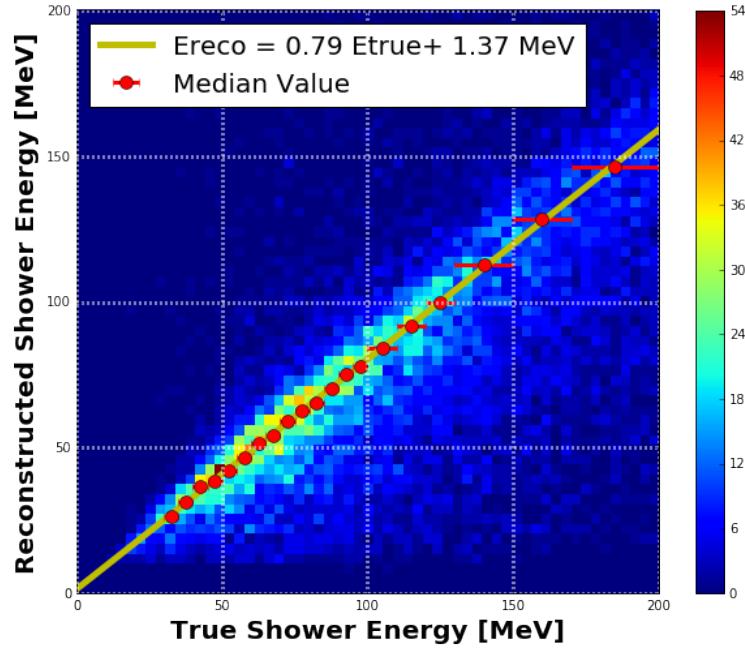


Figure F.13: Reconstructed vs. true photon energy. Red points represent the obtained truncated mean of the distribution of reconstructed shower energies for each true energy bin. The yellow line is the result of a linear fit to the data-points.

With α and β the intercept (1.37 MeV) and slope (0.79) respectively.

After applying this correction the fractional energy difference in bins of true energy is fit to a Gaussian plus exponential distribution, as shown in figure F.14. This functional form allows us to better model the one-sided impact of clustering and hit-thresholding on the energy reconstruction, and is presented in detail in appendix G. Three quantities profiling the energy reconstruction are

extracted: the mean and width of the Gaussian distribution, and the exponential contribution k to the distribution. These distributions, along with the obtained fit parameters and χ^2 values are shown.

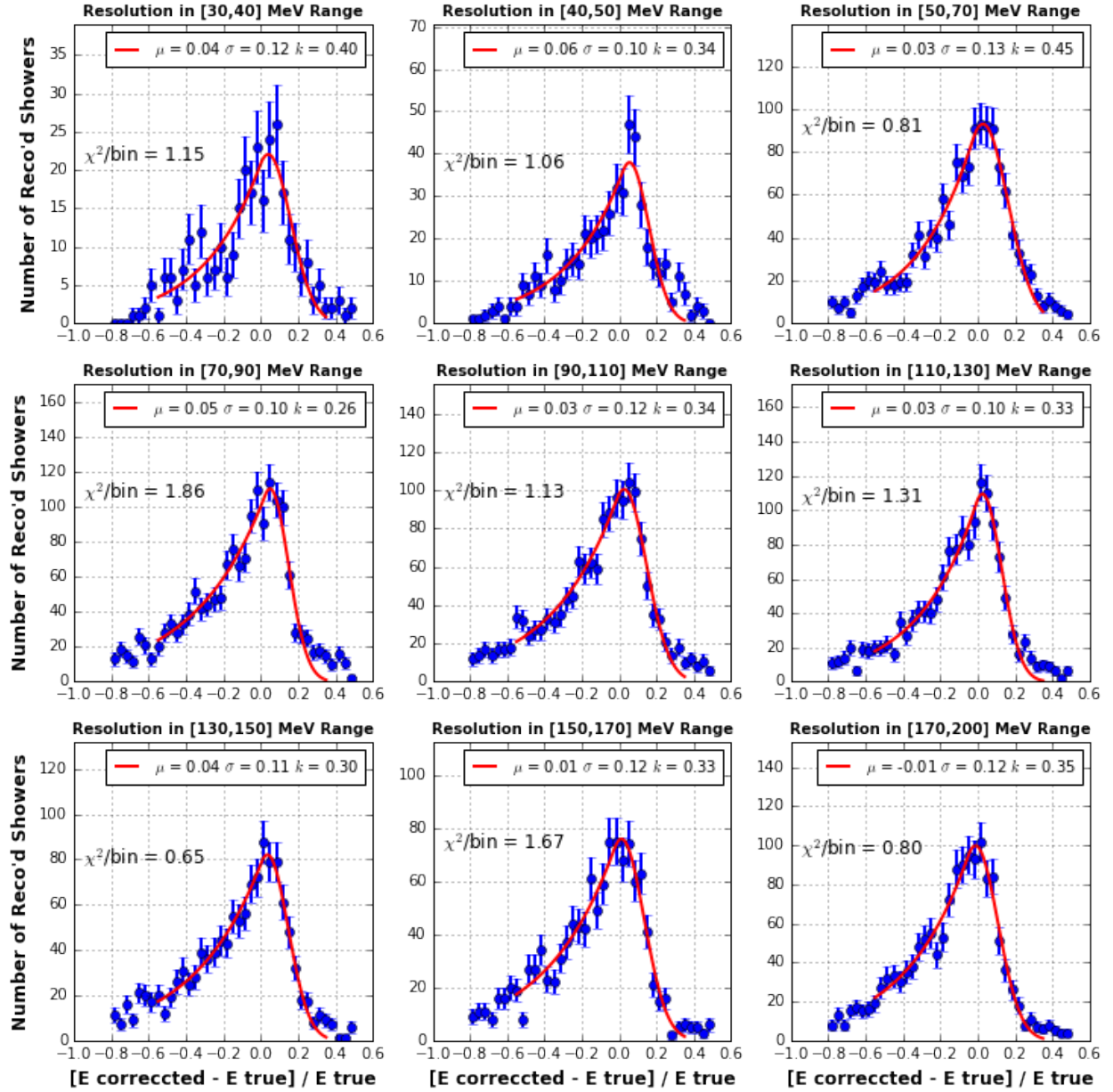


Figure F.14: In bins of true energy the fractional energy resolution, measured as the difference between reconstructed and true energy, over the true energy, is plotted. The distributions are fit to a Gaussian plus exponential distribution. The fitted Gaussian mean (μ), width (σ), and exponential contribution to the distribution (k) are shown, along with the χ^2 per bin from the fit.

The obtained fit parameters, with their associated uncertainties, are reported as a function of

photon energy in figure F.15. The obtained resolution parameters show little variation. The measured bias is constrained below 5%, with larger biases at lower energies. The Gaussian width of the distributions are approximately 10%, with the k parameter (indicating the contribution to the distribution modeled by the exponential) equal to ~ 0.3 - 0.4 . A k value of 0.3-0.4 corresponds to approximately 40-50% of all entries modeled by the exponential component of the distribution.

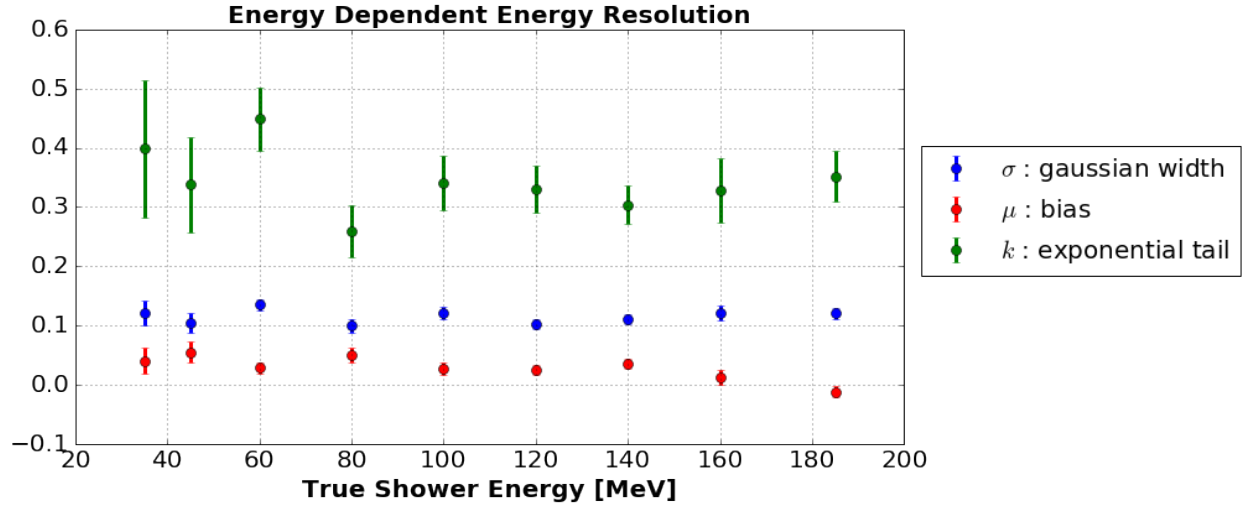


Figure F.15: Resolution fit parameters, shown in figure F.14, as a function of true photon energy.

Appendix G

Modeling Energy Loss Impact on EM Shower Energy Resolution

The nature of energy loss by EM showers causes the calorimetric energy reconstruction to be biased and exhibit significant negative tails in the distribution of reconstructed minus true energy. The primary contributions to this effect are due to energy thresholding and the impact of charge-clustering which hampers the ability to identify all charge deposited by an electron or photon. The bias and asymmetry of the energy reconstruction are important factors which will impact neutrino energy reconstruction and therefore must be accounted for. Specifically, the Gaussian modeling of energy resolution does not fully capture these effects and therefore may cause a systematic bias in the treatment of EM energy reconstruction. We propose the use of a different functional form to study the impact of detector and reconstruction effects on EM shower energy reconstruction: a Gaussian plus negative-tail exponential distribution (referred to as GaussExp), as presented in reference [87]. This function, reproduced in equation G.1 and plotted in figure G.1 for several input parameters, can better model the significant impact of thresholding and clustering on the energy reconstruction and provide a meaningful quantitative interpretation of their impact on the energy resolution.

$$\begin{aligned}
f(x, k, \mu, \sigma) &= e^{-\frac{1}{2}\left(\frac{x-\mu}{\sigma}\right)^2}, \text{ for } \frac{x-\mu}{\sigma} \geq -k \\
&= e^{-\frac{k^2}{2} + k\left(\frac{x-\mu}{\sigma}\right)}, \text{ for } \frac{x-\mu}{\sigma} < -k
\end{aligned} \tag{G.1}$$

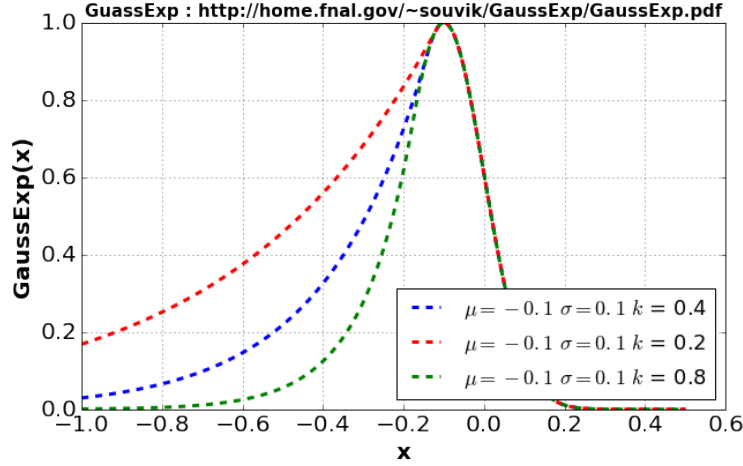


Figure G.1: GaussExp function for $\mu = \sigma = 0.1$ and different values of k .

The GaussExp function has three inputs: the mean and width of the Gaussian (μ and σ respectively), as well as a parameter which models the negative exponential tail: k . Different values of k determine the fraction of entries in the distribution which are not modeled by the Gaussian component alone, and impacts the mean and median of the full distribution. A large value of k means that the exponential component of the total distribution is small.

Figure G.2 shows the contributions to the total distribution which are modeled by the exponential component of the function. This is determined as the fraction of the total area of the distribution under the GaussExp function but above a simple Gaussian with the same μ and σ . The curve of the fractional area is shown for different values of k , and for three different values of the Gaussian width σ . There is generally little variation in the fractional contribution for different values of σ , meaning that the parameter k can be easily interpreted independently of the Gaussian component of the distribution. We note that for values of $k \sim 0.3$ approximately 50% of all entries are modeled by the exponential component of the distribution, 20% for $k \sim 0.6$, and 60% for $k \sim 0.2$.

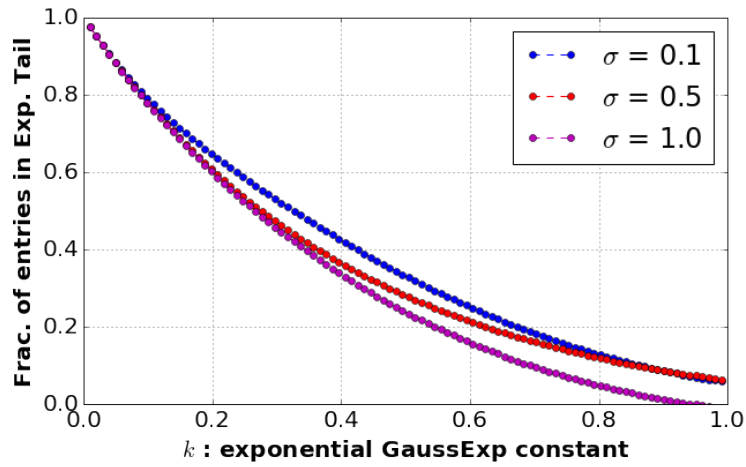


Figure G.2: Fraction of all entries in the GaussExp distribution modeled by the exponential component, calculated as the fraction of the total distribution's area not included by a Gaussian with the same μ and σ . This fraction is plotted as a function of k for different values of the Gaussian width σ .